Chair of Energy Network Technology

Doctoral Thesis

The Effects of Energy Storage Systems and Sector Coupling on the Integration of Intermittent Energy

Dipl.-Ing. Benjamin Böckl, BSc

December 2019

AFFIDAVIT

I declare on oath that I wrote this thesis independently, did not use other than the specified sources and aids, and did not otherwise use any unauthorized aids.

I declare that I have read, understood, and complied with the guidelines of the senate of the Montanuniversität Leoben for "Good Scientific Practice".

Furthermore, I declare that the electronic and printed version of the submitted thesis are identical, both, formally and with regard to content.

Date 12.12.2019

Signature Author
Benjamin, Böckl

ACKNOWLEDGEMENTS

First and foremost, I'd like to thank my head of chair and first supervisor Prof. Dr. Thomas Kienberger. He offered me this Ph.D. candidate position at a time where the Chair of Energy Network Technology was just recently founded and gave me a lot of opportunities to contribute to the shaping of this institute. Due to his trust and his attitude towards independent working, I was able to gain experience in leading research projects with industry partners, in planning and establishing the in-house energy laboratory and tackling complex challenges in research fields formerly completely new to me. I am very thankful for these opportunities and his enthusiasm towards the best possible guidance of my work in countless discussions and Ph.D. talks. I also would like to express my gratitude to Prof. Dr. Robert Schürhuber, who agreed to examine this Doctoral thesis.

My deepest appreciation goes to all my colleagues at the Chair of Energy Network Technology at Montanuniversität Leoben. I truly enjoyed working here and experiencing this atmosphere of open doors, intense discussions, ever-present helpfulness and true collegiality. Additionally, I was lucky to work in many research projects with a lot of different research partners and industry representatives. Thank you for all the constructive work within these projects.

I also owe a very important debt to all students, who wrote their Master's Thesis under my supervision or participated as staff and significantly contributed to projects in the scope of this Doctoral thesis. In particular, I want to thank DI Matthias Greiml and DI Lukas Leitner, who contributed a great deal to the implementation of the HyFlow modelling framework.

My time here in Leoben was shaped and influenced by wonderful friends and especially extraordinary flatmates. Thank you for making my time here so enjoyable and entertaining, but also for giving me someone to moan at, when work was not progressing according to plan. I will always keep you in best memory.

I am deeply thankful for having such a supportive and caring family. My deepest appreciation goes to my mother Anna Maria Böckl, my father Robert Hilger and my grandparents Helga & Herbert Böckl. Thank you for your unconditional support and all your firm beliefs in me. Without you, I would not be the person I am today.

Above all, I would like to thank my beloved fiancée Dominique Heuritsch. Performing the presented research, publishing it in Journal papers and writing this Doctoral thesis was undoubtedly the most challenging task in my working life. Thank you for your full endorsement to pursue this career path, despite mostly living apart for four additional years. I am grateful to you for keeping me optimistic in times of setbacks and for your understanding of my working priorities including countless night shifts, especially in the last year. You were my anchor and my best friend throughout the entire time of this Ph.D.

ABSTRACT

Global initiatives to decarbonize the energy system combined with technological innovation lead to a major expansion of the renewable energy generation capacity around the globe. This development brings advantages, but also new challenges for the overall energy system. One major challenge is the intermittency of renewable electricity sources, such as solar- and wind energy. An extensive expansion of these energy sources leads to fluctuating residual loads. This means that times with a lack of electricity from renewable energy sources can rapidly alternate with times of electricity surplus.

This Ph.D. thesis analyzes the effects of fluctuating residual loads on various hierarchical levels. The first considered level is a single electricity consumer with an assigned load profile, referred to as *Single-Nodal system*. The major goal of the work at this level is to develop a methodology, which determines the ideal PV generation- and energy storage capacity for any corresponding load profile. This task is performed by a novel mathematical optimization methodology, with the objective of minimizing the system size for a given degree of self-sufficiency within the considered single node. The optimization is applied to a wide range of household consumer types. All corresponding results are presented in this work.

The fact that energy systems consist of numerous different consumers and suppliers, interconnected by electricity-, gas- and district heating grids, leads to the second introduced modelling framework, called *HyFlow*. It is designed to consider multiple nodes of the energy system across all considered energy carriers. Fluctuating residual loads in these nodes lead to quickly changing load flows between them, with possible grid congestions. The presented modelling framework calculates these load flows for all considered grids, based on physical principles. This allows for the analysis of the locations and times of grid congestions in energy systems of all sizes. Furthermore, *HyFlow* is capable of evaluating the effectiveness of possible solution strategies to deal with these congestions, by implementing energy storage systems and cross-energy carrier sector coupling technologies. These technologies can be freely placed and configured in the presented software. This technical, scenario-based approach helps to identify weak spots in energy grids and allows for the analysis of different energy system scenarios with a broad range of spatial depth. The analyzed scenarios can contain increased renewable energy sources, but also changed consumer load profiles of individual energy carriers, due to a possible shift caused by electrification. Examples for this shift in consumption are electric vehicles, heat pumps or industrial processes, as well as technologies for balancing generation and demand. Results achieved with *HyFlow*, therefore, may provide valuable decision-support for grid operators and political decision-makers.

KURZFASSUNG

Internationale Bestrebungen zur Dekarbonisierung des Energiesystems, gepaart mit rascher technologischer Weiterentwicklung führen derzeit global zu einem massiven Ausbau von erneuerbaren Energieerzeugungskapazitäten. Diese Entwicklung bringt Vorteile, aber auch neue Herausforderungen für das Energieversorgungssystem mit sich. Eine der Hauptherausforderungen ist die Volatilität erneuerbarer Energieträger, wie der Sonnen- und Windenergie. Der starke Ausbau von Technologien zur Nutzung dieser Energiequellen führt zu stark schwankenden Residuallasten im Energieversorgungssystem. Das bedeutet, dass sich zukünftig Zeiten mit Energiemangel aus erneuerbaren Quellen mit Zeiten von Energieüberschüssen schnell abwechseln werden.

Die vorliegende Dissertation analysiert diese fluktuierenden Residuallasten und deren Auswirkungen auf verschiedenen Hierarchieebenen des Energiesystems . Die erste Ebene, die in der Arbeit betrachtet wird, ist ein Einknoten-System bei dem der elektrische Energiebedarf als Lastprofil vorgeben ist. Das Hauptziel, das dabei in der Arbeit verfolgt wird ist die Entwicklung einer Methodik, die bei vorgegebenem Eigendeckungsgrad eine minimale PV-Erzeugungs- und Energiespeicherkapazität ermittelt. Dazu wird eine neuartige mathematische Optimierungsmethodik vorgestellt, und auf die elektrischen Lastprofile zahlreicher Haushaltstypen angewendet.

Neben dem Einknotenmodell, wird in der Arbeit eine Mehrknoten-Simulationsumgebung präsentiert, die über mehrere hierarchischen Systemebenen hinweg ein energieträger-übergreifendes Zusammenwirken von Erzeugern, Verbraucher und flexiblen Elementen wie Speichern ermöglicht. Fluktuierende Residuallasten, die sich in den jeweiligen Systemknoten durchaus unterscheiden, führen zu rasch wechselnden Lastflüssen. Die neu vorgestellte Simulationsumgebung *HyFlow* berechnet diese Lastflüsse für die drei leitungsgebundenen Energieträger, Strom, Gas und Fernwärme, und erlaubt somit in allen betrachteten Hierarchieebenen eine zeitliche und örtliche Analyse von Netzüberlastungen. Zudem können mit *HyFlow* unterschiedliche Lösungsstrategien zu deren Vermeidung verglichen werden. Dabei kommen Technologien wie Energiespeicher, Sektorkopplung oder Laststeuerung zur Anwendung, die sich in *HyFlow* beliebig einsetzen, verorten und konfigurieren lassen. Szenarien in unterschiedlicher hierarchischer Tiefe ermöglichen es dabei über mehrere Netzebenen hinweg, u.a. eine vermehrte Nutzung fluktuierender Energiequellen, ein verändertes Lastverhalten in einzelnen Sektoren oder einen verstärkten Einsatz von flexiblen Elementen, wie z.B. Energiespeichern, zu untersuchen. Die mit *HyFlow* erzielten Ergebnisse können daher als wertvolle Entscheidungshilfe für Netzbetreiber und politische Entscheidungsträger dienen.

TABLE OF CONTENTS

NOMENCLATURE

List of Abbreviations

AC	Alternating Current
AEL	Alkaline water electrolysis
BESS	Battery Energy storage system
CHP	Combined Heat and Power
µCHP	Micro Combined Heat and Power
CP	Convex Programming
DC	Direct Current
DFT	Discrete Fourier Transform
DoD	Depth of Discharge
DR	Demand Response
DSG	Degree of self-generation
DSS	Degree of self-sufficiency
ES	Energy storage
ESS	Energy storage system
EV	Electric Vehicle
g.l.	Gradient limit
G2H	Gas-to-heat
G2P	Gas-to-power
GIS	Geographical Information System
H2P	Heat-to-power
HE	Hybrid Element
HP	Heat pump
IQR	Interquartile range
KPI	Key Performance Indicator

Nomenclature

LFC	Load Flow calculation
LP	Load profile
LTST	Local true solar time
MES	Multi Energy System
MPC	Model Predictive Control
MPTT	Maximum power point tracker
n.a.	Not available
NaN	Not a number
NPV	Net Present Value
NTC	Net Transfer Capacity
OPF	Optimal power flow
ORC	Organic Rankine Process
P2G	Power-to-gas
P2H	Power-to-heat
p.u.	Per unit
PEMEL	Proton exchange membrane electrolysis
PV	Photovoltaic
RES	Renewable energy sources
SC	Sector Coupling
SCR	Self-consumption ratio
SLP	Standardized Load Profile
SynLP	Synthetic Load Profile
SMES	Superconducting magnetic energy storage
SOE	State of Energy
SOEC	Solid oxide electrolyzer cell
STC	Standard Test Conditions

LIST OF FIGURES

LIST OF TABLES

List of Tables

1 INTRODUCTION

The global energy supply system is currently experiencing a shift towards integrating more renewable energy sources (RES). There are multiple reasons for this energy transition away from fossil fuels and towards RES. One of the main drivers is climate change, caused by CO_2 emissions, which are linked to the intense usage of fossil fuels. Global coalitions, like the IPCC and other similar organizations have been founded. Today's goal is to reduce climate-relevant emissions significantly to limit global warming to well below 2 °C. Other reasons to increase the share of RES are the conservation of natural resources, higher independence from energy imports by an increased local generation with RES and advantages in health-related issues such as fine dust. Additionally, countries that proactively push renewable energy (first movers) expect their developed energy technology to be exported to other regions, which could lead to economic benefits and an increased level of competitiveness. [1–3]

The major global driver to push RES and cut back on fossil fuels in the energy supply, however, remains the issue of global warming. Especially the agreements of several United Nations Climate Change Conferences (COP) are the main framework for breaking down goals on a more regional level, like the European Union or national initiatives such as the #mission2030 for Austria. Table 1-1 shows an example of political targets in the European Union and Austria. [3–7]

Table 1-1: Summary of EU goals and national targets of Austria in the energy transition

Scope and year of application [Location / Year]	Greenhouse gas Reduction [%]	Share of Renewable Electricity [%]	Share of Renewable Energy [%]
EU 2020	-20 %[1]	n.a.	+20 % (increase)
EU 2030	-40 %	n.a.	+27 % (increase)[2]
EU 2050	-80-95 %	n.a.	n.a.
Austria 2030	-36 %[3]	100 % (net balance)	45-50 % (total)

[1] All EU goals are referred to levels of 1990

[2] The European Parliament demands to increase the target value to 35 %. Negotiations between the European Parliament and the Council are ongoing.

[3] Compared to levels of 2005

However, even with all the potential benefits and necessities that come with an energy transition, there are major challenges that need to be addressed in order to reach the political targets. These challenges are related to the main goals of energy supply: energy security, energy equity and environmental sustainability. Energy security describes the reliable supply of the current and future energy demand at all times. Energy equity measures the affordability and accessibility of energy across the population. Environmental sustainability encompasses the achievement of efficient energy usage from renewable and low-carbon sources. [8] This thesis focuses mainly on energy security and environmental sustainability, while the economic aspects are only considered superficially.

One of Austria's main energy-related goals is to cover 100 % of its total electricity consumption (national net balance) from local renewable energy sources by 2030. In order for Austria to reach this goal of the #mission2030 within the short time span of approximately one decade, it needs to multiply its usage of volatile RES in the electric generation. Calculations by the Association of Austrian Electricity Companies indicate that an additional yearly energy output of 6 TWh in hydropower, 12-15 TWh in wind power and 12-14 TWh in solar power is necessary to fulfill this target. Figure 1-1 demonstrates the substantive volume of the required generation capacities. [3,9]

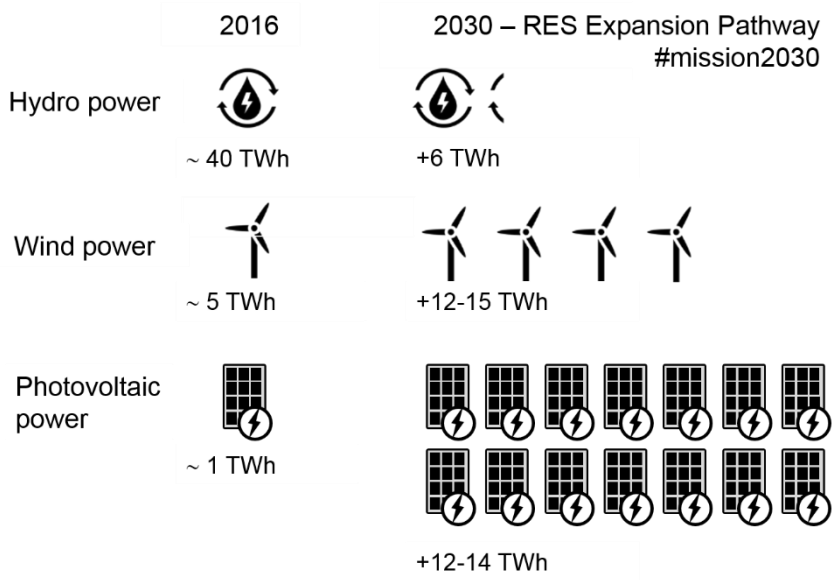

Figure 1-1: Energy generation of volatile RES (2016) and the pathway to fulfilling the #mission2030 [9–11]

The high annual expansion rate of RES generation capacities is not the only challenge regarding this specific goal. Additionally, the overall profile of Austria's residual load will have a completely different shape. Residual load is defined as the total load minus the fluctuating,

renewable generation at a specified time. A detailed definition follows in section 3.3. While negative residual loads are rare events nowadays, it might become the rule rather than the exception. By scaling up the generation data of 2016 [10,11] according to the expansion plan of [9], negative residual loads can be expected in more than 50 % of the time, over the period of one year. Figure 1-2 shows this change of the residual load. The x-axis represents the day of the year, while the y-axis indicates the time of the day in hours. The illustration on the left represents the current situation of 2016, and the diagram on the right stands for the described pathway to reach the goal of #mission2030, as illustrated in Figure 1-1. The colors symbolize the state of the residual load at a specific time. While blue areas represent positive residual loads with a residual demand in energy, green areas represent an approximately balanced energy generation and demand in Austria. Shades of red represent times of a higher fluctuating generation compared to the simultaneous demand. The scaling of the colors is identical in both illustrations. One can see that in Austria's current energy supply, residual loads tend to be positive or balanced, which means that additional electricity has to be imported or supplied by conventional energy generation technologies, in most times of the year. Negative residual loads appear only on rare occasions, especially in times with simultaneously high generation of hydropower and wind power, combined with lower electric consumption, for instance in summer nights. The negative peaks in today's residual load amounts to approximately -2.5 GW, and the positive values to just under 8 GW. On the contrary, at the illustration on the right of Figure 1-2, the negative residual loads are widespread and tend to accumulate in the midday hours of the summer months. In peak hours of the year, the negative residual loads reach less than -15 GW, while positive residual loads are not so widespread, but still reach almost the same peaks as today. In order to put these numbers into perspective, it has to be noted that the current annual peak network load amounts to approximately 10.8 GW. [10]

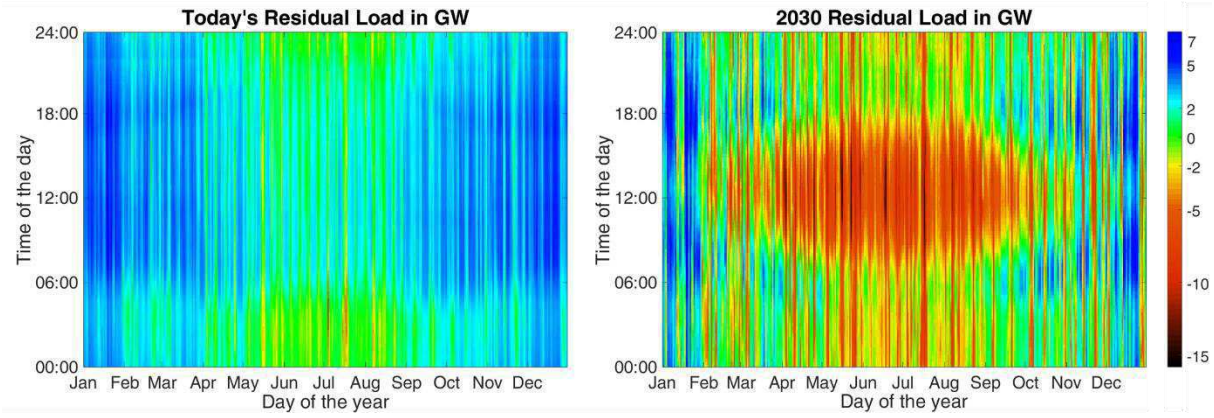

Figure 1-2: Comparison of the residual load in Austria of 2016 and the possible residual load of 2030 (based on the #mission 2030 goal) – own illustration based on data of [3,9–11]

In addition to the time-dependent variations of the residual load, there is a spatial dimension as well. While some areas perhaps show an energy surplus, others might experience a demand. [12] These regional imbalances need to be compensated by the grid, which will play a key role to solve this challenge.

Especially the frequent occurrence of surplus generation will be challenging in the future. Today in the rare event of excess electricity, the surplus is transferred to regions with positive residual loads via the integrated European electricity grid. As more and more countries set an agenda of expanding their share of RES, it can be expected that it will become more difficult to export the surplus generation to neighboring countries, which might have an electricity overcapacity due to seasonal influences as well. This is a strong driver for the so-called flexibility options, which are a major topic in energy system research. The main elements of flexibility options are energy storage systems (ESS), sector coupling (SC) and demand response (DR). [13] In this work ESS are defined as units, where the energy input and output consists of the same energy carrier. Sector coupling units convert energy from one energy carrier to another. An example is a gas turbine, which converts chemical energy in the form of natural gas into electricity and possibly heat. However, both flexibility options can also be combined. It is for example possible to use electricity to power an electrolyzer, which is capable of producing hydrogen. A subsequent storage unit of this hydrogen would complete a combination of a sector coupling technology with an energy storage unit. Demand response (DR) refers to an active intervention in the current energy load in order to react to a specific grid-related situation. A more detailed definition and explanation of the operating principle of ESS and SC units, as well as DR, is given in section 2.4.

This present thesis focuses on the effects of energy storage and sector coupling on generic energy systems. In doing so, this work takes volatile generation, individual load profiles and especially energy infrastructure of all main grid-bound energy carriers: electricity, natural gas and district heating into account. It demonstrates the effects of flexibility options for single users and larger energy systems with multiple consumers and generation facilities based on technical indicators. Examples for technical indicators are self-sufficiency, energy imports or exports, as well as associated load flows and possible grid congestions.

The following sections 1.1 and 1.2 contain a short summary of all findings within the scope of the conducted literature analysis and the derived research gap addressed in this work. The main purpose of section 1.3 is to guide readers through the structure of the thesis and to list the most relevant publications by the author, where parts of this thesis content are already published.

1.1 Summarized State of Research

The introduction presents the main occurring challenges that may arise with the expansion of renewable energy generation. In this thesis, two solution strategies on various hierarchical levels are introduced. The first approach is the appropriate design of decentral energy generation technologies and the additional effect of distributed ESS. Within this scope, it has to be analyzed how these elements can be ideally sized in order to align user-oriented optima and system-oriented implementation of Photovoltaic generation combined with ESS. The second approach is the analysis of grid congestions and the development of a tool, which is capable of evaluating the capability of flexibility options in order to enable the maximal integration of fluctuating RES.

Before tackling the challenge with the described solution concepts, a thorough literature analysis is performed to prevent overlapping research approaches. It is absolutely key to address the universal challenge with novel tools in order to really add scientific value and knowledge to the research field. The detailed literature analysis follows in section 2, while this extract only aims to be an extract of the analysis addressing the key findings of the current state of research. This helps to define the exact research gap and frame the corresponding research questions of this work in the next section. The following two paragraphs aim to summarize the key findings of both solution approaches.

There are numerous publications dealing with the ideal size of decentral Single-Nodal energy generation combined with ESS. The most widely used technology for energy consumers to become so-called prosumers is photovoltaic energy generation. PV systems can be divided into stand-alone applications and grid-connected applications. While the sizing of stand-alone plants is mostly based on a trade-off between reliability and cost, the sizing of the more relevant grid-connected PV-storage plants is to the greatest part based on economic reasons only. This has several disadvantages. One major problem with sole economic optimization is the replicability and transferability of the results. Electricity prices, feed-in tariffs, tax incentives and investment subsidies are regionally very different. Additionally, the unpredictability of these politically influenced parameters mean that it is difficult to calculate a precise optimization result that could be valid for a future time-period of 10-20 years. Additionally, the literature analysis shows that more than 80 % of customers of a PV-battery system are not solely interested in the economic payback of their investment, but want to contribute to the energy transition. However, publications dealing with the dependency between technical or system effects on the energy system and the size of the PV plant and the corresponding size are the absolute exception. Only one available publication examines the

impact of the PV-storage system size and different technical KPIs. However, this is only performed for one household load and there is no sizing methodology or sizing optimum based on technical parameters enclosed. This very research gap will be addressed in this work. A holistic tool being able to determine the optimal size of PV-storage plants, based on the individual load behavior shall be developed and applied to various consumer types. The detailed research questions regarding this topic are to be found in section 1.2.

To evaluate arising load flows between multiple energy generation facilities and energy consumers, energy transport models and the corresponding load flow calculation (LFC) models need to be established. The design of our current energy systems is based on these LFC, which are proven concepts. There are various specialized software solutions and well-documented methodologies to simulate occurring load flows for all individual energy carriers. However, these software tools are not able to interconnect energy carriers. In recent years, publications in the field of integrated energy systems, covering more than one energy carrier became more and more popular. These integrated energy approaches are often labelled Multi Energy Systems (MES). The conducted literature analysis contains a characterization and classification methodology of MES. One type of MES is referred to as grid-based MES, which is the most relevant type of MES for this work. However, the implemented LFC of most grid-based MES is based on so-called type 1 or type 2 LFC (for more details see section 2.6.1). This type of LFC is not based on physical models. Other concepts like optimal power flow (OPF) calculation offer the usage of LFC models based on the laws of physics and can be used to link energy grids with conversion efficiency units, called energy hubs. However, these approaches are mathematical optimization models with the goal of optimal energy dispatch only. They are not suitable as operational models, do not allow the implementation of user-oriented or system-serving control strategies and cannot combine more than one level of energy supply infrastructure. Additionally, there are limitations in spatial and temporal resolution, due to the high computational time needed for the mathematical optimization. Therefore, studies claim that OPF approaches with a higher spatial coverage and resolution do not account for system operation and infrastructure details, as they are usually only adapted as economic dispatch models with highly simplified LFC methods. This work addresses exactly this research gap by creating an operational, grid-based MES, which is capable of modelling physical load flows of the three relevant energy carriers and offer interconnections between them. These interconnections and other flexibility options, such as ESS, should be operated on a rule-based algorithm, which should be adaptable to work user-oriented or system-oriented (based on the current grid status). The specific research questions addressing the described research gap are found in section 1.2.

1.2 Research Questions

The addressed research gap focuses on the effects of flexibility options, such as ESS and sector coupling units on energy systems with high shares of RES. The related research questions are divided into two major parts. The first part deals with the effects within a single node. Single-Nodal energy systems do not consider energy transport and assume that the load, generation and ESS are located in a single node. The second part should cover the effects of these flexibility options in interconnected energy systems with multiple nodes, so-called Multi-Nodal energy systems. A more detailed definition with corresponding illustrations of Single-Nodal and Multi-Nodal systems can be found at the start of section 3. It should be emphasized that some research questions are related to a methodology development rather than for quantitative results. This means that some answers to specific research questions are to be found in section 3 – Modelling of the energy systems, rather than in section 4 – Application Results.

1.2.1 Single-Nodal Research Questions

The research questions deal with the influence of utilizing renewable, intermittent energy sources and energy storage systems in a single node. Especially the optimal sizing of renewable generation capacities and energy storage units is the primary interest.

Is it possible to find a methodology that optimizes the capacity of renewable generation units and the energy storage size regarding a given degree of self-sufficiency, based on technical parameters only?

- If possible, what are the quantitative results for ideal decentralized, renewable generation capacities and energy storage sizes in households? Is it possible to give general recommendations of ideal system sizes to different household types (e.g. Single household, Families, Pensioners)?
- How do emerging technologies, such as the usage of electric vehicles (EV) or sector coupling technologies (e.g. heat pumps), affect the ideal size of renewable generation capacity and energy storage size?
- If possible, are there differences between commonly used economic design optima? What are the reasons behind possible differences?

1.2.2 Multi-Nodal Research Questions

The research gap addressed in Multi-Nodal energy systems is the analysis of effects from integrating fluctuating electricity sources and the impacts of emerging technologies, such as electric vehicles or heat pumps, on the load flows of all energy grids. Possibly occurring grid congestions, determined by a load flow calculation, should be analyzed in terms of their temporal and spatial occurrence. Furthermore, the effectiveness of flexibility option integration, such as ESS and sector coupling technologies, to reduce these grid congestions shall be investigated. In addition to the relieving measures for the electricity grid, the implications of flexibility options on load flows of other energy grids (e.g. natural gas - or district heating grid) shall be considered, in order to gain a holistic picture of the overall energy grid infrastructure limitations. More specific research questions follow underneath:

How can a modelling framework be designed to model effects of integrating fluctuating energy sources on the load flows of all grid-bound energy carriers?

- How can energy storage systems and sector coupling elements be characterized and parameterized, in order to allow the user to implement all types of energy storage - and sector coupling technologies into the modelling framework? Is there a preferred control strategy of these flexibility options?
- Which indicators allow the user to quantify the effects on the overall energy system and compare load flows between interconnected nodes?
- How can load flows of all considered energy carriers (electricity, natural gas and district heating) be modelled and coupled, based on physical principles, with appropriate accuracy and acceptable computation time?
- Is it possible to develop the modelling framework in a generic approach that allows the user to model any kind of spatial scale from single household to a large region combined with any kind of temporal resolution?
- What kind of effects on the energy infrastructure can be expected from a high-level penetration of fluctuating energy sources into the grids? Are regular grid congestions to be expected in any type of typical settings of scales (stub line, city, region)?
- Which influence do energy storage systems and sector coupling elements have on energy systems at different spatial scales (stub line, city, region)? Are they capable of significantly relieving the grid from possible congestions?

1.3 Thesis Outline

The thesis is structured into five main chapters: The current chapter is the **Introduction**, which aims to present the needs and implied challenges of an energy transition and embeds the scope of the current research questions to the big picture.

The second chapter, **State of Technology & Research** presents the results of the conducted literature review. In the first part of this chapter the main fluctuating renewable energy generation technologies, common energy demand models, applied load flow calculations methods and the state of technology of available flexibility options are described. The second part deals with the state of research in sizing approaches of the renewable generation capacity and energy storage systems, different MES optimization methodologies with special regard to the consideration of grid limitations and sector coupling technologies.

In the third chapter, the developed **Methodology** is explained in detail to address the research questions. For this purpose, the established key performance indicators are defined in order to compare results between the conducted case studies. All components of the Single-Nodal model, including the physical model of the renewable generation, the energy storage system and grid integration, as well as the sizing and optimization methodology are presented within this section. Afterwards, the established Multi-Nodal modelling framework, named HyFlow, is explained in detail. All relevant components, such as grids, energy storage units, sector coupling technologies and overall operational modes are described and characterized. This chapter also contains the integrated load flow calculation methodologies of all considered grid-bound energy carriers (electricity, natural gas, district heating).

The **Results** chapter covers the outcome of the single node sizing methodology for renewable generation capacities and energy storage for different household profiles. A comparison of the determined technical optima to economical optima is also part of the results section. The Multi-Nodal part of this chapter defines three typical generic scenarios: a stub line, a municipality and a region including the municipality. It describes the input parameters of all case studies and analyses the effects of renewable generation on the grids, as well as the capability of integrated energy and energy storage systems to provide relief to the grid infrastructure.

This thesis concludes with the **Conclusion & Outlook**, where the lessons learnt and derived tasks for the future are described. Here, a final **Discussion** is given, with regards to the made assumptions and the limitation in scope.

1.4 List of Publications

A high share of this thesis content is already published in Journal papers and Conference Proceedings. The related publications are divided into “highly relevant” publications, where most of the content is included in this thesis and “partly relevant” publications, with partly overlapping content.

Highly relevant publications for this thesis:

- Böckl, B, Greiml, M, Leitner, L, Kriechbaum, L, Kienberger, T & Pichler, P 2019, 'HyFlow—A Hybrid Load Flow-Modelling Framework to Evaluate the Effects of Energy Storage and Sector Coupling on the Electrical Load Flows' Journal of *Energies*, Volume 12.2019, Nr. 5. https://doi.org/10.3390/en12050956
- Böckl, B, Leitner, L, Greiml, M & Kienberger, T 2019, Bedarfsermittlung von Energiespeichern und Sektorenkopplung durch hybride Lastflussberechnung. in Proceedings of 11. Internationale Energiewirtschaftstagung, Vienna, Austria
- Böckl, B & Kienberger, T 2019, 'Sizing of PV storage systems for different household types' Journal of Energy Storage, Elsevier, Jg. 2019, 100763, https://doi.org/10.1016/j.est.2019.100763
- Böckl, B & Kienberger, T 2018, Nutzergruppenabhängiger Photovoltaik-Heimspeicherbedarf. in 15. Symposium Energieinnovation, https://doi.org/DOI 10.3217/978-3-85125-586-7
- Vopava, J, Böckl, B, Kriechbaum, L & Kienberger, T 2017, 'Anwendung zellularer Ansätze bei der Gestaltung zukünftiger Energieverbundsysteme' Elektrotechnik und Informationstechnik : e & i, Jg. 3.2017, S. 238 – 245 https://doi.org/10.1007/s00502-017-0501-7
- Kienberger, T, Böckl, B & Kriechbaum, L 2016, 'Hybrid approaches for municipal future energy-grids' 10th International Renewable Energy Storage Conference, IRES 2016, Düsseldorf, Germany, 15/03/16 - 17/03/16
- Böckl, B, Kriechbaum, L & Kienberger, T 2016, Analysemethode für kommunale Energiesysteme unter Anwendung des zellularen Ansatzes. in 14. Symposium Energieinnovation: Energie für unser Europa. Technische Universtität Graz

Partly relevant publications for this thesis:

- Böckl, B, Kriechbaum, L, Kienberger, T, Wohltran, N, Hermann, R, Fritz, M, Rauter, R & Baumgartner, R 2019, Energieschwamm Bruck an der Mur: Projektbericht im Rahmen des Programms Stadt der Zukunft. Bd. 15/2019, Bundesministerium für Verkehr, Innovation und Technologie, Wien
- Grandl, T, Kienberger, T, Böckl, B & Pechtl, P 2018, 'Betrieb und Speicherbewirtschaftung einer "Closed-Loop" Power-To-Gas Anlage' Proceedings of EnInnov2018, Graz, Austria, 14/02/18 - 16/02/18, S. 1-11. https://doi.org/DOI 10.3217/978-3-85125-586-7

- Steinmüller, H, Tichler, R, Kienberger, T, Gawlik, W, Lehner, M, Muggenhumer, G, Kriechbaum, L, Böckl, B, Winter, A, Biegger, P, Fazeni, K, Goers, S, Vopava, J, Ellersdorfer, M, Medved, AR & Mayrhofer, J 2016, Smart Exergy Leoben
- Böckl, B 2016, 'Integration of fluctuating energy into the grid in consideration of multifunctional energy storage management' Poster “Future of a Common European Energy Strategy”, Frauenchiemsee, Germany, 29/06/16 - 3/07/16
- Karner, K, Böckl, B, Steinacker, S, Bärnthaler, J & Kienberger, T 2017, Smart City Judenburg durch Synergiepotenziale mit der Industrie. Klima- und Energiefonds
- Kriechbaum, L, Böckl, B, Vopava, J & Kienberger, T 2016, 'SmartExergy – Primary energy efficient and hybrid grid solutions for municipal energy supply systems', Hamburg, Germany, 15/09/16 - 16/09/16, ISBN: 978-3-658-15029-7, https://doi.org/10.1007/978-3-658-15029-7_21
- Böckl, B, Kriechbaum, L, Vopava, J & Kienberger, T 2016, „Eigenverbrauchssteigerung von Regionen: Sind Flexibilitätsoptionen bereits notwendig?“ Proceedings of Forum Econogy 2016 ISBN: 978-3-99062-036-6
- Böckl, B, Vopava, J, Kriechbaum, L & Kienberger, T 2016, Limitations of Integrating Photovoltaic Energy into Municipal Grids Excluding and Including Storage Systems. in T Ackermann & U Betancourt (Hrsg.), Proceedings of the 6th Solar Integration Workshop: International Workshop on Integration of Solar Power into Power Systems. S. 371, 6th Solar Integration Workshop, Vienna, Austria, 14/11/16, ISBN: 978-3-9816549-3-6

2 STATE OF TECHNOLOGY & RESEARCH

In this thesis, the literature review is divided into two main parts. The first part gives an overview of the most relevant technologies included in the modelling framework elaborated in chapter 3 and briefly describes State of the Art models to simulate energy demand and energy transport. The second part is meant to give an overview of the scientific knowledge in the area of this thesis.

The described technologies in this chapter are either existing renewable energy generation technologies, or technologies of so-called flexibility options. Examples for flexibility options are energy storage systems (ESS), the usage of sector coupling technologies, or demand response (DR) measures. All renewable electricity generation -, energy storage -, and sector coupling technologies included in this section are technically proven (TRL 7-9) [14] and well described in literature, and for this reason, the technologies are not discussed in detail. This chapter only aims to give a quick overview of the general working principle of said technologies and to outline their relevance to the energy system within the scope of this thesis.

2.1 Fluctuating Renewable Energy Generation

In this section, the functional principle of the most important intermittent renewable energy generation technologies is explained. Additionally, the characteristics of the generation profiles are presented in the form of duration curves. Furthermore, the current and possible future contribution to the Austrian Energy system is outlined in this section.

2.1.1 Photovoltaic power

The term “Photovoltaic” refers to the direct conversion of energy in the form of irradiation to electric energy by the usage of solar cells. The annual irradiation varies significantly on the geographic location. While an annual total global horizontal irradiation of 900-1,400 kWh/m^2 is common for Central Europe, some locations in Africa count more than 2,700 kWh/m^2 per year. Figure 2-1 shows the worldwide distribution of annual global horizontal irradiation energy per m^2. [15]

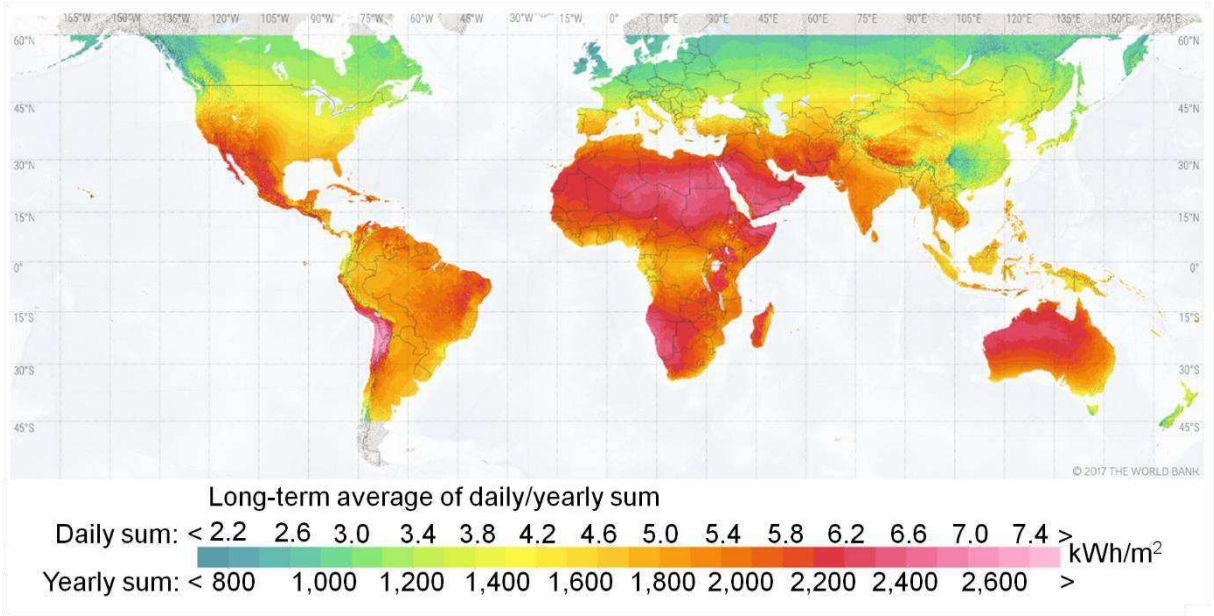

Figure 2-1: Global Map of annual Global Horizontal Radiation in kWh/m² [15]

The photovoltaic cells, converting the irradiation to electric energy are electronic devices made of semiconductor materials, usually two doped silicon layers. Figure 2-2 shows the two doped silicon layers on top of each other. An original crystal lattice of silicon atoms contains four valence electrons and doesn't conduct electricity well. If one substitutes a tiny amount of silicon atoms with a so-called donor impurity (an atom with five valence electrons from group 5 of the periodic table), such as phosphorus (P), arsenic (As) or bismuth (Bi), the semiconductor material becomes more conductive. This is due to the fact that the neighbouring silicon atoms of the donor impurity can only form covalent bonds with four electrons, but the fifth one is only weakly bonded and acts as a charge carrier. This effect is referred to as n-doping and the material is subsequently called n-doped, or n-type material. [16,17]

Similar to n-type doping, if one ejects an acceptor impurity (an atom with three valence electrons from group 3 of the periodic table), such as boron (B), aluminium (Al), or indium (In) into pure silicon, so-called "holes" are formed within the crystal lattice. This effect is referred to as p-doping and the material is subsequently called p-doped, or p-type material. [16,18]

If these two materials are put together, a pn-junction is formed. This allows some electrons from the n-region to migrate into the close-by p-region and fill the holes there. The resulting boundary layer between both materials contains no free electrons or holes and is called depletion region. Due to the electron migration, the n-side boundary becomes slightly positively charged, and the p-type side becomes negatively charged. This leads to the formation of an electric field between these charges. [16,18]

When solar irradiation reaches the depletion region of the p-n junction, the photon energy of the irradiation is sufficient to separate the previously formed electron-hole pairs in the depletion region. The existing electric field in the depletion region acts as the necessary driving force for the transport of electrons towards the n-type material and holes towards the p-type layer. With enough irradiation, the concentration of electrons in the n-layer and holes in the p-layer becomes so high, that a potential difference is developed between both layers. As soon as any connection of a load is established between both layers, electrons of the n-region will start flowing through the load towards the p-region, resulting in a direct current. [18,19]

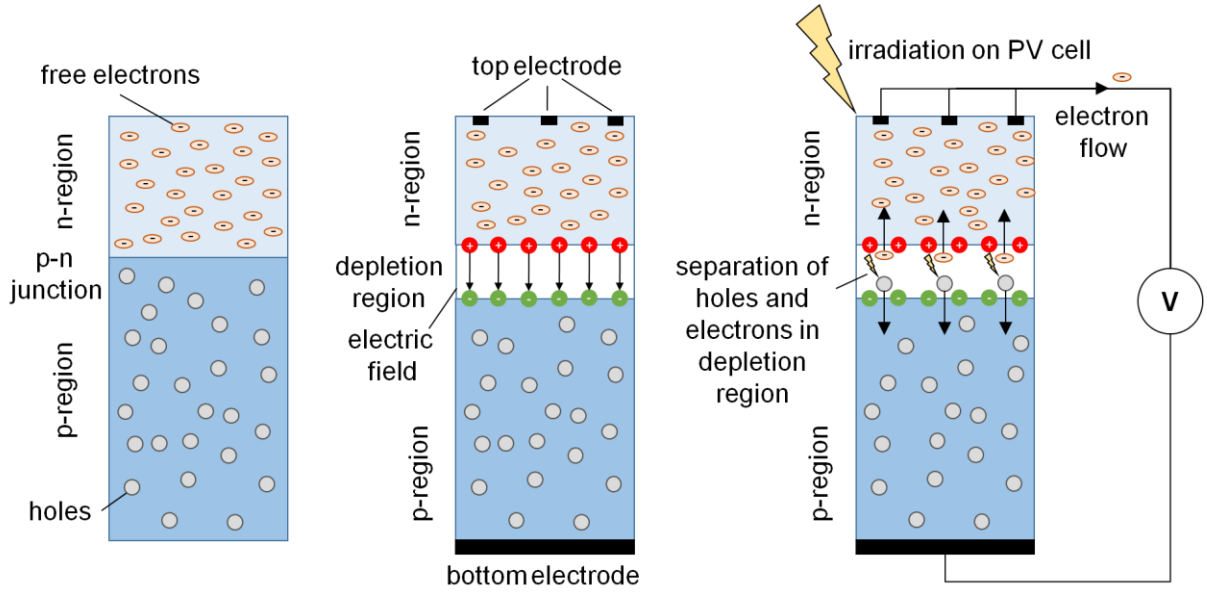

Figure 2-2: Structure and working principle of photovoltaic cells (own illustration based on [19])

There are multiple types of solar cells. The most common are monocrystalline silicon modules and polycrystalline silicon modules with a total market share of over 90 %. Typical efficiencies of photovoltaic modules are between 17-20 %. This implies that typical nominal powers of photovoltaic modules reach between 170-200 W/m^2. [20]

In order to model the PV cell, an equivalent circuit diagram is used. There are various levels of detail: the simplest model is the ideal single diode model without additional resistances, which consists of a diode connected in parallel with the generated current source. The current source represents the current of the photovoltaic cell I_{ph} and the diode represents the p-n junction.

A diode ideally conducts (without resistance) in one direction and has a high (ideally infinite) resistance in the other direction. In reality, however, the resistance is not infinite and there is always a voltage-dependent leakage current. The current through the diode is labeled as I_d After reaching the so-called breakdown voltage, the leakage current through the diode exponentially grows. If one applies Kirchhoff's law to the equivalent circuit diagram of the PV

cell, the characteristic I-V curve of a PV cell appears, with the resulting usable current I. The equivalent circuit diagram and the corresponding voltages and currents are illustrated in Figure 2-3.

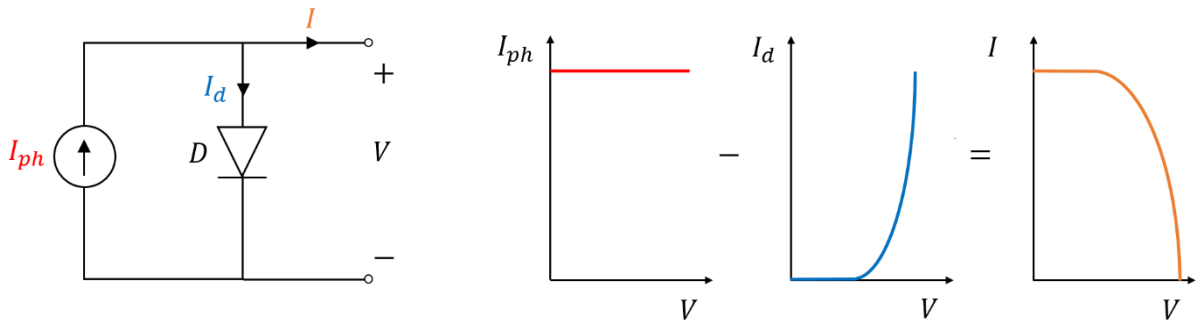

Figure 2-3: Equivalent circuit diagram of the single diode model including the formation of the characteristic I-V curve through the superposition principle. Own elaboration based on [21]

The ideal single diode model neglects the series resistance between the silicon material and the electrode surfaces, the parallel leakage current through the p-n junction and the temperature dependence of the open-circuit voltage. This is the reason most PV models additionally implement a series resistance R_s and a parallel resistance R_p to the PV model, in order to make the model more accurate. An example of such a single diode model is illustrated in Figure 2-4. Alternatively, to the presented single diode model, there is also a two-diode model, which has minor advantages of accuracy, especially at low temperatures (up to 0.6 % at -25 °C). However, the usual deviation between both models in the temperature range between 0-50 °C is below 0.3 %. This marginal improvement in accuracy comes at a price of a significant higher computation time, which is the reason for selecting the single diode model within this work. [22,23]

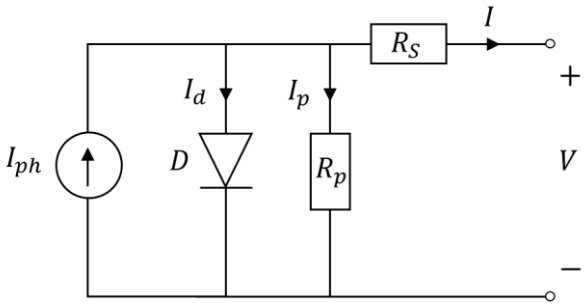

Figure 2-4: Equivalent circuit diagram of the single diode model including series and parallel resistance. Own illustration based on [21]

The contribution of Photovoltaic energy generation to the current electrical system in Austria is limited. In 2016 (the reference year of #mission2030) the total energy generation from photovoltaic power adds up to approximately 0.94 TWh. This represents around 1.5 % of the corresponding electricity consumption in 2016. According to the #mission2030, the overall energy generated from PV should increase to more than 12 TWh by 2030. Figure 2-5 shows the electrical load duration curve for 2016 and the duration curve for photovoltaic generation in 2016, as well as the projected duration curve for 2030. [10,24] One sees that the projected maximum power almost reaches as high as the maximum load of today's electricity system. However, the expected PV load hours are low, compared to other generation technologies, due to the natural day-night cycles and seasonal cycles.

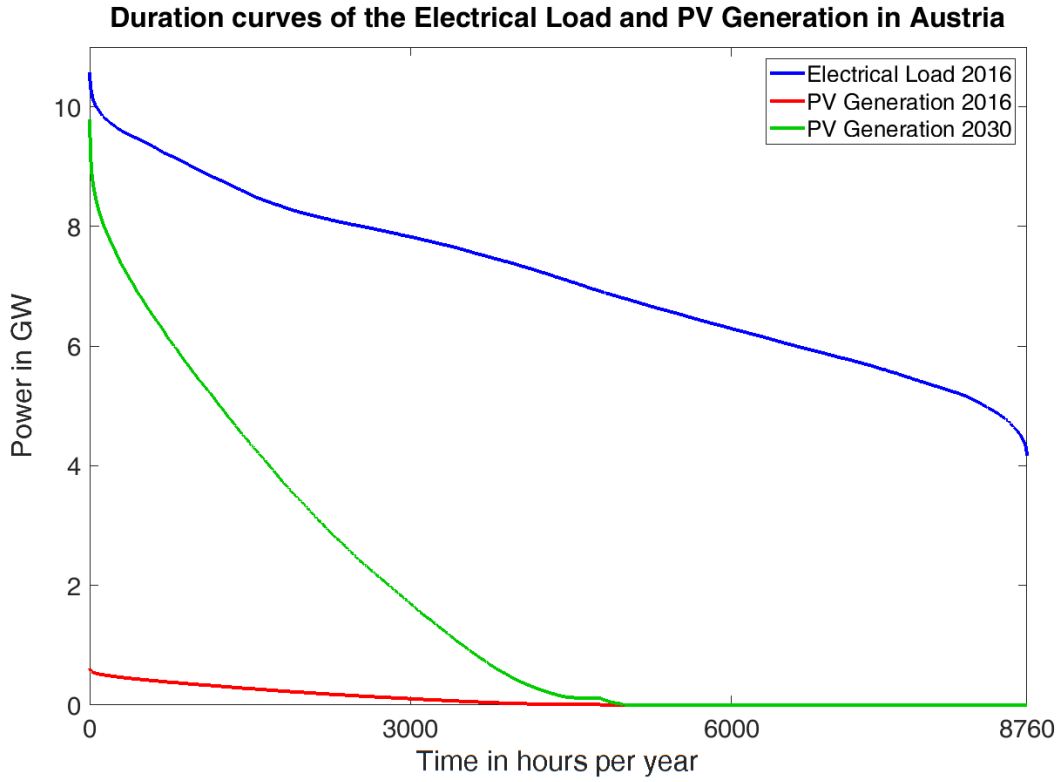

Figure 2-5: Duration curves of the Electrical load in Austria (2016) and the duration curves of PV generation in Austria (2016, 2030-projection) based on data of APG [10,24]

2.1.2 Wind power

The term wind power, nowadays, refers to the large-scale utilization of airflow through wind turbines, with the goal of generating electricity. Already in ancient times, wind energy was used in windmills or wind-powered water pumps, but only in the form of local mechanical energy. In the 1970s and 80s, modern wind power plants, combined with electric generators started to get more attention. The obtained electricity is dependent on the location of the

placement of the wind turbine. Steady high wind speeds are preferable. Regions along the coastline are very often sectors of high wind speeds and therefore target areas for wind parks. Figure 2-6 shows the global distribution of average wind speeds at a height of 100 meters above ground.

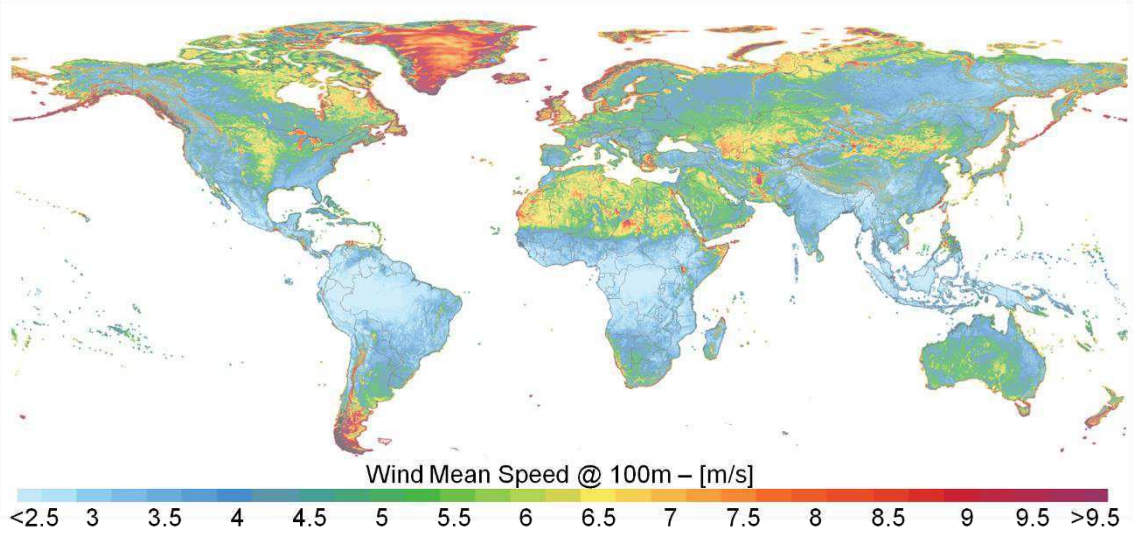

Figure 2-6: Global average wind speed at an altitude of 100 meters above the ground

The wind turbines use the kinetic energy of the wind flowing through the imaginary cross-sectional area of the wind turbine. The corresponding power is therefore dependent on the mass flow through the wind turbine area. The Equations 2-1 to 2-3 show, how the power output of a wind turbine is proportional to the wind speed v cubed, and the quadratic diameter of the wind turbine diameter.

$$E_{kin} = \frac{m \cdot v^2}{2} \rightarrow P_{wind} = \frac{\dot{m} \cdot v^2}{2} \tag{2-1}$$

$$\dot{m} = \dot{V} \cdot \rho_{air} = A \cdot v \cdot \rho_{air} = \frac{d^2 \cdot \pi}{4} \cdot v \cdot \rho_{air} \tag{2-2}$$

$$P_{wind} = \frac{d^2 \cdot \pi}{8} \cdot v^3 \cdot \rho_{air} \tag{2-3}$$

In Austria's electricity system today, wind power plays a larger role than photovoltaic power. The total generated energy from wind power in 2016 adds up to approximately 5.3 TWh. This means that more than 8 % of Austria's annual electricity demand is generated from national wind generation plants. In order to reach the target of Austria's energy strategy, the usage of wind power, however, needs to be significantly increased, to more than 12 TWh. The characteristic of the duration curve of wind power generation today and in future is put into perspective with the corresponding electricity load in Figure 2-7.

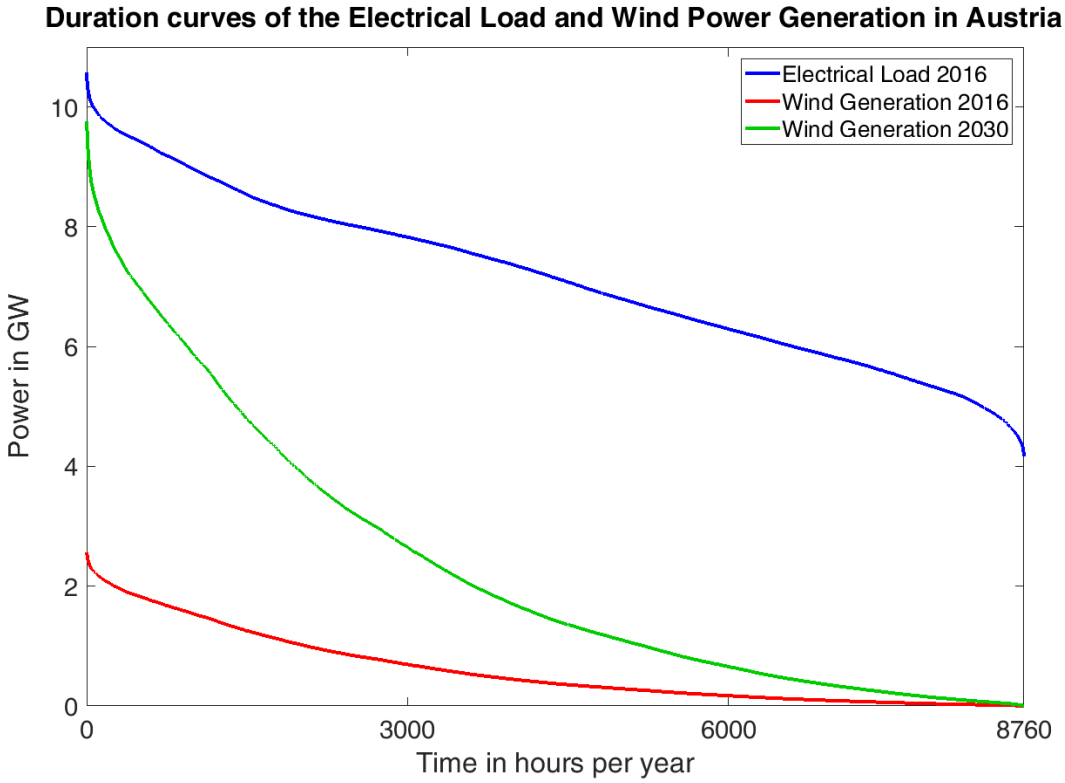

Figure 2-7: Duration curves of the Electrical load in Austria (2016) and the duration curves of wind power generation in Austria (2016, 2030-projection) based on data of APG [10,24]

2.1.3 Hydropower

The utilization of kinetic or potential energy of water for electricity generation is referred to as hydropower. It is the world's largest source of renewable electricity generation by far. While the overall renewable electricity accounts for 4,200 TWh and 26.5 % of the global electricity generation. The share of hydropower within the renewable electricity generation amounts to 62 %, thereby more than all other sources combined. [25]

While hydropower can be considered a renewable energy source, not all hydropower facilities can be classified as intermittent energy generation. Especially the power generation of storage

or pumped storage power plants is vastly controlled by the actual electricity demand or price signals and not by short-term weather conditions. Due to the topic of this thesis aiming for intermittent energy integration, this section on hydropower focuses only on run-of-river hydroelectricity. These power plants have little or no capacity for energy storage and hence have only limited or no opportunity to adjust the electricity output to the current consumer demand. It is subject to seasonal fluctuations and short-term weather variability (predominantly precipitation and snowmelt) and can, therefore, be considered an intermittent energy supply source, with certain advantages in terms of baseload operation capability.

The physical principle of the energy generation from run-of-river power plants are similar to wind power as it uses the kinetic energy of the flowing water. Equation 2-1 from section 2.1.2 is also valid for hydroelectricity. A major difference is the principle behind the media flow. While wind is generally caused by temperature and pressure differences in the planet's atmosphere, water flow is caused by gravity. This means that the flow velocity can be derived from the height of fall, as shown in Equation 2-5.

$$P_{hydro} = \frac{\rho_{water} \cdot v^2}{2} \cdot \dot{V} \cdot \eta \tag{2-4}$$

$$v = \sqrt{2 \cdot g \cdot h} \tag{2-5}$$

$$P_{hydro} = \rho_{water} \cdot g \cdot h \cdot \dot{V} \cdot \eta = \dot{m} \cdot g \cdot h \cdot \eta \tag{2-6}$$

Depending on the flow rate and the drop height of the water, an appropriate type of turbine is chosen to convert the kinetic energy into rotation energy to use it in a generator. The most common turbines are Francis, Pelton and Kaplan turbines. [19]

Austria has a very high share of hydropower for its electricity generation. This is due to its alpine topography, numerous rivers and its significant water resources and high precipitation. [25] Around two thirds of the electricity generation is accounted for by hydropower. Run-of-river power plants produced 28.2 TWh in 2016. [24] The proposed pathway to achieve the set goals of Austria's Energy and Climate strategy strives for an extra 6 TWh of hydropower generation. It does not distinguish between types of hydropower. Figure 2-8 assumes, that all additional energy is generated by run-of-river plants. One can see that in contrary to wind – and solar power, run-of-river generation is much more reliable, with a minimum annual generation power of around 1.5 GW.

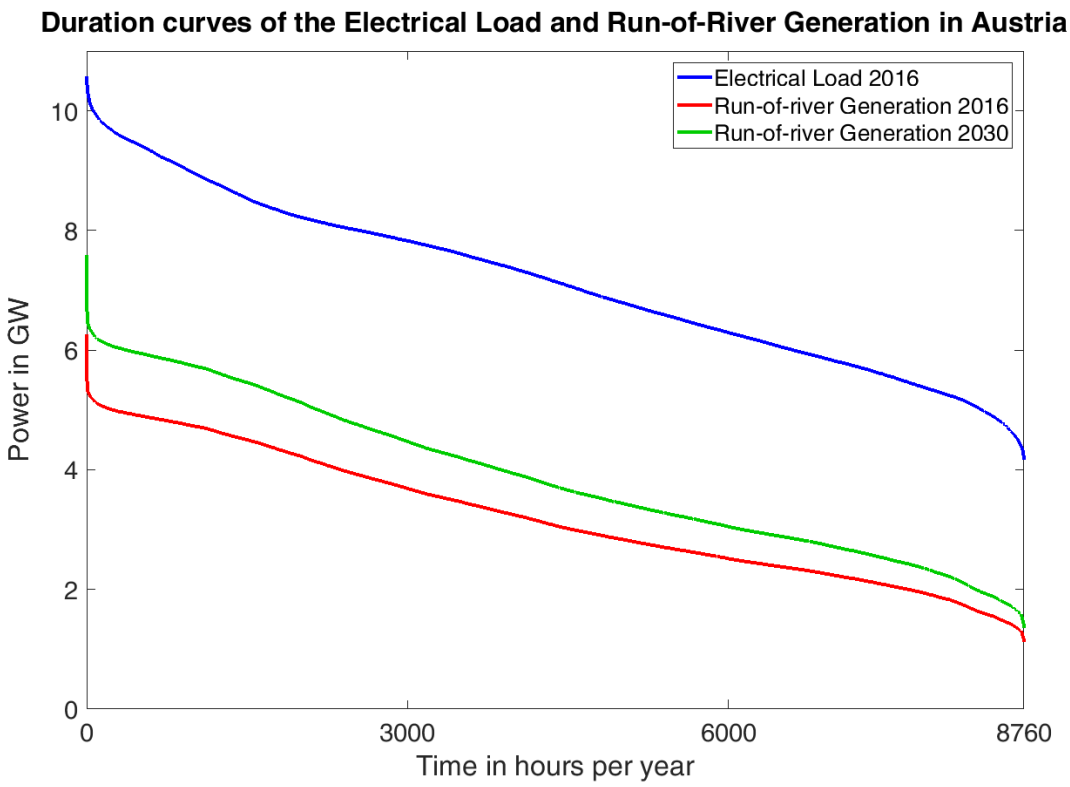

Figure 2-8: Duration curves of the Electrical load in Austria (2016) and the duration curves of run-of-river power generation in Austria (2016, 2030-projection) based on data of APG [10,24]

2.1.4 Resulting Generation Characteristics

If one sums up all three described energy generation duration curves for the years 2016 and 2030 and determines the residual load (see Equation 3-1 in section 3.3) of both years, one ends up with very different results. Figure 2-9 presents the calculated duration curves for 2016 and 2030. The result is another way of illustrating Figure 1-2 in section 1.

While just over 400 hours of negative residual loads are noted in 2016, more than 4,900 hours of negative residual loads are expected in 2030, if the pathway of the #mission2030 is realized. This means that during 56 % of the yearly hours, the renewable generation exceeds the simultaneous electricity demand (assuming an unchanged demand). Some of these generated electricity surpluses may be exported to neighboring countries, but with a general trend of increased renewable generation across the continent exporting electricity can be expected to get more difficult for the following reasons:

- The fluctuating generation in surrounding countries is a subject to the same seasonal fluctuations and similar weather situations of close-by regions. This may result in a simultaneous surplus of electricity generation in other countries as well.

- Even if there is a lack of demand in other European regions, the observed negative residual loads are very high at some times. This might lead to congestions of power lines and an incapability to transfer power to the area of demand.
- The negative peak of the residual load in 2030 exceeds the current annual peak network load of around 10.8 GW. It has to be noted that the residual load is on top of the network load, since the electric load still exists, despite the negative residual load.

These expected effects need to be dealt with. There are various solution strategies to balance the lack of energy at some times and the surplus energy at other times. All of these possible solutions are categorized into so-called flexibility options and presented along with the corresponding technologies to put them into practice.

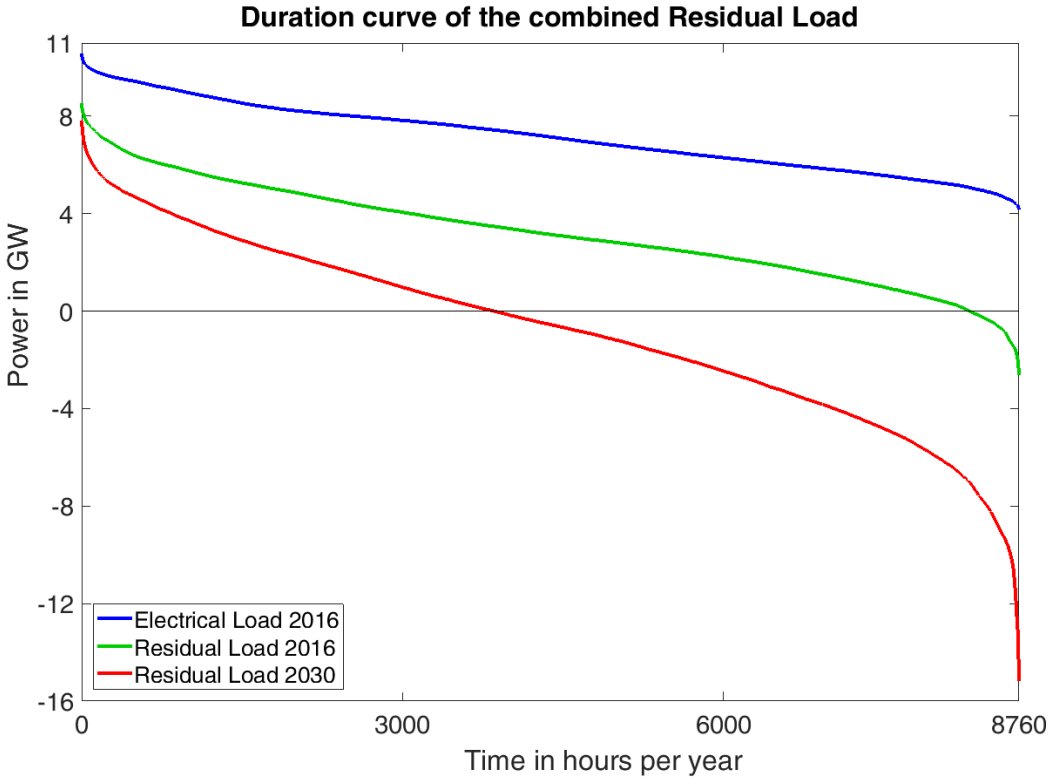

Figure 2-9: Combined residual load of Austria in 2016 and the forecast for 2030 based on APG data [10,24]

2.2 Energy demand models

The second major part of describing any energy system is the energy demand. As there is no comprehensive database for measured energy demand profiles, it is necessary to rely on energy demand models. This section presents a quick overview of the state of the art methodologies used, to determine the load of electricity, natural gas and district heating.

Additionally, it lists a variety of available open-source tools to model the energy demand and explains the differences between them.

Regardless of the modeled energy carrier, models can be classified into top-down models, bottom-up models and hybrid models, which combine them. The main difference between all bottom-up models and top-down models is the different data processing approach. Top-down models are always deterministic statistical disaggregation models that segment the energy demand from an aggregated area as described for instance in [26–28]. Bottom-up models can be further divided: one proposed classification methodology divides them into statistical random models, probabilistic empirical models and time-of-use based models. All of them calculate the energy consumption for a targeted energy consumer by extrapolating the microscopic data of smaller objects, such as dwellings or businesses. [29] The differences of both major approaches for single objects within the examined area may be significant, but the energy consumption of the total examined area should ideally be identical. An example of a top-down, as well as a bottom-up modelled single household electricity load is presented in Figure 2-10 in the following section 2.2.1, and compared with real measured data.

2.2.1 Electricity demand

There are numerous publications of electricity demand models, reaching from very different spatial resolutions (worldwide, national, regional, distribution level, single consumer) to all available temporal resolutions (yearly, monthly, daily, hourly, 15 minutes, seconds). The relevant model types for the presented research questions are highly resolved spatially (distribution level, single consumer) and medium to high, in terms of their temporal resolution (hourly, 15 minutes).

The classic example for top-down modelling of electricity demand is the standardized load profile (SLP). SLPs are published by different associations, utilities or regulatory authorities. In Germany and Austria the publishing institutions are VDEW [30] and econtrol [31] respectively. They consist of a number of different load profile coefficients in 15-minute time intervals, three different types of days (working day, Saturday, Sunday), three different seasons (summer, winter, transition periods), as well as a “dynamization function” for smoothing the transition between the seasons. To obtain the appropriate load profile for a chosen consumer group (e.g. household), one has to multiply the annual electricity consumption with the corresponding coefficients. This results in a yearly profile for any household. A comparison between actually measured household loads and the corresponding SLP for households reveals major differences. This shows that utilizing SLP for single households or smaller aggregations of users does not lead to the correct result for single customers. It should only

be used for a larger group of aggregated users (see also section 3.2). Additionally, SLP have limitations for geographical areas, as certain parameters such as climate conditions, the usage of electrical heating/cooling or individual daily routines tend to vary for different regions.

As this work presents its own aggregation methodology, bottom-up models are of particular importance in the scope of this work. In energy demand modelling, this approach is also referred to as synthetic load profiles (SynLP). These SynLP can either be aggregated to model a larger region or be used for individual consumers. Even though SynLP cannot model the electrical load for a single customer correctly (too individually different), the characteristic of the load profile is usually much more realistic than the SLP for the same consumer. Figure 2-10 aims to illustrate this circumstance. It shows that even though the SynLP underestimates the morning peak and overestimates the noon peak for this particular customer, the characteristic compared to the SLP is much more realistic. Additionally, the deviations may vary from day to day, because the used SynLP is different for each day, due to the applied probabilistic approach used in this example, and the measured load profile is also constantly changing on a daily basis.

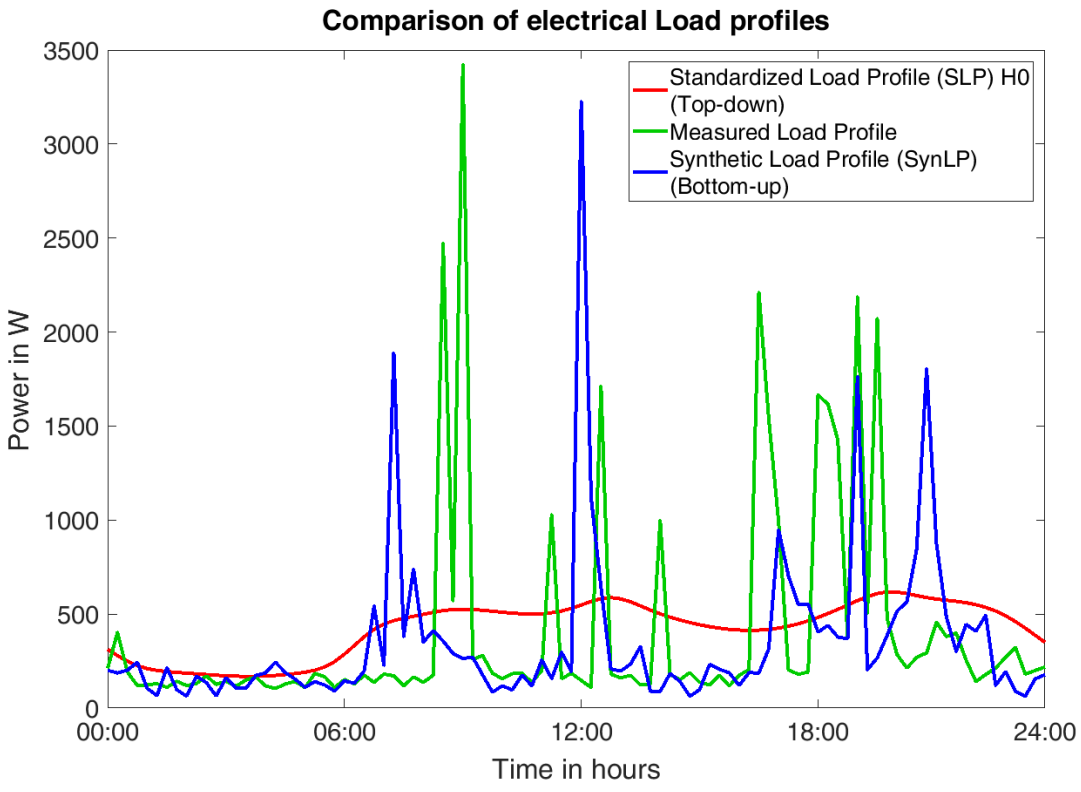

Figure 2-10: Comparison of different Load models and the actual measured load profile for an exemplary household on a random day

Examples of input variables for bottom-up electricity demand models can be the individual power consumption of electrical appliances and their usage likelihood over the day, weather information and thermal properties of the building, electricity bills, human behaviors and many more. Usually they are far more complex than the top-down models and take a longer computational time, due to the increased complexity. Statistic approaches also tend to deliver different results for the same input variables. There are numerous examples of models with different focuses, advantages and disadvantages. Examples of described SynLP in the electricity sector for single users can be found in [32–38].

Some of the mentioned scientific SynLP provide the public with an open-source tool to develop customized load profiles, based on the user's research needs. These tools are called load profile generators. Common tools are the classic probability distribution models of Stokes [35] and the "Load Profile Generator" of the IEA Annex 42 [39]. Other widespread load profile generators are based on the user's behavioral orientation. Examples for these types are Walker and Pokoski [36] and the follow-up model ARGOS of Capasso [40], as well as the model of Widen [41] and Richardson [34]. The most recent models are developed by Metz [42], the SynPro generator developed at Fraunhofer ISE from Fischer [43] and the *LoadProfileGenerator* from Pflugradt [44], which is mostly used in this work. It combines statistical methods with the physical and psychological demand model, developed by Dörner [45,46]. It was chosen because of its the large number of customizing options and the detailed predefined household types.

All in all, it can be stated that there are various options to model consumer profiles in the residential and mobility sector. A larger challenge lies in modelling load profiles of industrial companies with their very individual behavior. There are some approaches of developing top-down load profiles for industrial consumer branches [47,48], analogous to SLP for residential or commercial consumers, but the applicability is limited. This is due to the same reasons as already stated before for the residential sector. While it is possible to aggregate a number of residential consumers in order to achieve a statistically relevant sample size to work with SLP, it is highly unlikely to have the necessary sample size of industrial consumers of the same kind in one area. This means that the consumption profile of industrial electricity consumers relies on either measured data, or theoretical assumptions, as there are no bottom-up load profile generators available.

2.2.2 Natural gas and heating demand

Even though the number of publications to determine the natural gas demand in various spatial resolutions is considerably lower compared to the electricity sector, there are multiple methodologies published. However, most publications such as [49–51] deal with lower spatial resolutions and large regions like countries. Additionally, the mentioned publications also provide a low temporal resolution (monthly or yearly), which does not comply with the set research questions of this work. Bottom-up, open-source tools in high temporal resolution, compared to the presented load profile generators for electricity, do not exist for the natural gas sector.

This means that top-down models need to be used for smaller units as well, despite the expected errors for individual consumers, as described for the electricity sector. However, the main appliances for natural gas in the residential, commercial and public sector is the provision of domestic hot water and space heating. The thermal inertia for heating appliances is much higher compared the immediate response without any delays for electrical appliances. This effect results in a much smoother load profile of heating appliances compared to the highly fluctuating electrical load profiles. A possible way to model the demand of natural gas in the mentioned sectors is the usage of SigLinde profiles [52], which is a further development of Sigmoid profile functions discussed in [53]. The developed approach consists of two profiles (heating demand and warm water demand), which are both linearly dependent from the ambient temperature. While the heating demand function has a high gradient, the warm water is only weakly dependent on the outdoor temperature and seasonal effects. These two linear functions are complemented by the original Sigmoid function for natural gas demand, as described in [52]. This results in a specific natural gas demand for each ambient temperature, corrected by seasonal compensation factor. Additionally, non-temperature dependent load profiles, such as natural gas demand caused for cooking purposes are added. In total, there are three different household profiles and eleven commercial or industrial profiles with up to five different assorted characteristics each.

The heating demand for households, with no natural gas based space heating or hot water supply can be derived similarly to the temperature dependent share of the natural gas demand (converted by dividing by the heating value of natural gas). This means that all process applications, such as the mentioned natural gas demand for cooking purposes have to be deducted. To determine the temperature dependent energy demand for either natural gas or district heating of a single customer, the time-resolved ambient temperature, the annual heat consumption and the corresponding load profile have to be known.

2.3 Energy transport models

In the last sections, the energy generation from fluctuating sources, as well as the time-dependent energy demand profiles were introduced. While energy transport does not play a role in Single-Nodal models, it has significant effects on energy systems with multiple nodes. There are various ways to consider energy transport between the sites of generation and demand. This section describes the general types of energy transport models for all energy carriers and gives a more detailed overview of applied load flow models for the three major grid-bound energy carriers, electricity, natural gas and district heating.

Generally, there are three major types of considering load flows between defined nodes. The first type considers load flows between nodes, but they are not subject to any restrictions or losses. This highly simplified approach is called copper plate approach, which is derived from the high electric conductivity from the material copper. This approach does not need any network-related characteristics, but is of no real use for grid-related research questions. It is mostly used for economic models. [54] The second approach is referred to as transshipment model or NTC-based (Net Transfer Capacity) model. This type considers restrictions of power transportation, the maximum transfer capacity, for individual network segments and most of the time also transport-related energy losses. The load flow principles, however, are not based on physical principles and also the losses are usually considered as a constant share of the transported energy. [55] In the third modelling approach, actual physical principles are the basis of load flows between the defined nodes. These models are called flow-based models. They consider the time-dependent changes of the physical driving forces between nodes that cause the load flows and can therefore also calculate the distribution of energy in meshed grids. Flow-based load flow calculation models are classified as AC- and DC calculation methods for electrical load flow calculation methods. While DC models only take active power flows between the nodes into account, the AC load flow calculation additionally considers reactive power flows. More detailed descriptions on flow-based LFC for all three energy carriers can be found in the following sections. [54]

2.3.1 Electrical load flow calculations

This section will give an overview of the two common model types to simulate electrical load flows, based on physical principles: the more complex and realistic AC-model, and the simplified DC-model. First, the AC-model is described, then the assumptions that lead to the DC model are explained in detail. Finally, both model types are compared to each other in terms of their advantages and disadvantages.

The AC-model load flow model is state of the art for highly accurate electrical grid simulations in research and detailed network calculation programs as DIgSILENT [56], NEPLAN [57], PSS SINCAL [58] and others. To describe a transmission line with the corresponding load flow between node k and m, the π-model is used. The equivalent circuit diagram of this four-port model is illustrated in Figure 2-11.

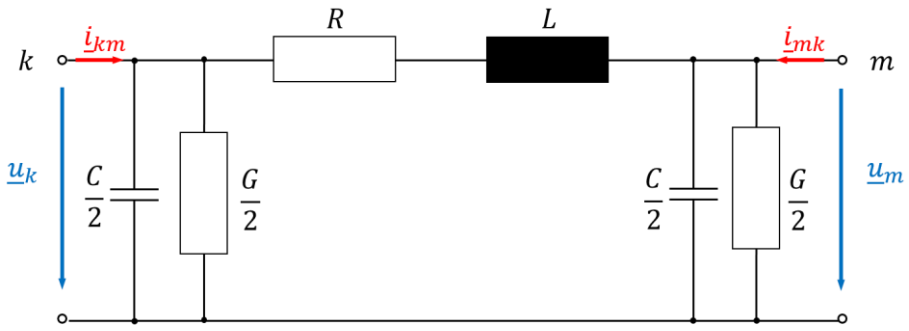

***Figure 2-11: Complete* π –model (equivalent circuit diagram) of a transmission line**

By aggregating some elements of the π-model (see Equations 2-7 and 2-8), the model can be simplified, as presented in Figure 2-12. This model is characterized by the series impedance and the shunt admittance, as shown in Equations 2-7 and 2-8. The nomenclature of all variable names is based on Andersson [59] listed underneath in Table 2-1.

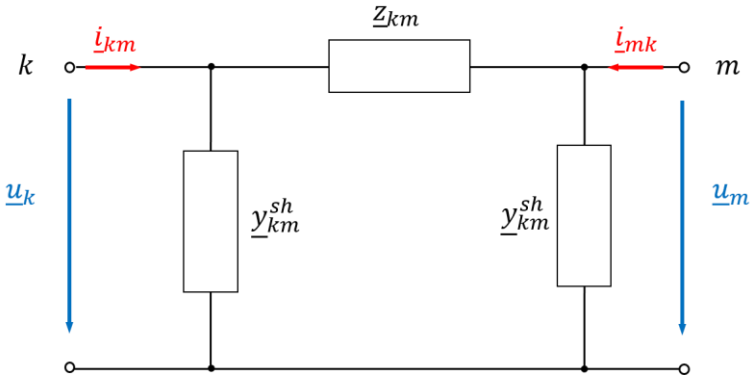

***Figure 2-12: Simplified* π –model (equivalent circuit diagram) of a transmission line [59]**

$$\underline{Z}_{km} = R_{km} + jX_{km} \tag{2-7}$$

$$\underline{Y}_{km}^{sh} = G_{km}^{sh} + jB_{km}^{sh} \tag{2-8}$$

Table 2-1: Variable label and the according name and unit

Variable	Name and Unit
$\underline{U}$	voltage [V]
$\underline{I}$	current [A]
R	series resistance [Ω]
X	reactance [Ω]
$\underline{Z}$	series impedance [Ω]
B^{sh}	shunt susceptance [Siemens]
G^{sh}	shunt conductance [Siemens]
$\underline{Y}$	admittance [Siemens]
θ	angle [°]
S	apparent power [VA]
P	active power [W]
Q	reactive power [Var]

To calculate the network equations, the nodal admittance matrix needs to be formulated. While the shunt admittance is specified as admittance already, the series impedance needs to be converted to an admittance for the nodal admittance matrix as well. This conversion is performed in Equation 2-9. Capitalized variables represent nominal values in the corresponding SI unit, while lower case letters express per unit (p.u.).

$$\underline{y}_{km} = \frac{1}{\underline{z}_{km}} = g_{km} + jb_{km} \tag{2-9}$$

with g_{km} and b_{km} being defined as follows in Equation 2-10 and 2-11. Since the series reactance x_{km} and the series resistance r_{km} are positive for actual power lines, the shunt conductance g_{km} has to be positive and the shunt susceptance b_{km} negative.

$$g_{km} = \frac{r_{km}}{{r_{km}}^2 + {x_{km}}^2} \tag{2-10}$$

$$b_{km} = -\frac{x_{km}}{{r_{km}}^2 + {x_{km}}^2} \tag{2-11}$$

According to Kirchhoff's Current law, the complex current from node k to node m can be specified as the complex current through the series impedance $\underline{i}_{z_{km}}$ and the shunt admittance $\underline{i}_{y_{km}}^{sh}$ according to Figure 2-12.

$$\underline{i}_{km} = \underline{i}_{y_{km}}^{sh} + \underline{i}_{z_{km}} \tag{2-12}$$

When applying Kirchhoff's law of voltage to the circuit of Figure 2-12, one can determine the currents $i_{y_{km}}^{sh}$ and $i_{z_{km}}$ derived from the complex voltages $\underline{u}_k$ and $\underline{u}_m$.

$$\underline{i}_{z_{km}} = (\underline{u}_k - \underline{u}_m) \cdot \underline{y}_{km} \tag{2-13}$$

$$\underline{i}_{y_{km}}^{sh} = \underline{u}_k \cdot \underline{y}_{km}^{sh} \tag{2-14}$$

With the complex voltages defined in Equations 2-15 and 2-16. It has to be noted, that u_k and u_m are amounts of the voltages in the nodes k and m and θ_k and θ_m are the angles of the voltages in the corresponding nodes.

$$\underline{u}_k = |u_k| \cdot e^{j\theta_k} = |u_k| \cdot (\cos(\theta_k) + jsin(\theta_k)) \tag{2-15}$$

$$\underline{u}_m = |u_m| \cdot e^{j\theta_m} = |u_m| \cdot (\cos(\theta_m) + jsin(\theta_m)) \tag{2-16}$$

The complex currents $\underline{i}_{km}$ and $\underline{i}_{mk}$ as illustrated in Figure 2-12 are expressed as functions of the complex voltages at the nodes k and m in matrix form, as shown in Equation 2-17. The presented matrix is symmetric and all diagonal elements are equal, which means that all elements of Figure 2-12 are symmetric elements.

$$\begin{pmatrix} \underline{i}_{km} \\ \underline{i}_{mk} \end{pmatrix} = \begin{pmatrix} \underline{y}_{km} + \underline{y}_{km}^{sh} & -\underline{y}_{km} \\ -\underline{y}_{km} & \underline{y}_{km} + \underline{y}_{km}^{sh} \end{pmatrix} \begin{pmatrix} \underline{u}_k \\ \underline{u}_m \end{pmatrix} \tag{2-17}$$

After defining the currents along the power line, the next step is to calculate the active power and reactive power transport over the power line. In transmission lines the shunt reactance G_{km}^{sh} (leakage current over isolators) is negligible in comparison to the shunt susceptance jB_{km}^{sh}.

This simplifies the current from node k to m as shown in Equation 2-18.

$$\underline{i}_{km} = (\underline{u}_k - \underline{u}_m) \cdot \underline{y}_{km} + \underline{u}_k \cdot jb_{km}^{sh} \tag{2-18}$$

This leads to the following apparent power s_{km}:

$$\underline{s}_{km} = \underline{u}_k \cdot \underline{i}_{km}^{*} \tag{2-19}$$

With $\underline{i}_{km}^{*}$ being the complex conjugate current. When combining Equation 2-18 with the complex voltage of Equation 2-15, the following Equation 2-20 is the outcome:

$$\underline{s}_{km} = \underline{y}_{km}^{*} \cdot |u_k| \cdot e^{j\theta_k}\left(|u_k| \cdot e^{j\theta_k} - |u_m| \cdot e^{j\theta_m}\right) - |u_k^2| \cdot jb_{km}^{sh} \tag{2-20}$$

The apparent power $\underline{s}_{km}$ can be divided into the active power p_{km} and the reactive power q_{km} along the power line by splitting the real part of Equation 2-20 from the imaginary part.

$$\underline{s}_{km} = p_{km} + jq_{km} \tag{2-21}$$

$$p_{km} = |u_k^2| \cdot g_{km} - |u_k||u_m|g_{km} \cdot \cos(\theta_{km}) - |u_k||u_m|b_{km} \cdot sin(\theta_{km}) \tag{2-22}$$

$$q_{km} = -|u_k^2| \cdot \left(b_{km} + b_{km}^{sh}\right) + |u_k||u_m|b_{km} \cdot \cos(\theta_{km}) - |u_k||u_m|g_{km} \cdot sin(\theta_{km}) \tag{2-23}$$

$$\theta_{km} = \theta_k - \theta_m \tag{2-24}$$

To describe particular nodes in any electrical grid configuration, four terms are needed to fully characterize it: the net active node power p_k , the net reactive node power q_k , the amount of the node voltage u_k and the corresponding voltage angle of the node θ_k. The voltage angle between two nodes k and m is referred to as θ_{km}, and can be calculated according to Equation 2-24. In a typical electrical load flow calculation, there are three kinds of nodes with different known and unknown variables. [60] In most grids, the most common node type is a PQ node. They act as a load node and have a known active and reactive power, but the amount of voltage and the voltage angle is unknown. The second type is a feed-in node, with

a known feed-in voltage and the according feed-in power. The voltage angle and the reactive power is unknown. This type of node is named PV node. The last necessary node type is the slack node. It gives a point of reference for the voltage and the voltage angle. This means that the known values are the node voltage, and phase angle while the active and reactive power remain to be distinguished. Depending on the node type, the according initial values have to be defined, while the unknown values are the result of the iterative load flow calculation process (see section 3.5.4). A summary of the three typical node types is shown in Table 2-2.

Table 2-2: Summary of node types and their known and unknown variables based on [60]

Node name	Abbreviation	Known variable	Unknown variable
Load node	PQ node	P, Q	U, θ
Feed-in node	PU node	P, U	Q, θ
Slack node	-	U, θ	P, Q

The equations of the AC load flow calculations are not linear (see Equations 2-22 and 2-23), which has a number of disadvantages related to the computational time. The linear DC load flow calculation can be derived from the presented AC load flow process by four simplifications. By doing so, the made assumptions lead to possible deviations. It has to be noted that before applying the DC load flow calculation, the user has to look into the assumptions in order to estimate its validity of the method for the specific task at hand. The following four assumptions transform the AC-load flow calculation to a DC load flow calculation.

1. Neglecting the reactive power flow

   The DC load flow calculation neglects all reactive power flows. This implies that only the active power flow between two nodes is relevant for the calculations. The first assumption leaves Equation 2-22 unchanged, while the reactive load flow described in Equation 2-23 is set zero. This is justified by the assumption that the reactive power needed to supply the specific demand in a node is provided by the node itself or a node in immediate proximity.

$$q_{km} = 0 \tag{2-25}$$

2. All node voltages correspond to the set voltage level. For reasons of comprehensibility Equation 2-22 is shown again at this point and Equation 2-27 is the direct consequence of assuming a uniform node voltage profile in Equation 2-26.

$$p_{km} = u_k^2 \cdot g_{km} - u_k u_m g_{km} \cdot \cos(p_{km}) - u_k u_m b_{km} \cdot sin(\theta_{km})$$

$$u_k = u_m = u \tag{2-26}$$

$$p_{km} = u^2 \cdot g_{km} - u^2 g_{km} \cdot \cos(\theta_{km}) - u^2 b_{km} \cdot sin(\theta_{km}) \tag{2-27}$$

3. The third assumption made is to neglect active power losses over power lines. Due to the reason that the reactance is significantly higher than the resistance in high voltage grids, active power losses and the resistance term along the lines can be neglected. The most important decisive factor, whether this assumption is justifiable can be expressed by the ratio of the reactance to the resistance of the according power line. Equations 2-28 to 2-30 show the implications of this assumption.

$$x_{km} \gg r_{km} \Rightarrow r_{km} = 0 \tag{2-28}$$

$$g_{km} = \frac{r_{km}}{r_{km}^2 + x_{km}^2} = 0 \tag{2-29}$$

$$b_{km} = -\frac{x_{km}}{{r_{km}}^2 + {x_{km}}^2} = -\frac{x_{km}}{{x_{km}}^2} = -\frac{1}{x_{km}} \tag{2-30}$$

By applying these implications to the already simplified power flow of Equation 2-27, an even further simplified power flow formula appears, as presented in Equation 2-31.

$$p_{km} = u^2 \cdot g_{km} - u^2 g_{km} \cdot \cos(\theta_{km}) - u^2 b_{km} \cdot sin(\theta_{km}) \tag{2-31}$$

$$p_{km} = -u^2 b_{km} \cdot sin(\theta_{km}) \tag{2-32}$$

$$p_{km} = -\frac{u^2}{x_{km}} \cdot sin(\theta_{km}) \tag{2-33}$$

4. Finally, the last assumption before getting the linear DC load flow equation is to assume small voltage angle differences. Since the sine of a small angle approximately equals the angle itself, the expression is substituted by the angle itself. Additionally, the expression of the squared voltage is replaced by the value 1. This is valid when calculating with per unit values. This leads to the consequent Equation 2-35.

$$\theta_{km} \ll \Rightarrow \ sin(\theta_{km}) \cong \theta_{km} \tag{2-34}$$

$$p_{km} = -\frac{1}{x_{km}} \cdot \theta_{km} = -\frac{\theta_{km}}{x_{km}} \tag{2-35}$$

One can see that the final Equation 2-35 for the DC power flow is significantly simplified compared to the original AC power flow, as described in Equation 2-22. The extended AC power flow equation provides increased accuracy of the calculation, with the disadvantage of larger data requirements. While some data, especially constant values for lines, may be available, other time-dependent input values, such as the reactive power of all implemented nodes are usually not available without measurements. It should be noted that the full benefits of an increased accuracy can only be exploited when the necessary input data is completely available. Table 2-3 provides an overview of the necessary input and output parameters for both calculation methodologies. The input values refer to a single voltage level without any transformers. Additional resistances, reactances and susceptances need to be provided for the implementation of transformers for the AC-LFC. The computational time is significantly higher for AC-LFC, due to the higher complexities and nonlinearities.

While there are only small deviations of conventional DC-LFC in high voltage grids, the decreased X/R ratio in medium and especially low voltage grids leads to a larger calculation error. This is due to the fact, that assumptions 2 and 3 are not applicable without accepting a certain amount of error. Purchala et al. [61] investigated the influence of the X/R ratio on the expected error margin between the AC-LFC and the simplified DC-LFC. They conclude that the error of using DC-LFC with X/R ratios below 4 can be neglected, but can theoretically reach up to 15 % at ratios well below 1. However, they mention that in all tested grids, the deviations virtually never exceed 5%, even with very low X/R ratios. The assumption of a uniform voltage profile is the far bigger source of active power estimation errors. [61]

Table 2-3: Comparison of parameters for the DC- and AC-LFC

	DC-LFC	AC-LFC
Necessary Input parameters	• Nominal voltage • Line reactances • Node active power	• Nominal voltage • Line resistances • Line reactances • Line susceptances • Node types • Node active power • Node reactive power • Node reactive power limits • Compensation susceptances
Output parameters	• Slack active power • Line active power • Node voltage angles	• Slack active power • Slack reactive power • Line active power • Line reactive power • Line power losses • Node voltages • Node voltage angles
Computation time	fast	slow

To solve the equations for multiple load flows between all defined nodes, iterative approximation methodologies are used. This is necessary for networks with multiple nodes in meshed networks. The most common option is the Newton-Raphson methodology. The practical approach of the Newton-Raphson method is described in the individual LFC in section 3.5. An alternative option to solve a linear system of equations is the Gauß-Seidel method.

Additionally to the standard DC load flow calculation methodology, *HyFlow* offers the choice of a second type of electrical load flow calculation. Since the standard DC-LFC is only applicable for high X/R ratios, a second methodology for grids with dominating ohmic resistances over reactances (low X/R ratios) is introduced. Depending on the application area, the user can freely choose between both options. A more detailed recommendation when to use which of the two LFC options and the corresponding description of both LFC methodologies is presented in the sections 3.5.4 and 3.5.5.

2.3.2 Natural gas load flow calculations

Flow-based calculation methodologies for natural gas grids are based on the fundamental equations of fluid mechanics. The most important equations to model the flow in pipelines are the Darcy-Weisbach equation, which relates the pressure difference and the flow rate of a medium in a pipeline, and the law of mass conservation with the corresponding continuity equation. In contrast to the fundamental equations of electrical networks (Ohm's law and Kirchhoff's laws), the analogous Darcy-Weisbach equation for media flow is non-linear. This is caused by the quadratic dependence of the pressure loss from the media flow rate. Since all modelling approaches for natural gas grids are based on this fundamental and non-linear equation, the main distinguishing criterion is the actual numeric calculation procedure and the corresponding solution methodology. [62] Apart from the differences between the linearity of Ohm's law to describe electrical grids and the quadratic dependency of mass flow in piplines described by Darcy's law, there are also similarities between to the electrical grid, as shown in the following Equations 2-36 to 2-38.

The pressure difference is equivalent to the voltage drop or the voltage angle difference and the volumetric flow represents the current in electrical grids. The quadratic dependence between the pressure loss and the volume flow can be seen in Equation 2-38. Additionally, it should be noted that additional input variables are necessary to characterize the natural gas grid, compared to the electrical load flow calculation procedure. These values are the Darcy friction factor λ, the density of the medium ρ and the inner diameter of the pipeline d (for round cross-sections).

$$\Delta p \triangleq \Delta\theta \triangleq \Delta U \tag{2-36}$$

$$\dot{V} \triangleq I \tag{2-37}$$

$$\Delta U = R \cdot I \quad \triangleq \quad \Delta p = \frac{\lambda \cdot l \cdot \rho \cdot 8}{d^5 \cdot \pi^2} \cdot \dot{V}^2 \;\rightarrow\; \Delta p = f(\dot{V}^2) \tag{2-38}$$

Equation 2-38 shows the result for the pressure difference between any two points separated by the length l and a straight pipeline in a circular design. It is derived from the Darcy-Weisbach equation, which is shown in Equation 2-39. It is important not to confuse the Darcy friction factor λ with the thermal conductivity of the district heating LFC in the next section. By substituting the general form of media velocity with the flow rate and inserting the formula for the circular area, it can be transformed into the previous Equation 2-38.

$$\Delta p = \frac{\lambda}{d} \cdot l \cdot \rho \cdot \frac{v^2}{2} \tag{2-39}$$

$$\dot{V} = A \cdot v \tag{2-40}$$

Additionally, the pipe friction is another source of a non-linearity. It depends on parameters like the flow rate $\dot{V}$, the specific pipe friction f and the geometry of the pipeline in the form of its length l and inner diameter d.

$$\lambda = f(\dot{V}, f, l, d) \tag{2-41}$$

To calculate the Darcy friction factor λ, the flow regime has to be distinguished. Within pipeline networks, there are three different flow regimes: laminar flow, fully turbulent flow and a transition range between laminar and turbulent flow. The dimensionless Reynolds number Re is used to characterize the flow regime. Laminar flow is defined by $Re < 2320$, while a fully turbulent flow occurs at $Re > 4000$. In between these numbers, the flow regime is in the transition range. To calculate the Reynolds number, the following Equation 2-42 is used, with η as the dynamic viscosity.

$$Re = \frac{4 \cdot \dot{V}}{\pi \cdot d \cdot \eta} \tag{2-42}$$

For laminar flows it is possible to determine the Darcy friction factor with the explicit Equation 2-43:

$$\lambda = \frac{64}{Re} \tag{2-43}$$

There is no explicit formula to determine the Darcy friction factor for the fully turbulent flow. This makes it necessary to use the semi-empirical, implicit Colebrook equation that needs to be iteratively solved using Newton's method.

$$\frac{1}{\sqrt{\lambda}} = -2 * \log\left(\frac{2{,}51}{Re\sqrt{\lambda}} + 0{,}27\frac{f}{d}\right) \tag{2-44}$$

Darcy's friction factor in the transition range between laminar and fully turbulent flow is characterized by random flow interruptions, which makes it difficult to predict the precise

state of flow. In the case of a flow regime in the transition range, *HyFlow* calculates the friction factor for both the laminar - and the fully turbulent flow and sets it to the median value. Since this state is not common in natural gas grids, this inaccuracy is considered as neglectable.

The detailed description of the applied natural gas LFC in this work is presented in section 3.5.6. The methodology is based on the approach of Rüdiger [63], which works similar to the electric nodal analysis of voltage potential differences and presents a solution to deal with the quadratic dependence between flow rate and pressure loss. This is necessary in order to use the solver strategy of the electrical LFC for the iterative calculation procedure (Newton-Raphson). Rüdiger validated his newly developed algorithm successfully and gives further insights on accuracy, optimal number of nodes and ideal choice of initial values to reduce necessary iteration steps in [63]. For the validation of his calculation process, Rüdiger compared the results of his methodology to the Hardy-Cross algorithm [64,65], which serves as proven numerical reference algorithm (first introduced in 1936) for meshed pipeline networks. The Hardy-Cross algorithm, which serves solely as validation source, bears certain similarities to Kirchhoff's laws for electrical networks. The approach is based on three types of equations. The first type is equivalent to Kirchhoff's current law for nodes, while the second type is similar to Kirchhoff's law of voltage for closed loops. The third type of equations necessary for the Hardy-Cross algorithm consists of correction equations for each closed loop to determine so-called "correction coefficients". These are used for the actual iterative procedure to determine the individual flow rates and pressure losses between all nodes. The corresponding equations of the described procedure are presented underneath. Equation 2-45 shows that the algebraic sum of all incoming and outgoing flow rates into a node equals 0, with n being the total number of connected nodes. Equation 2-46 shows that the sum of pressure differences within a closed loop equals 0, with n being the total number of measured pressures in nodes within the closed loop.

$$\sum_{i=1}^{n} \dot{V}_i = 0 \tag{2-45}$$

$$\sum_{i=1}^{n} \Delta p_i = 0 \tag{2-46}$$

2.3.3 District heating load flow calculations

A district heating model consists of two major parts. The first part is a flow-based model based on the physical characteristics of fluid mechanics, as described in the section of natural gas. Secondly, a thermal model on top of the media flow needs to be implemented to cover heat transfer mechanisms. While highly simplified models do not take heat losses between the supply temperature at the location of the heat supply and the supply temperature at the individual consumers into account, most advanced models consider the temperature drop between the locations of supply and demand. Another major difference between natural gas networks and district heating networks is the energy content. The medium flowing in the pipes of district heating grids is only used as a transfer medium and is not "consumed" itself, as it is the case for natural gas. This requires that district heating networks have a supply flow and a return flow, as illustrated in Figure 2-13. It has to be noted that most district heating grids have two separate water circuits and the actual heat demand is transferred to the individual consumers via heat exchanger units. This is mostly due to redundancy reasons.

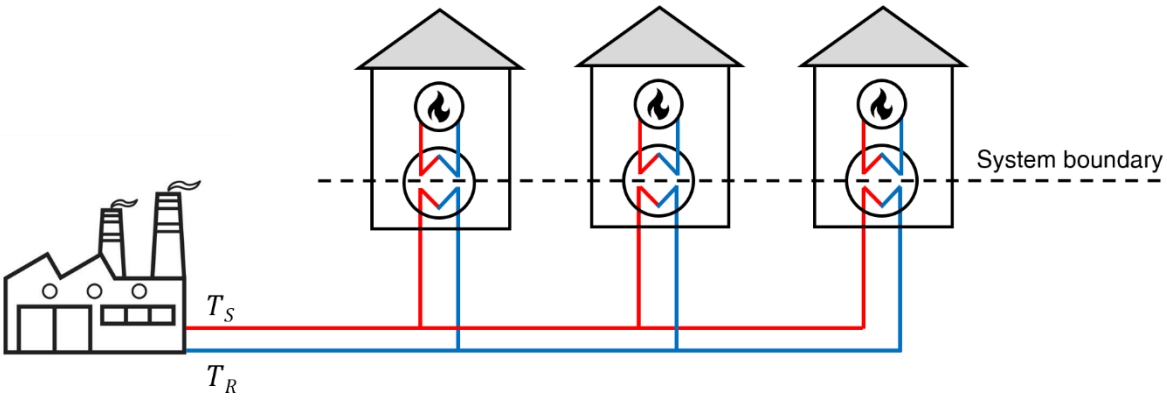

Figure 2-13: Simplified district heating network with supply temperature (red) and return temperature (blue)

The calculation process of the media flow is similar to the described methodology for natural gas. Only parameters such as the physical state and the corresponding density of the media need to be substituted. To calculate the supply temperature, the temperature drop between the locations of supply and demand, as well as the return temperature drop, thermal losses need to be determined. The heat flux through a pipe wall can therefore be described by Equation 2-47, with L being the length of the hollow cylinder. T_1 represents the fluid temperature of the media, T_2 is the outside temperature and k is the heat transition coefficient, which is calculated as shown in Equation 2-48. The included variables are the inner radius r_1, the outer radius r_2, the heat transfer coefficient between the inner medium and the pipe α_1, as well as between the pipe and the outer medium α_2 and the thermal conductivity λ.

Both equations are only applicable to hollow cylindrical pipes, which are state of the art in district heating systems. [66]

$$\dot{Q} = 2\pi \cdot L \cdot k \cdot (T_1 - T_2) \tag{2-47}$$

$$k = \frac{1}{\frac{1}{r_1 \cdot \alpha_1} + \frac{1}{\lambda} \cdot \ln\left(\frac{r_2}{r_1}\right) + \frac{1}{r_2 \cdot \alpha_2}} \tag{2-48}$$

While the main principles of calculating heat losses and the corresponding temperature drop are the same, the implementation of the flow-based LFC for district heating systems are entirely different. This is due to the entirely different purpose of energy system models with district heating grids and the associated complexity level of district heating systems, as presented in [67–69]. Talebi et al. [68] describe the associated model complexity as dependent on the number of utilized heating supply technologies, the applicable number of end-users, the level of detail of the temporal load profile and the spatial distribution. One out of many introduced classification options by Talebi et al. is the hydraulic and thermal equilibrium in distribution networks of district heating systems. They conclude that all known hydraulic models consider the network ideal in terms of mass conservation and therefore leak-free. In terms of the thermal characteristics, the analyzed sources [70–75] suggest two options: a steady-state or dynamic thermal equilibrium. They recommend using the steady-state approach for networks with an operational temperature below 70°C or well-insulated grids, while district heating systems with higher temperatures above 110°C or poorly insulated networks should preferably use dynamic approaches, according to [68]. Additionally, a comparison between experimental grid data and pipe model behavior of various open libraries is published by Schweiger et al. in [76]. The authors compare district heating models of general-purpose tools with the experimental data of two case studies and conclude that all tested dynamic models work accurately and are suitable for district heating network simulations.

2.4 Flexibility options

The described LFC methods can be used to distinguish time-dependent load flows for all implemented grid segments. Additional capacities of intermittent generation or a change in load profiles (e.g. electric vehicles, heat pumps, electrification of industrial processes) may lead to greater fluctuations of residual loads and possible grid congestions. In this section, four possibilities to deal with fluctuations of the residual load are presented. The main flexibility options are energy storage, sector coupling and demand response. Additionally, the effects of

grid expansion is described in this chapter, even though it is not a flexibility option in the conventional sense. However, for the sake of completeness, it is also included in this chapter, because grid expansion can provide larger spatial flexibility to the energy system. In the following sections, the general working principles of each individual flexibility option, as well as exemplary technologies are described.

2.4.1 Energy storage

Energy storage systems are an important flexibility option in energy systems with high shares of intermittent energy generation sources. In general, ESS are capable of balancing temporal fluctuations in energy generation and energy demand, in contrary to the described spatial balancing via energy grids. The principle of any energy storage is the capture of energy generated at one time and usage of the same energy content at a later time. There are multiple technologies to store energy in all kinds of forms, but all follow this simple principle, which is also illustrated in Figure 2-14. It shows the effect of ESS on a random residual load of an exemplary Region 1. It is also used for demonstration purposes in Figure 2-21 of section 2.4.4. The influence of the two most important ESS characteristics, the maximum energy content and the maximum power of the ESS on the residual load is explained and presented with the help of Figure 2-14. In order to show the impact of increased ESS capacities and increased charging/discharging powers, three demonstration examples are defined. The specifications of these three fictive ESS examples 1,2 and 3 are summarized in Table 2-4. Since Figure 2-14 is only shown for demonstrative purposes, other side characteristics (e.g. ramp rates, efficiencies etc.) are neglected.

Table 2-4: Exemplary parameters for demonstration purposes shown in Figure 2-14

	Maximum State of Energy SOE_{max}	Maximum battery power $P_{Batt,max}$
ESS 1	15 GWh	4 GW
ESS 2	35 GWh	4 GW
ESS 3	35 GWh	6 GW

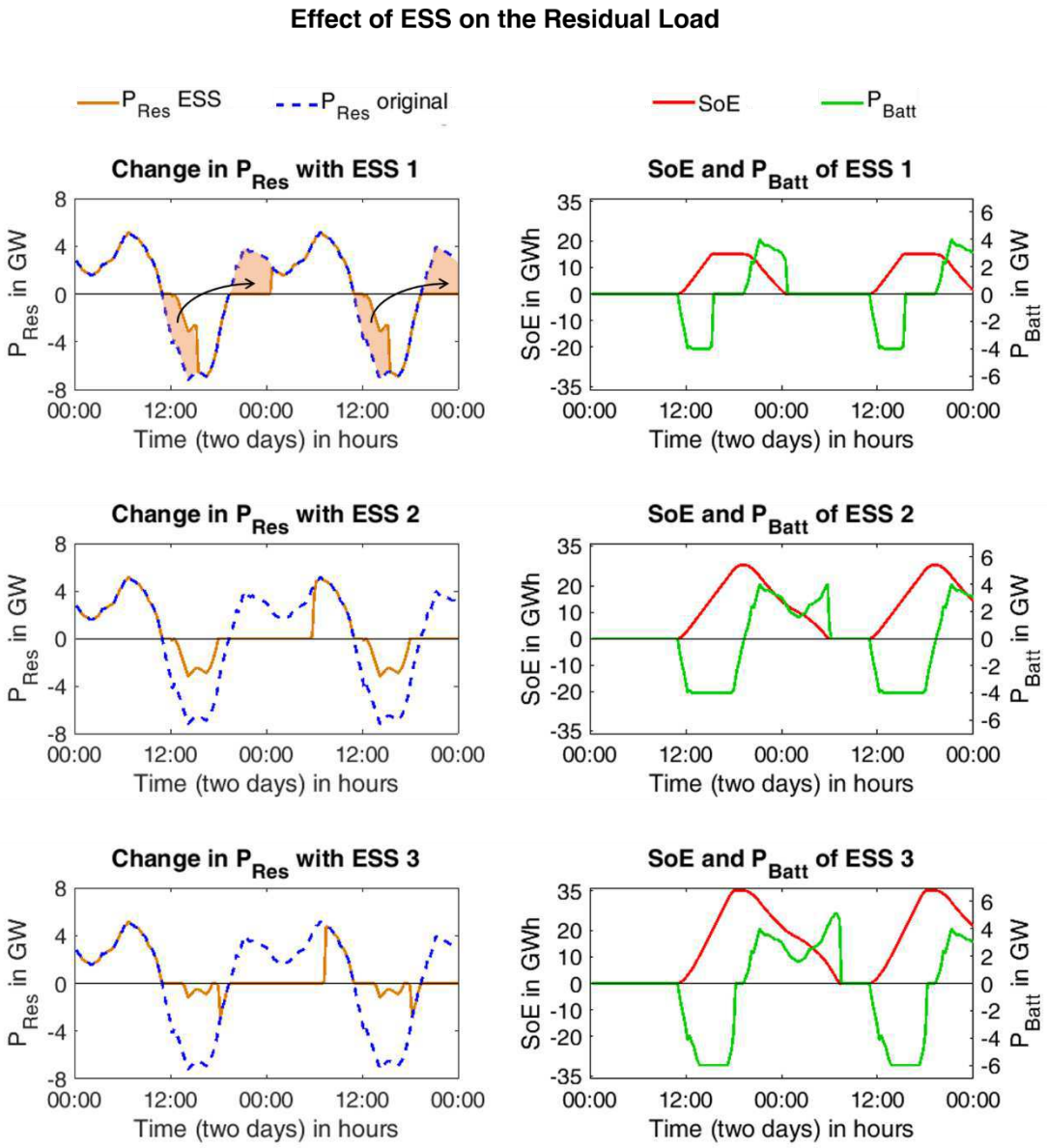

Figure 2-14: Effect of an ESS implementation to smoothen the residual load and increase energy autonomy. The figures on the left, show the original residual load (blue) and the modified residual load (orange), due to the implementation of ESS. The figures on the right side show the corresponding SoE (red) and the battery power (green)

The effect of the size of an energy storage system in terms of the maximum energy content SOE_{max} and $P_{Batt,max}$ is shown in Figure 2-14. The first energy storage system (ESS 1 – as shown in the top row of Figure 2-14) is able to charge the excess energy from around 12:00 until 15:00, with a maximum power of 4 GW. This leads to a changed residual load in the corresponding period (orange), before the SOE_{max} is reached. The stored energy is later (around 19:00) discharched, once the original residual load becomes positive again. Around

midnight, ESS 1 is empty and both residual loads are identical until the same cycle is repeated on the following day. The top right illustration of Figure 2-14, shows the corresponding development of the SOE (red) and the battery power P_{Batt} (green) for ESS 1. One can see, that the SOE starts to increase, as soon as the residual load in the left illustration becomes negative, until SOE_{max} is reached. This charging process is limited by the maximum battery power of 4 GW, as seen in the green graph. As soon as ESS 1 is fully charged, P_{Batt} is zero, before becoming positive again, at the discharging period.

ESS 2 is able to store 35 GWh, which is a significant increase to 15 GWh of ESS 1. The maximum power of the ESS stays the same, compared to ESS 1. This allows to examine the effect of an increased SOE_{max} on the same residual load. One can see, that the charged/discharged energy content is much higher compared to ESS 1.

In order to evaluate the influence of the maximum power or energy storages, ESS 3 has the same value maximum energy content SOE_{max}, but allows a higher charging/discharging power of 6 GW. The bottom row of Figure 2-14 clearly indicates, that this measure leads to a further increase of stored energy. The maximum value of energy stored amounts around 28 GWh, while ESS 3 is able to use the full SOE_{max}, due to the higher charging/discharging power. This allows to conclude that an increased SOE_{max} as well as a higher $P_{Batt,max}$ generally enables to store more energy. This may lead to a better balance of generation or demand fluctuations.

One way to characterize ESS is the methodology of Discrete Fourier transform (DFT). DFT enables to transform a time-discrete signal into its containing frequencies. This tool allows to analyze the periodicity of any signal, which can be used effectively to calculate the necessary temporal characteristic of an ESS. By applying the algorithm to a residual load, the main frequencies of charging and discharging an ESS including the charging/discharging powers (amplitude) can be determined.

Figure 2-15 illustrates the main process steps of the DFT analysis for an exemplary residual load. The total signal, which is analyzed, is shown in the left illustration as time-dependent residual load. The same signal is disassembled into single signal frequencies. It has to be noted that the superposition of these single signals results in the total signal again. The right illustration shows the amplitude and the frequency of the single signals. These amplitudes and frequencies contain the relevant information. When applying this principle to a residual load of any energy system, the frequency provides information on the periodicity of a possible ESS. It helps to determine whether an ESS is suitable to cover for hourly, daily, weekly or seasonal storage and therefore specify the appropriate temporal classification. The amplitude helps to

design the necessary power of the ESS. Furthermore, for the sake of completeness, it should be added that the DFT also provides information regarding the phasing shift of the signal, which defines whether positive or negative interference of signal components occurs. The phase shift is neglected in Figure 2-15.

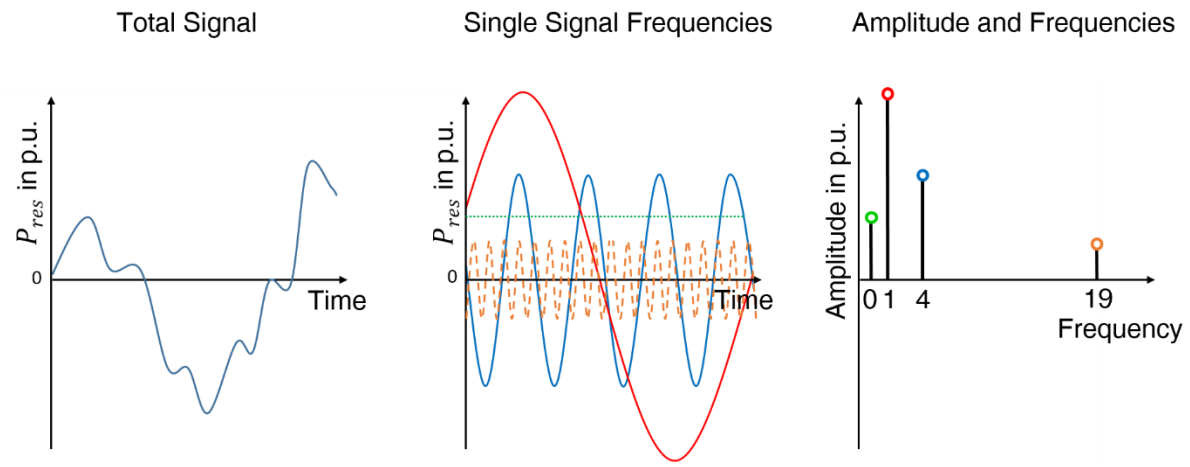

Figure 2-15: Illustration of DFT principle for an exemplary residual load. The total signal of the residual load (left) is disassembled into single signal frequencies (center), which is also illustrated as amplitude/frequency diagram (right). Own elaboration based on [77]

Another important consideration when designing an ESS is the expected number of full cycles. Storage cycles are calculated by the sum of discharged energy E_{Dis} over a certain time period, divided by the maximum energy capacity of the ESS Cap_{ESS}. The definition of the number of cycles Cy_{ESS} is presented in Equation 2-49.

$$Cy_{ESS} = \frac{E_{Dis}}{Cap_{ESS}} \tag{2-49}$$

In order to show the practical relevance of the number of full cycles, an example is presented for a PV battery system. Figure 2-16 presents the distribution of the expected full cycles for a PV storage system. The normalized PV system size is applied to the x-axis, which represents the PV system size related to the annual energy consumption of the consumer in kW_{peak}/MWh load. The y-axis analogously represents the normalized battery size in kWh/MWh load. A more detailed definition of the normalized PV system size and normalized battery size is presented in section 3.4.6. One can see that the number of full cycles is at its maximum in areas of low normalized battery sizes and medium PV system sizes. This is due to the reasonable amount of generated energy from the PV system, which exceeds the load and can be stored in the battery unit. More than one full cycle per day is possible (approximately 500 per year) for this

design configuration. Larger batteries or PV systems may increase the overall energy used to supply the load, but the number of cycles declines.

This number of full cycles is specifically important for economic evaluations. Very often ESS operate in charging mode in times of lower prices, while discharging energy in times of higher prices. This is called arbitrage principle. By achieving a high number of full cycles, the energy throughput per capacity of the ESS is increased, which is directly proportional to the economic profitability of the ESS.

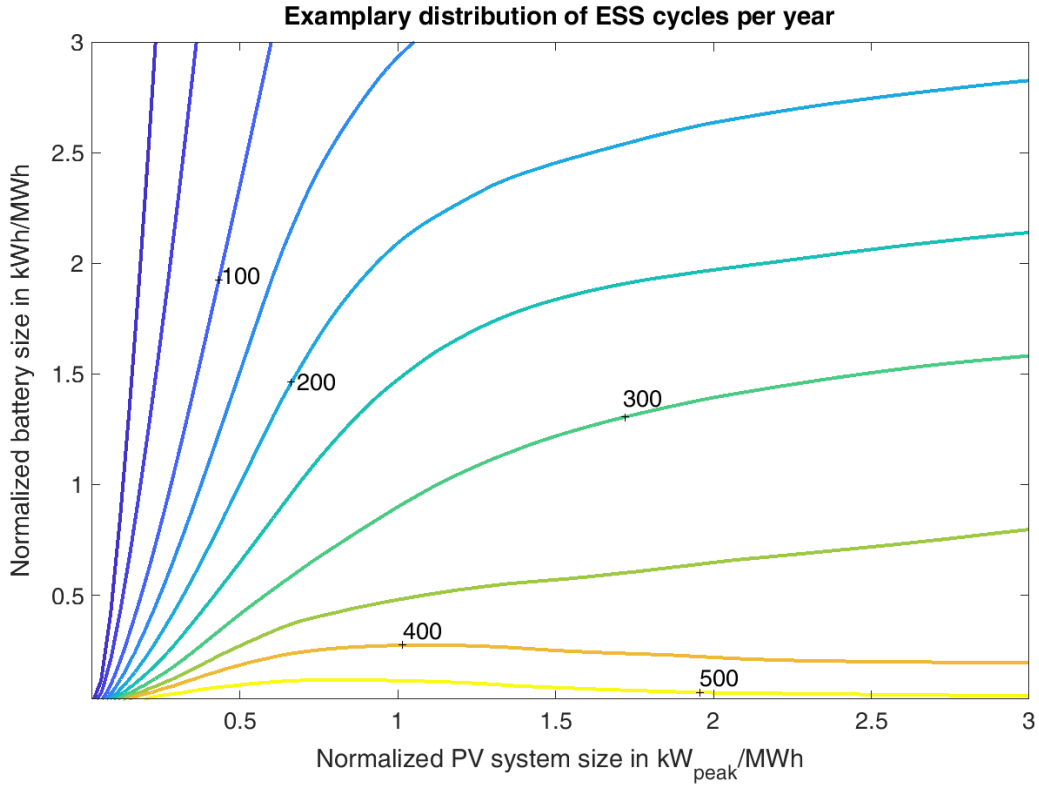

Figure 2-16: Exemplary distribution of the annual cycles of a PV storage system.

As demonstrated before, there are multiple options to characterize ESS and many aspects need to be considered. Sterner and Stadler [78] distinguish between physical, energetic, spatial, economic and temporal classifications. Examples for physical energy storages are electric, electrochemical, chemical, mechanical and thermal ESS. All of them can be further divided into multiple technology types. This category distinguishes between the energy form of the stored energy content. It has to be noted, that the input energy and output energy does not have to be consistent with the stored energy content. For example, electricity can be stored in the form of all mentioned physical categories.

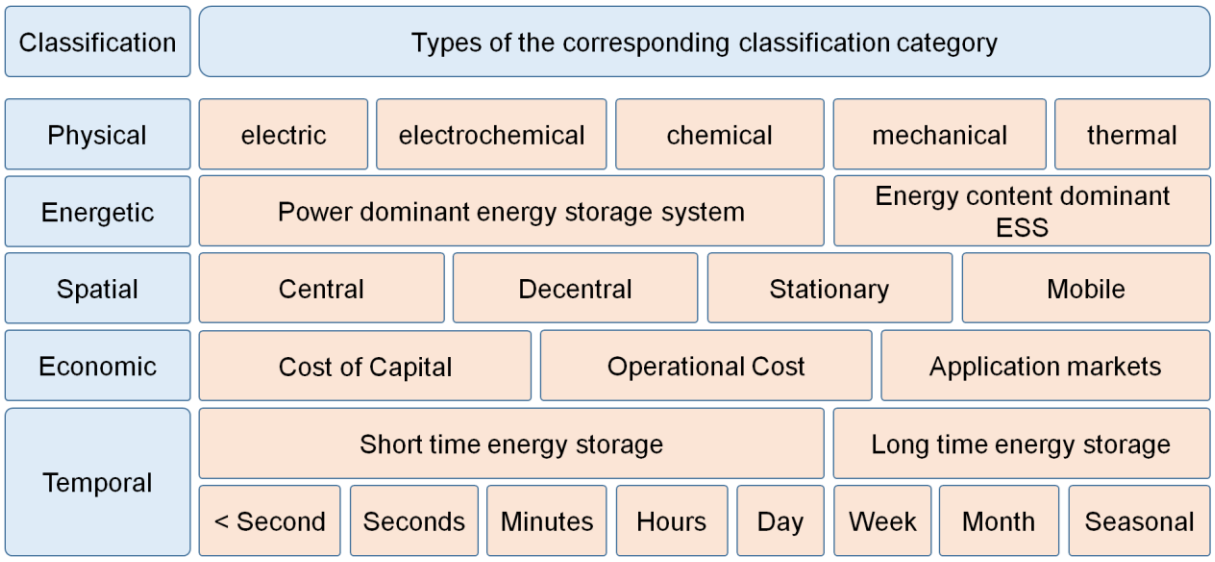

Figure 2-17: Classification categories of ESS – own illustration based on [78]

When implementing ESS into an energy system, many characteristics need to be considered. Energy content, maximum power, efficiency, self-discharge, space requirement or economic costs are examples for considerable properties to find the appropriate ESS for each application.

Table 2-5 gives an overview of selected ESS, sorted by their physical properties. Long-term storage probably needs an energy storage with low self-discharge and small CAPEX, mobile applications like electric vehicles need ESS with a high volumetric energy density, stationary applications may be ranked by efficiency, cost and lifetime and ESS to stabilize the electricity grid need a high power and a short reaction time. Not all ESS are freely scalable, it is for example not feasible to have electric ESS, such as Super-Caps or Condensators in the MWh range, while chemical storages are able to store huge energy amounts in former natural gas fields in the TWh range.

The bottom line is that many characteristics of ESS need to be taken into account. As the sector of energy storage is a rapidly changing research and technology area, sources may state deviating parameters. This is the reason Table 2-5 states a wider range of values for some characteristics.

One major insight of Table 2-5 is the limit of energy content that can be stored in electric, mechanical or electrochemical ESS. Although electrochemical storage, especially in the form of Lithium-Ion batteries has experienced a veritable boom in utility-scale installations, it will not be possible to store the enormous seasonal fluctuations of intermittent energy sources (see Figure 1-1) for the foreseeable future.

Other types of ESS (especially chemical storage) enable to store huge amounts of energy in the TWh range in exploited gas fields or salt caverns. This comes at the cost of lower efficiencies (if electricity needs to be converted to synthetic gas) compared to mechanical or electrochemical ESS, especially if the stored chemical energy is reconverted to electricity. This leads to another option of possible flexibility in the energy system: sector coupling, which is explained in the following section

According to Austria's energy regulator E-Control [79], the overall gas storage capacities are quantified with approximately 92.1 GWh, a charging power of 34.5 GW and a discharging power of 44.1 GW. To put that into perspective: there are 3.9 million households in Austria [80]. If every single household would buy a usual home storage battery with 5 kWh and a charging/discharching power of 3 kW, the total storage capacity of these units would be 19.2 GWh (around 20 % of the gas storage capacity) with a charging/discharging power of 11.7 GW (around 26-33 % of the charging/discharging power of the gas storages).

Table 2-5: Parameters of selected ESS [78,81–85]

		Efficiency	Self-discharge	Lifetime	Lifetime	CapEx	CapEx	Energy density	Energy density	Power density	Power range	Energy range	Discharge time	Reaction time
		%	%/time	cycles	years	€/kW	€/kWh	Wh/dm³	Wh/kg	W/kg	MW	MWh	time	time
Electric ESS	Condensator	60-70	40 %/d	>50,000	1-10	200-400	500-1,000	2-10	0.05-5	3,000-	<0.05	-	ms-1h	ms
	Super-Cap	95.8	20-40 %/d	10^5 - 10^6	5-10	250-450	300-2,000	10-30	2.5-15	500-5,000	<0.3	0.0005	<1 min	ms
	SMES	95-97	10-15 %/d	>100,000	20-30	200-300	500-72,000	0.2-2.5	0.5-75	500-2,000	0.1-10	≈10^-3	ms-30 min	ms
Mechanical ESS	CAES	50	0.5-1 %/d	unlimited	30	340-1,145	≥40	2-5	-	-	110-290	870-2,860	1-20 h	8-14 min
	Adiabatic CAES	70	0.5-1 %/d	unlimited	30	600-800	80	2.9	-	-	110-290	870-2,860	1-20 h	8-14 min
	Flywheel	80-95	3-20 %/h	> 100,000	20	125-275	1,000	10	<5	275	0.01-20	0.001-0.1	<5 min	< 1 s
	Pumped storage	70-84.5	0-0.5 %/d	20	50-100	550-2,040	Location	0.7	0.7	-	100-4,000	500-15,000	4-24 h	1-5 min
Electrochemical ESS	Lead-Acid	75-90	5 %/m	300-2,000	4-6	200-490	100-250	50-100	25-40	100-500	0.1-50	0.5-200	1-8 h	3-5 ms
	Li-Ion	90-95	5 %/m	5,000-15,000	15(stat.) 8(mob.)	1,200-4,000	800-1,500	250-350	95-190	700-1,300	0.01-2	0.001-200	0.025-4 h	3-5 ms
	NaS	70-80	0.1 %/d	10,000-15,000	10-15	1,000-3,000	500-700	150-250	100-200	160-220	1-50	1-380	1-8 h	3-5 ms
	NiCd	70	0.2-0.6	<3,000	10-20	500-1,500	800-1,500	50-150	40-60	150	<40	6.75	1-8 h	3-5 ms
	VRFB	75-85	0.2 %/d	>12,000	5-10	600-1,500	150-1,000	16-33	10-30	166	0.03-3	<60	2-12 h	ms
	Zinc-Bromine	65-80	0.24 %/d	>2,000	5-10	700-2,500	150-1,000	30-60	30-80	-	0.05-10	0.1-4	≈10 h	ms
	Polysulfide-Br	60-75	≈0	≈2,000	10-15	700-2,500	150-1,000	20-30	15-30	-	1-15	<120	≈10 h	20 ms
	ZEBRA	85-90	15 %/d	>2,500	10-14	150-300	100-200	150-180	100-120	150-200	2-50	0.5-250	2-4 h	1-60 s
	NiMH	70-75	0.4-1.2	300-500	5-10	420-1,200	240-1,200	<350	60-120	70-756	<0.2	<0.5	1-10 h	ms
	Zinc-Air	60	2 %/year	>2,000	30	785	120-130	800	400	1350	-	-	6 h	ms
Thermal ESS	Sensible	45-75	40-70 %/m	30	30	80-130	0.2-8	100-300	10-50	-	100-500	1000	5-15 h	5 min
	PCM	75-90	40-70 %/m	10	30	80-160	10-50	100	50-150	-	0.001-1	0.7	0.25-12 h	2 min
	Thermochemical	75-100	≈0	5	30	200-300	8-40	300	120-250	-	0.01-1	<250	1h	< 15 min
Chemical ESS	Power-H_2-Power	34-44	0.03-0.003 %/d	unlimited	20	800-1,500	Location	187	-	-	0.1-GW	0.1-TWh	sec-days	10 min
	Power-CH_4-Power	30-38	0.03-0.003 %/d	unlimited	20	1,000-6,000	Location	561	-	-	0.1-GW	0.1-TWh	sec-days	10 min

2.4.2 Sector coupling

The term “sector coupling” is derived from the idea of interacting energy sectors, such as electricity, heating, natural gas or mobility. These separated energy systems, whose parts are considered independently in today’s world should be connected and linked among each other. This approach is also referred to as “Multi-Energy systems”, “Integrated Energy” or “Cross-sectoral energy system” in literature. [86–88] All of them embrace a stronger integration between the sectors in order to exploit individual technical or economic advantages of the sectors and synergies between them. An illustration of possible sector coupling pathways and the corresponding technologies is presented in Figure 2-18.

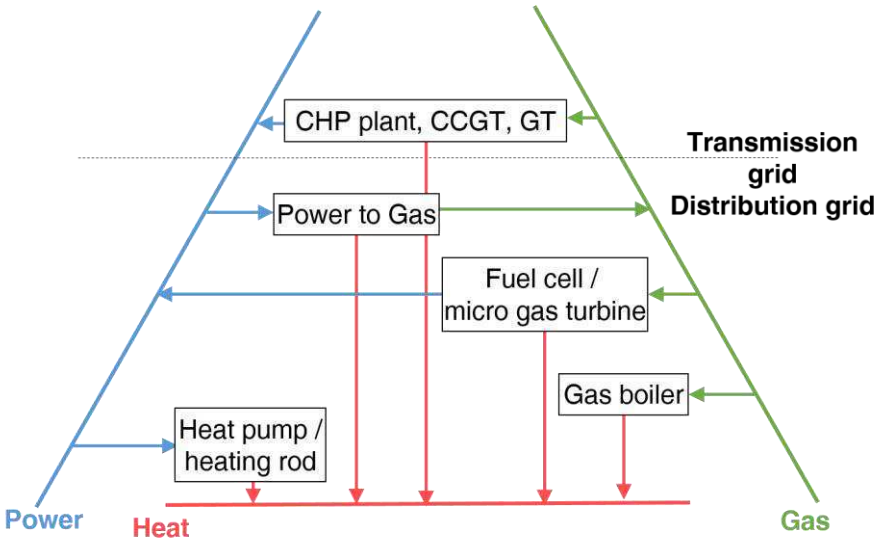

Figure 2-18: Sector coupling pathways and the corresponding technologies

When considering the three energy carriers, electricity, natural gas and district heating, there are six possible conversion paths. Technologies to convert electricity to heat are called Power2Heat (P2H). Possible examples are simple resistance heating or heat pumps. Both technologies are available at household scales and larger utility scales in the MW range. They are highly efficient and can be considered proven technologies. [89] The second possibility of electricity conversion is Power2Gas (P2G). Naturally power itself cannot be transformed to a chemical compound. Power is used to dissolve water into hydrogen (H_2O) and oxygen (O_2) via electrolysis. It is possible to use the generated hydrogen directly or further convert it to methane (CH_4) with the help of a carbon dioxide source (CO_2). To generate the necessary hydrogen technologies, such as AEL or fuel cell technologies like PEMEL or SOEC. Compared to P2H applications, the efficiency of today’s electrolyzers is significantly lower, with values between 55-90 %, depending on additional heat utilization. Power2X (P2X) describes the utilization of electricity to convert it to any other form of energy. [90–93]

The most conventional pathways in sector coupling are the natural gas conversion processes. There are large central technologies converting gas to power (G2P) in power plants. If the power plant additionally uses the heat of this process, the corresponding plant is designated as Combined Heat and Power plant (CHP). In recent times, this technology was scaled down to µCHP units, which can also be used for smaller, decentral energy generation. [94] If natural gas is only used for heat generation the conversion process is referred to as Gas2Heat (G2H). All of the mentioned technologies are long established at household and utility-scale.

The conversion of heat to other energy carriers, at temperature levels of district heating grids, is less common. There are technologies to use low-temperature heat to generate electricity, such as the Organic Rankine Cycle (ORC) or Peltier elements. The efficiency of Heat2Power (H2P) technologies is well underneath 20 % and therefore these technologies are not widespread. [95] Technologies for the utilization of low-temperature heat to generate gas are not available.

In addition to the conversion between grid-bound energy carriers, the literature also labels other forms of sector coupling, such as Power2Mobility or Power2Chemicals. These conversion pathways usually have the electrification of a process in common, which was previously supplied with fossil energy. An example of Power2Mobility is the replacement of a conventional petrol-driven car, by an electric vehicle. Austria's share of RES in the mobility sector is 9.7 %. [96]

While some sector coupling technologies are widespread in the current energy supply (e.g. CHP plants, electric heating), other conversion paths (e.g. Power2Gas) are not yet implemented. The future implementation of these conversion paths, especially of the P2X technologies, is the true novelty of sector coupling.

As illustrated in Figure 1-2 and Figure 2-9, Austria's residual load in the electricity sector is expected to be negative over long periods during the year. Apart from transporting the surplus electricity to neighbouring regions or storing it for following times of positive residual loads (as described in the previous sections), another option is to convert electricity to other energy forms with a positive residual load, like the heat sector or the natural gas sector. This has two major advantages:

- The share of Renewables in the cooling/heating sector with 32.1 % [96] and the natural gas sector with approximately 1 % [96] is significantly lower than in the electricity sector with 72.2 % [96]. Additionally, the residual load of heating and natural gas is positive throughout the year, which enables the absorption of a large share of converted electricity directly and without storage. Since both sectors (especially

natural gas) are supplied mostly by fossil fuels, this measure significantly improves the primary energy efficiency and reduces specific CO_2 emissions. The residual load of the natural gas sector in Austria is illustrated in Figure 2-19. It shows a peak load of 25 GW and a minimum load of 3.6 GW.

- The second main reason why sector coupling is considered crucial is the extended variety of energy storage opportunities. As stated in the overview of ESS technologies in Table 2-5, the CAPEX for ESS, as well as the feasible maximum energy content, heat and gas storages are significantly favorable compared to electric, electrochemical or even mechanical ESS. This means that sector coupling is the only viable option for long-term storage of electricity. P2G especially enables huge storage potentials and allows to reconvert the synthetic gas to electricity in times of higher electricity demand.

These advantages have to be set against certain disadvantages:

- While efficiencies of P2H applications, such as direct electrical heating or heat pumps are very high, P2G technologies tend to have much lower efficiencies. Especially if a reconversion to electricity is planned, round-trip efficiencies of significantly less than 50 % are today's achievable maximum. [78] Additionally, all P2G technologies currently struggle with economic barriers, because the "green" gas, synthesized with the help of electricity is more expensive compared to conventional natural gas today. [78,90]

- Furthermore, energy efficiency is not the only deciding factor if the usage of a sector coupling technology is reasonable. Energy can be divided into exergy and anergy, with exergy being the part of energy available to be used as work. [97–99] This is particularly relevant for P2H applications. When converting high-exergetic electricity to low temperature heat, most of the exergy content is lost. An exception to this exergy loss in P2H applications is the heat pump technology. Due to the ability of heat pumps to absorb energy from a cold environment (anergy) and release that energy as heat at a warmer environment by adding just a fraction of external electricity (exergy) compared to the energy of the heating application, it is an example of an exergy efficient process. Additionally, the seasonal demand peaks of heat in winter are not occurring simultaneously with the generation peaks of electricity in the summer. [89,100]

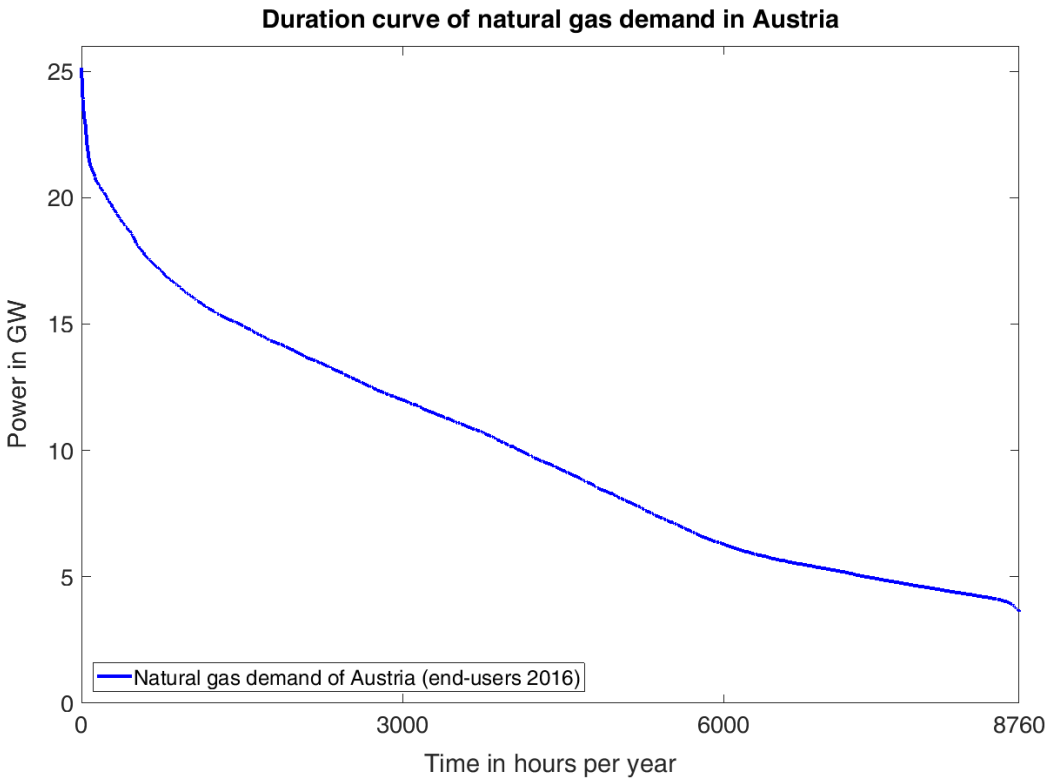

Figure 2-19: Duration curve of the natural gas demand of Austrian end-users in 2016

Both disadvantages imply that generated electricity should preferably be used for electrical applications. While energy efficiency is the key indicator to characterize P2G technologies, exergy efficiency is the more appropriate tool for P2H technologies. However, if surplus electricity cannot be transported to the location of electricity consumption or be stored in corresponding ESS, lower efficiencies are no longer a reason for the exclusion of P2X applications. [101]

2.4.3 Demand response

In today's energy system the consumer load is not influenced by the current status of the grid. While large consumers might react to price volatility, most end-users (e.g. households, small businesses) do not change their consumption pattern based on any external influences. Demand response (DR) refers to an active intervention in the current energy load in order to react to a specific grid-related or energy generation-related situation. This active change of consumption can be realized by price incentives or behavioral change through education. The European Commission defines Demand response as follows:

"Demand response is a series of programs sponsored by the power grid, the most common of which pays companies (commercial DR) or end-users (residential) to be on call to reduce electricity usage when the grid is stressed to capacity" [102]

This definition narrows the limits of DR to end-consumers actively choosing to enter into a commitment, where the grid operator is able to call for a reduction of the load in times of high stress for the grid. Other broader definitions, from the Department of Energy and the US Federal Energy Regulatory Commission describe DR as a consumer choice incentivized by price signals. [103] This means, that there are two major options, which are both labeled Demand response. The first option, as defined by Bertoldi et al. representing the European Commission [102] is called direct load control, which is performed remotely by a third party (e.g. grid operator, utility). In the second definition, as seen in [103], monetary incentives or financial penalties in the form of flexible tariffs give the consumer the choice of reacting to it, with no obligation to do so. [104] A more detailed distinction between the different types of DR can be found in Paterakis et al. [105]

Both approaches can also be referred to as demand side management (DSM), peak-shaving or simply load management. The main goal is to limit electricity load in times of peak hours, which potentially prevents grid congestions and enables shifting loads in peak hours to times of lower consumption. Figure 2-20 aims to illustrate possible effects of DR. [104]

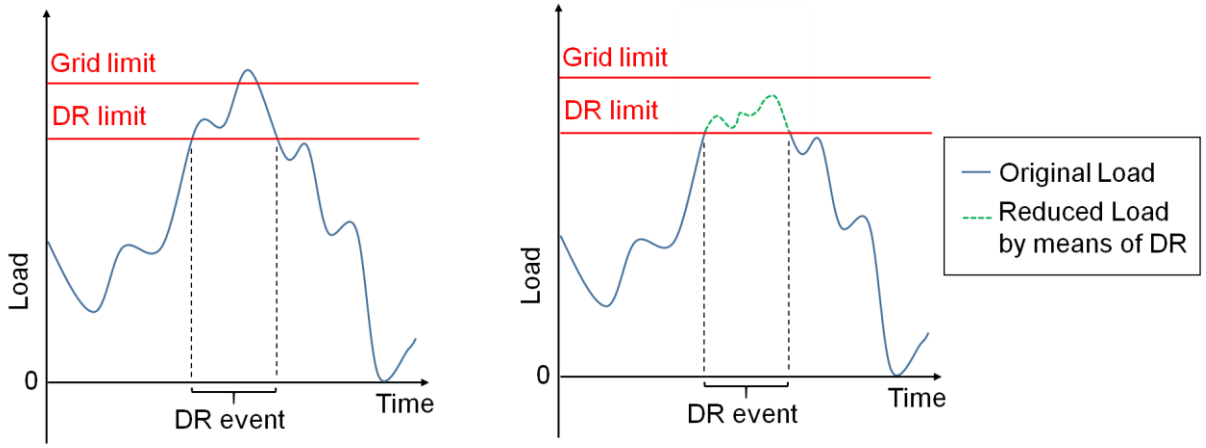

Figure 2-20: Illustration of a possible usage scenario of DR in order to prevent exceeding the grid limit

According to [105], the implementation of DR measures brings advantages to the energy system in terms of congestion management, renewable energy integration and market-based benefits such as lower and more stable electricity prices. Disadvantages of DR measures are usually the necessary quite extensive ICT infrastructure, data security of sensible load data and the need for change in legislation in most areas.

2.4.4 Grid expansion

An efficient, reliable grid is the basis to overcome the spatial distance between energy supply and demand. A well-developed network, connecting different regions can also play a significant role in providing the necessary system flexibility. It enables to supply the locally provided energy to a larger consumer base, which reduces random statistic fluctuations of the residual load caused by intermittent energy generation.

Figure 2-21 (a) presents an exemplary fictive residual load of region 1. Due to a high temporary generation in the afternoon hours, a negative residual load occurs. If one provides a grid connection to region 2, with a continuous positive residual load, as seen in Figure 2-21 (b), a new combined residual load occurs in Figure 2-21 (c). The total residual load of both regions is almost entirely positive throughout the reviewed time period. The influence of the grid expansion is illustrated in the three graphs (d), (e) and (f) of Figure 2-21. The green line in (d) represents the non-restricted load flow (up to 8 GW) from region 1 to region 2, while the red line represents a restricted grid connection, with a maximum power transport of 3 GW. The impact on the corresponding residual load of both regions is illustrated in (e) and (f).

This means that combining regions via strong grid connections enables a flexible exchange of energy between regions, which may reduce unused excess energy. Additionally, energy transport is mostly very efficient, with low energy losses compared to other flexibility options, such as energy storage or sector coupling. It allows the direct usage of the generated energy, without another conversion process. However, in order to exploit the flexibility potential, the residual loads have to be heterogeneous. If for example, negative residual loads occur simultaneously in multiple regions, high transfer capacities of grids will not have the desired effect. It can therefore be advantageous to connect regions with frequently occurring negative residual loads to industrial dominated regions with constantly positive residual loads.

Another point to consider is the increasing difficulty of grid expansion, due to the resistance of citizen's initiatives or lack of political will. There are numerous examples of grid expansion projects needing several years or even more than a decade from project submission to the last-instance legal approval decision, or the start of construction. [106–108]

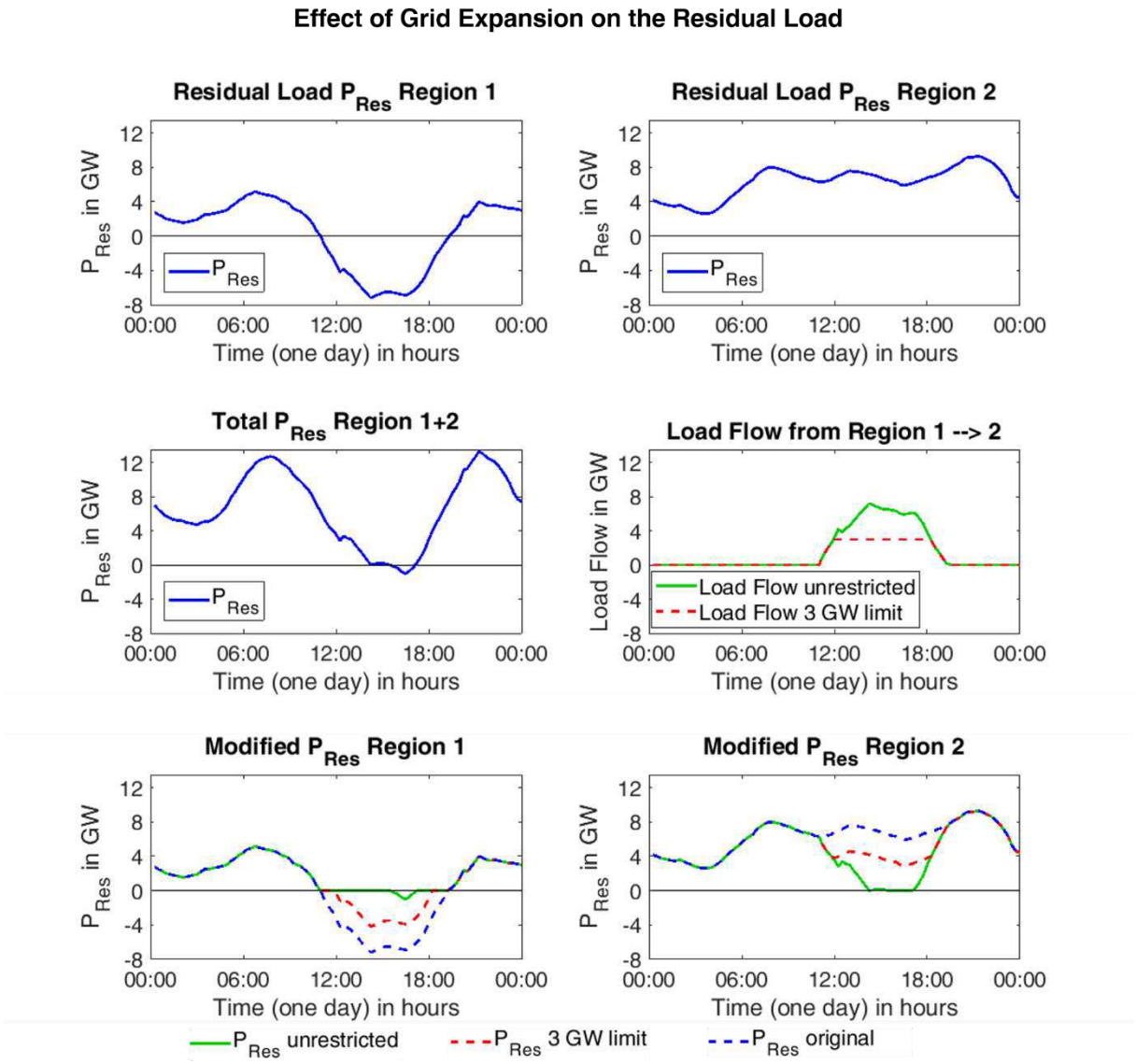

Figure 2-21: Exemplary case to demonstrate the importance of grid expansion for dealing with fluctuating residual loads. Top row figures from left to right: (a) residual load of fictive region 1, (b) residual load of fictive region 2, Middle row: (c) Combined residual load (d) Resulting load flow between Region 1 & 2, Bottom row: (e) Modified load flows of Region 1, (f) Modified load flows of Region 2

2.5 Single-Nodal energy systems

This section is dedicated to summarize the state of research of Single-Nodal energy systems. In the context of this work, Single-Nodal energy systems are defined as fluctuating energy generation, corresponding consumer load and an optional energy storage system in a single node, without the need of energy transport or distribution. This makes the modelling of networks redundant in Single-Nodal systems. However, the restriction of generation, demand, and ESS in one location implies a very decentral generation technology. Since fluctuating sources like wind parks or hydropower usually supply many consumers with electricity and

therefore make energy transport a necessity again, this section primarily deals with the most decentral fluctuating energy technology: Photovoltaic power.

There are two major types of Photovoltaic energy generation topologies, the stand-alone or island application without a grid connection and grid-coupled PV plants. The design concepts and results of PV plants are entirely different for these two types. While the security of supply and the so-called loss of load probability (LOLP) are predominant for island plants, economic optima and optimal share of self-consumption are the most common concepts when designing a grid-coupled PV power plant. The performance indicator LOLP, was first introduced by Calabrese in 1947 [109] and describes a state, where the system load exceeds the available generating capacity (including stored energy). It is usually expressed in terms of hours or days per year or as a percentage of time. [110] Other key performance indicators used to design and size elements in Single-Nodal energy systems are defined in section 3.3.

Batteries, in combination with PV systems in residential buildings, have a strong influence on the achievable degree of self-sufficiency (DSS) and the amount of power exchanged with the grid. While a single PV system can only supply electricity during the day when the PV panels generate power, a system combined with a battery unit allows the owner to store surplus energy and use it when it's needed. Therefore, the combination of a PV system with a battery system enhances the share of self-consumed energy from the PV system (SCR), and reduces dependency on the grid. Supported by decreasing feed-in tariffs for PV power and lower battery prices of today's main technology of lithium-ion-batteries (more than 95 % market share in 2017), the cumulated amount of installed batteries in combination with grid-connected PV systems has increased from close to 0 to 85,000 installations in Germany in the years from 2013 to 2017. 31,700 batteries were installed in combination with a PV system in 2017 alone, resulting in a cumulated energy capacity of 245 MWh, which corresponds to an increase of 60 % compared to 2016. The total energy capacity of decentralized storage systems is estimated to amount to 600 MWh, with an installed power of 280 MW_{peak} in Germany. [111,112]

In the years from 2010-2012, the average additional installed power of PV installations was still around 7-8 GW per year, before it dropped to 1.2 GW in 2014. Since 2014, a continuous slow increase has been registered again. Even though the PV installation boom in Germany started approximately a decade before the significant increase in residential battery systems, the cumulated installed PV power still grows with an additional 62,300 new PV plants (below 30 kW_{peak}) in Germany 2017. The additional installed power in 2017 amounts to 1.7 GW_{peak}, increasing the cumulated installed PV power of Germany to 42.4 GW_{peak}. [111,113]

As there are numerous publications on the topic of sizing PV storage systems, the aim of this section is to conclude the current state of research and differentiate the results arising therefrom. There are two major distinguishing features. One regards the technical integration of the system and divides systems into stand-alone applications and grid-connected PV systems. The other distinction considers whether the process of sizing the PV battery system is based on technical or economical aspects. A brief summary of the examined papers and their main objectives and results is presented in the following paragraphs.

2.5.1 Design of stand-alone PV battery systems

A very good illustration of the dependence between LOLP and investment costs for stand-alone PV plants is published by Topic et al. in [114]. They investigate the possible cost savings of Off-grid PV battery systems, if the user accepts a certain LOLP. The main conclusion suggests a possible reduction of investment costs of around 25 %, if one accepts a LOLP of 2 % and a further reduction to around 50 % at just 9 % LOLP. This shows how expensive the supply of load peaks with minor energy content can become and how accepting a LOLP in the single-digit percentage range can contribute to major cost reduction. Fragaki et al. [115] performed a technical assessment of a stand-alone PV storage system. The work defines the necessary energy storage capacity as a factor of the average daily electricity consumption. Dependent on the location (London, Salzburg and Heraklion), the necessary battery capacity ranges from 9 to 26 times the average daily consumed energy. Arun et al. [116] and Cabral et al. [117] also size the PV battery configuration for stand-alone systems. Arun et al. perform a mixed approach that considers technical and economical design parameters, and defines confidence intervals via a Monte Carlo approach for different system configurations that would be capable of supplying the specified demand. Cabral et al. calculate the PV and battery demand for a defined building in Brazil via the stochastic approach and compared it to a deterministic method. Semaoui et al. [118] compare the so-called energetic cost (losses) of different system configurations in a use case in Algeria. The paper focuses on the influence of load management strategies and different storage life cycles on the size of PV battery stand-alone systems. The authors did not publish absolute numbers of the ideal system size.

2.5.2 Design of grid-connected PV battery systems

In the recent past, publications tend to focus on the topic of sizing grid-connected PV battery systems. Hoppmann et al. [119] consider two scenarios where they size the PV power and battery capacity in various variations based on an economic model. They define two main cases: one which allows the feed-in of PV power into the grid (1), and one where it is forbidden (2). While the optimal storage size for a defined household from the years 2013-

2022 for case (1) varies between 3.5-6.5 kWh, the same scenario for case (2) suggests battery sizes between 3-8 kWh. The ideal PV size for the household as in case (1) suggests ideal PV system sizes between 2-4.5 kW_{peak} and in case (2) sizes between 2-14 kW_{peak}. The large differences between the ranges are justified by the severe economic uncertainties in a 10-year prognosis, and by the high sensitivity to the electricity price and feed-in tariffs. The most similar approach compared to the one presented in this work was found in Weniger et al. [120]. They normalize the values of the PV system - and battery size to the annual energy consumption of the household, calculate relevant technical parameters, such as the DSS or the self-consumption-rate (SCR), and show characteristic diagrams of those key performance indicators which depend on system parameters such as PV system - and battery size. The actual sizing process for different scenarios, however, is based on an economic assessment based on three different future assumptions for the German market. The results show, that today and in the short- to medium term, no battery should be installed at all, while in a long-term future scenario, a battery of around 0.7 kWh/MWh annual electricity consumption is recommended. Pflaum et al. [110] show the effects of uncertain PV power predictions and a model predictive control (MPC) approach on the size of PV storage system but don't publish any absolute numbers for households. Khalilpour et al. [121] compare the Net Present Value (NPV) of grid-connected system configurations ranging from 0-20 kW_{peak} PV power and 0-20 kWh battery capacity in different scenarios with variable investment costs, feed-in tariffs and load types. All six different compared household loads have their maximum NPV at no battery installation at all and rather small PV sizes below 7 kW. In another publication, Khalilpour et al. [122] present a decision support tool using mixed integer linear programing to maximize the NPV for stand-alone and grid-connected system configurations. The results are presented as an operational schedule for a hospital. Another relevant publication, which covers the sizing of grid-connected PV battery systems is from Magnor et al. [123]. This study shows another interesting economic optimization of a household with an energy demand of 4,500 kWh and a load type according to [124]. The optimization results are again based on the maximum NPV, which interestingly show different results compared to Khalilpour et al. [121], where the NPV was always at the maximum at no battery usage at all. Magnor et al. find that the optimal system configuration is a PV generation of 10 kW_{peak} and a storage capacity of 4,640 Wh. The reason for the different result is the optimistic assumption of battery capacity costs of 550 €/kWh compared to 1,000 €/kWh from Khalilpour et al. The authors also mention, that the assumed prices differ significantly from the current retail prices, which explains the deviating results. Moshövel et al. [125] compare different publicly available tools and online calculators from websites of various battery companies and presents her own tool to size battery systems at a given PV power regarding the NPV and self-consumption. The ideal

PV/Battery configuration however cannot be determined, because the PV size is an input value. The battery size is determined by a variation between 1-10 kWh in 1 kWh steps and a limited charge/discharge rate of 0.5 - 1.0 C. The final size has to be chosen by the user of the tool, because the economic results are not aligned with the results of the DSS curves, as the authors state. For given reference values of the year 2015, the author draws the conclusion that the NPV is at its maximum with no battery at all and that households reach positive NPV values for battery system prices below 500 €/kWh. When changing the reference values to 2030 assumptions (reduced battery system prices, higher electricity prices and lower feed-in tariffs), Moshövel et al. specify the most economic battery capacity for an average 4-person household (4,500 kWh annual electricity consumption, 8 kW_{peak} PV installation) as 7.6 kWh. Another interesting optimization methodology for sizing smart home systems – a term the author uses to refer to PV storage systems (partly including electric vehicles) – is convex programming (CP), published by Wu et al. The stated sizing approach is based on finding an economic optimum under consideration of the maximum battery power as an optimization variable. The outcome is an ideal battery power ranging from 2.26-4.26 kW, independent of the battery price.

As mentioned in the introduction of this section, the analysis of Single-Nodal energy systems is limited to decentral applications, where energy transport between generation, load and storage does not play a significant role. To enable energy system models with larger geographical scopes, where energy transport plays a major role, Multi-Nodal energy system models are necessary. The current state of research in Multi-Nodal energy system modelling is presented in the following section.

2.6 Multi-Nodal energy systems

There are basically two options for Single-Nodal energy system models. The first option is described in the previous section and describes applications, where energy generation, demand and storage are situated in the same location. The second type of Single-nodal energy models are top-down models with a copper-plate approach. This means, energy transport is not subject to any limitations or losses. A more detailed description of this approach can be found in section 2.3. A soon as the energy transport is included in the model, the energy system can no longer be considered a Single-Nodal model, independently of the used transportation model. Therefore, it can be concluded that all energy systems considering energy transport between various locations can be considered Multi-Nodal energy systems. This is not a new topic, the actual novelty is the coupling of different Multi-Nodal systems with different energy carriers, which is described in the next section.

2.6.1 Multi Energy Systems

The following section gives a brief overview of existing MES modelling approaches and their characteristics in order to classify the presented *HyFlow* (see section 3.5) approach into various categories and point out its advantages and disadvantages compared to other modelling frameworks. In order to compare *HyFlow* with other MES modelling approaches, the main categories used to distinguish between types of MES modelling approaches are discussed.

Mancarella et al. [88] identify four main distinguishing features used to characterize MES modelling approaches: multi-fuel, multi-service, spatial resolution and network connections. Additionally, they argue that time resolution of MES should be considered as an additional distinguishing factor. These five factors seem suitable to classify the *HyFlow* modelling framework compared to other MES modelling approaches and will be further discussed in the section 3.5. As the main focus of the presented system is on the spatial – and the time resolution and especially on the network connections, these features are discussed in more detail than the multi-fuel and multi-service perspective, which the *HyFlow* framework considers as well.

Multi-fuel means that the same final energy demand (e.g. domestic heat) can be supplied by different energy sources like district heating, a heat pump or a gas boiler. Multi-fuel approaches can be divided in full – and hybrid approaches. While full approaches consider all available energy carriers, the hybrid approaches consider only the relevant energy carriers for the task. As the *HyFlow* modelling framework focuses on grid-bound energy supply, only three energy carriers are implemented (electricity, natural gas and district heat). Full approaches consider additional energy carriers like coal, uranium, kerosene or hydrogen as well.

The second mentioned differentiation characteristic is multi-service. A multi-service MES modelling approach can include energy supply appliances that supply more than one energy service from one energy carrier (e.g. CHP plants that produce heat and power from natural gas) at the same time. The combination of a multi-fuel and multi-service modelling approach allows a wide range of technical - and economical comparisons to be addressed. For example, between different energy sources and demands like primary energy efficiency, specific CO_2 emissions or operational costs.

The time horizon and the temporal resolution are important factors to consider when designing a MES modelling tool. Planning tools or economic assessments tend to have longer time horizons (30-50 years) than technical models, which analyze operational conditions (day-year) [126,127]. Many models use time-aggregated data and time-steps ranging from µs for

certain research questions in electrical grids to months in the case of seasonal influences of integrating RES [128] to years in strategic planning tools. All models that use time-steps and a static approach assume that fast phenomena have reached equilibrium at the end of the time-step used. It should be noted, that the selection of an appropriate time interval is critical as different time-steps can lead to deviations in the results [129–131]. MES modelling approaches that focus on the integration of RES, [132] recommend 15-minute time-steps.

The spatial coverage and resolution describes the geographical scope and the defined system boundaries of the MES modelling approach. There is a variety of spatial resolutions used in MES modelling approaches: These range from high resolution single buildings, which may be used to model residential demand [133] or in the design stage of buildings [134], to large regions or countries [135,136]. Most publications of MES modelling approaches, however, use a spatial resolution that falls between these two extremes, such as suburbs, districts, cities or smaller regions. This may be seen in [127,137,138]. The spatial coverage also has a significant effect on other characteristics of MES modelling approaches. Specially the level of detail, the time horizon and the possible network calculations is usually decreased for larger spatial coverage and resolution due to the higher computational time needed [126,139]. Models covering more than a few buildings usually use a simplified and highly aggregated modelling approach [126]. The presented *HyFlow* modelling framework is combined with a cellular approach (presented in section 3.2) to be as versatile and generic in terms of spatial coverage and resolution as possible, allowing a high degree of accuracy in terms of the original situation. It can be used for multiple buildings to large regions.

To transport energy from the location of supply to the location of demand, an energy transportation network is needed. Grid-bound MES may also be characterized by their network structure. Since *HyFlow*, as a modelling framework, focuses on network infrastructure, this point of characterization is of particular interest in this paper. The network interconnections may also be distinguished by their level of detail. The interconnections range from highly detailed load flow calculations based on real physical conditions, to no restrictions or losses for the transport of energy at all. Geidl et al. [140] suggest a differentiation between power flow models and network models. The latter can be further divided into type 1 and type 2 network models, which are both highly simplified. Type 1 models (also referred as copper plate approach or single node model) feature flows that transport energy without experiencing losses, while type 2 models (transshipment model) consider energy losses as a function of the corresponding flow [54]. In MES modelling approaches that use the type 2 network calculations, no differentiation between energy carriers is necessary. On the contrary, power flow models are based on physical principles like conservation laws and are

the most accurate. Since the applied physical laws such as the relation between electric voltage and current, or hydraulic pressure and mass flow differ among the modelled energy carriers, no general model is applicable to all grid types [140]. There are calculation tools for each grid type, which are dedicated to static load flow calculations based on physical principles. Examples for the electricity sector are DIgSILENT PowerFactory [56], PSS Sincal [58] or Neplan [57], while the last two can also be used for calculations concerning the gas - and district heating grids. It is important to remark that none of these tools are able to interconnect the mentioned energy carriers. Further distinctions between different types of power flow calculations for the electricity –, the gas – and district heating networks are discussed in section 2.3 – Energy transport models. A visualization of a grid-bound MES is shown in Figure 2-22.

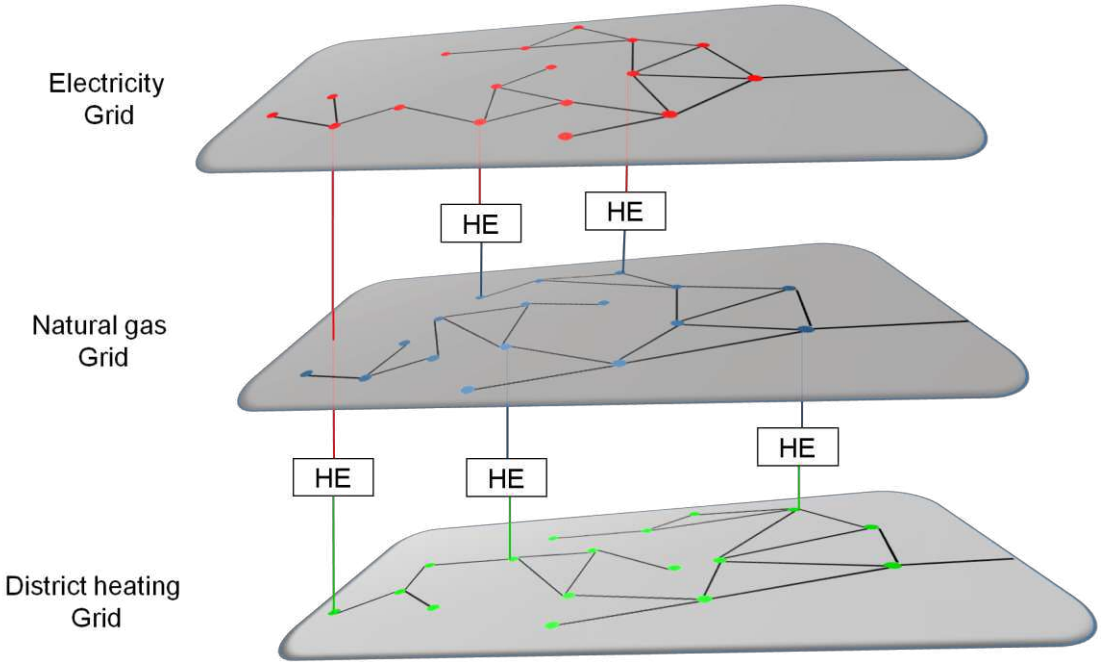

Figure 2-22: Own visualization of a grid-bound MES with hybrid elements (HE) to couple the energy carriers

The most common possibility to implement sector coupling elements in grid-bound MES is the Energy Hub concept by Geidl et al. [140,141] This approach is a generic way to couple different energy carriers based on technological conversion efficiencies. These interfaces between energy carriers are labelled energy hubs and are referred to as “Hybrid Elements” (HE) in the modelling section of this work. A conversion unit is described by a power input p^{in}, a power output p^{out} and the energy efficiency between the input energy carrier and output energy carrier η. The input and output values and the corresponding efficiencies are not limited to single values. An energy hub can consist of a single conversion unit or multiple conversion paths, which is realized in a matrix concept, as shown in Equation 2-50. All energy carriers are labelled with the corresponding greek letter as a subscript.

$$\begin{pmatrix} p_{\alpha}^{out} \\ p_{\beta}^{out} \\ \vdots \\ p_{\omega}^{out} \end{pmatrix} = \begin{pmatrix} \eta_{\alpha,\alpha} & \eta_{\beta,\alpha} & \cdots & \eta_{\omega,\alpha} \\ \eta_{\alpha,\beta} & \eta_{\beta,\beta} & \cdots & \eta_{\omega,\beta} \\ \vdots & \vdots & \ddots & \vdots \\ \eta_{\alpha,\omega} & \eta_{\beta,\omega} & \cdots & \eta_{\omega,\omega} \end{pmatrix} \cdot \begin{pmatrix} p_{\alpha}^{in} \\ p_{\beta}^{in} \\ \vdots \\ p_{\omega}^{in} \end{pmatrix} \quad (2\text{-}50)$$

This presented approach has a variety of different applications for integrated energy approaches. One of the most widespread application areas is optimal dispatch of energy carriers [142] and the optimal power flow concept [141], which is briefly introduced in the next paragraph. Additional purposes of the energy hub concept are exergy optimizations [143], or robust, reliable and resilient energy systems [144].

The optimal power flow model (OPF) is a common optimization tool, especially for energy dispatch models. It was first introduced by Geidl et al. [141] with the usage of the energy hub concept. Basically, it assigns each input energy carrier a specific cost and calculates the optimal energy generation dispatch in the form of the minimal cost. With the help of the implemented energy hubs, the specified demand can be met by more than one energy generation device or energy carrier input. The assigned cost for different energy inputs and the corresponding conversion efficiencies between the individual energy carriers influence the optimal result. This OPF methodology can also be coupled with various LFC approaches. Additionally, the assigned costs do not necessarily have to be monetary costs. Instead of €/kWh, other KPIs can be used for the implemented objective function as well. Examples can be primary efficiency, CO_2 emissions, exergy or reliability-related indicators.

3 MODELING OF THE ENERGY SYSTEMS

This chapter contains all essential information regarding the models created within this work. The first section defines the two introduced model types, which are necessary in order to answer the research questions, as described in section 1.2. Additionally, the necessity for both modelling approaches, the general structure, as well as the inputs and outputs are described in the first section of this chapter. The second part of this chapter describes the developed cellular approach, which allows combining the introduced models and therefore enables a wider range of applications. In order to quantify results of the models, a set of significant KPIs needs to be defined, which is done in the third section of this chapter. The last two sections describe the two introduced models.

3.1 Model definitions

In this thesis, two general model types are introduced: the “Single-Nodal model” and the “Multi-Nodal model”. A Single-Nodal model can contain elements like a generic load profile $P_{Load}(t)$, a fluctuating renewable energy source $P_{Gen,F}(t)$, an ESS and the corresponding integration with the energy grid. The entire surrounding of the Single-Nodal model is a black box and no load flows or implications from other nodes are considered in this approach. Due to the neglect of load flows or transportation losses, Single-Nodal models are ideally limited to a spatially small area, in order to prevent calculation errors by this assumption. This implies that all implemented elements of the single node, like a renewable generation technology, the load of the energy consumer and a possible ESS are ideally located in the same spot. However, this generic approach allows for technology-independent optimization regarding the sizing of the renewable energy generation capacity and the ESS.

The thematic focus and the corresponding research questions of the presented Multi-Nodal model differ significantly. It combines multiple nodes with network interconnections aiming to represent the existing grid infrastructure of all grid-bound energy carriers. Each node has an assigned residual load (as defined in Equation 3-1 in section 3.3) for every energy carrier. Additionally, ESS and HE can be parameterized individually and allocated in these nodes of the grid. The load flow calculations, which are based on physical principles, are performed for all energy carriers, considering the residual loads of the nodes and the specified grid parameters.

The main goal of this is to determine possible congestions of the grids. These calculations are based on scenarios. Due to the possibility to implement HE and ESS for each energy carrier into the modeled energy system, the effects of this implementation on the grid and the according operation profiles can be determined. A complete description of the complex model is presented in section 3.5.

In order to perform a comprehensive energy system analysis, it is necessary to combine both approaches. Since energy systems generally consist of multiple nodes and energy grids that connect them, a Multi-Nodal model is necessary to describe the interaction between these nodes and the corresponding load flows. However, it is necessary to take a deep dive into individual single nodes for the following reason. The requirement for the level of detail in order to design the optimal size of renewable generation capacity $P_{Gen,F,peak}$ in kW_{peak} and energy storage system SOE_{max} in kWh can not be realized within the framework of the complex Multi-Nodal model. This task implies a need for a separate, and more detailed model of a single, individual node. Figure 3-1 illustrates the Multi-Nodal system on the left, with a selected, specific node, which is furthermore illustrated within Single-Nodal model. More specifications and the generic description of Multi-Nodal models and Single-Nodal models are to be found in the following paragraphs.

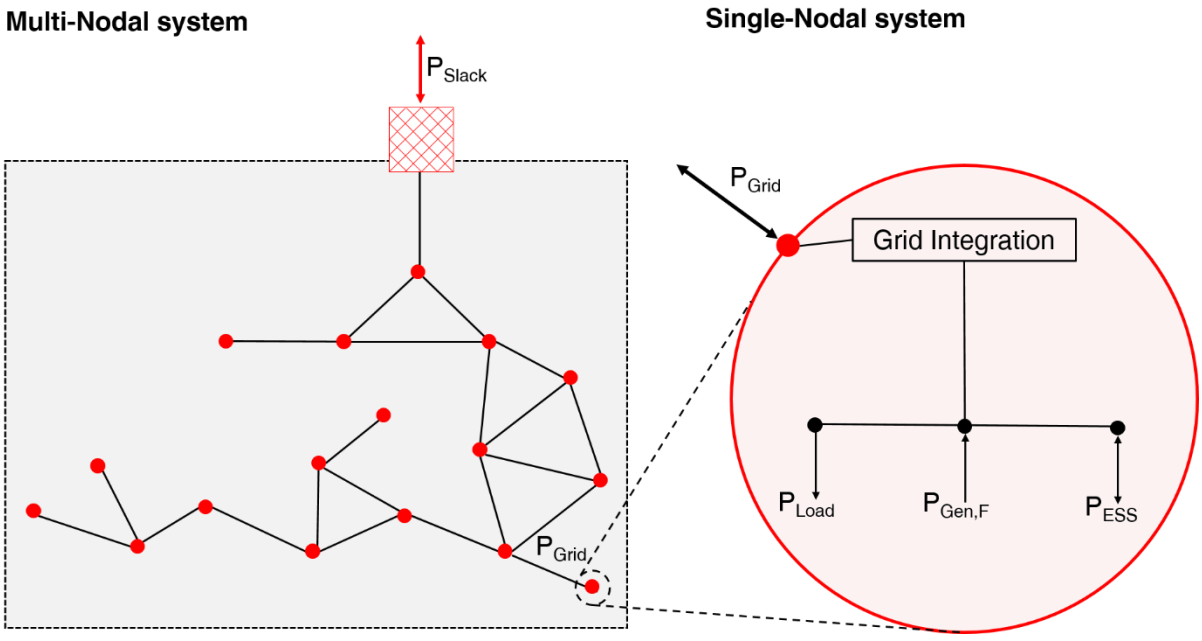

Figure 3-1: Exemplary illustration of a Multi-Nodal model, with a selected node to demonstrate the more detailed Single-Nodal model (right)

The key message of Figure 3-1 is that both models are needed in order to answer the research questions. While the Multi-Nodal model is capable of providing information regarding the load flows and the corresponding grid infrastructure requirements, the Single-Nodal model is necessary to appropriately design ideal renewable generation capacities and energy storage systems. This sizing information allows to maximize the DSS of single nodes. The results of optimized renewable generation capacities and ESS from the Single-Nodal system can subsequently be transferred to the Multi-Nodal system. A combination of both models therefore leads to a more comprehensive overall picture, which can furthermore contribute to relieving the grid.

In contrast to the later-described Multi-Nodal models, Single-Nodal models are ideally limited to a spatially small area, because load flows or transportation losses are not taken into account within the single node. This implies that the renewable generation technology within the scope of a single node is a technology, which is typically used in a decentralized form. A significant share of self-consumption on the spot is possible, without large energy transmission within the single node.

The most widely used technology for providing decentralized, fluctuating energy and relevant local self-consumption is solar power. Other alternatives in the electricity sector, such as wind power are usually already full injectors on the medium or high voltage grid, without a direct usage on the spot. Naturally, it is possible to use a low spatial resolution and consider a city and a close-by wind farm to be in the same node. However, in the context of the described research questions, it is recommended to solve such tasks within the scope of a Multi-Nodal system with two separated nodes (see Figure 3-1 in section 3.5). This has the advantage of taking the grid infrastructure and the corresponding load flows and possible transport losses into account. Other renewable forms of energy like biogas, geothermal energy or hydropower are usually also more centralized units and cannot be considered as fully fluctuating sources.

While the Multi-Nodal model uses technology independent black box models, the Single-Nodal model varies dependent on the selected generation technology and ESS technology. This level of detail and the dependence on technologies implies that Single-Nodal models have to be adapted to the task and the corresponding technologies. Due to the stated arguments and the scope of the research questions, it has been decided to present the Single-Nodal model using the example of a residential PV battery system, as seen in section 3.4. The reason for this choice is the easily definable level of aggregation.

All relevant parts of the Single-Nodal model: the fluctuating renewable generation (Photovoltaic system), the ESS unit (Battery system) and the electricity demand (household load profile) are located behind the meter and are considered as one node. Other fluctuating renewable generation units are not neglected within this work, but solely considered in the scope of the Multi-Nodal model by using historic data.

The sector coupling options, as described in section 2.4.2 are also limited, because many technologies are only feasible in more centralized environments. For example, it is not common to have large P2G technologies such as electrolyzer units or gas turbines in small decentralized units, as intended for single nodes. The most common sector coupling technologies in the scale of decentralized units are P2H technologies such as electric direct heating devices or heat pumps or in a wider context of sector coupling also P2Mobility becomes more common in the form of electric vehicles. Implementations of P2H devices usually result in a complete substitution of fossil fuel-based heating (e.g. natural gas, oil) with electricity. Also, P2Mobility application results in increased domestic electricity demand and a changed electric load profile. This means that the most widespread form of sector coupling in households represents an electrification and a changed electricity load profile. Other sector coupling options such as µCHP plants or micro fuel cells are hardly used in Austria, Europe and also worldwide (with the exception of Japan). [145,146] In addition, most of these technologies are connected to the natural gas grid and are therefore neither renewable nor do they operate on fluctuating energy sources. [147] As a result, the consideration of HE at single nodes is considered solely in the form of changed electricity demand and – profile. The consideration of all other sector coupling technologies is implemented in the Multi-Nodal model, where other technologies such as P2G are implemented as a flexibility option.

Additionally, to the detailed descriptions in the following sections, Table 3-1 shows an overview of the main characteristics of the “Single-Nodal Model” and the “Multi-Nodal model”. Table 3-1 characterizes the model and optimization type and presents the necessary input data, as well as the results.

Table 3-1 Overview of the main characteristics of the "Single-Nodal model" and the "Multi-Nodal model"

	Single-Nodal model	Multi-Nodal model
Input data	**Generation model** – Weather data – Generation type – Physical model of chosen generation type – Results in $P_{Gen,F}(t)$ **Load Profile model** – Results in $P_{Load}(t)$ **ESS model** – ESS specifications – Bus bar model – Selection of a control strategy **Grid Integration model**	**Nodal specifications** – Residual load $P_{Res}(t)$ – Number of nodes – ESS allocation – ESS parameterization (e.g. P_{max}, $Cap_{ESS,max}$, η) – HE allocation – HE parameterization (e.g. P_{in}, P_{out} η) **Network specifications** – Structure of the grid for each energy carrier – Grid parameterization (e.g. V, p, T, losses)
Output data (Results)	**Primary output** – DSS – Minimized size of the renewable generation $P_{Gen,F,Peak}$ – Minimized ESS capacity Cap_{ESS} **Secondary output** – DSG – SCR – Cy_{ESS}	**Primary output** – Load Flows + Congestions – Operation profiles of ESS and corresponding SOE – Operation profiles HE – ESS capacity Cap_{ESS} **Secondary output** – DSG – SCR
Model type	Optimization model	Operational model
Mathematical Optimization	Yes – Adapted methodology of Lagrange multipliers	No - Scenario based model

3.2 Cellular approach

To model the behavior of more than one participant in an energy system, it is indispensable to extend the described Single-Nodal model to a Multi-Nodal model. If an attempt is made to develop MES scenarios for municipalities, districts or larger regions, it is necessary to aggregate numerous single-user datasets of all energy carriers to individual nodes. This is necessary, because it is not possible to simulate the residual load of every single household of a larger region, due to the enormous amount of data and the availability of the latter. The therefore used, self-developed cellular-approach works with detailed aggregation guidelines, as described in [148,149].

Additionally, it is necessary to model load profiles for all considered energy carriers (electricity, district heating and natural gas) and consumer types. In order to calculate the appropriate residual load according to Equation 3-1, the generation profiles have to be determined as well. Examples of these procedures are described in section 4.3.

The developed cellular-approach allows a scenario analysis with a similar accuracy, as if data of single nodes is used. It is a flexible method, which allows the user to achieve a compromise between an accurate allocation and fast computation times. Energy systems with sizes between a single household and whole countries can be depicted with the same tools by applying the cellular approach. In the case of a household, all available energy consuming devices are depicted as individual nodes and form a Multi-Nodal system within the household. In contrast, a single node of an energy system of a whole country might represent a district with a few thousand energy consumers and producers. To apply the presented cellular approach on large energy systems, it is required to follow a specific guideline, in order to achieve the most representative results possible.

In step 1, one has to identify and classify energy consumers, producers and energy storage units for each energy carrier in the target area. To ensure a correct localization of the objects, it is necessary to perform the classification based on a geographical information system (GIS). Step 2 is probably the most critical step. In this step, the appropriate cells have to be defined. It is required to follow a guideline at the stage of the spatial division into cells. The cell size depends on the task at hand and the data availability within the cells. At high levels of data availability within a cell, smaller cell sizes lead to higher accuracy of the results regarding the spatial resolution at the cost of additional computation time. When working with standardized load profiles (SLP) based on top-down stochastic approaches, it is crucial to have a certain minimum amount of SLP within a cell. For example, the energy consumption and the related load profile of a residential cell is to be determined, with no measured data in the cell. When

using the SLP for this task, it is recommended to have a minimum of 150 households in the cell, before one can expect a satisfactory reflection of the real load profile. Figure 3-2 shows, the average power consumption of a household with different levels of aggregation. One can see that the power peaks decline with a rising number of households pooled together. While the maximum power peaks per household almost reach 2000 W at an aggregation level of 5 households, the maximum power at 150 households is around 700 W. When one compares the published values of Figure 3-2 with the SLP for a household published by econtrol [31], it becomes apparent that with a higher aggregation level, one approaches the SLP of a household (H0 profile).

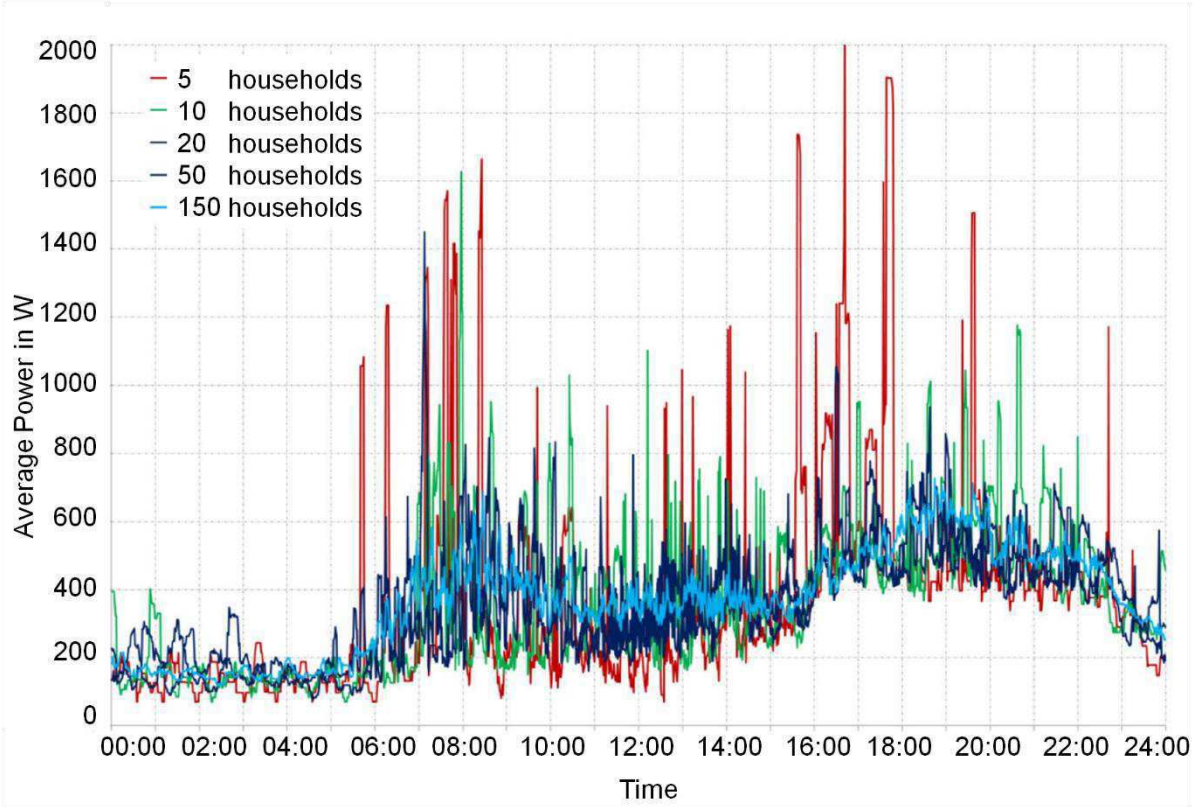

Figure 3-2: Average power per household for an exemplary day as a function of the aggregation level [150]

Esslinger et al. illustrates (Figure 3-2) this relationship very well. It can therefore be stated, that for cells with low levels of data availability, an increased cell size leads to a smaller computation time but also to more accurate results with the disadvantage of a lower spatial resolution. Additionally, when working with SLP it is advantageous to cooperate with municipal authorities to further distinguish the identified object structure into building types, such as single- and apartment houses, commerce- and industry complexes and public buildings. Considerations regarding the grid topology of all energy carriers, the geographic structure and the appropriate cell size finally lead to the cell definition as illustrated in Figure 3-3.

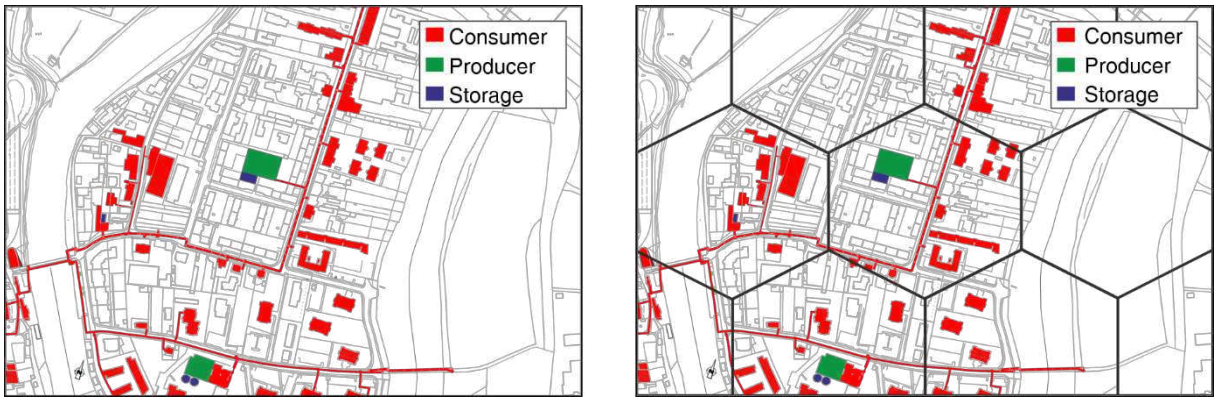

Figure 3-3: Step 1 (left) represents the identification and classification of energy-related infrastructure – Step 2 (right) illustrates a generic definition of the cell structure

As soon as the cells are defined, the actual aggregation process starts, which is step 3. All modeled energy consumers, - producers and storage structures are aggregated into a single node, as illustrated in the left part of Figure 3-4. If an object combines a generation and a load profile within itself, both are considered separately until this point. Once the time-resolved generation and load profiles are completed, both are combined into a residual load. The end result of step 3 is a node, which contains a single node covering all relevant information of the surrounding cell. Step 4 implements the energy-related network infrastructure between the established nodes. If there is a real power line, natural gas pipeline or district heating network connection between two cells, this grid infrastructure needs to be considered in the cellular approach as well. This also shows the importance of a well thought out cell structure. A homogeneous supply within the same cell is highly recommended. This means that areas with the supply of a certain energy carrier (e.g. access to natural gas) shall not be placed in the same cell without access to the same energy carrier. This helps to receive results that are representative for the whole cell.

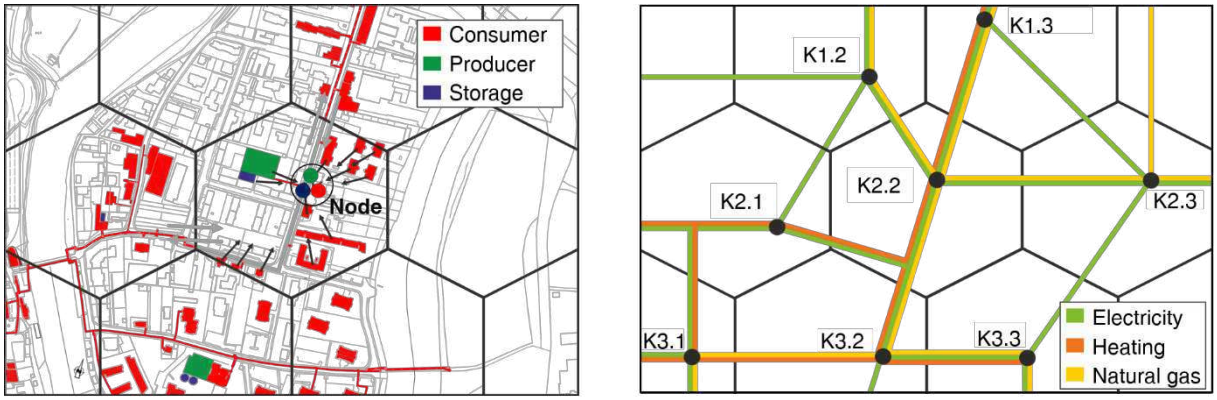

Figure 3-4: Step 3 (left) – Illustration of the aggregation of all identified energy related structures in a central node within the cell. Step 4 (right) illustrates the grid infrastructure between the aggregated nodes

The cellular approach is the interface between the real world energy system and its model. It allows the user to aggregate the analyzed target area into nodes that are capable of representing the real world energy system in a digital version for a wide range spatial expansion (e.g. single household, small settlements, cities or large regions). The cell level hierarchy allows defining any number of low-level cells to be aggregated into higher-level cells, which makes it a very flexible tool.

The correct use of the cellular approach allows to balance the energy consumption and generation at the smallest cell level.

This balancing process starts at the lowest cell level in order to consume the locally generated energy on-site, as long as possible. This measure should help to avoid the transport of energy over a long distance or to superior cell levels, which could lead to congestions of the infrastructure. A superior cell level would typically be a higher voltage level for electricity grids or a higher pressure level for pipeline-based grids such as natural gas – and district heating grids. The cellular approach is therefore a bottom-up approach.

In order to get a better understanding of the cellular approach, Figure 4-18 in section 4.3.2 illustrates a possible example of a real project study of the municipality Leoben (Styria, Austria). The medium-sized town with around 30,000 inhabitants is divided into 44 cells. All cell numbers with access to at least one grid-bound energy carrier are marked in Figure 4-18.

3.3 Definition of Key Performance Indicators

In order to characterize and evaluate energy scenarios, a structure of assessment criteria has to be established. Therefore, selected Key Performance Indicators (KPIs) are introduced and presented in this section. The selected KPIs enable the user to compare various scenarios of Single-Nodal and Multi-Nodal energy systems of all available energy carriers. This section defines the selected KPIs and gives visual examples for easier comprehensibility.

Figure 3-5 shows a load function P_{Load} (blue) and a generation function $P_{Gen,F}$ (red). In this example, the visualized load represents a household electricity demand curve for one day. The generation curve shows an exemplary PV generation curve of a generic system (1 p.u.), on a sunny summer day. One can see, that the generation function exceeds the demand function by day and the load function tops the demand function by night.

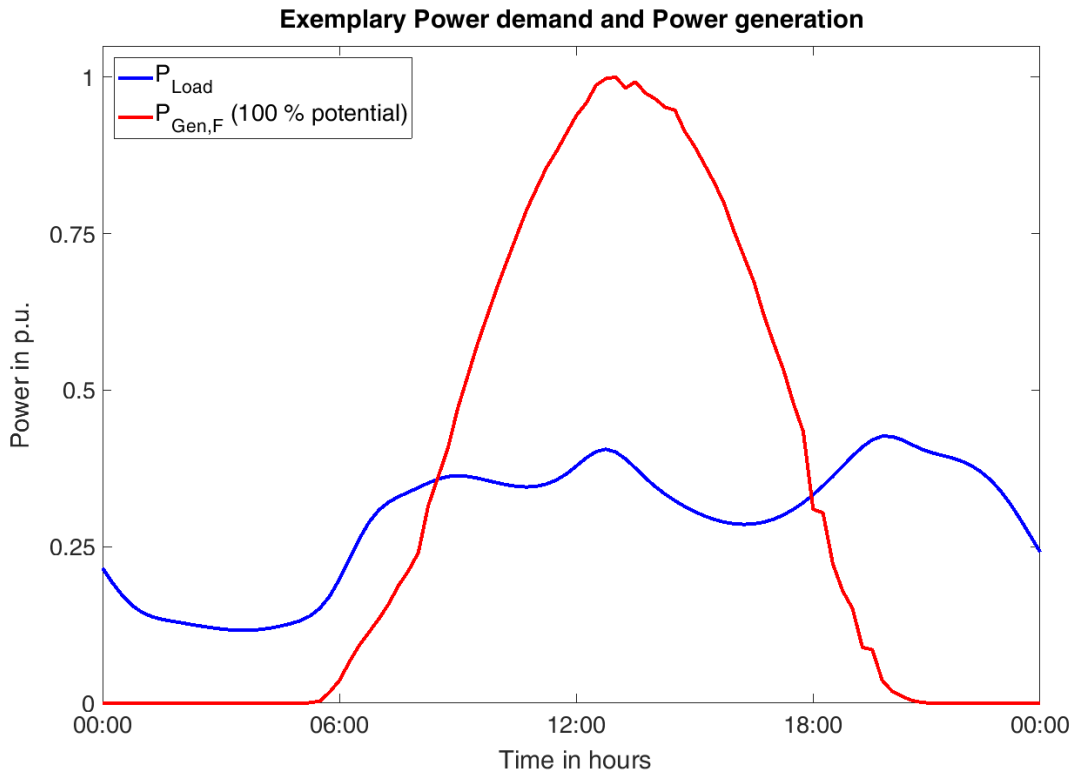

Figure 3-5: Exemplary generation function (red) and demand function (blue)

In order to describe both functions in one single curve, the residual load function P_{Res} is introduced. It is defined by Equation 3-1 and shows the demand function P_{Load} minus the function of fluctuating energy generation $P_{Gen,F}$ in the same node. Positive residual loads represent a predominant demand, while negative values show a surplus of energy generation on the assigned node. In order to show the development of the residual load as function of the PV expansion for the exemplary day illustrated in Figure 3-5, the power of the generation function has been linearly scaled in Figure 3-6. At 0 % expansion of the generation function – no generation takes place and the residual load is congruent to the demand function P_{Load} of Figure 3-5 and shows constantly positive values (blue). The residual load of 100 % (green) represents the expansion of the full PV potential shown in Figure 3-5. The red function illustrates a resulting residual load when only half the PV potential is used. One can see, that in the night hours all residual loads are equal to the original demand function P_{Load}, but they significantly differ during the daylight hours.

$$P_{Res}(t) = P_{Load}(t) - P_{Gen,F}(t) \tag{3-1}$$

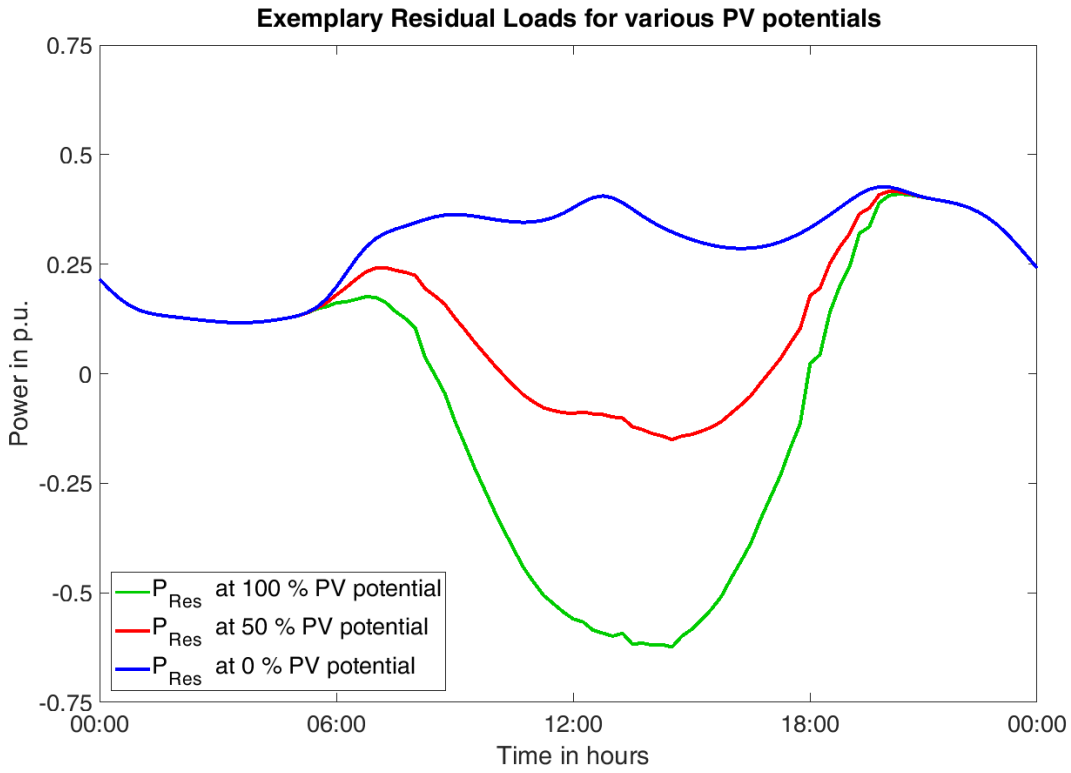

Figure 3-6: Residual loads for three different PV potential utilizations

The residual load P_{Res} is important because it can be used to identify the maximum power demand and the maximum power surplus for the assigned node. These maxima are the decisive factor for dimensioning the energy grid infrastructure. Additionally, the condensed information of residual loads can be used to determine other relevant KPIs, such as the imported/exported energy E_{Im} and E_{Ex} the self-consumption ratio (SCR), the degree of self-generation (DSG) and the degree of self-sufficiency (DSS). The stated KPIs are explained, their definition is mathematically defined in the Equations 3-2, 3-3 and 3-4 and they are additionally illustrated in Figure 3-7.

The DSG demonstrates the ratio between energy demand and energy generation within a defined time period of an exemplary day. It obtains values smaller than 1 if the total energy demand within the system boundary is larger than the energy demand. If the total energy generation exceeds the energy demand the DSG obtains values larger than 1. Equation 3-2 defines the DSG, while Figure 3-7 illustrates the calculation based on the data of Figure 3-5. It has to be stated that the required amounts of energy can either be calculated by integrating a continuous function or by summing up the mean power values $\bar{P}$ of a specific time interval Δt, as presented in Equation 3-2. Both options are equivalent. For the sake of simplicity, this section illustrates all following equations in the form of continuous functions only.

$$DSG = \frac{E_{Gen,F}}{E_{Load}} = \frac{\int_{t_{start}}^{t_{end}} (P_{Gen,F}(t))\, dt}{\int_{t_{start}}^{t_{end}} (P_{Load}(t))\, dt} = \frac{\sum_{t_{start}}^{t_{end}} (\bar{P}_{Gen,F}[t]) \cdot \Delta t}{\sum_{t_{start}}^{t_{end}} (\bar{P}_{Load}[t]) \cdot \Delta t} \quad (3\text{-}2)$$

The DSS puts the self-consumed part of the generated energy per considered time-step into perspective with the total energy demand. This shows how much of the demanded load can be covered by the locally generated energy from fluctuating energy sources. The value of the DSS can only be in the range of 0 - 1. Additionally, it can never exceed the value of the DSG. If both values are equal, it means that all the generated energy is self-consumed. Equation 3-3 and Figure 3-7 illustrate the calculation of the DSS.

$$DSS = \frac{E_{SC}}{E_{Load}} = \frac{\int_{t_{start}}^{t_{end}} (\min\{P_{Load}(t), P_{Gen,F}(t)\})\, dt}{\int_{t_{start}}^{t_{end}} (P_{Load}(t))\, dt} \quad (3\text{-}3)$$

Another KPI of relevance within this work is the SCR. It describes the share of self-consumed energy parted by the total generated energy. Therefore, analogous to the previously described DSS it cannot exceed the numeric value of 1. Equation 3-4 defines the SCR and Figure 3-7 illustrates the corresponding related areas. Additionally, the SCR can also be defined as the ratio between the DSS and the DSG.

$$SCR = \frac{E_{SC}}{E_{Gen,F}} = \frac{\int_{t_{start}}^{t_{end}} (\min\{P_{Load}(t), P_{Gen,F}(t)\})\, dt}{\int_{t_{start}}^{t_{end}} (P_{Gen,F}(t))\, dt} = \frac{DSS}{DSG} \quad (3\text{-}4)$$

Figure 3-8 illustrates the informative value of the defined KPIs. It shows the value of the stated KPI dependent on the usage of the exemplary linearized PV potential of Figure 3-5. One can see that below 35 % usage of the PV potential the DSG and the DSS are equal, which means that all of the generated energy is self-consumed. This also leads to the constant SCR of 1 until that specified point. Afterwards, the growth in DSS is much lower compared to the linear growth of the DSG. The difference between the DSG and the DSS marks the potential contribution of flexibility options (e.g. energy storage, sector coupling, demand response) to the overall DSS of the analyzed energy system.

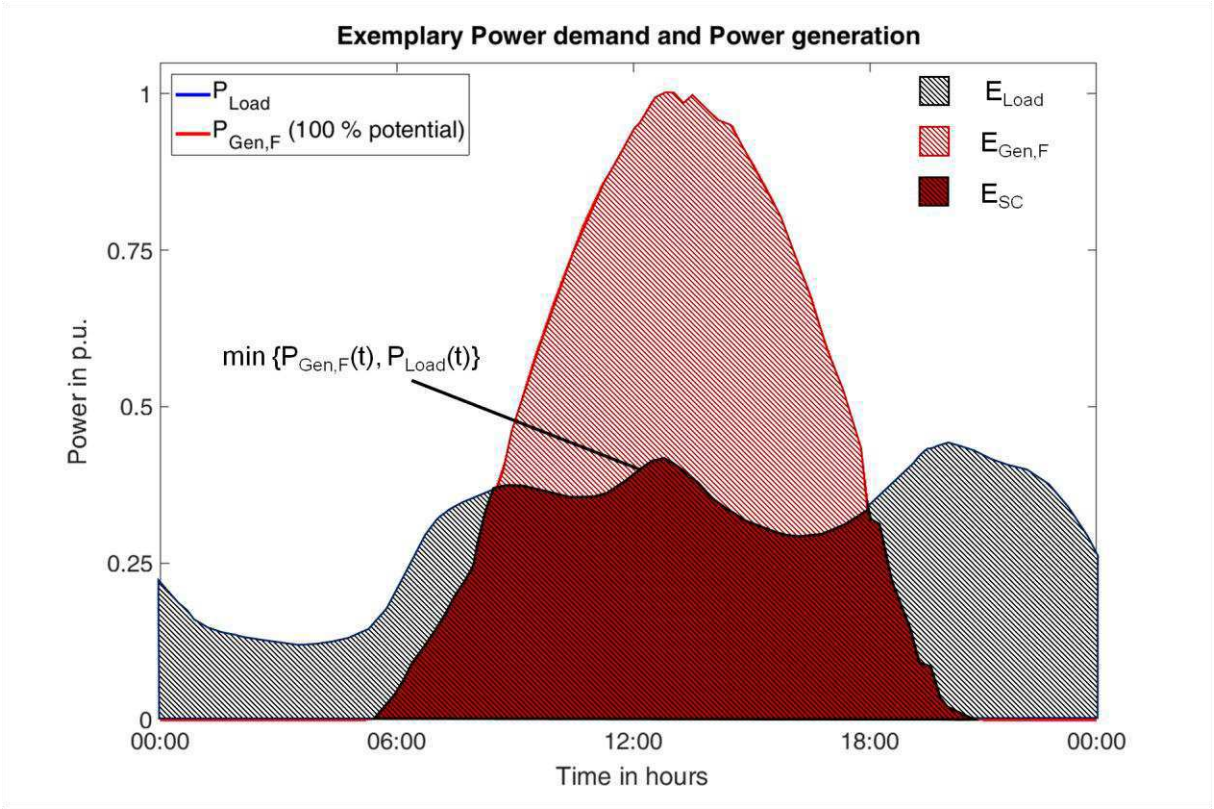

Figure 3-7: Visualization of the relevant areas for calculating the DSG, DSS and SCR

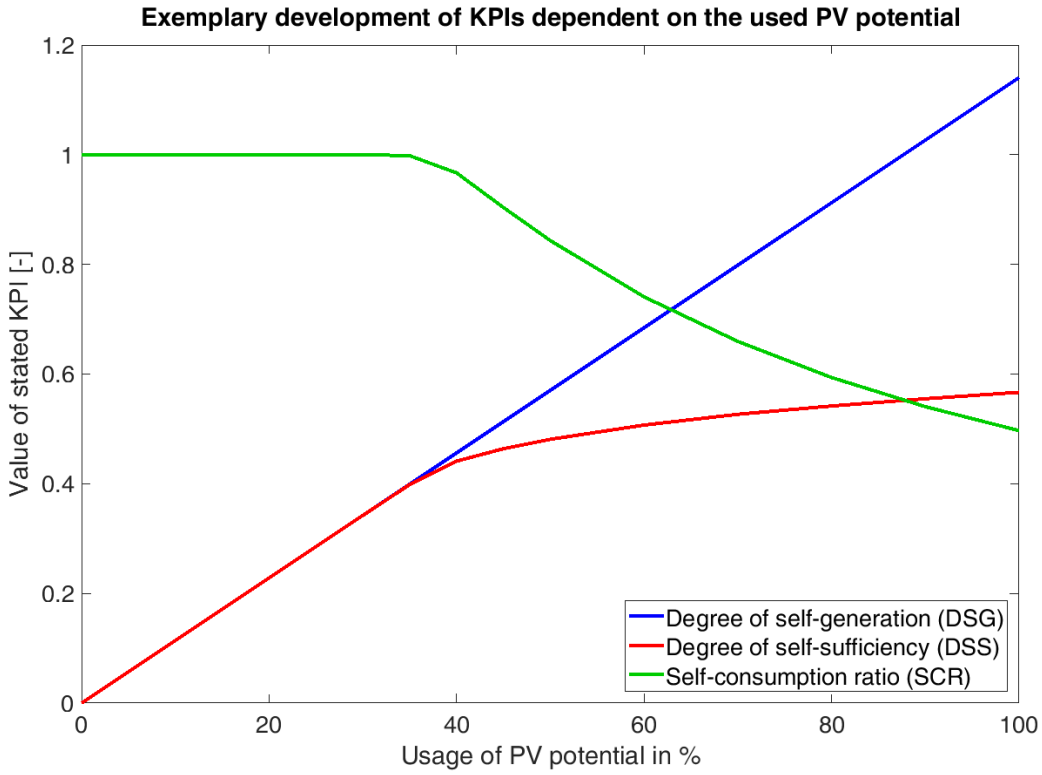

Figure 3-8: Exemplary development of selected KPIs with increasing utilization of the PV potential

As stated before, the implementation of flexibility options can significantly affect the characteristics of the analyzed energy system and the according KPIs. While the DSG is not affected by flexibility options, the DSS and SCR can be increased. Therefore, the Equations 3-3 and 3-4 need to be modified, if additionally used flexibility options allow a time-shift of the generated energy before it is used. This modification according to Equation 3-5 and 3-6 is valid for energy storage systems, but not for demand response or sector coupling implementation. Demand response is changing the demand function $P_{Load}(t)$ itself, which keeps the stated Equations 3-3 and 3-4 correct and sector coupling measures enable a load demand function at one energy carrier, while allowing additional generation at another energy carrier. This multi-energy carrier consideration is further explained at the end of this section. In the case of energy storage systems, the additional energy from the storage that can be used to supply the local demand function, has to be added to the denominator of the original Equation 3-3 of the DSS. Similarly, the SCR also needs to consider the additional self-consumed energy, which is discharged from the ESS. The modified equations are presented in 3-5 and 3-6. The additional parameter $P_{ESS,Dis}(t)$ represents the time-dependent discharge power of an energy storage element. It is presumed, that the energy storage only discharges power in times of positive residual loads $P_{Res}(t)$.

$$DSS = \frac{E_{SC}}{E_{Load}} = \frac{\int_{t_{start}}^{t_{end}} (\min\{P_{Load}(t), P_{Gen,F}(t)\} + P_{ESS,Dis}(t) \in \mathbb{R}^{+}) dt}{\int_{t_{start}}^{t_{end}} (P_{Load}(t))\, dt} \tag{3-5}$$

$$SCR = \frac{E_{SC}}{E_{Gen,F}} = \frac{\int_{t_{start}}^{t_{end}} (\min\{P_{Load}(t), P_{Gen,F}(t)\} + P_{ESS,Dis}(t) \in \mathbb{R}^{+}) dt}{\int_{t_{start}}^{t_{end}} (P_{Gen,F}(t))\, dt} \tag{3-6}$$

For the sake of simplicity, the explanatory example shows all definitions for one energy carrier only. It is, however, possible to use the presented KPIs for multi-energy carrier systems as well. For this purpose, it proves to be useful to determine all KPIs for every individually assessed energy carrier and an additional set of KPIs for the overall energy system. Equations 3-7 to 3-11 show the general determination of overall system KPIs. It has to be stated, that the KPIs cannot be derived from the single energy carrier KPIs, with the exception of the DSG. This implies that the DSS and the SCR values of single energy carriers do not allow any conclusions for multi-energy carrier systems.

$$P_{Load,tot}(t) = P_{Load,el}(t) + P_{Load,gas}(t) + P_{Load,heat}(t) \quad (3\text{-}7)$$

$$P_{Gen,F,tot}(t) = P_{Gen,F,el}(t) + P_{Gen,F,gas}(t) + P_{Gen,F,heat}(t) \quad (3\text{-}8)$$

$$DSG_{tot} = \frac{E_{Gen,F,tot}}{E_{Load,tot}} = \frac{\int_{t_{start}}^{t_{end}} (P_{Gen,F,tot}(t))\, dt}{\int_{t_{start}}^{t_{end}} (P_{Load,tot}(t))\, dt} \quad (3\text{-}9)$$

$$DSS_{tot} = \frac{E_{SC,tot}}{E_{Load,tot}} = \frac{\int_{t_{start}}^{t_{end}} (\min\{P_{Load,tot}(t), P_{Gen,F,tot}(t)\} + P_{ESS,Dis,tot}(t))dt}{\int_{t_{start}}^{t_{end}} (P_{Load,tot}(t))\, dt} \quad (3\text{-}10)$$

$$SCR_{tot} = \frac{E_{SC,tot}}{E_{Gen,F,tot}} = \frac{\int_{t_{start}}^{t_{end}} (\min\{P_{Load,tot}(t), P_{Gen,F,tot}(t)\} + P_{ESS,Dis,tot}(t))dt}{\int_{t_{start}}^{t_{end}} (P_{Gen,F,tot}(t))\, dt} \quad (3\text{-}11)$$

Another relevant parameter is the sum of imported and exported energy within a defined timeframe. The Equations 3-12 and 3-13 present the corresponding calculation.

$$E_{Im} = \int_{t_{start}}^{t_{end}} P_{Res}(t) \in \mathbb{R}^{+}\, dt \quad (3\text{-}12)$$

$$E_{Ex} = \int_{t_{start}}^{t_{end}} P_{Res}(t) \in \mathbb{R}^{-}\, dt \quad (3\text{-}13)$$

Highly relevant for the grid infrastructure are the power peaks of the imported/exported power flows $P_{Im,max}$ and $P_{Ex,max}$. The calculation methodology is presented in Equation 3-14 and 3-15. The calculations according to the Equations 3-12 to 3-15 have to be performed for all considered energy carriers separately as well.

$$P_{Im,max} = \max_{t=1 \quad t=n} (P_{Res}(t) \in \mathbb{R}^{+}) \tag{3-14}$$

$$P_{Ex,max} = \max_{t=1 \quad t=n} (P_{Res}(t) \in \mathbb{R}^{-}) \tag{3-15}$$

The listed KPIs in this section are the most used KPIs in this work, but the list is not comprehensive. KPIs for special applications, as well as selected economic KPIs within this work, are presented at the section of usage.

3.4 PV storage system model (Single-Nodal model)

The PV storage system model is responsible to represent an accurate system model of the renewable generation, the load, the energy storage system and the grid integration. However, this physical model is the model of all necessary hardware elements in the regarded node, as well as the interaction between these elements and the grid integration. In this context, it is also possible to use (open source) models of external sources and combine them to an overall model instead of the self-developed model. The main components of the "Single-Nodal model" are the model of the renewable generation (based on weather data, e.g. PV, wind, hydropower), the model of the load, the model of the energy storage system and the grid connection. Section 2.1 and 2.2 summarize possible sources for generation – and load models. However, it has to be stated that even if all individual component models are obtained by an external source, it is necessary to establish an overall system topology of the single node that models the interaction between the component models and the grid. In this case, a physical model of PV modules, the energy storage system and inverter model and the corresponding grid integration is described. The load data is obtained by an external source and afterwards integrated into the overall "Single-Nodal model". The following section describes the separate parts of the physical PV storage model, which together represent the Single-Nodal model. Figure 3-9 illustrates the parts of the physical PV storage model and the chronological order of description in the next sections. As the labels at the bottom of the illustration suggest, the model needs to apply a generation model (2), including the application of weather data (1), the system integration model (3), the load model (4) and an overall system logic (5). In this work, this is done for a PV-storage system for households.

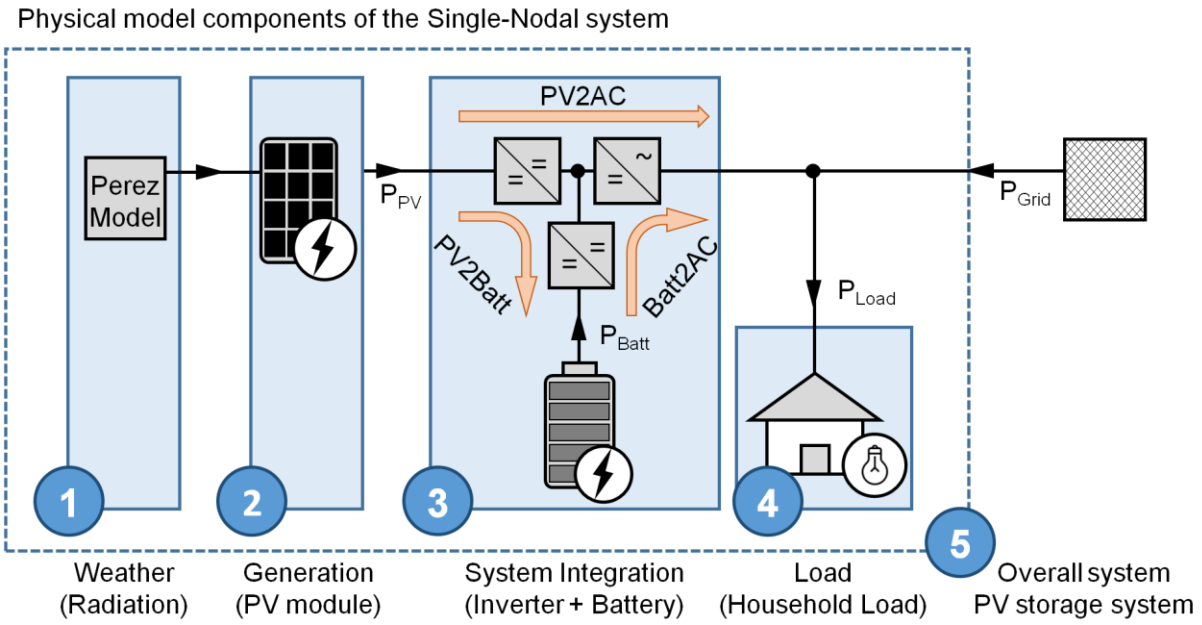

Figure 3-9: PV-storage system as used in the described Physical model of the "Single-Nodal model"

3.4.1 Perez model (Weather model)

The first sub-system of the PV storage model is the radiation model, which is designed according to Perez et al., as described in [151,152]. The measured global irradiance I on a horizontal plane is divided into the direct irradiance I_b and the diffuse irradiance $I_d(\rho_g)$ according to Skartveit/Olseth [153], with an assumed Albedo factor ρ_g of 0.2.

$$I(t) = I_b(t) + I_d(t) \tag{3-16}$$

The diffuse irradiation $I_d(t)$, however, has shares of isotropic diffuse-, circumsolar diffuse-, horizon diffuse- and ground reflection diffuse radiation. It can be calculated according to Equation 3-17 and as illustrated in Figure 3-10. All variables and the corresponding equations are described in detail after Equation 3-17.

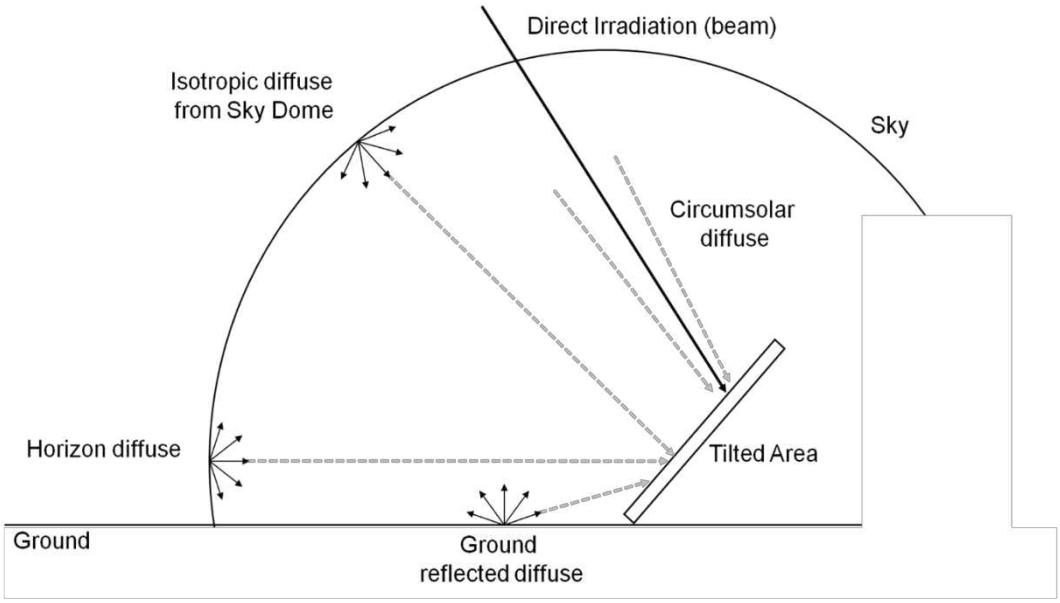

Figure 3-10: The different irradiation components (own illustration after [154])

$$I_T = I_b R_b + \underbrace{I_d(1-F_1)\left(\frac{1+cos\beta}{2}\right)}_{\text{Isotropic diffuse}} + \underbrace{I_d F_1 \frac{a}{b}}_{\text{Circumsolar diffuse}} + \underbrace{I_d F_2 sin\beta}_{\text{Horizon diffuse}} + \underbrace{I\rho_g\left(\frac{1-cos\beta}{2}\right)}_{\text{Ground reflected diffuse}} \quad (3\text{-}17)$$

I_T	Irradiation on a tilted surface
I_b	Direct irradiation
I_d	Diffuse Irradiation
R_b	Ratio a/b (I_T tilted surface/ I)
F_i	Brightness Coefficient (Empiric factors)
ρ_g	Diffuse reflection coefficient (Albedo Factor)
β	Inclination angle
a, b	Geometric Factors to describe the course of the sun

Since most of the stated parameters of Equation 3-17 have to be determined themselves, additional calculations for all individual variables are required. Before any irradiation model can be applied, the first step is to determine the time-dependent zenith angle on any given tilted and oriented surface. In order to do so, various physical conditions have to be considered. To characterize any location regarding its solar irradiation, four angles need to be defined.

1. Geographical latitude

The geographical latitude ϕ marks the angular distance between the equator and the specified location. All locations north of the equator have a positive latitude. This value is the only angle that is not time-dependent. The value of latitude amounts to 47.38 ° for the location of Leoben, where most scenarios are located.

2. Declination of the sun

The declination of the sun δ describes the distance of the sun from the equator at the zenith, at 12:00 LTST. It is responsible for the earth's seasons and occurs due to the inclination of the Earth's axis. Depending on the number of the day n in the year, it varies between -23.5 ° and +23.5 °. For practical reasons, the declination of the sun is considered constant for the same day. It can be calculated for each day with Equation 3-18.

$$\delta = 23.45 \cdot \sin 360 \cdot \left(\frac{284 \cdot n}{365}\right) \tag{3-18}$$

3. Hour angle

The hour angle ω describes the daily cycles of the sun's position. Due to the rotation of the globe, the angle of the sun changes 15 ° every hour. The hour angle is considered to be 0 ° at its zenith. The value of the hour angle is negative before noon and positive in the afternoon. Equation 3-19 shows the related formula to calculate the hour angle. The variable x represents the time in hours in the decimal form.

$$\omega = (\mathrm{x} - 12) \cdot 15 \tag{3-19}$$

4. Zenith angle

The zenith angle θ of the solar irradiation on a horizontal area describes the angular difference between the solar beam and the vertical perpendicular to the horizontal area. When the investigated area is not horizontal but tilted, two additional angles are required to describe the zenith angle. The inclination angle (tilt) β of the examined area and the azimuth angle a. The azimuth angle describes the orientation related to the south. A southern orientation is considered 0 °, an eastern orientation -90 °, a western orientation +90 ° and a northern orientation 180 °. Naturally, all intermediate orientations are possible as well. Figure 3-11 illustrates the described angles and shows the zenith angle on a horizontal area as well as a tilted area. The zenith angle shown in Equation 3-20 calculates the actual angle on any orientated and tilted surface, at any time of the year.

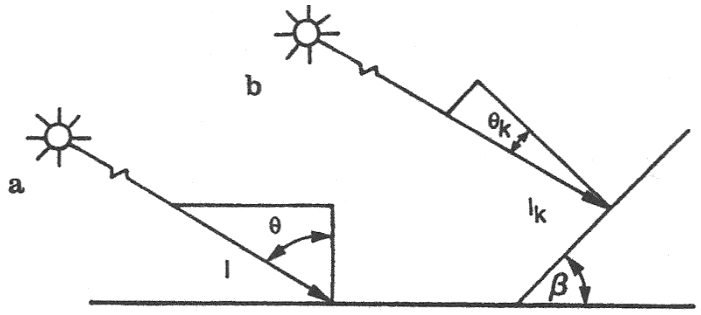

Figure 3-11: The zenith angle on a horizontal plane (left) and a tilted plane (right)

$$\cos(\Theta) = \sin\delta\,(\sin\phi\cos\beta - \cos\phi\sin\beta\cos a) + \cos\delta\cos\omega\,(\cos\phi\cos\beta + \sin\phi\sin\beta\cos a) + \cos\delta\sin\beta\sin a\sin\omega \quad (3\text{-}20)$$

Once the time-dependent angle of the irradiance on any surface is clarified, the irradiation model comes into place. As mentioned before, the key of a precise irradiation model is the correct consideration of all parts of the diffuse irradiance. In this work, the model of Perez was chosen over models from Liu/Jordan [155], Hey, Skartveit/Olseth [156] or Klucher [157], due to reasons of precision stated in [158]. It considers all three types of diffuse irradiation, as seen in Equation 3-17. The geometric factor R_b is defined as the ratio of a and b, representing the angles of incidence of the cone of circumsolar radiation. It can be calculated according to Equation 3-21. The geometric factors a, b and R_b therefore represent the time-dependent irradiation angle of Equation 3-17 apart from the inclination angle β of the analyzed tilted plane. The coefficients F_1 and F_2 specify the circumsolar and horizon brightness, which are determined by a table of brightness coefficients (Perez Anisotropic Sky) with the corresponding Clearness index ε. The Clearness index is further calculated by the model of Skartveit/Olseth. [156] In highly simplified terms: The Clearness index marks the share of the extraterrestrial irradiation (solar constant) to the measured global irradiation on the horizontal surface. The detailed model, the empiric factors and the according equations can be found in Duffie et al. [154], as this is beyond the scope of this work.

$$\mathrm{R}_b = \frac{\mathrm{a}}{b} = \frac{\max(0, \cos(\Theta))}{\max(\cos(85)\,, \cos(\Theta))} \quad (3\text{-}21)$$

The used weather data is supplied by the *Zentralanstalt für Meterologie und Geodynamik* (*ZAMG*) for the location of Leoben, Styria in Austria [159]. The selected year is 2014 because this specific year corresponds well with the long-term average in global radiation, sun hours as well as temperature. The time resolution of the measurement is 10 minutes. The measured cumulated global irradiation is 1,110 kWh/m^2 and the average annual temperature is 10.48°C.

The examined location (Leoben) is situated at the following geographical coordinates: 15.09113 °of longitude and 47.37639 ° of latitude. The assumed orientation is south (azimuth angle °) with an inclination of 30 °. As described by Weniger et al. in [120], the DSS is far less dependent on the azimuth and tilt angle as it is on the dimensioning of the system parameters (the battery and the PV system). In order to align all time-resolved data points to the same database of 15 minutes, the data was reconfigured via linear interpolation. This reduces the measured values from 52,560 data points to 35,040 data points while the mean radiation as well as the cumulated global irradiation over the year stays constant. An example of the interpolation is shown in Table 3-2. All radiation values are assumed to be constant for the measured time period.

Table 3-2: Linear interpolation of the measured 10 minute time steps to 15 minute time steps

10 minute time steps		15 minute time steps	
time [min]	radiation [W/m^2]	time [min]	radiation [W/m^2]
0	50	0	50
10	100	15	125
20	150		
30	200	30	200
40	250	45	275
50	300		
60	350	60	350

The main reason for using radiation data with a PV model instead of the measured output power of a real PV system is the versatile application. While radiation values are globally available and can be compared easily, output data of PV systems may not be available for all regions. Additionally, they are very hard to compare, due to the different plant-specific parameters, like the efficiency.

3.4.2 The Photovoltaic System model (Generation model)

The PV module converts the radiation on the tilted surface calculated by the described Perez model into electricity. Besides the time-resolved irradiance on the module, the temperature is an important input variable. The model provides the current and voltage, and thus the resulting power as output parameters. In this work, the detailed model of the photovoltaic module follows the methodology of Bellia et al. [160]. The main parameters (excluding physical constants) in order to determine the output parameters V, I and P are summarized

in Table 3-3. The resulting $I(V)$ and $P(V)$ curves, gained by varying temperature and irradiation, are validated with the set parameters of a PWX 500 PV module with 49 W published in [160] and afterwards set to the stated values of Table 3-3.

Table 3-3: Main parameters of the modelled PV module and the according values

Parameter	Value
T_{Ref} [°C]	24.8
V_{OC} [V]	22.6
I_{SC} [A]	5.35
P_{mpp} [W]	91.32
V_{mpp} [V]	18.33
I_{mpp} [A]	4.98
η_{module} [%]	13.34
η_{cells} [%]	16.54
Fill Factor [-]	75.55
Ideality Factor [-]	1.2
N_s [-]	36
R_p [Ω]	415.4
R_s [Ω]	0.221

The physical model of the Photovoltaic system is, as previously stated, derived from Bellia et al. [160] and adapted to the individual requirements of the task at hand by [161]. The whole modelling process takes place in the Simulink environment with the goal of a final implementation in the overall MATLAB model. In order to do so, the model of the PV system is set-up and initially parameterized, with standard PV parameters and in accordance to the PV model used. Afterwards, the $I(V)$ and $P(V)$ curves can be calculated for a certain pair of the two input parameters: irradiation on the module and ambient temperature. The maximum power, that can be obtained from the PV module at a specific irradiation and temperature is marked by the maximum value in the $P(V)$ curve. It is called the maximum power point (MPP). By varying the two input parameters in the application range, a correlation between the output power and the two input parameters can be established. This should be a simple mathematical equation that is later on used in the overall system model in MATLAB. In the next steps, the Simulink model and its results leading to the final mathematical equation, is explained step by step.

The main mask of the Simulink model is shown in the upper part of Figure 3-12. The two input parameters going into the black box of the PV system model are shown on the left: T_{sim} temperature and G_{sim} irradiance on the module according to the Perez model. The change of variable names for irradiation from I to G is made, because all the literature related to the Perez model labels irradiation as I, while this letter is reserved for the current in PV literature. There are three resulting parameters, as shown on the right: current I, voltage V and power P. All these parameters are determined at the maximum power point. Additionally, the complete $I(V)$ and $P(V)$ curves are given out as a result. The black box between the input and the output parameters can be further divided into four submodels, as shown in the lower illustration of Figure 3-12.

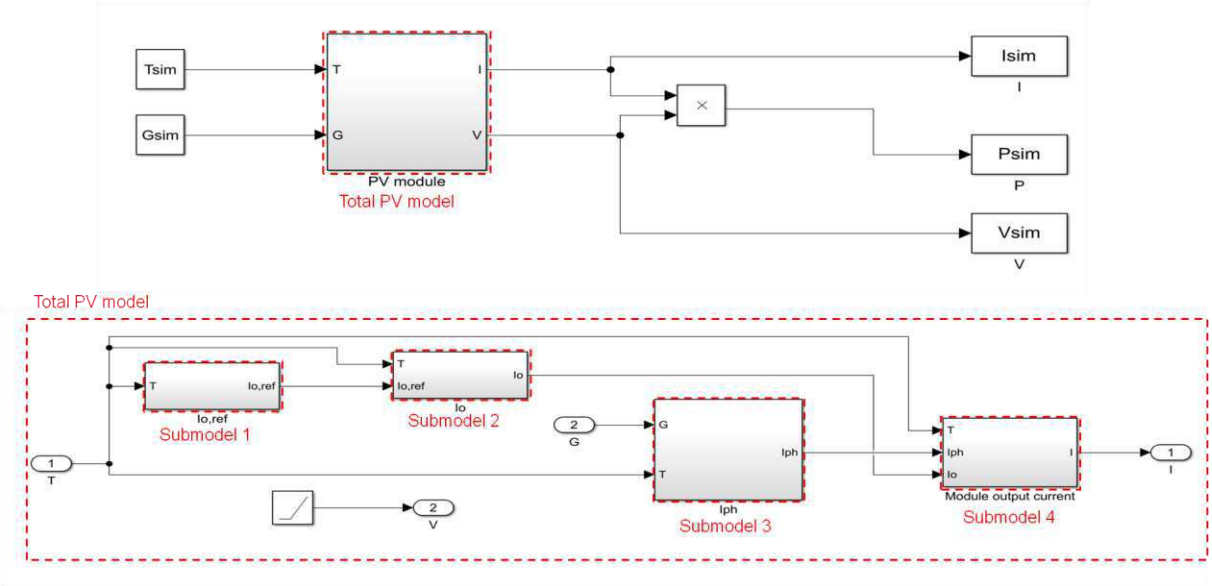

Figure 3-12: Simulink model of the total PV module [160,161]

These four submodels are now presented in more detail. Submodel 1 calculates the reference diode saturation current (leakage current) $I_{0,ref}$ at standard testing conditions (STC). Those conditions refer to a cell temperature of 25 °C, an irradiance of 1,000 W/m² and an air mass coefficient of 1.5. This coefficient defines the optical path length of the solar beams, expressed as a ratio relative to the vertical path length. Figure 3-13 shows the implementation of the calculation in Simulink. Additionally to the cell specifications in the form of the open-circuit voltage V_{OC} and the short circuit current I_{SC}, input variables like the cell-dependent ideality factor A, the number of cells in series N_S and the fundamental Boltzmann constant k_B along with the elementary charge q_e are used for this matter. This reference diode saturation current will be used as input in the next submodel in order to calculate the temperature-dependent diode saturation current I_0 according to the methodology shown in Figure 3-14. The methodology mostly uses the same input parameters, plus the actual temperature and

the so-called band gap energy E_g. This is a material related and temperature-dependent factor, which is measured in electronvolts. It describes the width of the gap between the conduction energy and valence energy. For Silicon, the gap of energy amounts to 1.12 eV.

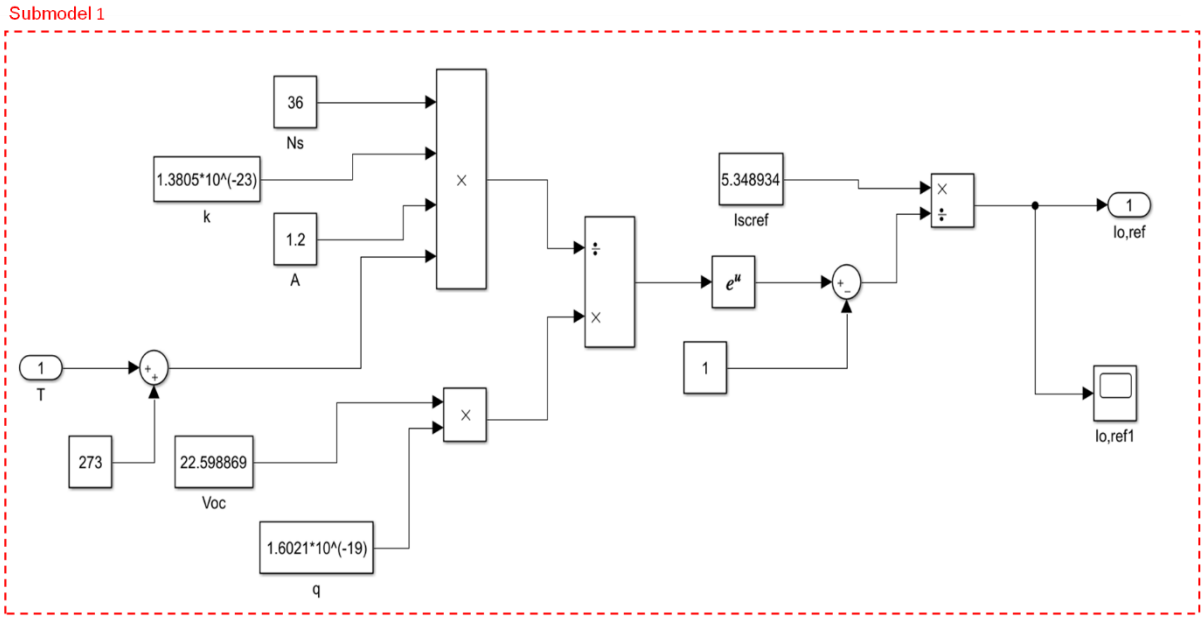

Figure 3-13: Simulink submodel 1: Calculating the reference diode saturation current at STC [160,161]

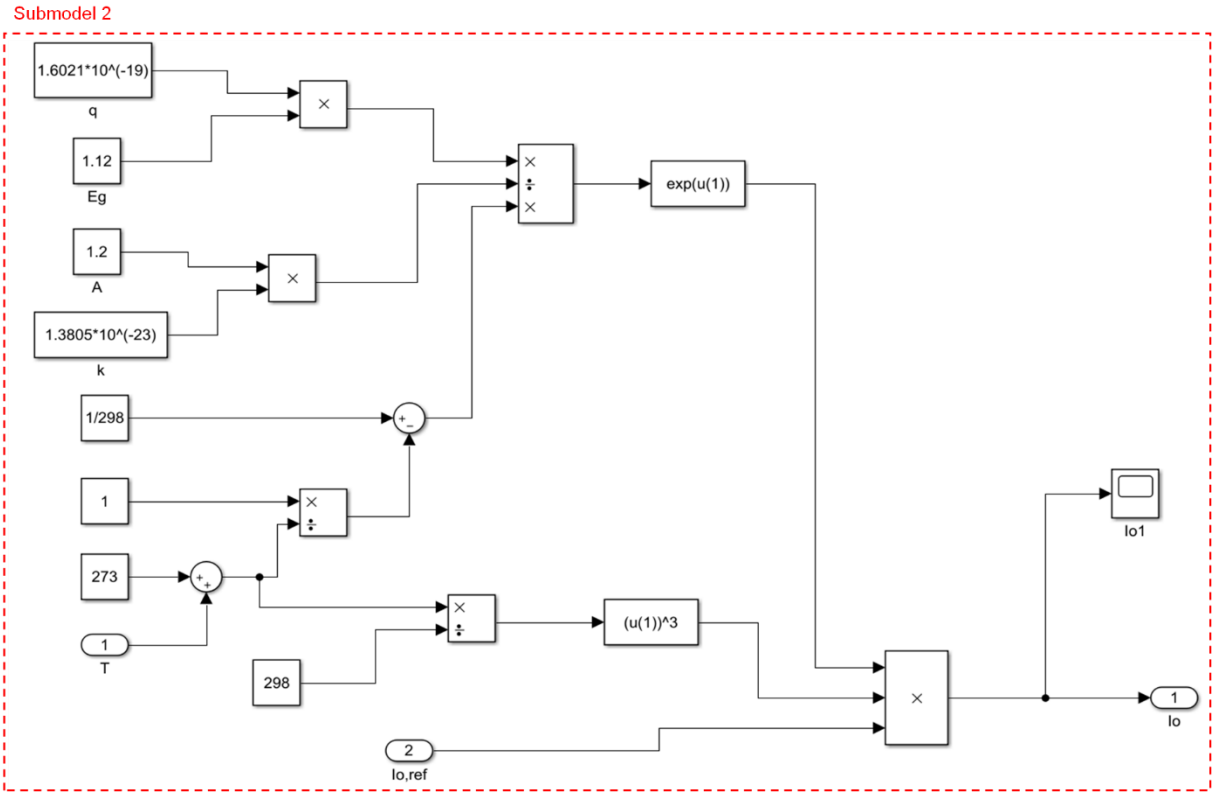

Figure 3-14: Simulink submodel 2: Calculating the temperature-dependent diode saturation current [160,161]

Submodel 3, as illustrated in Figure 3-15 calculates the photo current I_{ph}, from the two weather-dependent input parameters, irradiation G and temperature T. Additionally, the short circuit current I_{SC}, which is a cell parameter, and the so-called temperature coefficient are used for this purpose. The temperature coefficient describes the dependency between the short circuit current and the temperature. It is measured in Ampere per Kelvin and the value is usually supplied by the module manufacturer. Submodel 4 calculates the PV system output current. For the electrical current, it uses the photo current of submodel 3, the diode saturation current of submodel 2, as well as the temperature of the cell again. Additionally, it takes the series resistance and the much higher parallel resistance into account. The detailed calculation methodology is presented in Figure 3-16.

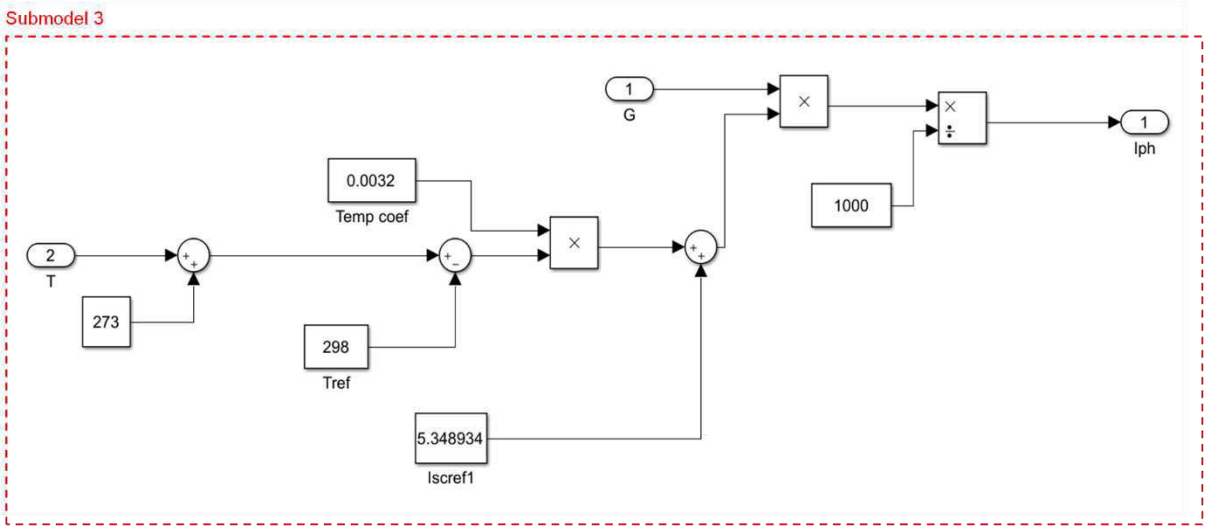

Figure 3-15: Simulink submodel 3: Calculating the temperature dependent photo current [160,161]

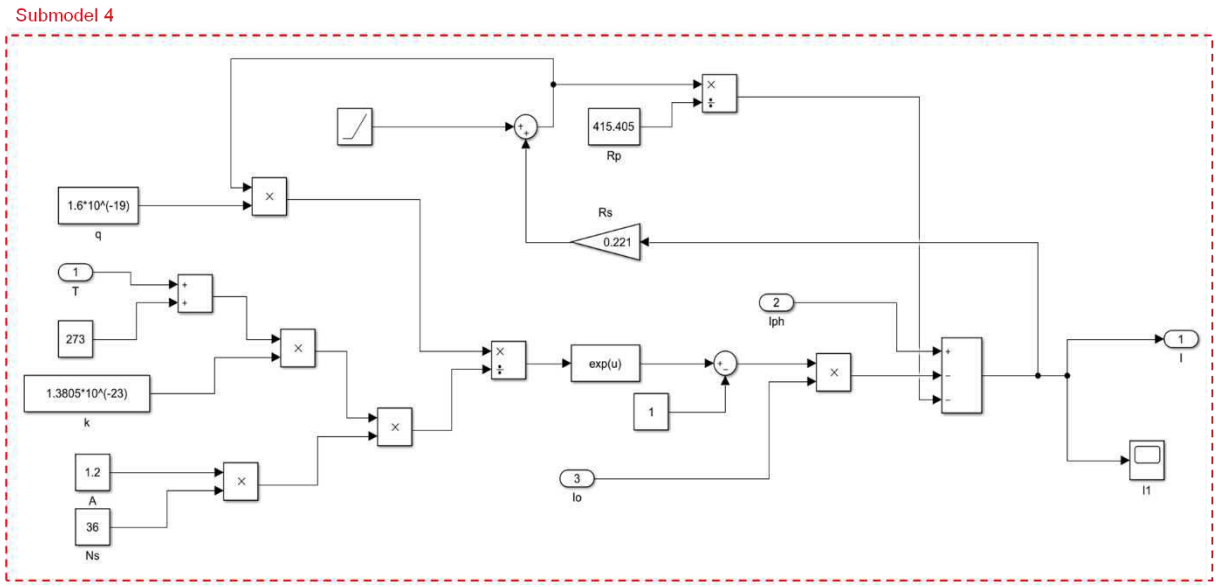

Figure 3-16: Simulink submodel 4: Calculating the PV module output current for the electrical equivalent circuit with a parallel an series resistance [160,161]

In order to develop the mentioned $I(V)$ and $P(V)$ curves, the corresponding voltage is ramped up to calculate the current for voltages between zero and the open-circuit voltage. The resulting power of the photovoltaic system at any given irradiation and temperature can be calculated by multiplying the resulting power for each pair of values (voltage and current) on the $I(V)$ curve. An illustration of the modeled $I(V)$ and $P(V)$ curves for selected temperatures and irradiations can be found in Figure 3-17. On the top left, one can see the modeled $I(V)$ curve at the reference temperature of 25 °C for different irradiations and to the right the resulting $P(V)$ curve. The two graphs at the bottom show the corresponding $I(V)$ and P(V) curves for a constant irradiation of 1,000 W/m^2, while the temperature of the PV modules is varied for exemplary temperatures between 0-60 °C. Additional details on the Simulink model can be found in the original paper in [160] and in [161].

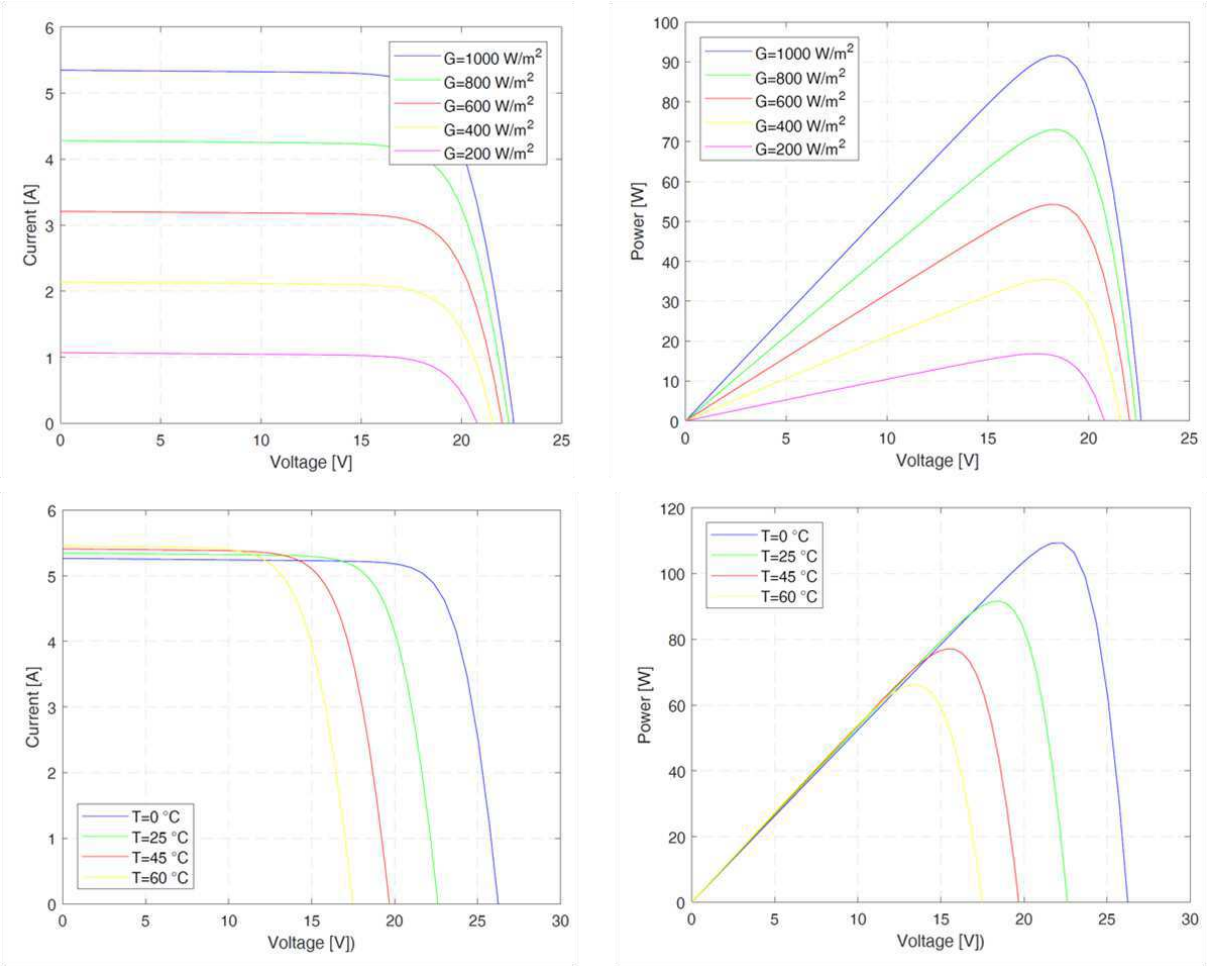

Figure 3-17: I(V) and P(V) curves for the modelled PV modules in a variation of irradiations and temperatures (own illustration based on [160,161])

Despite the simplicity and the suitability of the Simulink model for this task, it is not practical to use it within the overall model. Therefore, it is necessary to extract the information of this physical model and transfer it into a simple mathematical equation for further usage in the

overall Single-Nodal model. This is advantageous in terms of computation time. Since the overall system model is based on power and not on voltage and current, the only parameter of relevance is the maximum power point for variations of input values. It is assumed that the MPP tracker always finds the MPP without delay. To transfer the results of a specific PV module into a mathematical fit function, two dependencies were expressed in formulas. First, the irradiation war steadily increased at a constant temperature and secondly the temperature was varied at constant irradiation. These two functions are shown in Figure 3-18. Both correlations show a strong linearity. When combining both variations in a polynomial fit curve, the following overall equation (with largely reduced decimal places) occurs:

$$P_{PV}(G,T) = (3 \cdot 10^{-11} \cdot G^4 - 7.3 \cdot 10^{-8} \cdot G^3 + 6 \cdot 10^{-5} \cdot G^2 + 0.07 \cdot G) \cdot \left[(-0.72 \cdot T + 18.0) \cdot \frac{G}{1000}\right]$$

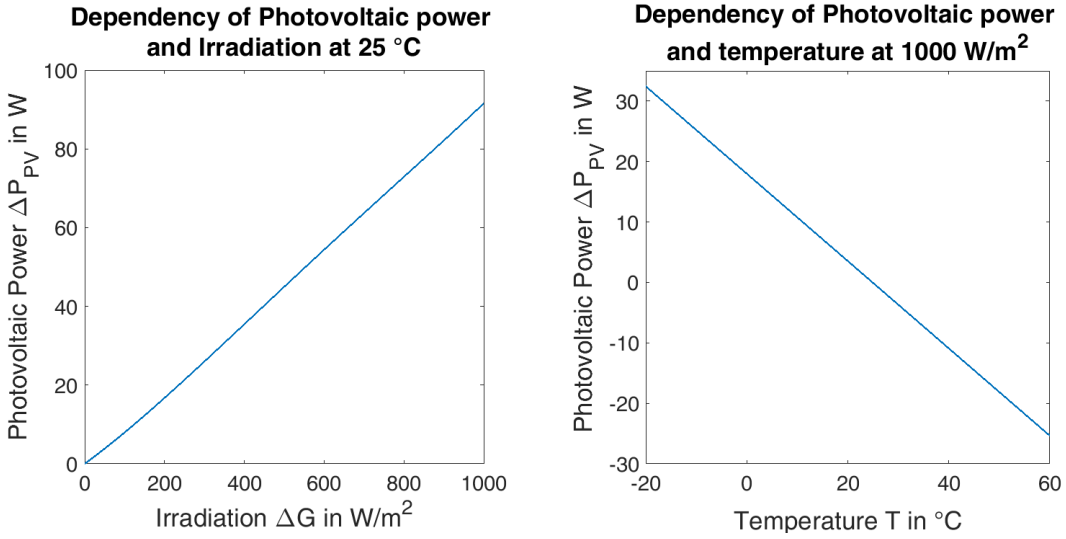

Figure 3-18: Curve fitting of the dependency between the photovoltaic power and the irradiation and the temperature respectively

Additionally, it has to be mentioned that the following sizing process (see section 3.4.6) of the PV system assumes a linear growth of the resulting PV yields with increasing PV system size. As a result of stating all PV system sizes in kW_{peak} and not in m^2, the efficiency of the PV panel does not have any considerable effects on the outcome of the sizing process. Any change in the efficiency only affects the necessary panel area and not the results of the ideal system size in kW_{peak} itself.

3.4.3 The battery and inverter model

Before modelling the battery and inverter, a general system topology of the PV storage system has to be selected, as there are different configuration alternatives: there are two main types of system topologies for PV storage systems: AC – and DC-coupled systems. Both types have advantages and disadvantages concerning flexibility, possible retrofit installation of batteries and system efficiencies. The distribution of the available topologies in Germany 2017 is 57 % AC coupled and 43 % DC coupled systems. [111] There is also a third system topology, called PV-coupled, which is rarely used but mentioned for the sake of completeness. An illustration of all topologies can be found in Figure 3-19.

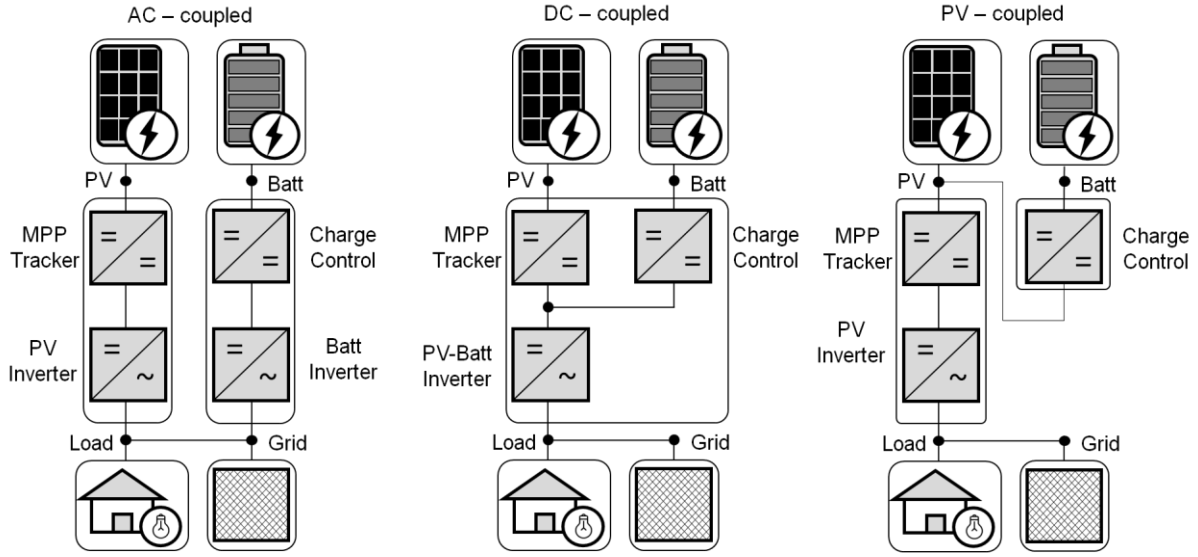

Figure 3-19: System topologies of PV-storage systems (Own illustration based on [162])

The chosen topology for this battery and inverter model used here is a DC-coupled residential battery system, as already presented in Figure 3-9. This means, that the DC power flow from the PV panel, which exceeds the current electricity demand is directly stored in the battery system without conversion into AC power. P_{Grid} and P_{Batt} can be positive and negative, while P_{PV} and P_{Load} can assume positive values only. In this exemplary model, the PV power P_{PV} represents $P_{Gen,F}$, as described in section 3.3. The positive values of all parameters are marked by the direction of the arrows in Figure 3-9. The overall model is created in a MATLAB environment.

The generated power of the PV system is in DC, which means it has to be inverted to AC, before it is either used to meet the current load of the consumer or fed into the grid. When a battery is added to the system, the surplus energy can be stored in the battery, to be used in a following time step. The necessary power electronics elements for DC-coupled PV storage systems are illustrated in Figure 3-9 and the middle illustration of Figure 3-19. The first element after the PV module is a DC converter in the form of a MPP tracker (MPPT). A MMPT is used to maximize the power extraction of the PV systems under varying conditions of voltage and current. This is especially critical under partial shading conditions. Therefore, several types of MPPT techniques are available, as described for instance in Mohapatra et al. in [163]. In this model, it is assumed that the MPPT finds the maximum output power on the $P(V)$ curve, at all times without delay. Following the PV2Batt path to the battery, another DC converter in the form of the battery charge controller is necessary. The main purpose of the charge controller is to prevent batteries from events such as overcharging or overvoltage. This is done by limiting the rate of electric current from and to the connected battery. The third power electronics element is placed on the path to the AC system side: the DC/AC inverter. The efficiencies of these energy paths, depending on the maximum output power of the elements, are illustrated in Figure 3-20 and named $PV2AC$, $PV2Batt$ and $Batt2AC$ in this work.

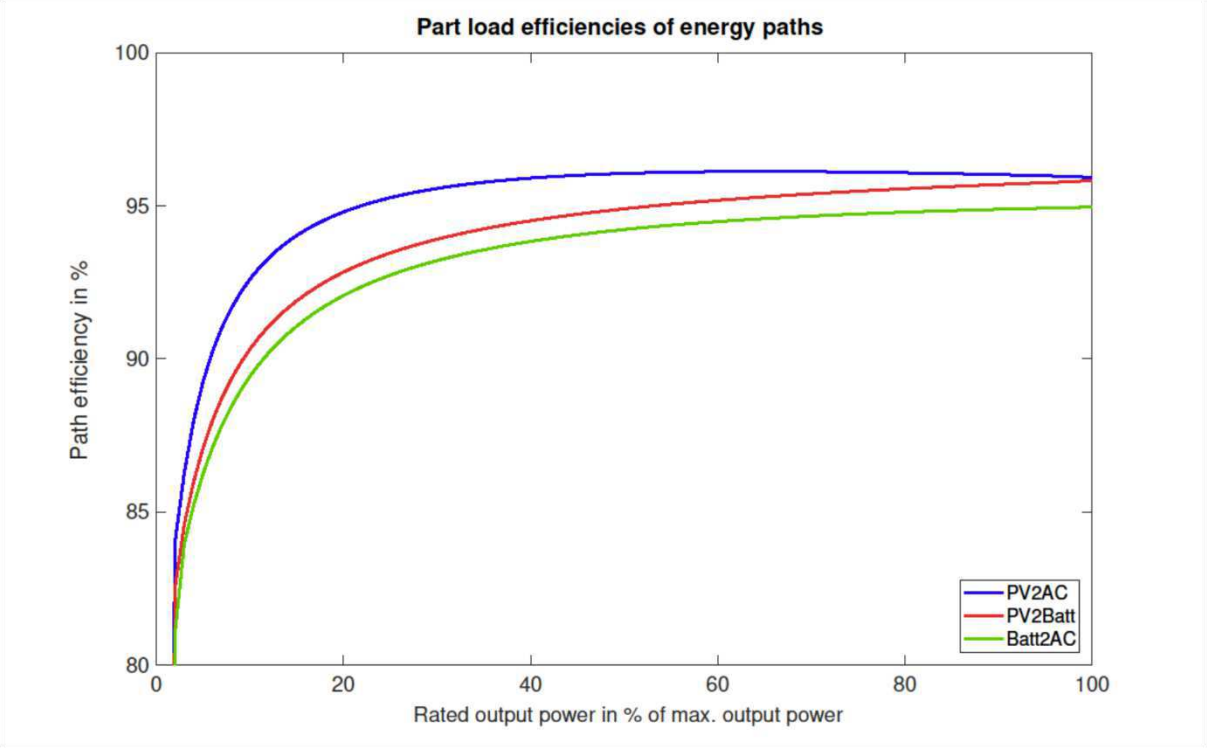

Figure 3-20: Part load efficiencies of the energy paths PV2AC, PV2Batt and Batt2AC

In addition to the losses caused by part load efficiencies of the described energy paths, various other losses occur in real systems of battery and inverter system topologies. Weniger et al. distinguish between sizing losses, conversion losses, control losses and standby losses in [162]. Sizing losses occur by power limitations caused by the power electronics. For example, if the power from the Photovoltaic module exceeds the inverter power at times of a fully charged battery, the exceeding power cannot be consumed or fed into the grid. This lost power falls in the category of sizing losses. Conversion losses are by far the largest losses throughout all tested systems and system topologies in [162]. They cover all losses in the conversion processes of the power electronics and the battery itself. All losses of the pathways PV2AC, PV2Batt or Batt2AC of Figure 3-20 are categorized as conversion losses. Control losses are caused by time lags and imprecise power input and outputs of the battery. This type of losses represents only a tiny fraction of the total losses and are usually only considered in models, where dynamic behavior is at the center of attention. Standby losses are the last type of PV-battery system losses of significance. They are the result of the small continuous power consumption of control devices and power electronics in standby mode. These losses are usually responsible for a small constant loss between 1-5 W.

The part load efficiency curves of Figure 3-20 (conversion losses) are derived from available data for DC-coupled systems published in [162]. This means that the specific losses of the energy paths are not derived from physical modelling of the power electronics components, but by a black box modelling approach via the usage of characteristic curves. All part load efficiencies were scaled to the corresponding output power and by calculating a medium system value of all published system configurations. In addition to the conversion losses, the energy management losses and the sizing losses are implemented in the model. The control losses are neglected since the reaction time of a few seconds is not depictured in a 15 min time-step consideration. The modes of operation and deployed standard control strategy of the battery is described in section 3.4.5.

As the battery size is to be determined in the described sizing process (section 3.4.6) the battery power needs to be set. To gain comparable results, it is advantageous to define the maximum battery power related to the energy content of the ESS. Weniger et al. analyzed 16 different BESS from various manufacturers in [162]. The range between the max. battery power and the energy content of the ESS ranged between 0.32 - 0.88 kW/kWh with a mean value of 0.64 kW/kWh. This value is used as the standard parameter for all battery configurations within this work and the maximum inverter power is set to the maximum PV power or battery power to ESS capacity ratio, depending on the higher value.

To evaluate the possible range of error made by a change in the battery power to ESS capacity ratio, a sensitivity analysis has been conducted with the result that the battery power does not have a large influence on the DSS within a certain range (0.35 kW/kWh - 1.2 kW/kWh) with deviations of DSS within 1 %. This is due to the implemented part load efficiencies. While PV or load peaks can be utilized/supplied with higher battery/inverter powers, the energy content in those peaks are relatively small and the gain in DSS is contradicted by a lower average efficiency of the storage system, due to a higher share of operating hours in non-optimal efficiencies. The operating hours in conditions of lower part load efficiencies are very limited and do not change significantly in the mentioned range. When the ratio of battery power to capacity is lower than the mentioned range, significant losses of 30 % in DSS and above are observed.

3.4.4 The Load model

In order to generate user-oriented results, it is essential to model different household types. This is because, contrary to the PV production, the behavior of the consumer is very individual. In order to create realistic types of household electricity loads, the open software-tool “Load Profile Generator” by Pflugradt [44] is used. 64 pre-defined household configurations that are aggregated to 15-minute mean values for power are already adopted in the tool. The household load profiles are built upon a behavior model and lifestyle patterns of different (pre-defined) users in a stochastic approach. A more detailed description of all used load profiles in this work and their background is to be found in section 2.2.1. The results of selected households in terms of their annual electricity usage profile and the corresponding ideal PV system and battery system sizes for the investigated households can be found in section 4.2.

3.4.5 The overall system topology

The main input parameters and assumptions of the mentioned system components are described in the previous sections. In the overall model, there have to be additional specifications regarding the fundamental functionality and operating principles, in addition to the specific parameters of the model parts. Figure 3-21 illustrates the input and output parameters of the overall PV storage system. The main input parameters are the time-resolved values of the irradiation, temperature and the individual load profile, while the output parameters are the time-resolved power values of the PV system, the battery system and the exchanged power with the grid. These power flows are necessary for the following sizing process described in section 3.4.6.

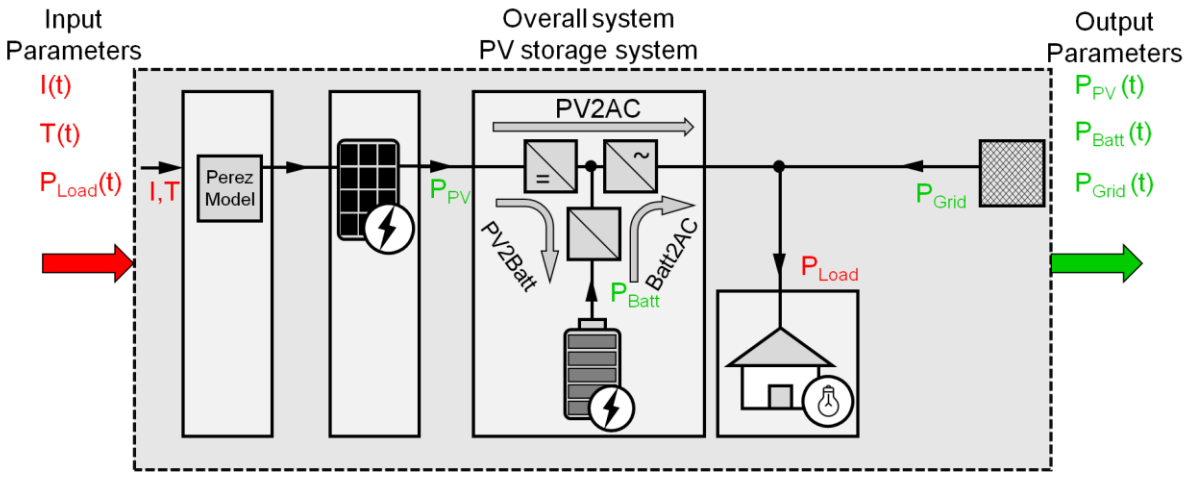

Figure 3-21: Visualization of the input and output parameters of the overall PV storage system

An example of the observed power flows in the overall system is presented in Figure 3-22 showing an example of a randomly chosen day. It shows the time-resolved power flows of the PV system and the supplied and consumed power to and from the grid as well as the cumulated energy in the battery. The mathematical description of the overall grey-box model and its functionality follows Equation 3-22 to Equation 3-24. Figure 3-22 shows the four described power flows in the analyzed system according to the set-up and sign convention, shown in Figure 3-9 (arrow directions mark positive values). The red line in Figure 3-22 marks the PV yield over time, peaking in the noon hours and showing a typical daily cycle for a clear day without passing clouds. P_{Load} (orange line) represents the power demand of the modeled household load. To the left of the PV yields, the load is entirely covered by the grid P_{Grid} (green line), which results in an overlap of the two lines. After the sun sets, which is marked by the end of the daily PV yields at around 19:00, the load is covered by the discharge of the battery power P_{Batt} (blue line). If one looks closely, one can see that the load is slightly underneath the battery power in the evening, due to the Batt2AC losses. Shortly before midnight, when the battery is fully discharged again P_{Batt} becomes zero and the grid supplies the energy of the load again. The battery is charged continuously over the morning hours with P_{Batt} until it reaches its maximum capacity of 1.5 kWh at around 9 am (SOE – 2nd graph – black line). Due to the sustained trend of high PV production, the surplus energy is fed into the grid from 9 am until the evening, with a small exception at around 16:00. A higher load peak exceeds P_{PV} at this time and leads to a stop in the grid feed-in and a positive value of P_{Batt}. This is also shown in the right graph, where the SOE takes a minor dip, before getting fully charged again.

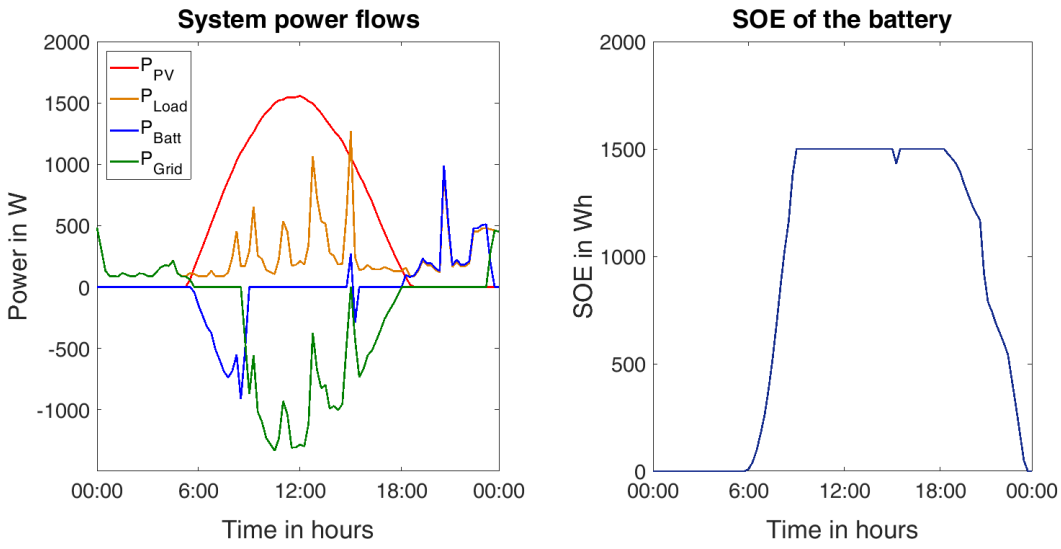

Figure 3-22: System power flows (left) and according SOE (right) of the battery for an exemplary day

The power balance of the overall model is defined in Equation 3-22 assuming no losses.

$$P[t]_{PV} + P[t]_{Batt} - P[t]_{Load} + P[t]_{Grid} = 0 \tag{3-22}$$

When considering the losses in the inverter and the battery, two defined operating modes exist: for all P_{Load} equal or higher than $P_{PV} + P_{Batt}$, and P_{Batt} greater than 0, Equation 3-23 applies and the battery is discharged. Equation 3-23 only applies for positive load flows from the battery, where the battery is discharged.

$$\{ P[t]_{Load} \mid P[t]_{Load} \geq P[t]_{PV} + P[t]_{Batt} \wedge P[t]_{Batt} \geq 0 \}$$

$$(P[t]_{PV} + P[t]_{Batt} \cdot \eta_{Batt}) \cdot \eta_{Inv} - P[t]_{Load} + P[t]_{Grid} = 0 \tag{3-23}$$

If P_{Batt} is negative and P_{Load} is equal or smaller than P_{PV}, Equation 3-24 is applied. If P_{Batt} becomes negative because of a charging process, only the reduced load flow of P_{PV} is transferred via inverter to meet the power demand of the load.

$$\{ P[t]_{Load} \mid P[t]_{Load} \leq P[t]_{PV} \wedge P[t]_{Batt} \leq 0 \}$$

$$(P[t]_{PV} + P[t]_{Batt}) \cdot \eta_{Inv} - P[t]_{Load} + P[t]_{Grid} = 0 \tag{3-24}$$

All formulas are valid for the following system constraint: when $P_{Inv}(= P_{PV} + P_{Batt})$ is smaller than the defined maximum inverter load $P_{Inv,max}$ (being 1 kW/1kW$_{peak}$ of $P_{PV,max}$). The maximum battery load/discharge power $P_{Batt,max}$ is equal to P_{PV}.

The chosen control strategy of the battery was the simple "greedy" algorithm. That is, as soon as $P_{PV} > P_{Load}$, the battery is charged with $P_{Batt} = P_{PV} - P_{Load}$ with no regard to any predictive control strategies based on weather forecasts or load prediction. [164] When $P_{PV} < P_{Load}$, the battery gets discharged with $P_{Batt} = P_{PV} - P_{Load}$ resulting in a negative value of P_{Batt}. This means that there are three priority levels for supplying the load: The first option will be direct consumption of the PV power, the second option is the battery and if neither option is available, the grid has to supply the demand.

3.4.6 Sizing methodology

The aim of the sizing methodology shown in this section is to determine the optimal system parameters for the PV system size in kW$_{peak}$ and the battery size in kWh. This process is performed with the help of the described model of the PV battery system. The sizing approach has been published in the Journal of Energy Storage. [165] In the following section, the design process to find the optimal PV/Battery ratio is carried out with one representative household for illustrative purposes only. The results for all other conducted household types are found in the results section. The first step in the sizing process is the definition of the performance indicators, to be optimized. The degree of self-sufficiency (DSS) is the key parameter selected, due to its high informative value both for the assessment of the PV – and the battery system. It has to be stated, that the presented sizing optimization methodology also works with other presented KPIs, mentioned in section 3.3.

In order to compare different household types with each other, it is necessary to normalize all variable parameters. Otherwise, in terms of optimum storage and PV system size, a comparison between a household with an annual energy consumption larger than 5,000 kWh and a smaller consumer of 1,500 kWh would not lead to significant conclusions. This is why all relevant parameters are normalized to the annual electricity demand of the household according to Equation 3-25.

$$P_{PV,max,normalized}\left[\frac{kW_{peak}}{MWh}\right] = \frac{P_{PV,max}}{E_{Load,annual}}\left[\frac{kW_{peak}}{MWh}\right] \cdot \frac{1000}{1}\left[\frac{kWh}{MWh}\right] \qquad (3\text{-}25)$$

The usable battery capacity is expressed in Equation 3-26 as the battery capacity (kWh) per annual load (MWh), and the PV size is indicated as kWpeak per MWh annual electricity demand, analogous to Equation 3-25.

$$E_{Batt,cap,normalized}\left[\frac{kWh}{MWh}\right] = \frac{E_{Batt,cap}}{E_{Load,annual}}\left[\frac{kWh}{MWh}\right] \cdot \frac{1000}{1}\left[\frac{kWh}{MWh}\right] \quad (3\text{-}26)$$

The two parameters $P_{PV,max,normalized}$ and $E_{Batt,cap,normalized}$ are varied from 0-3 in 100 linear steps in order to calculate the DSS. When combining the two variables, a 100x100 matrix leads to a characteristic diagram of 10,000 system design combinations. The matrix contains battery sizes between 0-3 kWh/MWh and PV system sizes of 0-3 kW_{peak}/MWh. The result of the calculated DSS for all 10,000 system design opportunities is presented in Figure 3-23 in normalized system parameters as well as in absolute system sizes (green axis). The distribution of DSS also matches with previously published results in Weniger et al. [120]. All DSS levels are presented as so-called indifference curves. These indifference curves represent graphs with the same level of satisfaction (utility) to the consumer for a specific indicator. This means that the achievable DSS level is identical for all shown graphs of Figure 3-23, which means a consumer is indifferent between two points on the same indifference curve.

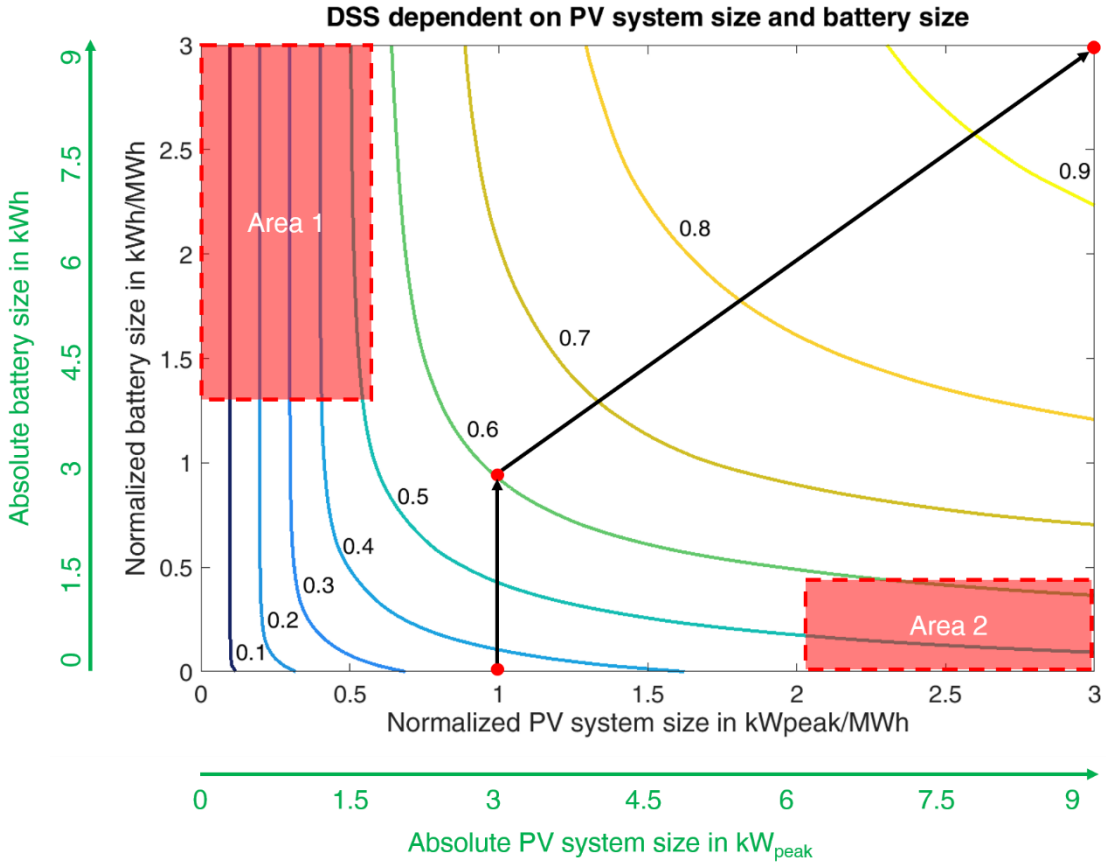

Figure 3-23: Characteristic diagram of the DSS for various system configurations

Figure 3-23 shows that the DSS increases with larger PV system sizes and battery capacities. For instance, at a normalized PV size of 1 kW_{peak}/MWh and with no battery at use, the achievable DSS is roughly 0.3 (see P1 on the graph). When an additional battery with 1 kWh/MWh is added to the system the DSS can be increased to around 0.6 (P2). The achievable DSS at a PV size of 3 kW_{peak}/MWh combined with a battery of 3 kWh/MWh can be raised by another 31 % to 0.91 (P3). This increase requires a tripling of both the PV system and battery sizes from P2. In analysing the mentioned figure, one can clearly identify areas of unreasonable system configurations, especially at unbalanced PV/Battery ratios in the marked Area 1 (large battery, small PV system) and marked Area 2 (small battery, large PV system). As depicted by Area 1, there is practically no gain in self-sufficiency when increasing storage from 1 kWh/MWh to 3 kWh/MWh, if the PV system size is held at a small constant value of below 0.5 kW_{peak}/MWh. The reason for this effect is that there is not enough energy to store in a battery, regardless of its size. Area 2 marks PV storage systems with a large PV system and a small storage capacity. This means that the DSS is only slightly improved by further increasing the PV system, because it is out of proportion with the electricity demand to be supplied. Most additional energy produced by the PV system can no longer be self-consumed and needs to be fed-in to the grid without contributing to the DSS.

Determining the ideal PV system to battery size ratio is an important exercise when optimizing the DSS. Therefore, it is desirable to avoid combinations like those described by Area 1 and Area 2. The determination of this ideal system design is explained in the following paragraphs. The main approach of finding a technical optimum is defined as follows:

An optimal system configuration has a maximum degree of self-sufficiency with minimum PV system size and storage capacity.

This definition is the main guiding principle when trying to reach a precisely determined technical optimum. The way of finding this configuration is to mathematically exclude all areas where large increases in storage capacities or PV system sizes add only little value to the degree of self-sufficiency. Two different ways of performing this analysis are presented in this work: A methodology Pareto Principle that allows the user to have a specific value as the optimum output and the optimization by Lagrange Multipliers, which shows the distribution of optima for all levels of DSS. Both operations are performed in multiple process steps, which are depicted in Figure 3-24 and described in detail in the next pages.

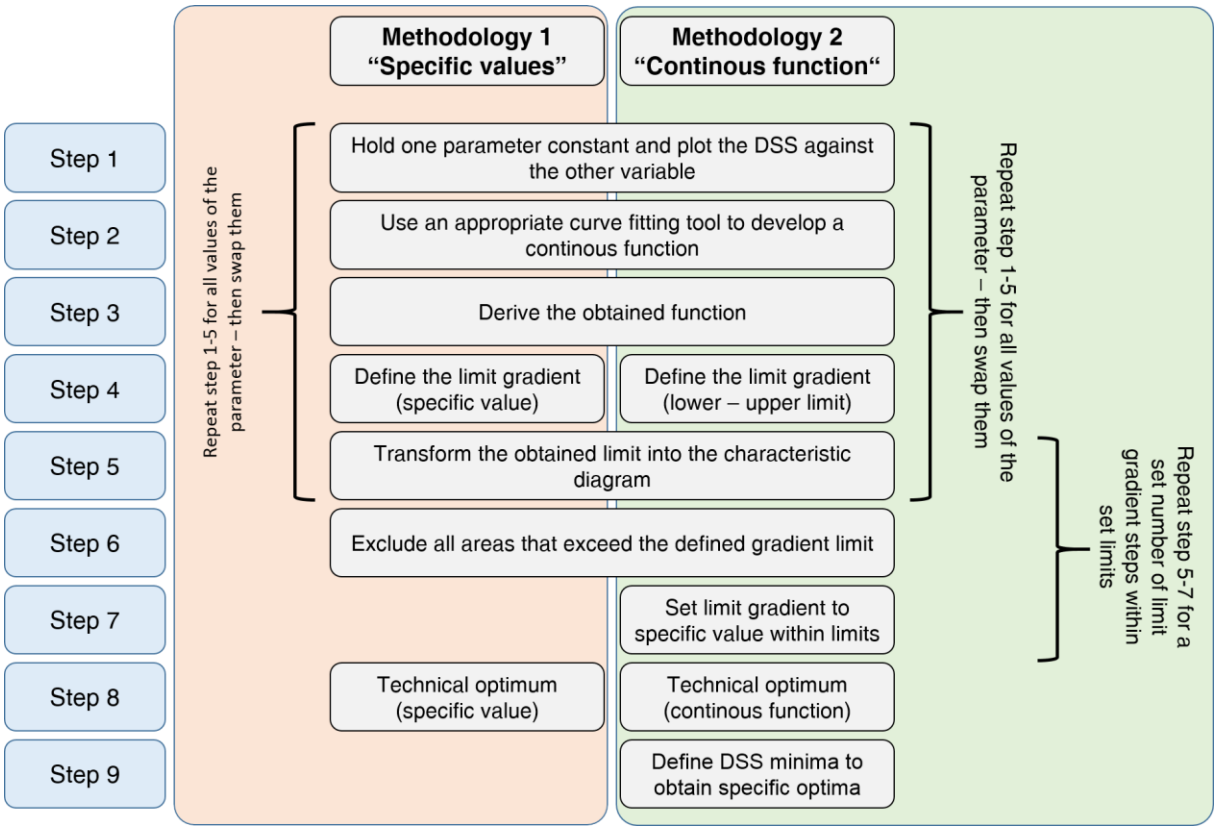

Figure 3-24: Visualization of the two methodology variants

Step 1

Step 1 involves choosing the initial parameter and its value. In this example, the PV system size is initially varied and the battery size is held constant at 2.5 kWh/MWh, which is randomly chosen for this example in Figure 3-25. To visualize the difference between the normalized and the absolute system sizes, a second axis for the absolute PV and battery size is introduced with an annual electricity consumption of 3 MWh. As an example, steps 1-5 occur at the horizontal line of the left part in Figure 3-25 (red line). One can see that the distance between lines of constant DSS-values increases with higher PV system sizes. This phenomenon can also be observed in Figure 3-25 on the right, when plotting the DSS against the PV system size at a constant battery size of 2.5 kWh/MWh. The obtained data points (blue) of the DSS increase quickly at the beginning and level off with increased PV system size. Both visualizations are equal to each other, but the transfer to visualization 2 is necessary for the following process steps 2-5.

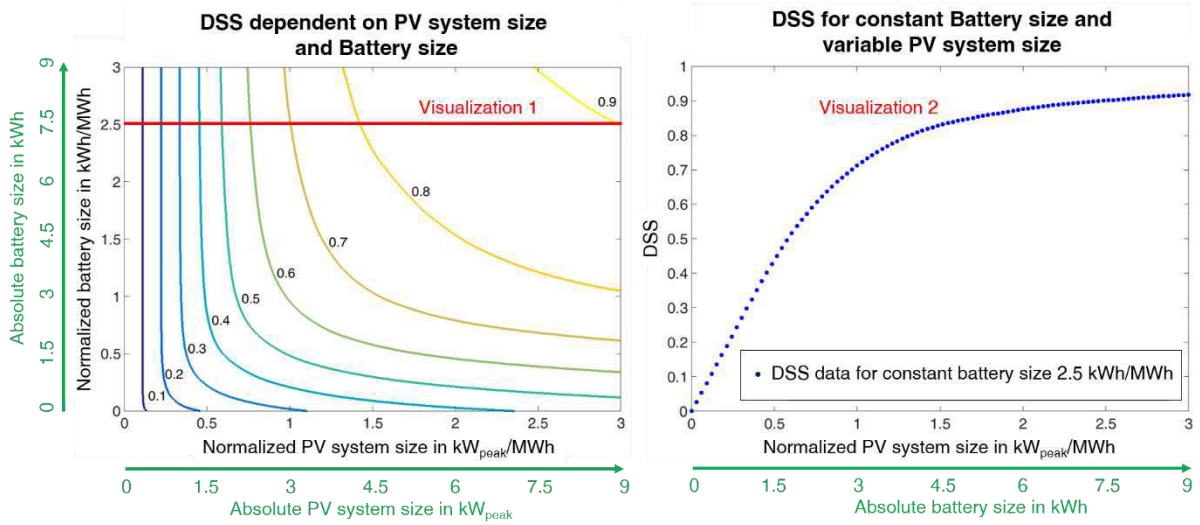

Figure 3-25: Two visualizations of step 1. The red line of the illustration on the left shows a constant normalized battery size of 2.5 kWh/MWh – The blue data points in the right illustration represent the DSS values for the same constant battery size, depending on the PV system size

Step 2

In step 2, a curve is fitted to the data via a 4 term Fourier series approximation in MATLAB, which serves as the curve fitting tool in this work. The result is shown in Figure 3-26 (upper picture – pink regression line). The Fourier approximation leads to a function of Equation 3-27 with a_n , b_n and w being the determined individual constants. $f(x)$ represents the DSS values and x the normalized PV system size, as shown in Equation 3-27.

$$f(x) = a_0 + a_1 \cdot \cos(xw) + b_1 \cdot \sin(xw) + a_2 \cdot \cos(2xw) + b_2 \cdot \sin(2xw) + a_3 \cdot \cos(3xw) + b_3 \cdot \sin(3xw) + a_4 \cdot \cos(4xw) + b_4 \cdot \sin(4xw) \quad (3\text{-}27)$$

The shape of the obtained functions is particularly suitable for a Fourier fit method, which results in usual Root Mean Squared Errors (RMSE) in the magnitude of 10^{-4}. This indicates very low deviations from the calculated results and the created regression.

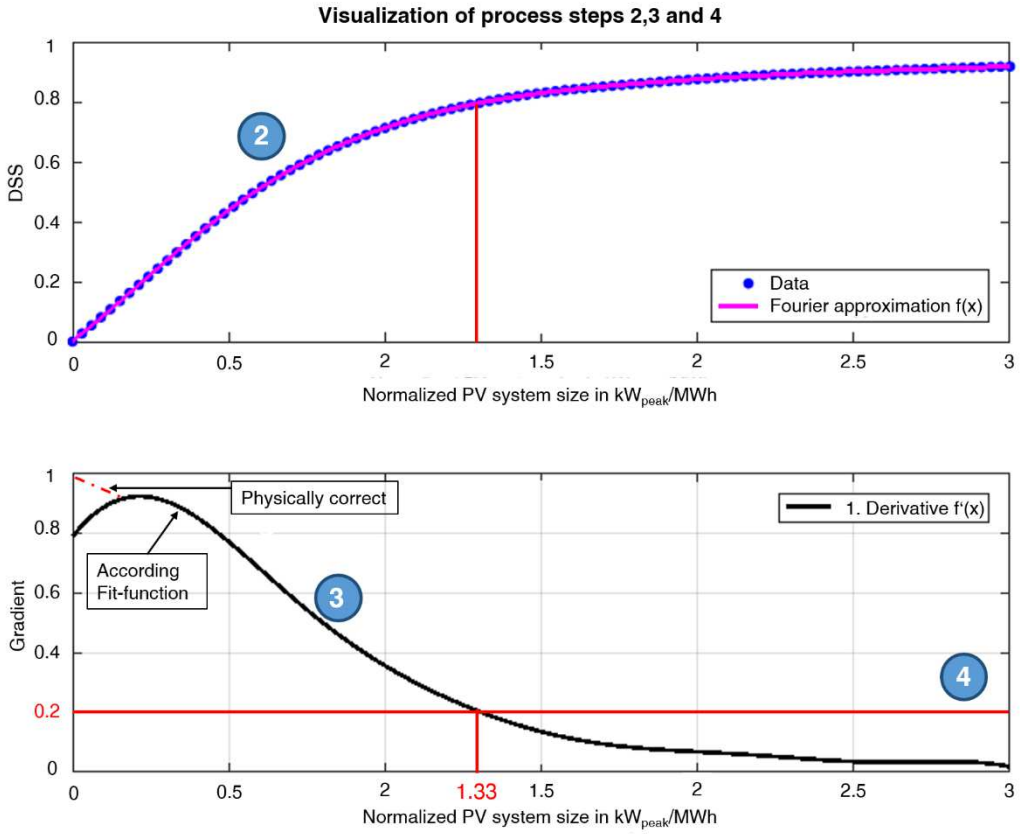

Figure 3-26: Visualization of the process steps 2,3 and 4

Step 3

The goal of step 3 is to create the first derivative of the obtained Fourier series function. It represents the gradient of the original function and is shown in the lower graph of Figure 3-26 (black function).

$$f'(x) = b_1 \cdot w \cdot \cos(xw) + 2b_2 \cdot w \cdot \cos(2xw) + 3b_3 \cdot w \cdot \cos(3xw) + 4b_4 \cdot w \cdot \cos(4xw) - a_1 \cdot w \cdot \sin(xw) - 2a_2 \cdot \sin(2xw) - 3a_3 \cdot w \cdot \sin(3xw) - 4a_4 \cdot w \cdot \sin(4x \cdot w) \quad (3\text{-}28)$$

One can see high gradient values at the beginning and lower gradients of the DSS at increased system sizes. The small initial increase of the gradient curve, as seen in Figure 3-26 at PV system sizes below 0.25 kW_{peak}/MWh, is observed in a small number of datasets. The effect is caused by the fact that a Fourier series is used to approximate a linear trend. The plotted gradient function highlights this effect, which was first not very noticeable in the original Fourier approximation. However, the initial increase doesn't affect the automatic sizing process, because it doesn't occur close enough to the defined gradient limit.

Step 4

The fourth step is slightly different in the two methodologies illustrated in Figure 3-24. Both methodologies define a gradient limit, but Methodology 1 sets a specific value. In the example shown in Figure 3-26, the gradient limit is 0.2 and is marked with a red line. Methodology 2, however, defines the lower and upper border of the gradient limits. In step 7, the gradient limit is then specifically calculated to be between these limits.

By increasing the normalized PV system size, it will fall below the defined gradient limit. The last specific x-value (PV system size) that meets the defined limit gradient of Equation 3-29 is marked and transferred into the original characteristic diagram depicted in Figure 3-25. The boundary is clearly identifiable and produces no computational issues when determining the ideal PV system and battery configuration.

$$f'(x) \leq gradient\ limit\ (g.l.) \tag{3-29}$$

In the case depicted below, the determined limit is 1.33 kW_{peak}/MWh. This means that a DSS of 81.4 % can be achieved with a PV system size of 1.33 kW_{peak}/MWh and a battery size of 2.5 kWh/MWh. The maximum achievable DSS with this battery size is 91.8 %, which corresponds to an absolute increase by only 10.4 % if the PV system size is scaled up by 230 %. This disproportionate effort for minor gains in DSS is prevented by this methodology, when choosing the appropriate gradient limits.

Step 5

The process of determining the limits at which a further increase of PV system size is no longer rewarding in terms of the DSS required by the defined gradient limit is now performed for all values of the battery size. These limits can then be transformed back into the characteristic diagram of the original Figure 3-23, resulting in a continuous vertical border line. The demonstrated example of the border determination in Figure 3-25, for a constant battery size of 2.5 kWh/MWh is marked in Figure 3-27 with red circles. To obtain Border 2, the same five steps are repeated for constant values of the PV system size and variable battery dimensions. This means that the PV system size is held constant and the battery size is varied, analogous to steps 2-4 shown in Figure 3-26. The only difference is that the x-axis will now represent the battery size in kWh/MWh. If the limit gradient is determined for all constant PV sizes, one receives a second border line to transfer into the original diagram. The result can be seen in Figure 3-27.

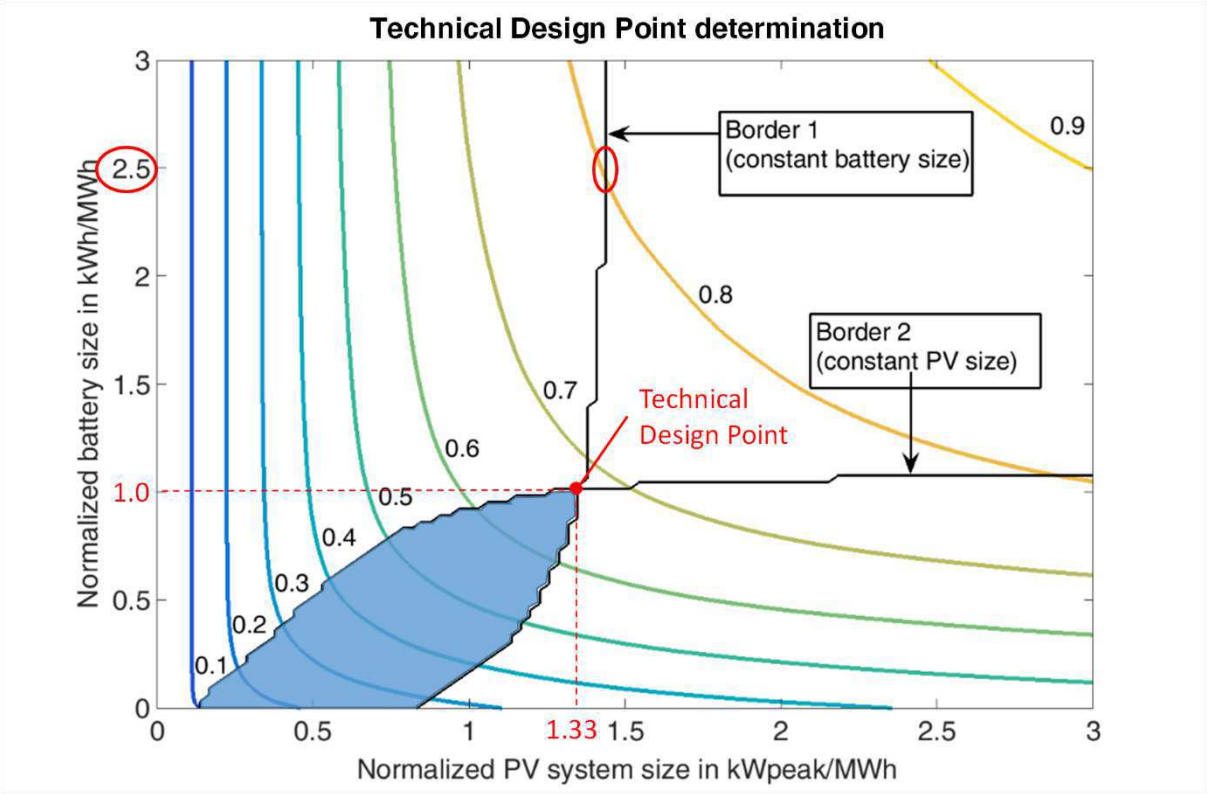

Figure 3-27: Visualization of the obtained borders from process steps 1-5

Step 6

Border 1 in Figure 3-27 represents the sum of all limits for constant battery sizes as described in the steps 1-5. The area to the right of Border 1 is considered unreasonable as the gain in DSS value is disproportionately small compared to the necessary effort of scaling up the PV system. Analogous to Border 1, the second border line represents the calculated limits for constant PV system sizes and variable battery dimensions. Similarly, the area above Border 2 represents disproportionate gains in DSS value. Moreover, the bottom left corner of Figure 3-27 shows that the reasonable battery size is very small for small PV systems. The combination of both borders excludes most areas of the diagram and therefore rules out many system designs. The defined technical optimum is, according to the previous definition, the system configuration within the obtained boundaries that has the highest value of the design parameter, the DSS. In this example, the ideal system consists of a battery unit capacity of 1.0 kWh/MWh and a PV system size of 1.33 kW_{peak}/MWh and reaches a DSS of 67 %. The determined technical design Configuration as marked in Figure 3-27 also equals the result of Equation 3-29 and therefore represents a minimum of system sizes for the achieved DSS.

By increasing the gradient limit, the obtained Border 1 is shifted to the left, while the Border is shifted further right at lower gradient limits. The equivalent is valid for Border 2 as well,

which means that the determined border line moves up at lower gradient limits and down at higher gradient limits. All system designs in areas above any of the two borders are considered poorly designed. They all have in common, that the gains in DSS are disproportionate to the additional necessary system efforts.

Step 7

In step 4 of methodology 1, a specific gradient limit is defined. This step is missing for methodology 2 so far, as only the upper and lower limits of the gradient limit have been defined in step 4. In this step, the gradient limit is initially set to the upper limit and is gradually reduced until the lower gradient limit is reached. The number of interval steps between both limits needs to be defined by the applicant.

Step 8

Since there is only one specific value for the gradient limit in Methodology 1, the technical optimum matches the technical design point of Figure 3-27. This specific system design marks the configuration with the highest possible DSS for a given PV-storage size. By multiplying the normalized storage - and PV system size with the annual electricity demand, the nominal values of the PV system size and the battery size can be determined according to the reversed Equations 3-25 and 3-26. It is important to keep in mind that all resulting storage sizes are indicated as usable battery capacities. The depth of discharge according to Equation 4-2 in section 4.1 must be considered. The final result of this method should be the ratio of the determined PV system size and the battery size (PV system/battery ratio) stated as kW_{peak}/kWh.

Methodology 2 takes a slightly different approach. In order to obtain a continuous function of technical sizing optima depending on defined DSS constraints, a variety of gradient limits is used. These gradient limits are varied between an upper and a lower limit. The calculation procedure of step 1 to step 6 results in a specific technical optimum for each gradient limit. Since many gradient limits are used in methodology 2, numerous optima can be determined. These optima are illustrated as blue dots in Figure 3-28. By applying a curve fitting tool to the sizing optima, a continuous progression curve of optimal technical designs can be determined for a wide range of DSS levels. This allows the user again to create a continuous function of optimal design points for all DSS levels. In order to compare technical designs for different consumer loads, three exemplary design points at the intersections of the DSS indifference curves of 0.3, 0.5 and 0.7 are determined and later compared in the results section.

An exemplary progression curve of design points including the marked intersection with the mentioned DSS indifference curves is shown in Figure 3-28. The course of the curve is different for every load profile, due to the individual structure of achievable DSS indifference lines depending on the consumer load profile.

Step 9

The mathematical formulation of the presented process to establish a maximum DSS with a minimum of PV and storage size can be phrased as follows: The DSS is a function of the PV system size S_{PV} and the battery size S_{Batt}, which has to be maximized by the following procedure. It has to be stated that there cannot be a global optimum since this is not a single-objective optimization approach, but there is one clearly identifiable optimum for each indifference curve, as the following equations will show.

$$DSS = f(S_{PV}, S_{Batt}) \tag{3-30}$$

Figure 3-28 shows the indifference curces with equivalent levels of DSS and the design optima for different gradient limits. Each configuration of S_{PV} and S_{Batt} leads to a specific DSS value. In this optimization problem the DSS value is set and S_{PV} and S_{Batt} are minimized. This leads to the minimum system size in order to reach the specific DSS constraint. It has to be stated, that these indifference curves are not limited to the 8 curves (DSS-levels from 0.1-0.8) shown in Figure 3-28. There is an infinite number of indifference curves, only limited by the data resolution. The equation of the necessary cost to achieve a level of DSS is defined by Equation 3-30. Since the sizing process is based on technical parameters, the specific cost describes the technical effort and is assumed to be equal for the PV system and the battery system, as shown in Equation 3-32.

$$TC - c_{PV} \cdot S_{PV} - c_{Batt} \cdot S_{Batt} = 0 \tag{3-31}$$

$$\frac{c_{PV}}{c_{Batt}} = 1 \tag{3-32}$$

To maximize the function $DSS(S_{PV}, S_{Batt})$ under the constraint of Equation 3-31, the methodology of Lagrange multipliers is used for this optimization problem, as shown in Equation 3-33. Following the guidelines through the standard optimization method Equation 3-33 is partially derived for each parameter and set equal to 0 afterwards. The gradients of both functions $DSS = f(S_{PV})$ and $DSS = f(S_{Batt})$ need to be parallel vectors at

the design optimum. However, the length of both gradient vectors can be different, which requires a factor to describe the constant difference in length. This is the so-called Lagrange λ, which is introduced in the Equations 3-33 to 3-36.

$$\mathcal{L}(S_{PV}, S_{Batt}, \lambda) = DSS(S_{PV}, S_{Batt}) - \lambda \cdot (TC - c_{PV} \cdot S_{PV} - c_{Batt} \cdot S_{Batt}) \quad (3\text{-}33)$$

$$\frac{\partial \mathcal{L}}{\partial S_{PV}} = \frac{\partial DSS}{\partial S_{PV}} - \lambda c_{PV} = 0 \quad (3\text{-}34)$$

$$\frac{\partial \mathcal{L}}{\partial S_{Batt}} = \frac{\partial DSS}{\partial S_{Batt}} - \lambda c_{Batt} = 0 \quad (3\text{-}35)$$

$$\frac{\partial \mathcal{L}}{\partial \lambda} = TC - c_{PV} \cdot S_{PV} - c_{Batt} \cdot S_{Batt} = 0 \quad (3\text{-}36)$$

Equations 3-34 and 3-35 can further be simplified and rearranged as follows.

$$\frac{\partial DSS}{\partial S_{PV}} \cdot \frac{1}{c_{PV}} = \lambda \quad (3\text{-}37)$$

$$\frac{\partial DSS}{\partial S_{Batt}} \cdot \frac{1}{c_{Batt}} = \lambda \quad (3\text{-}38)$$

After equating both functions the solution shown in Equation 3-39 appears.

$$\frac{\frac{\partial DSS}{\partial S_{PV}}}{\frac{\partial DSS}{\partial S_{Batt}}} = \frac{c_{PV}}{c_{Batt}} \quad (3\text{-}39)$$

This means that the DSS for every indifference curve is maximized at the point where the slope of the indifference curve is equal to the slope of the cost ratio. To identify the slope of the indifference curve, the DSS being a function of the PV system size and the battery size needs to be differentiated with respect to both parameters, which has been introduced in eight practical steps earlier on. The results of the intersections between the function of the technical design points for various indifference curves is shown in the following results section.

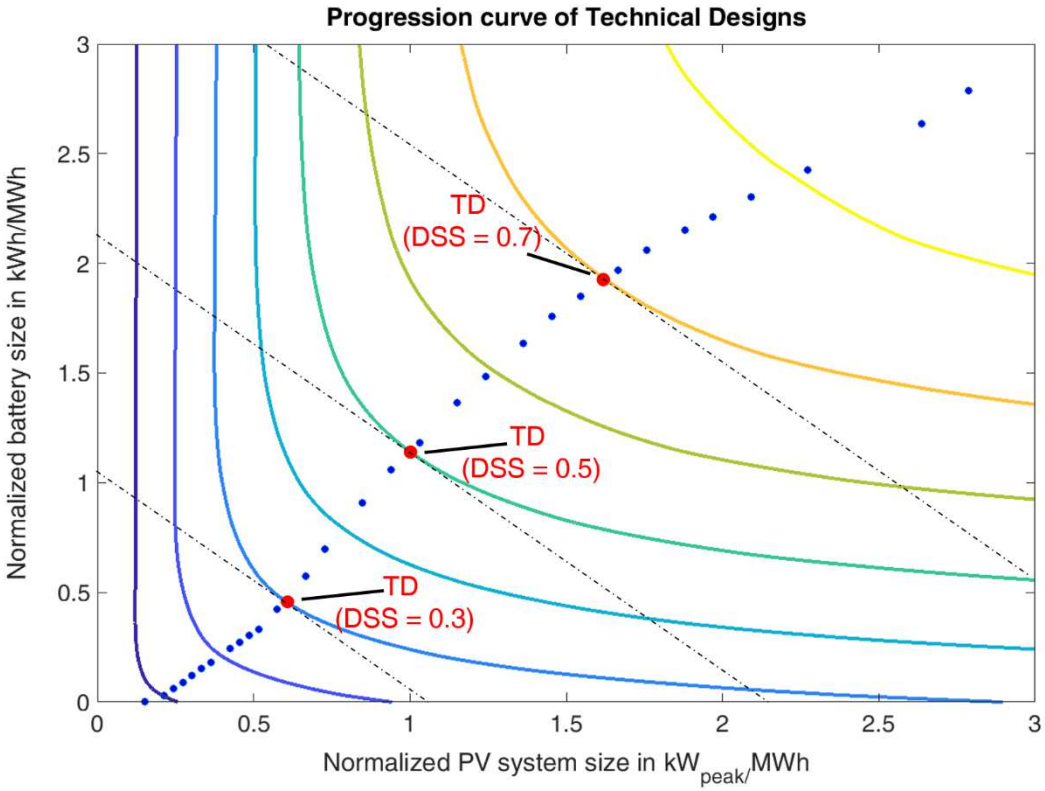

Figure 3-28: **Progression curve of technical designs and intersections at the DSS indifference curves of 0.3, 0.5 and 0.7**

3.5 Multi-Nodal model (*HyFlow*)

This section shows how the objectives of the cellular approach are implemented in the *HyFlow* modelling framework. Additionally, all relevant components and their characterization, as well as the implementation of the load flow calculations (LFC) and the workflow of *HyFlow* are described in this section. *HyFlow* is the name of the developed Multi-Nodal model for the three considered energy carriers. It is important to note, that a cell is always represented by a single node, as presented in section 3.2. This means that the Multi-Nodal model is also a Multi-Cell model and the expressions cells and nodes are used synonymously in all following sections. Additionally, I want to emphasize that the development of *HyFlow* was not my sole achievement. While the idea and the conceptual design was created by me, the predominant part of the programming, however, was performed within the framework of two Master Thesis from Greiml [166] and Leitner [167], both under my supervision. The stated references are therefore representative for the whole section, because major parts of the *HyFlow* methodology described here, are already documented in these Master Thesis.

The cellular approach in *HyFlow* is implemented at three different cell levels. The lowest cell-level, a level-1 cell, contains residual loads, energy storage systems, hybrid elements and network connections between level-1 cells. Since *HyFlow* can adapt to various sizes of system boundaries via the cellular approach, a level-1 cell can be represented for instance by smaller units such as households or larger units like city districts or entire regions. The level-2 cell should be accordingly sized one aggregation level above and must consist of at least one level-1 cell. This is necessary because all data regarding energy demand or energy supply is specified exclusively in level-1 cells.

As seen in Figure 3-29, most level-2 cells will consist of several level-1 cells. It is important to note, that no load flows within level-1 cells are considered. The network between level-1 cells, however, is the first target of the load flow calculation. The residual load of one specific level-2 cell is the result of balancing all corresponding level-1 cells, including possible losses within the level-1-network, dependent on load flow calculations. To transfer energy from superior cell level to a lower cell level or vice versa, a slack-node is used. Due to the chosen mathematical procedure, Newton–Raphson, only one slack-node can be used per cell to transfer energy from one cell level to another. However, each slack-node may have several network connections. Further properties of a level-2 cell, such as the current state of energy (SOE) and the operational status of existing hybrid elements, are the sum of all assigned level-1 cells. A level-3 cell represents the highest cell level and must contain all level-2 cells. It represents the overall system boundary. Analogous to the level-2 cell, the residual load of the level-3 cell is the result of the calculations in the level-2 domain. The remaining residual load in the level-3 cell has to be balanced from outside the system boundary, via the level-3 slack node.

According to the presented goal of the cellular approach in section 3.2, the target is to minimize the energy obtained from outside the system boundary and the maximum load flows over the level-3 slack node. Figure 3-29 displays an example of two possible scenarios for the application of the cellular approach in *HyFlow*, based on an electrical grid model. Example 1 uses single households as level-1 cells. All households in the area of a local grid transformer are aggregated into a level-2 cell, which is further summarized with all other level-2 cell to the total system boundary (level-3 cell), representing a city quarter. Example 2 shows another possible cell configuration. In this case, the lowest cell level represents a local grid transformer and the level two cells four different city quarters. All of them are aggregated into the superior level-3 cell, which represents a whole region, including the four city quarters.

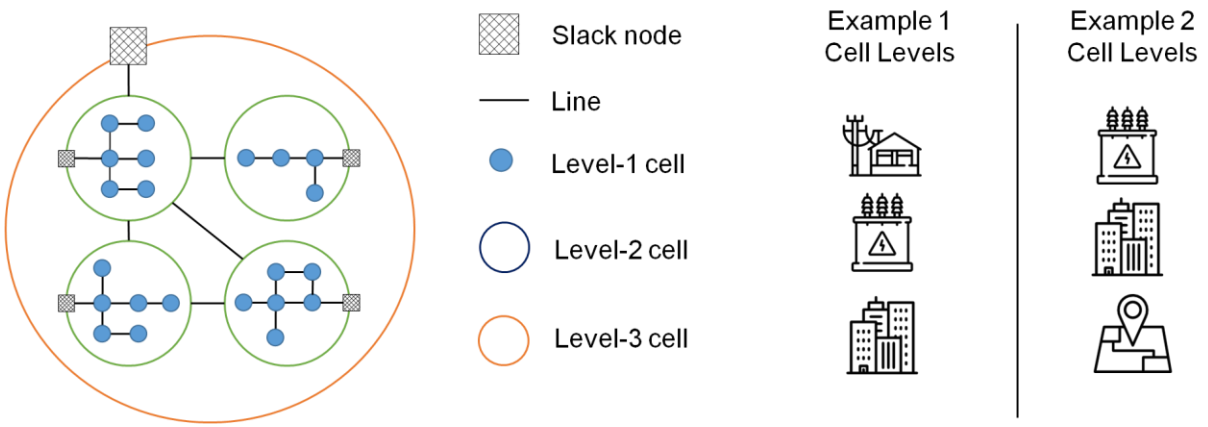

Figure 3-29: Implementation of cell levels in HyFlow and examples of cell representations for electricity grids

3.5.1 Modelling Framework Components

The following sections show how the most important system elements are characterized in *HyFlow*. The key components are the energy generation and demand, the energy storage units, and the hybrid elements necessary for the sector coupling and the grid connections.

3.5.2 Energy Generation/Demand

Energy generation and demand in *HyFlow* is implemented by the use of residual loads for each considered energy carrier (electricity, natural gas and district heating) and level-1 cell. The residual load is defined as power demand minus power generation as shown in Equation 3.1.

When considering all three implemented energy carriers, the usage of residual loads instead of separate data for production and demand allows the reduction from six necessary values to three values for each time-step. In the case of a negative residual load, the cell is a net energy producer, a positive residual load represents a net demand for energy. Each level-1 cell has to be defined for each time step and energy carrier before using *HyFlow*. A possible source for residual loads is either measured data, load or generation profiles. Level-2- and level-3 cells are not specified with generation or demand data as the residual loads in higher cell levels are solely the result of the calculations in *HyFlow*.

This introduced software architecture enables four calculation dimensions:

First, the energy carrier dimension with all major grid-bound energy carriers (electricity, natural gas and district heating). The associated input and output variables can be distinguished between nodal parameters and edge parameters. Nodal parameters are assigned to individual nodes, such as for instance the residual load $P_{Res,i}$, the nodal voltage U_i, nodal pressure p_i or the temperature T_i of a generic node i. Edge variables always refer to parameters between two nodes. Examples for edge parameters can be the load flow between the slack node S and node i, which is labelled as P_{Si}, or the load flow between any two nodes i and j, as indicated by the edge power flow P_{ij}.

The second dimension is the flexibility option dimension, which allows to control energy storage systems or hybrid elements. There is wide variety of potential operation strategies, depending on the objective function. These operation strategies can aim for a higher utilization of RES, for minimal cost, for higher DSS values or for preventing congestions in the grid infrastructure. Apart from a following external mathematical optimization, it is possible to implement customized control strategies into the modelling framework. Two control strategies are implemented in *HyFlow* at this stage, allowing for a cell-serving and system-serving behavior. Both control strategies are described in section 3.5.8 and 3.5.9. Within defined boundary conditions, they can freely operate the power of the associated energy storage unit P_{ESS} and the hybrid element P_{HE}, according to the implemented objective function.

The third dimension is the temporal dimension. Each time step is individually calculated, but the interval of the set time step and the number of calculated time steps can be defined by the user.

Finally, the fourth dimension is the selected spatial dimension. As described in the cellular approach in section 3.2 and more specifically illustrated in Figure 3-29, the modelling framework allows to calculate energy systems of different sizes. Additionally, the considered grid infrastructure of multiple levels (e.g. voltage levels, pressure levels) can be implemented in the energy system model at once. Table 3-4 illustrates the four dimensions and the corresponding node and edge types of the considered energy carriers.

Table 3-4: Regarded dimensions of the HyFlow modelling framework

		Node type/ operation strategy	Nodal input parameter	Nodal output parameter	Output edges
Energy carrier dimension	Electrical system	Slack node	$U_S; \theta_S$	$P_{S,el}$	$P_{Si,el}$
		Residual load node	$P_{Res,el,i}$	$U_i; \theta_i$	$P_{el,ij}$
	Natural gas system	Slack node	p_S	$P_{S,gas}$	$P_{Si,gas}$
		Residual load node	$P_{Res,gas,i}$	p_i	$P_{gas,ij}$
	District heating system	Slack node	p_S, T_S	$P_{S,heat}$	$P_{Si,heat}$
		Residual load node	$P_{Res,heat,i}$	p_i, T_i	$P_{heat,ij}$
Flexibility option dimension	Energy storage system	Cell serving o.s.	$P_{Res,cell}$	P_{ESS}	
		System serving o.s.	$P_{Res,system}$	P_{ESS}	
	Hybrid element	Cell serving o.s.	$P_{Res,cell}$	P_{HE}	
		System serving o.s.	$P_{Res,system}$	P_{HE}	
		Spatial dimension			
		Temporal dimension			

3.5.3 Grids

In order to perform LFC in all three energy carriers considered (as described in section 4.3), the network interconnections between the level-1 cells and the level-2 cells must also be characterized. The grid is used to overcome the fact that energy is often produced at a different location to where it is required. Since the properties of the networks vary for the individual energy carriers, the characterization differs among them, as seen in Table 3-5.

Table 3-5: Summarized input parameters of all load flow calculation types

Type of load flow calculation	Required Input parameters	Name	Type
Electricity LFC Option 1 (U, P)	Slack voltage	U_S	Scalar
	Line resistances	R_{ij}	Matrix
	Line lengths	L_{ij}	Matrix
	Residual loads of nodes	P_i	Vector
Electricity LFC Option 2 (θ, P)	Slack voltage angle	θ_S	Scalar
	Line resistances	R_{ij}	Matrix
	Line lengths	L_{ij}	Matrix
	Residual loads of nodes	P_i	Vector
Natural Gas LFC (p, P)	Slack pressure	p_S	Scalar
	Pipe lengths	L_{ij}	Matrix
	Pipe inner diameter	d_{ij}	Matrix
	Specific pipe friction	f_i	Matrix
	Residual loads of nodes	P_i	Vector
District heating LFC (p, P)	Slack pressure	p_S	Scalar
	Slack temperature	T_S	Scalar
	Nodal return temperature	T_{Ret}	Scalar
	Pipe lengths	L_{ij}	Matrix
	Pipe inner diameter	d_{ij}	Matrix
	Specific pipe friction	f_i	Matrix
	Residual loads of nodes	P_i	Vector
	Thermal transmittance	k	Scalar

A similarity for all energy carriers is the method grid-interconnections are characterized. This works through a linkage matrix. When there is a direct connection between cells, the linkage matrix L shows the value 1, if there is no direct connection, the value is 0. In practice, linkage matrices are not limited to the values 0 and 1, but are used for important characterization values already, depending on the specific energy carrier. This means that for an electricity grid, the matrix used contains the assigned length, reactance or resistance of the power line. This helps to compress necessary input data for the LFC (to be done in the subsequent step) into a single matrix, as illustrated in the example shown in Figure 3-31. The heating – and natural gas grid use different input matrices. The relevant data for heating grids are the length, inner diameter of the pipes, thermal conductivity and surface roughness. Water is considered to be the heat transfer medium and temperature-dependent differences in density and viscosity are neglected. Natural gas grids use the same characterization data, without the thermal conductivity as heat losses are not considered in this type of grid. The detailed description of the LFC is presented in the following sections. Table 3-5 summarizes the necessary input values for all implemented load flow calculation methods.

The LFC differ between energy carriers. However, it was important in the creation of *HyFlow* to work with equivalent mathematical procedures in order to link the energy carriers and allow the calculations to work with acceptable computational times. All LFC are solved with the help of the Newton-Raphson approach. While the main input parameters of all LFC are summarized in Table 3-5, all parameters for the iterative Newton-Raphson methodology are presented in Table 3-4. The following sections describe the procedure of the load flow calculations for electricity, natural gas and district heating and point out the similarities among them.

3.5.4 Electrical load flow calculation – Option 1

As described in section 2.3.1, there are various possibilities to describe the load flow in electricity grids. Due to the stated reasons, the DC-LFC is selected as the model of choice for the tasks at hand. Since *HyFlow* is designed to work in use cases of a wide range of scales, two different DC-LFC methods are implemented. The user has to evaluate both options for the particular use case, in order to select the most adequate version. First, a calculation method for low voltage grids with a low X/R ratio is presented. This approach corresponds to a grid, which is operated in DC. In order to illustrate all LFC methodologies in the most understandable way, all theoretic explanations are supplemented by calculation examples of a simple network after the generic description.

The following equations describe complex variables of the AC load flow calculation for cell-voltage $\underline{\mathrm{U}}_i$, current $\underline{\mathrm{I}}_i$ and admittance $\underline{\mathrm{Y}}_{ij}$ between cells. The admittance is defined as the inverse of impedance.

$$\underline{\mathrm{U}}_i = \left[\underline{U}_1 \dots \underline{U}_i \dots \underline{U}_n\right]^T \tag{3-40}$$

$$\underline{\mathrm{I}}_i = \left[\underline{I}_1 \dots \underline{I}_i \dots \underline{I}_n\right]^T \tag{3-41}$$

$$\underline{\mathrm{Y}}_{ij} = \frac{1}{\underline{\mathrm{Z}}_{ij}} = \begin{bmatrix} \mathrm{Y}_{11} & \cdots & \mathrm{Y}_{1n} \\ \vdots & \ddots & \vdots \\ \mathrm{Y}_{n1} & \cdots & \mathrm{Y}_{nn} \end{bmatrix} \tag{3-42}$$

Equation 3-43 describes the dependence between admittance $\underline{\mathrm{Y}}_{ij}$, node voltage $\underline{\mathrm{U}}_i$ and node current $\underline{\mathrm{I}}_i$.

$$\underline{\mathrm{I}}_i = \sum_{j=1}^{n} \underline{\mathrm{Y}}_{ij} \cdot \underline{\mathrm{U}}_i \tag{3-43}$$

The complex apparent power $\underline{\mathrm{S}}_i$ can be calculated by multiplying node voltage $\underline{\mathrm{U}}_i$ by the conjugated complex node current $\underline{\mathrm{I}}_i^*$. By using Equation 3-44, the complex apparent power $\underline{\mathrm{S}}_i$ can be calculated as follows:

$$\underline{\mathrm{S}}_i = \underline{\mathrm{U}}_i \cdot \underline{\mathrm{I}}_i^* = \underline{\mathrm{U}}_i \cdot \left(\sum_{j=1}^{n} \underline{\mathrm{Y}}_{ij} \cdot \underline{\mathrm{U}}_j \right)^* \tag{3-44}$$

Up to this point, the equations are valid for both AC and DC applications. Considering a DC network, the following modifications need to be applied: all imaginary parts of the node current $\underline{\mathrm{I}}_i$, node voltage $\underline{\mathrm{U}}_i$ and admittance $\underline{\mathrm{Y}}_{ij}$ are neglected. This means that no reactive power is considered and the apparent power equals the active power.

$$Im\left(\underline{\mathrm{I}}_i, \underline{\mathrm{U}}_i, \underline{\mathrm{Y}}_{ij}\right) = 0 \tag{3-45}$$

Applying Equation 3-44 to Equation 3-45, the node power P_i and edge power P_{ij} can be calculated according to Equation 3-46. It has to be noted that it is important to distinguish between nodal variables and edge variables. Nodal variables, such as the node power are

related to the residual load of the corresponding node. Edge powers are for example related to load flows between two nodes, due to the voltage difference between two node voltages.

$$P_{ij} = \underline{U_i}\left(\underline{U_j} - \underline{U_i}\right) * \underline{Y_{ij}} \tag{3-46}$$

Since the active power P_{ij} stated in Equation 3-46 does not follow a linear function, a Newton-Raphson Solver is used for solving the equation. A step by step calculation for a simple numerical example, including all steps of the Newton-Raphson methodology, is presented in the following section.

Calculation Example of Electrical load flow – Option 1

This electrical load flow calculation option can be applied to networks with a predominant share of ohmic resistance and small reactance. This implies that the reactances and the voltage angle between the nodes are neglected, while active power losses of power lines are considered in this option. Figure 3-30 illustrates a small electrical grid with a slack node, four consumer/generation nodes and the corresponding interconnections. The residual loads of all nodes P_i are available for the exemplary time-step, as well as the slack voltage U_S and the grid characteristics in the form of the specific resistance R_{ij} and the corresponding length L_{ij}. In order to calculate the active power flows between the nodes P_{ij}, the corresponding active power losses $P_{Loss,ij}$ and the overall residual power of the slack node P_S, the node voltages U_i have to be determined. Additionally, the abort conditions for the nominal fault tolerance and the maximum number of iteration steps have to be defined in *HyFlow* as well. In the following paragraphs, this procedure is explained step by step with the numeric values based on the grid example of Figure 3-30, and the flow chart presented in Figure 3-32.

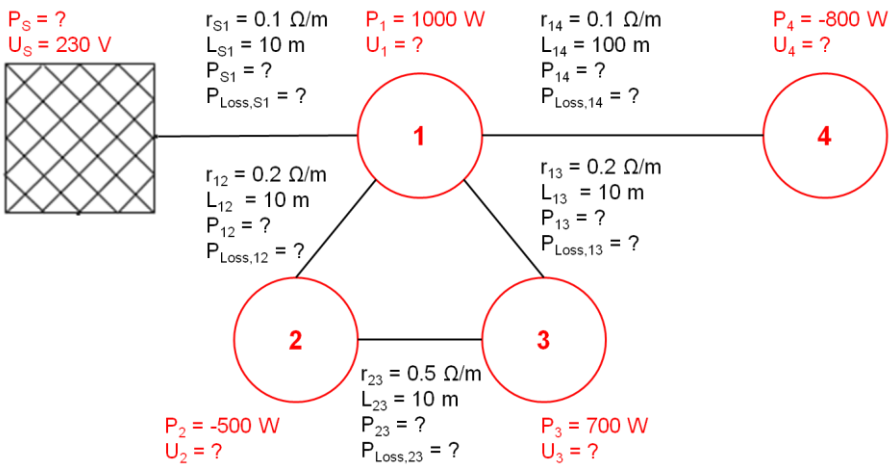

Figure 3-30: Exemplary grid for the first electric load flow calculation version

First of all, the linkage matrix L is set up to show whether a direct connection between two nodes exists. Zero stands for no connection and 1 represents a direct connection. To characterize the grid for this version of electrical load flow calculation, two parameters are needed: the specific resistance value r_{ij} and the corresponding length L_{ij}. Equation 3-47 shows the formula, that leads to the nominal resistance R_{ij} of the connection.

$$R_{ij} = r_{ij} \cdot L_{ij} \tag{3-47}$$

The left part of Figure 3-31 shows the results of the resistance matrix for all grid connections. Due to the number of 25 values in the matrix, the detailed explanations are limited to the grid connections of node 1, which is marked in blue. Additionally, the nodal admittance matrix $\underline{Y}$, which is solely derived from the resistance matrix R, is presented on the basis of node 1. It has to be noted that the sum of all nodal admittances has to be zero, which can also be seen in the nodal admittance matrix $\underline{Y}$ in Figure 3-31.

$$R_{1S} = r_{1S} \cdot L_{1S} = 0.1 \cdot 10 = 1\ \Omega$$

$$R_{12} = r_{12} \cdot L_{12} = 0.2 \cdot 10 = 2\ \Omega$$

$$R_{13} = r_{13} \cdot L_{13} = 0.2 \cdot 10 = 2\ \Omega$$

$$R_{14} = r_{14} \cdot L_{14} = 0.1 \cdot 100 = 10\ \Omega$$

L =

	S	1	2	3	4
S	0	1	0	0	0
1	1	0	1	1	1
2	0	1	0	1	0
3	0	1	1	0	0
4	0	1	0	0	0

R =

	S	1	2	3	4
S	0	1	0	0	0
1	1	0	2	2	10
2	0	2	0	5	0
3	0	2	5	0	0
4	0	10	0	0	0

Y =

	S	1	2	3	4
S	1	-1	0	0	0
1	-1	2.1	-0.5	-0.5	-0.1
2	0	-0.5	0.7	-0.2	0
3	0	-0.5	-0.2	0.7	0
4	0	-0.1	0	0	0.1

Figure 3-31: The stages of the coupling matrices. The simple linkage matrix (left), the resistance matrix (center) and the admittance matrix (right). The values marked in blue are calculated in the numeric examples.

$$\underline{Y}_{ij} = \frac{1}{\underline{Z}_{ij}} = \frac{1}{R_{ij} + jX_{ij}} \tag{3-48}$$

$$Y_{1S} = -\frac{1}{R_{1S}} = -\frac{1}{1} = -1$$

$$Y_{11} = \frac{1}{R_{1S}} + \frac{1}{R_{12}} + \frac{1}{R_{12}} + \frac{1}{R_{14}} = \frac{1}{1} + \frac{1}{2} + \frac{1}{2} + \frac{1}{10} = 2.1$$

$$Y_{12} = -\frac{1}{R_{12}} = -\frac{1}{2} = -0.5$$

$$Y_{13} = -\frac{1}{R_{12}} = -\frac{1}{2} = -0.5$$

$$Y_{14} = -\frac{1}{R_{14}} = -\frac{1}{10} = -0.1$$

After characterizing the grid connection via nodal admittance matrix, the residual load P_i has to be imported according to the users' specification in Excel. In this demonstration, only one time-step is calculated. The residual powers are listed underneath, along with the nominal voltage of the slack node U_S. All values are illustrated in Figure 3-30.

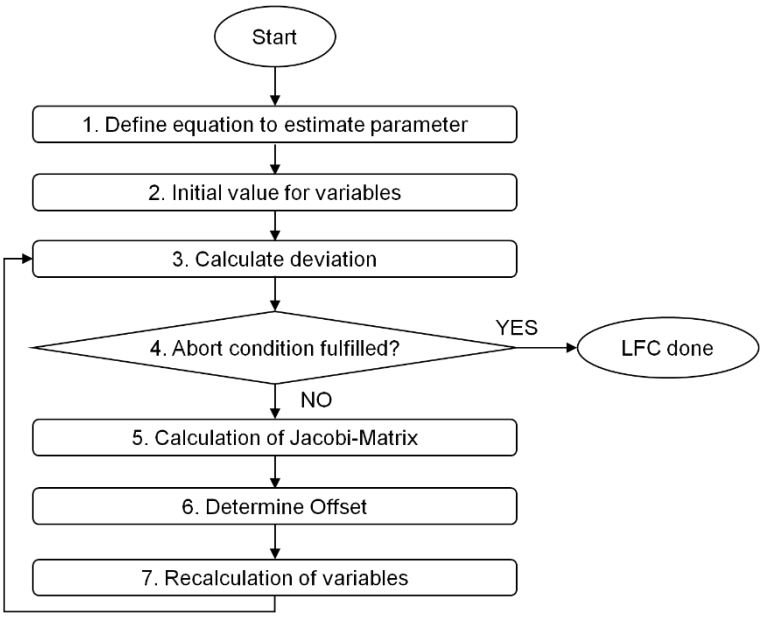

Figure 3-32: **Flow chart of the DC load flow calculation to model the electrical grid**

To start the iterative process according to Figure 3-32 (flow chart), the nodal power balances need to be defined. In order to solve these equations, a value for all nodal voltages needs to be initialized. In *HyFlow*, the current value is set to 98 % of the slack voltage U_S. To keep it simple, the numerical values are only presented for node 1 again, while all other nodes are presented with the final result only. As one can see, the result of the first node is coincidentally already very precise, while all the other nodes have a result of 0 W, and are far from the known residual loads in the respective node. This is due to the fact, that none of the other nodes has a direct connection to the slack node and all other power flows are cancelled out due to the same starting voltages of the connected nodes.

$P_{1,known} = 1000\ W;\ P_{2,known} = -500\ W;\ P_{1,known} = 700\ W;\ P_{1,known} = -800\ W$

$U_S = 230\ V$

$$U_{1,Start} = U_{1,[t0]} = U_{2,[t0]} = U_{3,[t0]} = U_{4,[t0]} = 0.98 \cdot U_S = 225.4\ V$$

$$P_1 = U_1 \cdot (U_S \cdot Y_{S1} + U_1 \cdot Y_{11} + U_2 \cdot Y_{12} + U_3 \cdot Y_{13} + U_4 \cdot Y_{14})$$

$$P_{1,[t0]} = 225.4 \cdot (230 \cdot (-1) + 225.4 \cdot 2.1 + 225.4 \cdot (-0.5) + 225.4 \cdot (-0.5) + 225.4 \cdot (-0.1) = -1036.8\ W$$

$$P_{2,[t0]} = U_2 \cdot (U_S \cdot Y_{S2} + U_1 \cdot Y_{12} + U_2 \cdot Y_{22} + U_3 \cdot Y_{23} + U_4 \cdot Y_{24}) = 0\ W$$

$$P_{3,[t0]} = U_3 \cdot (U_S \cdot Y_{S3} + U_1 \cdot Y_{13} + U_2 \cdot Y_{23} + U_3 \cdot Y_{33} + U_4 \cdot Y_{34}) = 0\ W$$

$$P_{4,[t0]} = U_4 \cdot (U_S \cdot Y_{S4} + U_1 \cdot Y_{14} + U_2 \cdot Y_{24} + U_3 \cdot Y_{34} + U_4 \cdot Y_{44}) = 0\ W$$

The error between the calculated nodal power and the known specified nodal power is calculated as follows:

$$error_{1,[t0]} = -P_{1,known} - P_{1,[t0]} = -1000 - (-1036.8) = 36.8$$

$$error_{2,[t0]} = -P_{2,known} - P_{2,[t0]} = -(-500) - 0 = 500$$

$$error_{3,[t0]} = -P_{3,known} - P_{3,[t0]} = -700 - 0 = -700$$

$$error_{4,[t0]} = -P_{4,known} - P_{4,[t0]} = -(-800) - 0 = 800$$

The next step is to set up the Jacobi matrix J. It contains the partially derived nodal powers as illustrated below. The origin of numeric values is only presented for the selected power in node 1.

$$J = \frac{\partial P}{\partial U} = \begin{bmatrix} \frac{\partial P_1}{\partial U_1} & \frac{\partial P_1}{\partial U_2} & \frac{\partial P_1}{\partial U_3} & \frac{\partial P_1}{\partial U_4} \\ \frac{\partial P_2}{\partial U_1} & \frac{\partial P_2}{\partial U_2} & \frac{\partial P_2}{\partial U_3} & \frac{\partial P_2}{\partial U_4} \\ \frac{\partial P_3}{\partial U_1} & \frac{\partial P_3}{\partial U_2} & \frac{\partial P_3}{\partial U_3} & \frac{\partial P_3}{\partial U_4} \\ \frac{\partial P_4}{\partial U_1} & \frac{\partial P_4}{\partial U_2} & \frac{\partial P_4}{\partial U_3} & \frac{\partial P_4}{\partial U_4} \end{bmatrix} = \begin{bmatrix} 468.7 & -112.7 & -112.7 & -22.5 \\ -112.7 & 157.8 & -45.1 & 0 \\ -112.7 & -45.1 & 157.8 & 0 \\ -22.5 & 0 & 0 & 22.5 \end{bmatrix}$$

If the equation for the power balance in node 1 is derived from the nodal voltages, the following equations and results can be observed:

$$\frac{\partial P_1}{\partial U_1} = (U_S \cdot Y_{S1} + 2 \cdot U_1 \cdot Y_{11} + U_2 \cdot Y_{12} + U_3 \cdot Y_{13} + U_4 \cdot Y_{14})$$

$$\frac{\partial P_1}{\partial U_1} = \big(230 \cdot (-1) + 2 \cdot 225.4 \cdot 2.1 + 225.4 \cdot (-0.5) + 225.4 \cdot (-0.5) + 225.4 \cdot (-0.1)\big)$$
$$= 468.7\text{A}$$

$$\frac{\partial P_1}{\partial U_2} = U_1 \cdot Y_{12} = 225.4 \cdot (-0.5) = -112.7\ A$$

$$\frac{\partial P_1}{\partial U_3} = U_1 \cdot Y_{13} = 225.4 \cdot (-0.5) = -112.7\ A$$

$$\frac{\partial P_1}{\partial U_4} = U_1 \cdot Y_{14} = 225.4 \cdot (-0.1) = -22.5\ A$$

The inverted Jacobi matrix J^{-1} is now multiplied with the vector of all nodal power errors, as calculated earlier. The result can be seen underneath:

$$offset_i = J^{-1} * error_i$$

$$offset_{t1} = \begin{bmatrix} 45.3 & 45.3 & 45.3 & 45.3 \\ 45.3 & 114.3 & 65.0 & 45.3 \\ 45.3 & 65.0 & 114.3 & 45.3 \\ 45.3 & 45.3 & 45.3 & 22.5 \end{bmatrix} \cdot 10^{-4} \cdot \begin{bmatrix} 36.8 \\ 500 \\ -700 \\ 800 \end{bmatrix} = \begin{bmatrix} 2.88 \\ 4.95 \\ -0.96 \\ 38.38 \end{bmatrix} V$$

The determined offsets are in the unit of volts, which can now be added to the previous nodal voltages from the beginning of this process. Since this is the first iteration, it is added to the starting voltages.

$$\begin{bmatrix} U_{1,[t0]} \\ U_{2,[t0]} \\ U_{3,[t0]} \\ U_{4,[t0]} \end{bmatrix} + offset_{t1} = \begin{bmatrix} U_{1,[t1]} \\ U_{2,[t1]} \\ U_{3,[t1]} \\ U_{4,[t1]} \end{bmatrix}$$

$$\begin{bmatrix} 225.4 \\ 225.4 \\ 225.4 \\ 225.4 \end{bmatrix} + \begin{bmatrix} 2.88 \\ 4.95 \\ -0.96 \\ 38.38 \end{bmatrix} = \begin{bmatrix} 228.28 \\ 230.35 \\ 224.44 \\ 263.78 \end{bmatrix}$$

With these new nodal voltages, the whole process starts from the nodal power balances again. This whole process is stopped, as soon as the exit condition is stopped. The term of the exit condition is a certain margin of error, that all nodal powers need to fulfill in order to terminate the iteration process.

To illustrate the approximation process, the following Table 1 shows how the nodal powers, the nodal voltages and the error margin develops from iteration step to step. It usually takes around five iteration steps to reach a very precise numeric result below 0.001 %.

Table 3-6: Voltage of all four nodes from the exemplary grid shown in Figure 3-30 and the error of the nodal corresponding nodal powers for all five iteration steps.

Parameter	Unit	Iteration 0	Iteration 1	Iteration 2	Iteration 3	Iteration 4
U_1	V	225.40	228.28	227.76	227.75	227.75
U_2	V	225.40	230.35	229.75	229.75	229.75
U_3	V	225.40	224.44	223.86	223.85	223.85
U_4	V	225.40	263.78	258.76	258.68	258.68
$error_1$	W	36.84	-0.64	$-6.76 \cdot 10^{-3}$	$-1.50 \cdot 10^{-6}$	$7.39 \cdot 10^{-12}$
$error_2$	W	500.00	-10.99	$-2.51 \cdot 10^{-2}$	$-2.61 \cdot 10^{-7}$	$2.22 \cdot 10^{-12}$
$error_3$	W	-700.00	-2.98	$-1.23 \cdot 10^{-2}$	$-1.43 \cdot 10^{-6}$	$2.05 \cdot 10^{-12}$
$error_4$	W	-800.00	-136.21	-2.25	$-6.52 \cdot 10^{-4}$	$-5.39 \cdot 10^{-11}$

Once all the node voltages are determined and the calculated nodal powers are aligned with the set residual loads of the users, the load flows between the nodes can be easily determined. The only needed variables are both nodal voltages and the linked admittance, as presented earlier in the nodal admittance matrix. The results are illustrated in Figure 3-33

$$P_{S1} = U_S \cdot (U_1 - U_S) \cdot Y_{S1} = 230 \cdot (227.8 - 230) \cdot (-1) = 517.2\ W$$

$$P_{12} = U_1 \cdot (U_2 - U_1) \cdot Y_{12} = 227.8 \cdot (229.8 - 227.8) \cdot (-0.5) = -227.2\ W$$

$$P_{13} = U_1 \cdot (U_3 - U_1) \cdot Y_{13} = 227.8 \cdot (223.9 - 227.8) \cdot (-0.5) = 443.8\ W$$

$$P_{14} = U_1 \cdot (U_4 - U_1) \cdot Y_{14} = 227.8 \cdot (258.7 - 227.8) \cdot (-0.1) = -704.4\ W$$

$$P_{23} = U_2 \cdot (U_3 - U_2) \cdot Y_{23} = 229.8 \cdot (223.9 - 229.8) \cdot (-0.2) = 270.8\ W$$

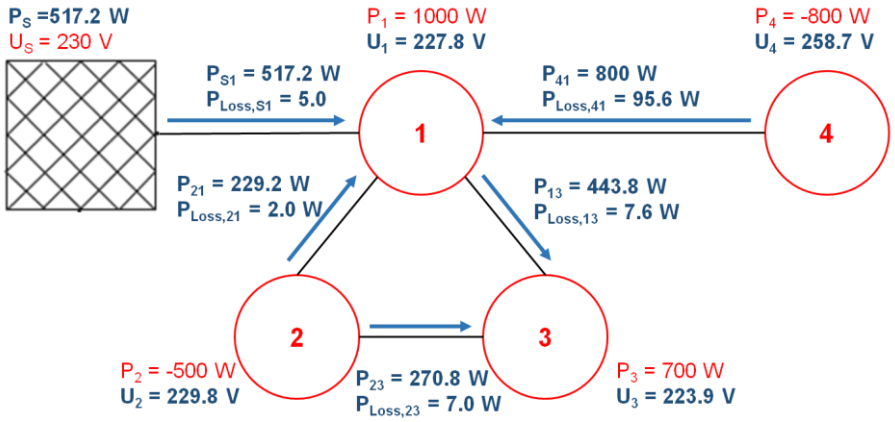

Figure 3-33: Resulting load flows after the described iterative calculation process

It has to be noted, that in this case $P_{ij} \neq P_{ji}$ due to the different reference voltage levels. Negative values of P_{ij} indicate a power flow that this is an incoming power flow to the node P_i, which means that the absolute value $|P_{ij}|$ is smaller than $|P_{ji}|$. The difference between these two power flows is equal to the occurring losses. This is presented on the example of the load flow between the slack node and node 1.

$$P_{S1} = U_S \cdot (U_1 - U_S) \cdot Y_{S1} = 230 \cdot (227.8 - 230) \cdot (-1) = 517.2\ W$$

$$P_{1S} = U_1 \cdot (U_S - U_1) \cdot Y_{S1} = 227.8 \cdot (230 - 227.8) \cdot (-1) = -512.2\ W$$

$$P_{Loss,S1} = |P_{S1}| - |P_{1S}| = 5.0\ W$$

Alternatively, the power losses derived from Ohm's law can be used to calculate the losses with the same result as stated before. It can therefore also be used to test the results.

$$P_{Loss,S1} = I_{S1}^2 \cdot R_{S1} = ((U_1 - U_S) \cdot Y_{S1})^2 \cdot R_{S1}$$

$$P_{Loss,S1} = ((227.8 - 230) \cdot (-1))^2 \cdot 1 = 5.0\ W$$

The slack node is calculated by adding all powers connected to it. In this case, the only slack connection is to node 1. Additionally, the slack power has to match the sum of all residual loads added by the sum of all occurring losses.

$$P_S = P_{S1} = 517.2\ W$$

$$P_S = P_1 + P_2 + P_3 + P_4 + P_{Losses}$$

$$P_S = 1000 + (-500) + 700 + (-800) + 117.2 = 517.2\ W$$

3.5.5 Electrical load flow calculation – Option 2

The second (regular) DC-LFC method is a standard approach, as described in van Hertem et al. [44], based on the theoretical work presented of Andersson et al. [59]. The simplifications of the DC-LFC, as described in section 2.3.1 are the foundation of the second calculation methodology. It is ideally used for high voltage grids with a high X/R ratio, to minimize model-related deviations. As explained in the literature part in section 2.3.1, the X/R ratio plays an important role in order to select the appropriate LFC methodology. If X is far greater than R, the voltage drop caused by ohmic resistances can be neglected and the power transport between two nodes is driven by the voltage angle difference between them θ_{ij}. However, for grids with a large share of ohmic resistance compared to the reactances, the active power transport is induced by the voltage differenc between two nodes U_{ij}.

$$\frac{\mathrm{X}}{R} \gg 1 \;\rightarrow\; \Delta\mathrm{U} \sim 0 \qquad\qquad \frac{\mathrm{X}}{R} \ll 1 \;\rightarrow\; \Delta\theta \sim 0$$

There are many analogies to the first electrical LFC method. However, the nodal voltage vector stated in Equation 3-40 is substituted by the nodal angle vector in order to calculate the nodal power vector.

$$\theta_i = [\theta_1 \dots \theta_i \dots \theta_n]^T \tag{3-49}$$

The admittance matrix is calculated analogously to the low voltage electrical load flow calculation methodology. The only difference between the two options is the negligence of R_{ij}, which makes the admittance between two nodes $\underline{Y}_{ij}$ solely dependent on the reciprocal reactance X_{ij} between them.

$$\underline{Y}_{ij} = \frac{1}{\underline{Z}_{ij}} = \frac{1}{R_{ij} + jX_{ij}} \triangleq \frac{1}{jX_{ij}} \tag{3-50}$$

Once the voltage angle matrix and the admittance matrix are set up, the electrical load flow between node i and j is defined as follows:

$$P_{ij} = \frac{\theta_{ij}}{X_{ij}} \tag{3-51}$$

After the determination of the edge load flows between the nodes P_{ij}, a power balance is set up for every node. The resulting residual load of a node P_i can be determined by adding all edge power flows from and to the node.

This is formulated in Equation 3-52.

$$P_i = \sum_{j=1}^{n} P_{ji} \tag{3-52}$$

Once the nodal powers to be calculated are determined, they are compared to the known residual loads that need to be specified for all nodes. If there is a deviation between both powers larger than the defined abort condition, a new iteration step starts. The detailed iteration process with the additional description of initial parameters and the usage of the Newton-Raphson methodology follows in the calculation example underneath.

Calculation Example of Electrical load flow – Option 2

The second implemented option for electrical load flow calculations is based on the standard DC load flow methodology described in Anderson et al. [59]. It has a lot in common with the first described method. A summary of the assumptions derived from the AC-LFC and the corresponding assumptions are presented in section 2.3.1. In this type of LFC, the user needs to specify the network interconnections and the corresponding line reactances, as well as the residual loads of the specified nodes and a reference voltage angle at the slack node. One can say that the nominal voltage is substituted with the voltage angle as a driving force of the load flows and instead of using line resistances, one uses the corresponding reactances. The numeric calculation is only presented in detail for calculation steps that differ from the first option.

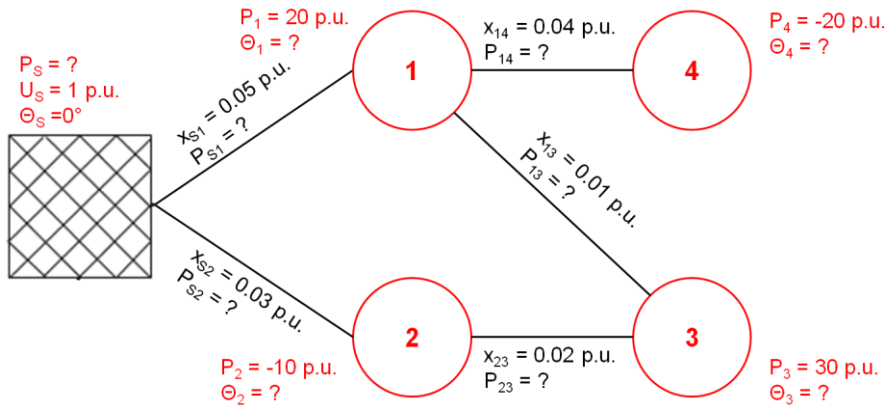

Figure 3-34: Exemplary grid for the second electric load flow calculation option

The first step is to calculate the admittance matrix from the reactances of the line connections. This step is equal to the first version of the load flow calculation, with one small difference: The reactances are stated in per unit. The results can be seen in the linkage matrix, the reactance matrix and the admittance matrix in Figure 3-35.

$$L = \begin{array}{c|ccccc} & S & 1 & 2 & 3 & 4 \\ S & 0 & 1 & 1 & 0 & 0 \\ 1 & 1 & 0 & 0 & 1 & 1 \\ 2 & 1 & 0 & 0 & 1 & 0 \\ 3 & 0 & 1 & 1 & 0 & 0 \\ 4 & 0 & 1 & 0 & 0 & 0 \end{array} \quad x = \begin{array}{c|ccccc} & S & 1 & 2 & 3 & 4 \\ S & 0 & 0.05 & 0.03 & 0 & 0 \\ 1 & 0.05 & 0 & 0 & 0.01 & 0.04 \\ 2 & 0.03 & 0 & 0 & 0.02 & 0 \\ 3 & 0 & 0.01 & 0.02 & 0 & 0 \\ 4 & 0 & 0.04 & 0 & 0 & 0 \end{array} \quad \underline{y} = \begin{array}{c|ccccc} & S & 1 & 2 & 3 & 4 \\ S & 53 & -20 & -33 & 0 & 0 \\ 1 & -20 & 145 & 0 & -100 & -25 \\ 2 & -33 & 0 & 83 & -50 & 0 \\ 3 & 0 & -100 & -50 & 150 & 0 \\ 4 & 0 & -25 & 0 & 0 & 25 \end{array}$$

Figure 3-35: The stages of the coupling matrices. The simple linkage matrix (left), the reactance matrix (center) and the admittance matrix (right).

Apart from the grid specifications in the form of the line reactances, the residual power of all nodes needs to be known. Since the reactance is given in per unit, the nodal powers are also given in per unit. The conversion in nominal units is necessary at the end of this example, because it is important to determine whether the maximum current carrying capacity I_{therm} is exceeded or not. Additionally, the voltage angle of the slack node is set to 0 by default. The initial guess for the voltage angles of all other nodes is specified with the help of a random number. This random value varies between 0 – 5° and is added to the set slack node voltage. All starting voltage angles, therefore, differ between 0 – 5°.

$$p_{1,known} = 20\ p.u.;\ p_{2,known} = -10\ p.u;\ p_{3,known} = 30\ p.u;\ p_{4,known} = -20\ p.u$$

$$\theta_S = 0°$$

$$\theta_{i,Start} = \theta_{i,[t0]} = \theta_S + rand(5)$$

In this example, the starting voltage of the four nodes are determined as follows:

$$\theta_{1,[t0]} = 2.11°;\ \theta_{2,[t0]} = 4.58°;\ \theta_{3,[t0]} = 3.96°;\ \theta_{1,[t0]} = 4.80°$$

The next step in this type of electrical load flow calculation method is to establish the resulting load flows between the nodes. This works as follows:

$$p_{S1} = \frac{\theta - \theta_S}{x_{S1}} = \frac{2.11 - 0}{0.05} = 42.2\ p.u.$$

The results for all other calculated power transports between the connected nodes of the first iteration steps are calculated analogous and can be seen underneath. In contrast to the first calculation methodology $|p_{ij}| = |p_{ji}|$ since no power losses occur along the lines.

$$p_{S2,[t0]} = 152.6\ p.u;\ p_{13,[t0]} = 185.2\ p.u;\ p_{14,[t0]} = 67.2\ p.u; p_{23,[t0]} = -30.9\ p.u$$

Afterwards a nodal power balance is set up covering all power inputs and outputs of a node.

$$p_1 = \sum p_{S1} + p_{21} + p_{31} + p_{41}$$

$$p_1 = \sum 42.2 + 0 + (-185.2) + (-67.2) = -210.3$$

The equivalent results for all other nodes are:

$$p_{S,[t0]} = -194.8\ p.u.;\ p_{2,[t0]} = 183.5\ p.u;\ p_{3,[t0]} = 154.3\ p.u;\ p_{4,[t0]} = 67.2\ p.u$$

Once the nodal powers of the first iteration steps are determined, the corresponding error between the calculated nodal powers and the known nodal powers can be calculated analogously to the first load flow methodology. The numeric calculation is shown for the first node, the results for all other nodes are listed underneath.

$$error_{i,[t0]} = p_{i,known} - p_{1,[t0]}$$

$$error_{1,[t0]} = -p_{1,known} - p_{1,[t0]} = 20 - (-210.3) = 230.3\ p.u.$$

$$error_{2,[t0]} = -193.5\ p.u.;\ error_{3,[t0]} = -124.3\ p.u;\ error_{4,[t0]} = -87.2\ p.u;$$

Analogous to the first load flow calculation, a Jacobi matrix needs to be formulated. Instead of partially deriving the nodal powers with respect to the nodal voltages, they are derived with respect to the corresponding voltage angles.

$$J = \frac{\partial p}{\partial \theta} = \begin{bmatrix} \frac{\partial p_1}{\partial \theta_1} & \frac{\partial p_1}{\partial \theta_2} & \frac{\partial p_1}{\partial \theta_3} & \frac{\partial p_1}{\partial \theta_4} \\ \frac{\partial p_2}{\partial \theta_1} & \frac{\partial p_2}{\partial \theta_2} & \frac{\partial p_2}{\partial \theta_3} & \frac{\partial p_2}{\partial \theta_4} \\ \frac{\partial p_3}{\partial \theta_1} & \frac{\partial p_3}{\partial \theta_2} & \frac{\partial p_3}{\partial \theta_3} & \frac{\partial p_3}{\partial \theta_4} \\ \frac{\partial p_4}{\partial \theta_1} & \frac{\partial p_4}{\partial \theta_2} & \frac{\partial p_4}{\partial \theta_3} & \frac{\partial p_4}{\partial \theta_4} \end{bmatrix} = \begin{bmatrix} 145 & 0 & -100 & -25 \\ 0 & 83 & -50 & 0 \\ -100 & -50 & 150 & 0 \\ -25 & 0 & 0 & 25 \end{bmatrix}$$

The calculation of the elements of the first row (node 1) in the Jacobi matrix is pointed out in detail underneath, while all other numeric results are stated above.

$$J_{11} = \frac{\partial p_1}{\partial \theta_1} = \frac{1}{x_{S1}} + \frac{1}{x_{13}} + \frac{1}{x_{14}} = \frac{1}{0.05} + \frac{1}{0.01} + \frac{1}{0.04} = 145\ p.u.$$

$$J_{13} = \frac{\partial p_1}{\partial \theta_3} = -\frac{1}{x_{13}} = -\frac{1}{0.01} = -100\ p.u.$$

$$J_{14} = \frac{\partial p_1}{\partial \theta_3} = -\frac{1}{x_{14}} = -\frac{1}{0.04} = -25\ p.u.$$

According to the Newton-Raphson methodology, the Jacobi matrix is inverted and multiplied with the previously calculated $error_i$, to obtain the voltage angle $offset_i$.

$$offset_i = J^{-1} * error_i$$

$$offset_{[t0]} = \begin{bmatrix} 2.73 & 1.36 & 2.27 & 2.73 \\ 1.36 & 2.18 & 1.64 & 1.36 \\ 2.27 & 1.64 & 2.73 & 2.27 \\ 2.73 & 1.36 & 2.27 & 6.73 \end{bmatrix} \cdot 10^{-2} \cdot \begin{bmatrix} 230.3 \\ -193.5 \\ -124.3 \\ -87.2 \end{bmatrix} = \begin{bmatrix} -1.56 \\ -4.31 \\ -3.31 \\ -5.05 \end{bmatrix}°$$

The $offset_i$ is added to the voltage angles of the current iteration step to get the new voltage angles for the next time step.

$$\begin{bmatrix} \theta_{1,[t0]} \\ \theta_{2,[t0]} \\ \theta_{3,[t0]} \\ \theta_{4,[t0]} \end{bmatrix} + offset_{[t0]} = \begin{bmatrix} \theta_{1,[t1]} \\ \theta_{2,[t1]} \\ \theta_{3,[t1]} \\ \theta_{4,[t1]} \end{bmatrix}$$

$$\begin{bmatrix} 2.11 \\ 4.58 \\ 3.96 \\ 4.80 \end{bmatrix} + \begin{bmatrix} -1.56 \\ -4.31 \\ -3.31 \\ -5.05 \end{bmatrix} = \begin{bmatrix} 0.55 \\ 0.27 \\ 0.65 \\ -0.25 \end{bmatrix}°$$

In this simple exemplary case, the new voltage angles lead to already very precise nodal powers according to Equation 3-52. The obtained $error$ of the known and calculated nodal power with the stated voltage angles is in the range of 10^{-14}, which is way below the set abort condition of 10^{-4} p.u. This means, that the stated voltage angles are already the end results. The speed of convergence of this calculation option proved to be the fastest among all implemented load flow calculations. Figure 3-36 graphically displays the end result of this example. In order to ensure that no power line exceeds the allowed load flow, it is necessary to determine the actual current in the power lines with the help of Ohm's linear law. For this purpose, it is necessary to retransfer the per unit values into SI units and compare the obtained currents I_{ij} with the maximum current carrying capacity I_{therm} of the corresponding power line.

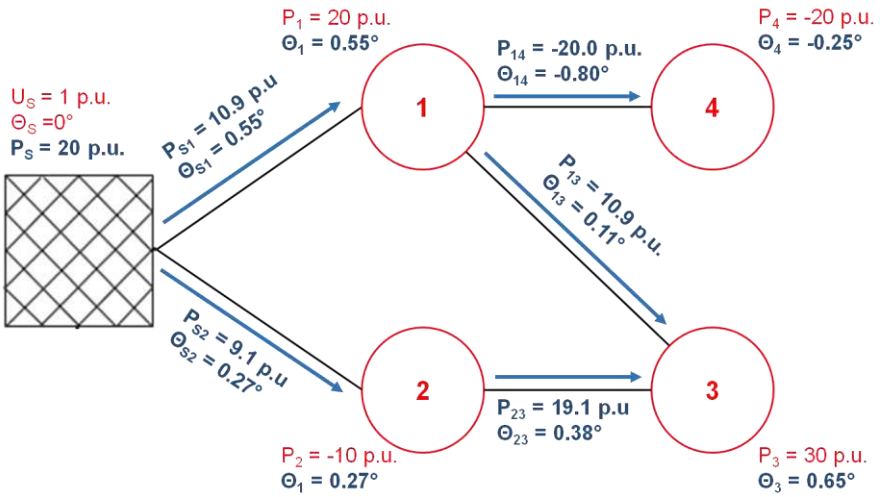

Figure 3-36: Resulting load flows after the described iterative calculation process

3.5.6 Natural Gas load flow calculations

The natural gas load flow calculation is based on known residual loads of all nodes and a specified gas grid to connect the nodes amongst each other. To characterize the necessary information, the following parameters need to be set: the residual power of all nodes P_i, the length between connected gas pipelines l_{ij}, the diameter of the pipelines d_{ij} and the specific pipe friction f_{ij}. Usually, the variable name k is chosen for the pipe friction, but in order to prevent possible confusion with the thermal transmittance, the variable was renamed.

$$P_i = [P_1 \dots P_i \dots P_n]^T \tag{3-54}$$

$$l_{ij} = \begin{bmatrix} l_{11} \dots l_{1j} \dots l_{1n} \\ \vdots \ddots \vdots \ddots \vdots \\ l_{i1} \dots l_{ij} \dots l_{in} \\ \vdots \ddots \vdots \ddots \vdots \\ l_{n1} \dots l_{nj} \dots l_{nn} \end{bmatrix} \quad d_{ij} = \begin{bmatrix} d_{11} \dots d_{1j} \dots d_{1n} \\ \vdots \ddots \vdots \ddots \vdots \\ d_{i1} \dots d_{ij} \dots d_{in} \\ \vdots \ddots \vdots \ddots \vdots \\ d_{n1} \dots d_{nj} \dots d_{nn} \end{bmatrix} \quad f_{ij} = \begin{bmatrix} f_{11} \dots f_{1j} \dots f_{1n} \\ \vdots \ddots \vdots \ddots \vdots \\ f_{i1} \dots f_{ij} \dots f_{in} \\ \vdots \ddots \vdots \ddots \vdots \\ f_{n1} \dots f_{nj} \dots f_{nn} \end{bmatrix} \tag{3-55}$$

The calculation process to determine the load flows and the node pressures of the natural gas grid is carried out iteratively with the Newton-Raphson solver as well. At first the necessary flow rate $\dot{V}$ to meet the demand of the residual load is calculated. Furthermore, the flow rates in the pipeline network and the nodal pressure levels are determined. The necessary flow rate of natural gas is directly proportional to the power demand. As sensible heat can be neglected in natural gas grids, it depends solely on the lower heating value H_U and the mass flow $\dot{m}$.

$$\dot{V}_i = \left[\dot{V}_1 \dots \dot{V}_i \dots \dot{V}_n\right]^T \tag{3-56}$$

$$P_i = H_U \cdot \dot{m}_i = H_U \cdot \rho \cdot \dot{V}_i \tag{3-57}$$

$$\dot{V}_i = \frac{P_i}{H_U \cdot \rho} \tag{3-58}$$

The fundamental equations necessary for calculating the natural gas load flow are described in detail in section 2.3.2. As mentioned before, the quadratic dependence between the pressure loss and the flow rate prevents the direct usage of the same solver algorithm used in the electric LFC. In order to eliminate these nonlinearities from the Darcy equation presented in Equation 2-39., the quadratic flow rate is separated into two terms according to Equation 3-60. All variables are now summarized in a resistance term R^*. Analogous to the electrical load flow calculation, this can also be rephrased as a conductance term g, which is the reciprocal value of the resistance R^*.

$$\Delta p_{ij} = {R^*}_{ij} \cdot \dot{V}_{ij} \tag{3-59}$$

$${R^*}_{ij} = \lambda_{ij} \cdot \frac{8 \cdot l_{ij} \cdot \rho}{{d_{ij}}^5 \cdot \pi^2} \cdot \dot{V}_{ij} \tag{3-60}$$

$$g_{ij} = \frac{1}{{R^*}_{ij}} = \frac{1}{\lambda_{ij}} \cdot \frac{{d_{ij}}^5 \cdot \pi^2}{8 \cdot l_{ij} \cdot \rho} \cdot \frac{1}{\dot{V}_{ij}} \tag{3-61}$$

$$\Delta p_{ij} = {R^*}_{ij} \cdot \dot{V}_{ij} = \frac{1}{g_{ij}} \cdot \dot{V}_{ij} \tag{3-62}$$

Analogous to the electric load flow calculation, a conductance matrix is formulated in Equation 3-63 based on Equation 3-61 for all interconnections. This enables to solve a linear system of equations by forming the inverse conductance matrix Y^{-1}, which results in the pressure differences Δp and the corresponding nodal pressure values p_i.

$$Y_{ij} = \begin{bmatrix} g_{11} \cdots g_{1j} \cdots g_{1n} \\ \vdots \quad \ddots \quad \vdots \quad \ddots \quad \vdots \\ g_{i1} \cdots g_{ij} \cdots g_{in} \\ \vdots \quad \ddots \quad \vdots \quad \ddots \quad \vdots \\ g_{n1} \cdots g_{nj} \cdots g_{nn} \end{bmatrix} \tag{3-63}$$

$$p_{i,[t]} = Y^{-1}_{[t-1]} \cdot \dot{V}_i \tag{3-64}$$

Both used flow rates of Equation 3-62 (one is included in the R^* term) are now assigned different values – from different iteration steps. The difference between the flow rate at the calculated iteration step $\dot{V}_{ij,t(x)}$ and the previous iteration step $\dot{V}_{ij,t(x-1)}$ is also the relevant value of the abort condition for the iterative calculation process.

$$\Delta p_{ij,[t]} = \lambda_{ij,[t-1]} \cdot \frac{8 \cdot l_{ij} \cdot \rho}{{d_{ij}}^5 \cdot \pi^2} \dot{V}_{ij,[t-1]} \cdot \dot{V}_{ij,[t]} = R^* \cdot \dot{V}_{ij,[t]} \tag{3-65}$$

This linearization enables to solve the system of equations in order to calculate the pressure drops along the grid connections, as well as the nodal pressures. By rearranging Equation 3-65 it is possible to calculate the volumetric flow rates between the pipeline connections. Since losses occur, all flow rates need to be assigned the right flow direction. Due to the fact that the solution of the quadratic equation does not allow the determination of the sign of the volume flow and the related flow direction the sign function is used to solve this problem as seen in Equation 3-66.

$$\dot{V}_{ij,t} = sign\left(\Delta p_{ij,[t]}\right) \cdot \sqrt{\frac{{d_{ij}}^5 \cdot \pi^2}{8 * \rho * l_{ij} \cdot \lambda_{ij,t-1}} \cdot \left|\Delta p_{ij,[t-1]}\right|} \tag{3-66}$$

The necessary definition of the initial flow rates to start the first time step of the iterative calculation process is described in the following example.

Calculation example natural gas load flow

Figure 3-37 shows the exemplary natural gas grid, which is used to demonstrate the detailed numeric calculation procedure. Given parameters are the pressure level at the slack node p_S, the residual loads of all nodes P_i, the length L_{ij}, diameter d_{ij} and the roughness of the pipeline connections f_{ij}.

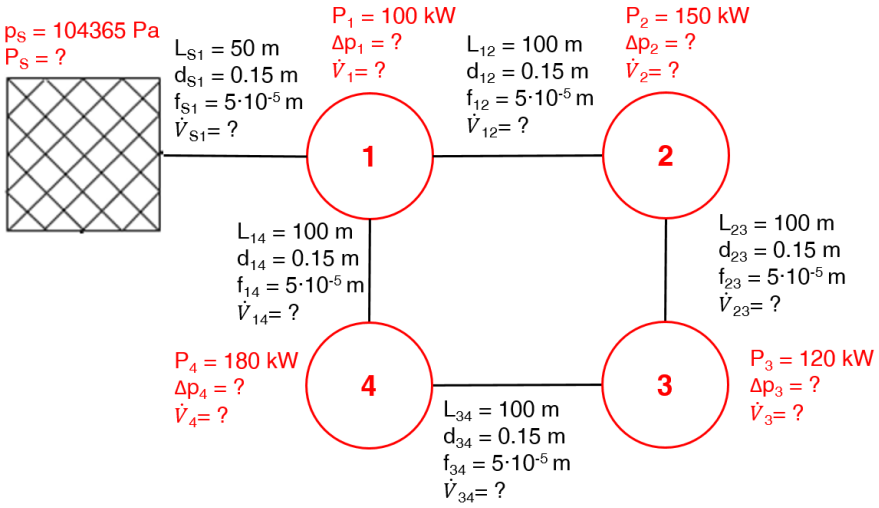

Figure 3-37: Exemplary grid for the natural gas load flow calculation

The input parameters for this example are listed underneath:

$$p_S = 104365\ Pa;\ d_{ij} = 0.15\ m;\ f_{ij} = 5 \cdot 10^{-5}$$

$$P_1 = 100\ kW;\ P_2 = 150\ kW;\ P_3 = 120\ kW;\ P_4 = 180\ kW$$

$$L_{S1} = 50\ m;\ L_{12} = L_{14} = L_{23} = L_{34} = 100\ m$$

Additionally, the necessary physical parameters of natural gas are indicated. It has to be noted that these parameters are assumed to be constant.

$$\rho = 0.84\ \frac{kg}{m^3};\ \eta = 14.2 \cdot 10^{-6}\ \frac{m^2}{s};\ H_U = 55.5 \cdot 10^6\ \frac{J}{kg}$$

The necessary flow rate to deliver the set power demand of the nodes is calculated according to Equation 3-58. This is performed for all nodes, but only demonstrated for the first node. The nodal flow rate matrix is shown underneath. Due to the sign convention, all demands are indicated as negative values. The attentive reader will notice the sixth and highest value in the matrix, while the chosen example consists of five nodes only, including the slack node. This value is used for calculation purposes only, in order to consider the reference pressure at the slack node.

$$\dot{V}_1 = \frac{P_1}{\rho \cdot H_U} = \frac{-100000}{55.5 \cdot 10^6 \cdot 0.84} = -0.0021 \ \frac{m^3}{s}$$

$$\dot{V}_i = \begin{bmatrix} 0 \\ -0.0021 \\ -0.0032 \\ -0.0026 \\ -0.0039 \\ -28.9903 \end{bmatrix} \frac{m^3}{s}$$

Derived from the necessary nodal flow rates, the edge flow rates are calculated. To determine the initial values, all nodal flow rates are averaged and multiplied by a random number between 0 – 1, analogous to the second electrical load flow methodology.

$$\overline{\dot{V}}_i = \sum_{i}^{n} \frac{\dot{V}_i}{n} = \sum_{i=1}^{4} \frac{\dot{V}_i}{4} = -4.834 \frac{m^3}{s}$$

$$\dot{V}_{ij,Start} = \dot{V}_{ij,[t0]} = \ rand_{ij} \cdot \overline{\dot{V}}_i$$

$$\dot{V}_{ij} = -\dot{V}_{ji}$$

The starting values of the flow rate for the connections of the first node are shown underneath. The initial values for all edge flow rates are shown in the matrix below.

$$\dot{V}_{1S} = rand_{ij} \cdot \overline{\dot{V}}_i = 0.0975 \cdot 4.834 = 0.4713 \ \frac{m^3}{s}$$

$$\dot{V}_{12} = 0.2785 \cdot 4.834 = 1.346 \ \frac{m^3}{s}$$

$$\dot{V}_{14} = 0.5468 \cdot 4.834 = 2.643 \ \frac{m^3}{s}$$

$$\dot{V}_{ij,[t0]} = \begin{bmatrix} 0 & 0.4713 & 0 & 0 & 0 \\ -0.4713 & 0 & 1.346 & 0 & 2.643 \\ 0 & -1.346 & 0 & 4.628 & 0 \\ 0 & 0 & -4.628 & 0 & 4.664 \\ 0 & -2.643 & 0 & -4.664 & 0 \end{bmatrix} \frac{m^3}{s}$$

Once these edge flow rates are known, the Reynold's number according to Equation 2-42 can be calculated. The flow rates are considered as positive amounts since the Reynold's number does not have a direction.

$$Re_{1S} = \frac{4 \cdot \left|\dot{V}_{1S}\right|}{\pi \cdot d_{1S} \cdot \eta} = \frac{4 \cdot 0.4713}{\pi \cdot 0.15 \cdot 14.2 \cdot 10^{-6}} = 2.817 \cdot 10^5$$

$$Re_{ij} = \begin{bmatrix} 0 & 2.817 & 0 & 0 & 0 \\ 2.817 & 0 & 8.046 & 0 & 15.80 \\ 0 & 8.046 & 0 & 27.76 & 0 \\ 0 & 0 & 27.76 & 0 & 27.88 \\ 0 & 15.80 & 0 & 27.88 & 0 \end{bmatrix}$$

All values fall into the state of fully turbulence flow, which requires the usage of the implicit Equation 2-44 to calculate Darcy's friction factor. The Newton methodology is applied once again to obtain Darcy's friction factor λ_{ij} from the said implicit equation.

$$\lambda_{ij} = \begin{bmatrix} 0 & 0.0173 & 0 & 0 & 0 \\ 0.0173 & 0 & 0.0161 & 0 & 0.0157 \\ 0 & 0.0161 & 0 & 0.0155 & 0 \\ 0 & 0 & 0.0155 & 0 & 0.0155 \\ 0 & 0.0157 & 0 & 0.0155 & 0 \end{bmatrix}$$

Now all variables to calculate the conductance matrix are available, which is presented underneath:

$$g_{1S} = -\frac{1}{\lambda_{1S}} \cdot \frac{{d_{1S}}^5 \cdot \pi^2}{8 \cdot l_{1S} \cdot \rho} \cdot \frac{1}{\left|\dot{V}_{S1}\right|} = -\frac{1}{0.0173} \cdot \frac{0.15^5 \cdot \pi^2}{8 \cdot 50 \cdot 0.84} \cdot \frac{1}{0.4713} = -2.735 \cdot 10^{-6} \frac{m^4 s}{kg}$$

$$Y = \begin{bmatrix} 0 & -27.35 & 0 & 0 & 0 \\ -27.35 & 0 & -5.147 & 0 & -2.688 \\ 0 & -5.147 & 0 & -1.551 & 0 \\ 0 & 0 & -1.551 & 0 & -1.540 \\ 0 & -2.688 & 0 & -1.540 & 0 \end{bmatrix} \cdot 10^{-5} \frac{m^4 s}{kg}$$

It is necessary to fill the main diagonal of the admittance matric with the positive sum of the rest of the row values, in order to get results according to the nodal-voltage methodology. Additionally, another column and row have to be introduced to the admittance matrix to implement the pressure source, as described above. This leads to an extended admittance matrix.

$$Y = \begin{bmatrix} 27.35 & -27.35 & 0 & 0 & 0 & 10^5 \\ -27.35 & 35.19 & -5.147 & 0 & -2.688 & 0 \\ 0 & -5.147 & 6.698 & -1.551 & 0 & 0 \\ 0 & 0 & -1.551 & 3.091 & -1.540 & 0 \\ 0 & -2.688 & 0 & -1.540 & 4.228 & 0 \\ 10^5 & 0 & 0 & 0 & 0 & 0 \end{bmatrix} \cdot 10^{-5} \frac{m^4 s}{kg}$$

To calculate the pressure difference between the nodes, the conductance matrix needs to be inverted. If the rank of a square matrix (n x n) is unequal n, there is an infinite number of

solutions. In order to still achieve a usable result, MatLab uses the Moore-Penrose inverse (pseudoinverse) $Y^{\dagger}$. [168]

$$\Delta p = Y^{-1} \cdot \dot{V}_i \rightarrow \Delta p = Y^{\dagger} \cdot \dot{V}_{Knoten}$$

$$Y^{\dagger} = \begin{bmatrix} 0 & 0 & 0 & 0 & 0 & 1 \\ 0 & 3656 & 3656 & 3656 & 3656 & 1 \\ 0 & 3656 & 21060 & 14328 & 7546 & 1 \\ 0 & 3656 & 14328 & 49733 & 20450 & 1 \\ 0 & 3656 & 7546 & 20450 & 33453 & 1 \\ 1 & 1 & 1 & 1 & 1 & 0 \end{bmatrix}$$

$$\begin{bmatrix} 0 & 0 & 0 & 0 & 0 & 1 \\ 0 & 3656 & 3656 & 3656 & 3656 & 1 \\ 0 & 3656 & 21060 & 14328 & 7546 & 1 \\ 0 & 3656 & 14328 & 49733 & 20450 & 1 \\ 0 & 3656 & 7546 & 20450 & 33453 & 1 \\ 1 & 1 & 1 & 1 & 1 & 0 \end{bmatrix} \cdot \begin{bmatrix} 0 \\ -0.0021 \\ -0.0032 \\ -0.0026 \\ -0.0039 \\ -28.9903 \end{bmatrix} = \begin{bmatrix} -28.99 \\ -72.12 \\ -170.61 \\ -289.91 \\ -242.91 \\ -0.0118 \end{bmatrix} Pa$$

By adding the slack pressure to the determined pressure difference, the nominal nodal pressure can be calculated.

$$p_i = p_{Slack} + \Delta p_i$$

$$p_1 = p_S + \Delta p_1 = 104365 - 0.0247 = 104364.9753\ Pa$$

$$p_i = \begin{bmatrix} 104336.01 \\ 104292.88 \\ 104194.39 \\ 104075.09 \\ 104122.09 \\ 104364.99 \end{bmatrix} Pa$$

With the help of Equation 3-66, new edge flow rates can be calculated with the determined nominal pressure levels of all nodes.

$$\dot{V}_{1S} = sign(p_1 - p_S) \cdot \sqrt{\frac{{d_{1S}}^5 \cdot \pi^2}{8 \cdot \rho \cdot l_{1S} \cdot \lambda_{1S}} \cdot |p_1 - p_S|}$$

$$\dot{V}_{ij.[t1]} = \begin{bmatrix} 0 & 7.457 & 0 & 0 & 0 \\ -7.457 & 0 & 9.905 & 0 & 12.327 \\ 0 & -9.905 & 0 & 9.255 & 0 \\ 0 & 0 & -9.255 & 0 & -5.809 \\ 0 & -12.327 & 0 & 5.809 & 0 \end{bmatrix} \cdot 10^{-2}\ \frac{m^3}{s}$$

Table 1 shows the nodal pressure and the flow rates for the exemplary node 1 and selected iteration steps. The iterative process is aborted once the calculated error falls short of the defined error difference, which was defined with a maximum deviation of $10^{-4}\,\frac{m^3}{s}$ at every node. Analogous to the electrical load flow calculation, the result of the calculated flow rate is defined as the starting value for the next iterative step.

Table 3-7: Calculation results of edge flow rates and the nodal pressure at node 1 for selected iteration steps

Iteration step	$\dot{V}_{1S}$ $\frac{m^3}{h}$	$\dot{V}_{12}$ $\frac{m^3}{h}$	$\dot{V}_{14}$ $\frac{m^3}{h}$	p_1 Pa
0	-1696.7	4845.6	9514.8	-
1	-268.45	356.58	443.772	104292.88
2	-106.78	72.32	82.47	104327.13
3	-67.35	35.26	38.05	104331.72
4	-53.48	24.63	25.84	104333.00
13	-42.48	17.02	17.74	104333.86

The resulting flow rates and nodal pressures at the end of the iterative process is illustrated underneath. The units of the flow rate have been changed to $\frac{m^3}{h}$, in order to get a better feeling for the results.

$$\dot{V}_{ij} = \begin{bmatrix} 0 & 42.48 & 0 & 0 & 0 \\ -42.48 & 0 & 17.02 & 0 & 17.74 \\ 0 & -17.02 & 0 & 5.432 & 0 \\ 0 & 0 & -5.432 & 0 & -3.839 \\ 0 & -17.74 & 0 & 3.839 & 0 \end{bmatrix} \frac{m^3}{h}$$

$$\begin{bmatrix} p_S \\ p_1 \\ p_2 \\ p_3 \\ p_4 \end{bmatrix} = \begin{bmatrix} 104364.99 \\ 104333.86 \\ 104333.19 \\ 104333.05 \\ 104333.15 \end{bmatrix} Pa$$

The end results are additionally illustrated in Figure 3-38.

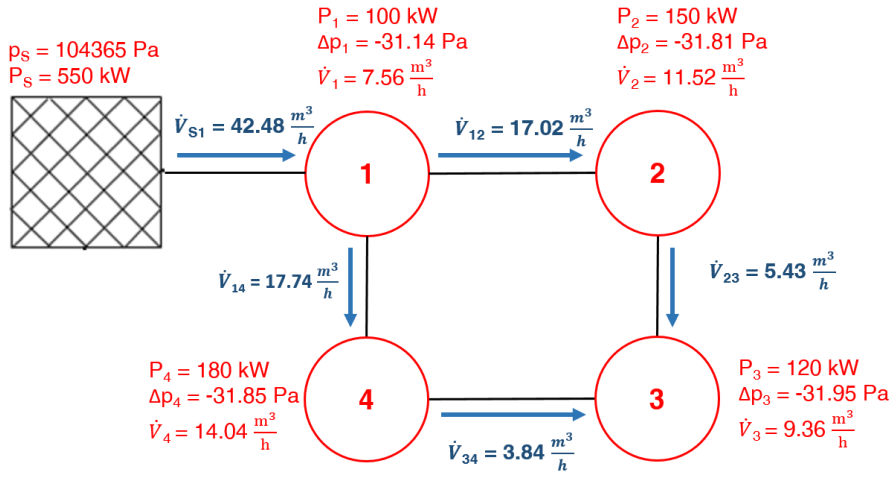

Figure 3-38: Resulting flow rates between the nodes and nodal pressure values

3.5.7 District Heating load flow calculations

The load flow calculation for district heating networks is based on the described natural gas load flow calculation with four main differences:

1. The flow media is now in the liquid state (water) instead of the gaseous state. This implies a non-compressible medium with a much higher density.
2. The media in the pipelines is now only used as transfer medium and is not "consumed" itself. This requires that district heating networks have a supply flow and a return flow.
3. Besides friction losses, heat losses are the main source of energy losses in the pipes (see Equations 3-69 and 3-70) and can no longer be neglected, like in the natural gas load flow calculation. This implies that mass flows with different temperatures and therefore energy content could mix in a node if there is a meshed network.
4. Heating losses occur independently of the energy consumption of the consumers, since the hot water also cools off in the pipes without any consumption at the nodes.

All input values of the natural gas load flow calculation, the pressure level at the slack node p_S, residual loads of all nodes P_i, length L_{ij}, diameter d_{ij} and the roughness of the pipeline connections f_{ij} are input values again. The temperature at the slack node T_S and the heat transition coefficient of the pipes k_{ij} are additional input factors for the district heating load flows.

The thermal power P_{th} is calculated according to Equation 3-67. As one can see, the transferred power is not solely dependent on the flow rate $\dot{V}$, as seen in the natural gas load

flow, but also on the spread between the supply temperature T_{Sup} and the return temperature T_{Ret} after the heat transmission at the nodes.

$$P_{th} = c_p \cdot \rho \cdot \dot{V} \cdot \Delta T = c_p \cdot \rho \cdot \dot{V} \cdot (T_{Sup} - T_{Ret}) \tag{3-67}$$

To start the iterative calculation process, it is necessary to calculate the necessary flow rate at all nodes to meet the demand. In contrast to the natural gas load flow, this cannot be predicted exactly, because the exact supply temperature at a specific node is not known, due to heat losses along the path. This circumstance requires an initial guess of the supply temperature at all nodes for the first iteration. In *HyFlow* all return temperatures have to be defined. It is assumed, that the return temperature at each node is constant and that all consumers control the heating demand with the flow rate through their heat exchanger based on the return temperature. The specific initial flow rate at the specific nodes can be calculated according to Equation 3-68.

$$\dot{V}_{i,Start} = \frac{P_{th,i}}{c_p \cdot \rho \cdot (T_{Sup,Start} - T_{Ret})} \tag{3-68}$$

The flow rate calculations are similar to the natural gas load flow calculations. As soon as the first approximation of the flow rates in the pipelines is calculated, the determined flow rates are used to calculate the heat losses to the individual nodes. To calculate the heat losses in a pipe, it is necessary to describe the heat losses through a pipe (Equation 3-69) and the energy content of the lost heat, depending on the reduced temperature in the pipe (Equation 3-70).

$$P_{Loss} = -2 \cdot \pi \cdot k \cdot l \cdot (T_{FLuid} - T_{amb}) \tag{3-69}$$

$$E_{Loss} = c_p \cdot \rho \cdot V \cdot \Delta T \tag{3-70}$$

By equating 3-69 and 3-70, the following differential Equation 3-71 appears, which can be reformulated to 3-72.

$$-2 \cdot \pi \cdot k \cdot l \cdot (T_{Fluid}(t) - T_{amb}) = c_p \cdot \rho \cdot V \cdot \frac{dT_{Fluid}(t)}{dt} \tag{3-71}$$

$$\frac{dT_{Fluid}(t)}{dt} = \frac{-2 \cdot \pi \cdot k \cdot l \cdot (T_{Fluid}(t) - T_{amb})}{c_p \cdot \rho \cdot V} \tag{3-72}$$

The differential Equation 3-72 can be solved via separation of variables. Equation 3-73 shows the solution. The temperature at the end of the pipe is defined as follows:

$$T_i = \left(T_j - T_{amb}\right) \cdot e^{\left(\frac{-2 \cdot \pi \cdot k \cdot l_{ij}}{c_p \cdot \rho \cdot |\dot{V}_{ij}|}\right)} + T_{amb} \tag{3-73}$$

Equation 3-73 implies another challenge, which didn't occur in the electrical – or the natural gas load flow calculation. The actual load flow in the considered network is depending on the pressure profile in the network. However, the required power to supply the energy demand of a specific node is provided by the temperature difference between the supply and return flow temperature. To calculate the supply temperature of a specific node, the temperature of all previous nodes in the network with an inflow to the inquired node has to be known. In meshed networks with joints, where flows with different media are mixed, this is not a trivial task. To solve this problem, a recursive search procedure is implemented. This means that for all nodes to be determined, the recursive algorithm detects all inflows. If node i is to be determined and node j is the only inflow, the recursive search checks whether the temperature of node j is known. If so, the temperature of node i can be determined with Equation 3-73. If the temperature of node j is not yet known, the algorithm checks all inflows of node j. This search continues until a known temperature is found. The last option is always the slack node. If a node i has multiple inflows from connected nodes, the temperatures are calculated and memorized for every individual connected node and mixed according to the corresponding flow rates and temperatures at node i, as shown in Equation 3-74. A simple example of the recursive search algorithm is also available at the end of this section.

$$T_i = \frac{\sum(\dot{V} \cdot T)}{\sum \dot{V}} \tag{3-74}$$

After all nodal temperatures are determined, the new supply temperatures at the nodes lead to a changed spread of temperature, which again leads to a changed demand of flow rate at the nodes. This means that the new flow rates are calculated, based on Equation 3-68, which starts the next iteration step. The iterative process stops, once the change of the supply temperatures of the nodes is smaller than the defined abortion condition.

Calculation example district heating load flow

The described district heating load flow calculation procedure is also visualized with the aid of a small numeric network example. All steps, that are similar to the natural gas load flow are only mentioned, but not described in detail.

The example of the district heating network is similar to the previous natural gas example.

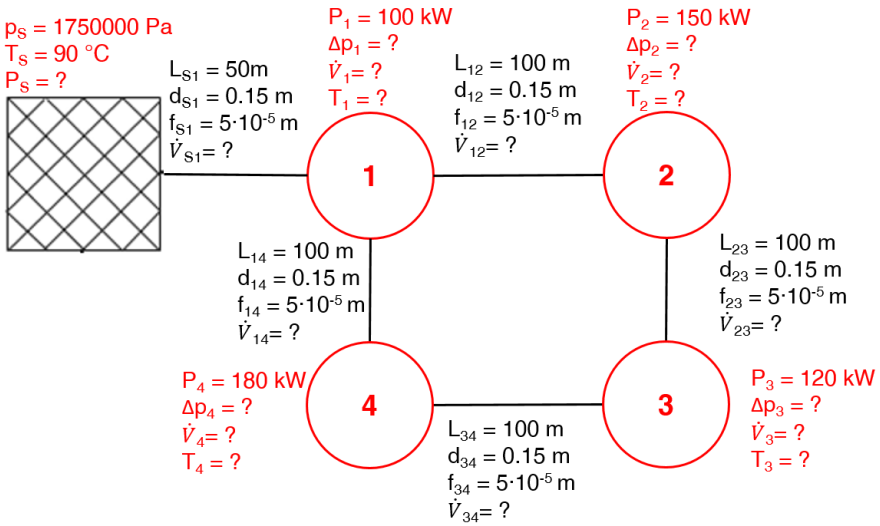

Figure 3-39: Exemplary grid for the district heating load flow calculation

Many input variables of the district heating load flow calculation are identical to the natural gas load flow. The complete list of all input parameters for this example is shown underneath. The most relevant output parameters are the flow rates between the nodes and at the nodes, the node pressure levels, the supply temperatures of the nodes and the necessary thermal power of the slack node to supply the demand and compensate the transport losses.

$$p_S = 17.5\ bar;\ T_S = 90\ °C;\ T_{Ret,i} = 55\ °C;\ T_{amb} = 10\ °C;$$

$$P_{th,1} = 100\ kW;\ P_2 = 150\ kW;\ P_3 = 120\ kW;\ P_4 = 180\ kW$$

$$d_{ij} = 0.15\ m;\ f_{ij} = 5 \cdot 10^{-5}$$

$$L_{S1} = 50\ m;\ L_{12} = L_{14} = L_{23} = L_{34} = 100\ m$$

$$\rho = 973.5\ \frac{kg}{m^3};\ \eta = 0.326 \cdot 10^{-6}\ \frac{m^2}{s}\quad c_p = 4190\ \frac{J}{kgK};\ k = 0.2\ \frac{J}{kg}$$

As previously handled, the numeric examples correspond to node 1 or to the connections of node 1, while other results are only mentioned without detailed explanation.

$$\dot{V}_{1,[t0]} = \frac{P_{th,1}}{c_p \cdot \rho \cdot (T_{Sup,[t0]} - T_{Ret})} = \frac{100000}{4190 \cdot 973.5 \cdot (77.5 - 55)} = 10.896 \cdot 10^{-4} \frac{m^3}{s}$$

$$\dot{V}_{i,[t0]} = \begin{bmatrix} 0 \\ -0.0011 \\ -0.0016 \\ -0.0013 \\ -0.0020 \end{bmatrix} \frac{m^3}{s}$$

The flow rate vector is used to start the fluid mechanic calculation, similar to the natural gas load flow. For this reason, this step is not included in the demonstration again. The required flow rate to meet the heat demand at the individual nodes are shown in the edge flow rate vector. The nodal pressure levels are expressed in the corresponding vector underneath. The necessity of the additional values of the nodal pressure vector is already explained in section 3.5.6.

$$\dot{V}_{ij} = \begin{bmatrix} 0 & 5.996 & 0 & 0 & 0 \\ -5.996 & 0 & 2.412 & 0 & 2.494 \\ 0 & -2.412 & 0 & 0.7763 & 0 \\ 0 & 0 & -0.7763 & 0 & -0.5320 \\ 0 & -2.494 & 0 & 0.5320 & 0 \end{bmatrix} \cdot 10^{-3} \frac{m^3}{s}$$

$$p_i = \begin{bmatrix} 1749513.89 \\ 1749169.25 \\ 1749041.40 \\ 1749024.79 \\ 1749033.31 \\ 1749999.99 \end{bmatrix} Pa$$

After the pressure levels and the flow rates between the nodes are determined, the calculation of the temperatures starts. As explained in the generic description before, this part of the calculation is executed in the form of a recursive algorithm. The algorithm starts with the highest number of nodes, to minimize the number of calls of the recursive function. Since the flow direction between the nodes is known based on the sign, the number of inflows can easily be determined for all nodes. In this example, the first node asked is node 4. Figure 3-40 illustrates the separate steps of the calculation process.

Node 4 has only one inflow from node 1. The recursive algorithm checks whether the temperature of node 1 is already known. Since no temperature is yet assigned to node 1, the algorithm checks the inflows of node 1. It detects only one inflow again, coming from the slack node. This is the only temperature defined from the very start. By knowing the grid parameters, the flow rate and the starting temperature in the slack node, the temperature of node 1 can be calculated.

$$T_1 = (T_S - T_{amb}) \cdot e^{\left(\frac{-2 \cdot \pi \cdot k \cdot l_{S1}}{c_p \cdot \rho \cdot |\dot{V}_{S1}|}\right)} + T_{amb}$$

$$T_1 = (90 - 10) \cdot e^{\left(\frac{-2 \cdot \pi \cdot 0.2 \cdot 50}{4190 \cdot 973.5 \cdot |-5.996 \cdot 10^{-3}|}\right)} + 10 = 89.79\ °\mathrm{C}$$

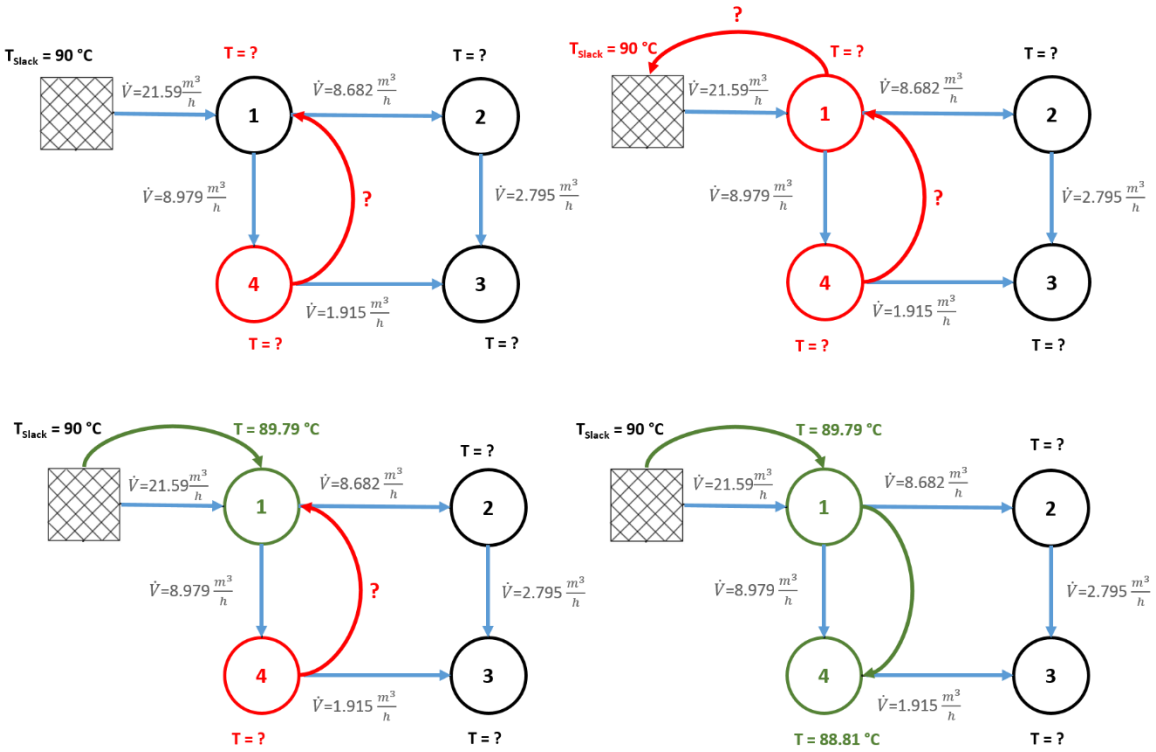

Figure 3-40: The steps of the recursive algorithm to determine the nodal temperatures

Now, temperature 4 can also be calculated with the same equation and adapted values.

$$T_4 = (T_1 - T_{amb}) \cdot e^{\left(\frac{-2 \cdot \pi \cdot k \cdot l_{14}}{c_p \cdot \rho \cdot |\dot{V}_{14}|}\right)} + T_{amb}$$

$$T_4 = (89.79 - 10) \cdot e^{\left(\frac{-2 \cdot \pi \cdot 0.2 \cdot 100}{4190 \cdot 973.5 \cdot |-2.494 \cdot 10^{-3}|}\right)} + 10\ = 88.81\ °C$$

Temperature 3 is the next required value. It has two inflows, one of them is already calculated (node 4). The second inflow of node 2, cannot yet be calculated, as the temperature of node 2 is unknown. Node 2 has only one inflow, coming from node 1, which was calculated earlier. This allows for the determination of nodal temperature 2.

$$T_2 = (89.79 - 10) \cdot e^{\left(\frac{-2 \cdot \pi \cdot 0.2 \cdot 100}{4190 \cdot 973.5 \cdot |-2.412 \cdot 10^{-3}|}\right)} + 10 = 88.78\ °C$$

Now temperature 3 can be calculated from two nodes, as node 3 has two inflows.

$$T'_3 = (88.81 - 10) \cdot e^{\left(\frac{-2 \cdot \pi \cdot 0.2 \cdot 100}{4190 \cdot 973.5 \cdot |-0.5320 \cdot 10^{-3}|}\right)} + 10 = 84.38\,°C$$

$$T''_3 = (88.78 - 10) \cdot e^{\left(\frac{-2 \cdot \pi \cdot 0.2 \cdot 100}{4190 \cdot 973.5 \cdot |-0.7763 \cdot 10^{-3}|}\right)} + 10 = 85.71\,°C$$

These two temperatures are mixed and weighed according to the corresponding flow rate in order to calculate the correct supply temperature at node 3. Figure 3-41 illustrates the iterative approach to determine the temperature at node 3.

$$T_3 = \frac{T'_3 \cdot |\dot{V}_{43}| + T''_3 \cdot |\dot{V}_{23}|}{|\dot{V}_{43}| + |\dot{V}_{23}|}$$

$$\frac{84.38 \cdot |-0.5320 \cdot 10^{-3}| + 85.71 \cdot |-0.7763 \cdot 10^{-3}|}{|-0.5320 \cdot 10^{-3}| + |-0.7763 \cdot 10^{-3}|} = 85.18\,°C$$

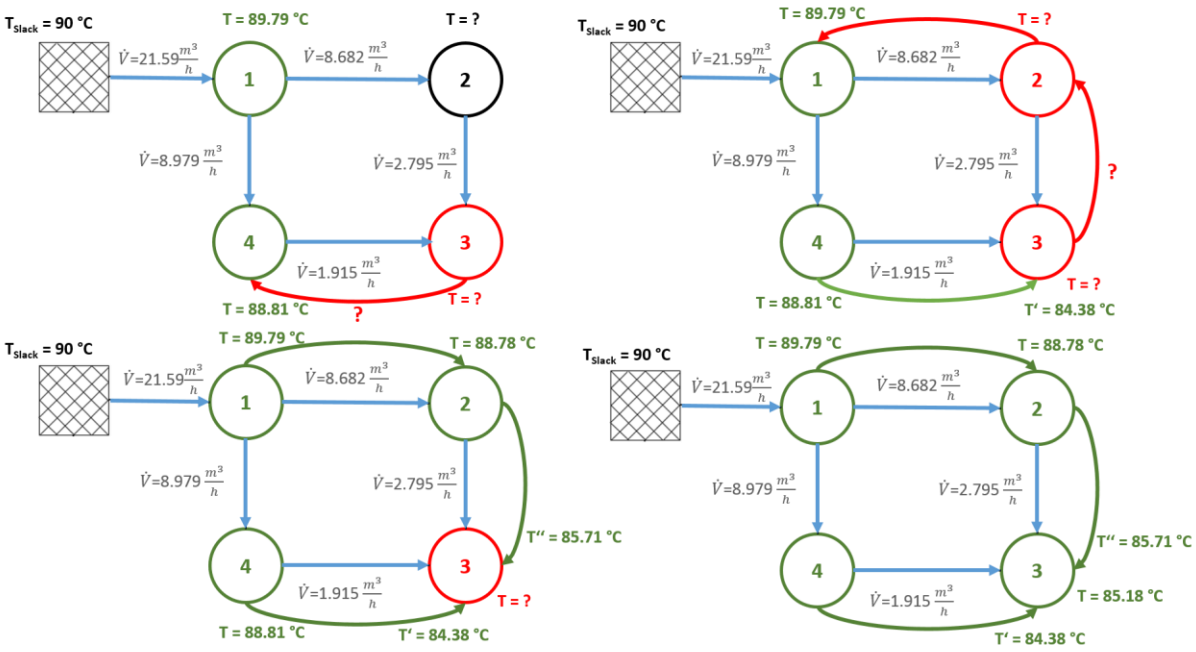

Figure 3-41: The steps of the recursive algorithm to determine the nodal temperatures

This means that all nodal supply temperatures of the first iteration step are now determined. The temperature matrix, shown below, is now the starting point to calculate the required incoming flow rates to the individual nodes.

$$T_{Sup} = \begin{bmatrix} 90 \\ 89.79 \\ 88.78 \\ 85.18 \\ 88.81 \end{bmatrix} °C$$

The results of the iteration steps are shown in Table 3-8. The required precision of a change in temperature of less than 10^{-4} °C is reached in the fourth iteration step. Due to the fact that the flow rate needs to be iterated as well in between, the total number of all iterations adds up to 29.

Table 3-8: Results of edge flow rates and the nodal temperature at node 1 for selected iteration steps

Iteration step	$\dot{V}_{1S}$	$\dot{V}_{12}$	$\dot{V}_{14}$	V_1	T_1
	$\frac{m^3}{h}$	$\frac{m^3}{h}$	$\frac{m^3}{h}$	$\frac{m^3}{h}$	°C
0	-21.59	8.682	8.979	3.96	89.79
1	-14.67	5.963	6.173	2.537	89.70
2	-15.02	6.129	6.344	2.544	89.71
3	-14.97	6.108	6.323	2.543	89.70
4	-14.98	6.109	6.324	2.543	89.70

The results of the calculated values are illustrated in Figure 3-42.

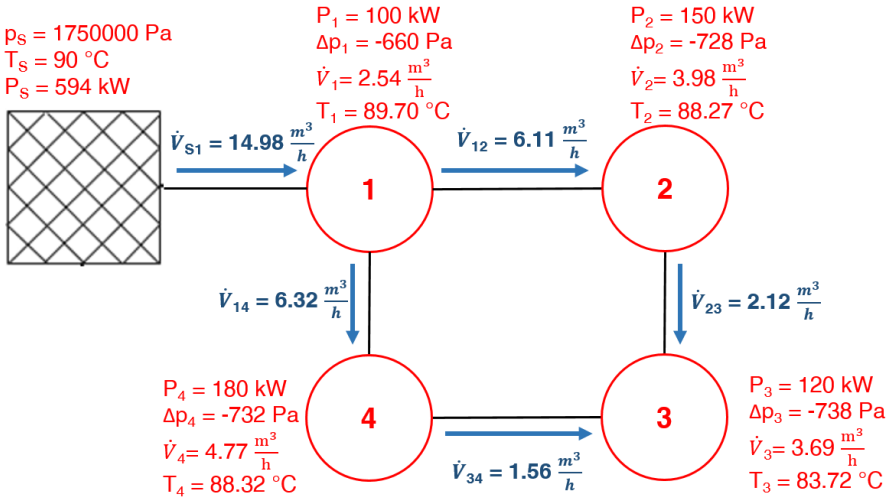

Figure 3-42: Resulting flow rates and nodal temperatures for the calculated exemplary network

It should be mentioned that the return flow is calculated in a similar way. The flow direction is reversed, the nodal return temperature is constant for all nodes, but the temperatures of the return flow decreases completely analogous to the supply flow temperature.

3.5.8 Energy Storage

Energy storage in the *HyFlow* modelling framework is used to balance demand and production over time. For each level-1 cell and energy carrier, one corresponding energy storage can be defined. As most energy storage units on a system level (batteries, pumped hydro, compressed air, flywheels, district heating storage tanks) are able to respond to changes in demand within seconds [169,170] to under 10 minutes [171,172], *HyFlow* does not consider ramp rates for energy storages. In case of a chosen smaller interval length of time steps compared to the technologies' ramp rates, certain deviations in the results may occur. Results may deviate if the selected time step is smaller than the technology's ramp rate. All characterization parameters being used are to be found in Table 3-9.

Table 3-9: Generic energy storage characterization in HyFlow

Parameter	Value [Unit]	Description
Storage capacity	positive [Wh]	Maximum energy storage capacity of the corresponding energy storage. If storage capacity for any energy carrier is zero, no energy storage is available.
Maximum charge and discharge power	positive [W]	Both values have to be defined to define the maximum charge and discharge power of the corresponding energy storage.
Operation mode	0/1	This parameter indicates whether the energy storage operates in cell-serving- (parameter = 0) or system-serving-mode (parameter = 1). If the energy storage operates in cell-serving-mode it operates according to the residual load of the associated cell only. This mode of operation can also be called "private mode", if the used minimum aggregation is the household level as no other user can access the energy storage. In case of an energy storage in system-serving-mode, the energy storage operates in response to the systems residual load, enabling third-parties to access the energy storage capacity. This storage type is implemented to depict the behavior of "central storages.
Efficiency charge / discharge	0-1	This value represents the efficiency of the charging - as well as a discharging process.
Self-discharge	0-1 [1/h]	The time-based efficiency considers self-discharge of energy storage within a time period of one hour.

The necessary parameters to define an energy storage unit in the *HyFlow* modelling framework are explained in the following table. This rather generic approach allows one to model a wide variety of energy storage units and other flexibility options like demand side management (DSM) to be implemented in the same way for all energy carriers. It enables the user to quickly change parameters in terms of technology improvements.

Aging effects, such as reduced capacity of batteries over its life cycle, depth of discharge or other detailed effects like thermic stratification in thermal storage units are neglected in the model. Such improvements may be subject of the next evaluation step of the *HyFlow* modelling framework.

3.5.9 Hybrid Elements

In order to enable the conversion from one energy carrier to another, hybrid elements are implemented in *HyFlow*. Hybrid elements as well as ESS are foreseen exclusively on cell level 1 and need to be defined prior to the calculation steps. This limitation is necessary due to the possibility of a large number of very different deployment scenarios if more than one hybrid element is included. Based on three separate energy carriers, up to six different hybrid technologies could theoretically be defined (P2H, P2G, G2P, G2H, H2P, H2G). However, today's technological and economic environment focuses on four different kinds of hybrid element technologies as seen in Figure 3-43. These are P2H (power to heat), P2GH (power to gas and heat), G2PH (gas to power and heat) and G2H (gas to heat). It is also possible to generate power from heat sources, but in the context of *HyFlow*, the heat segment is seen on temperature levels of district heating grids at around 60–130 °C [173]. The efficiency of process technologies that generate power from heat at this temperature is very low (Organic Rankine Circle (ORC) process—well below 20% [95]) and economic feasibility is usually not possible.

P2H can represent any technology that converts electricity into heat. On a household level, this may be a heat pump or a heating rod, while high-voltage electrode boilers can be an example for a P2H plant at a utility level. P2G is a technology where hydrogen is produced via electrolysis and can be further processed via methanation to natural gas. If the infrastructure connection and the demand allow it, the resulting heat can also be utilized, which makes the technology to P2GH. If there is no option for waste heat utilization, the heat term remains 0. It has to be stated that the P2G plant, if operated as electrolysis plus methanization, does not consider the necessity of a CO_2 source. G2PH is the abbreviation of gas to power and heat. Examples of this technology are (micro) gas turbines, combined cycle gas turbines, fuel cells or ICE based combined heat and power units (CHP). Analogous to the P2GH technology, the heat term only applies if the occurring heat can be utilized. The last implemented hybrid element is G2H. This can be a gas boiler for heating purposes.

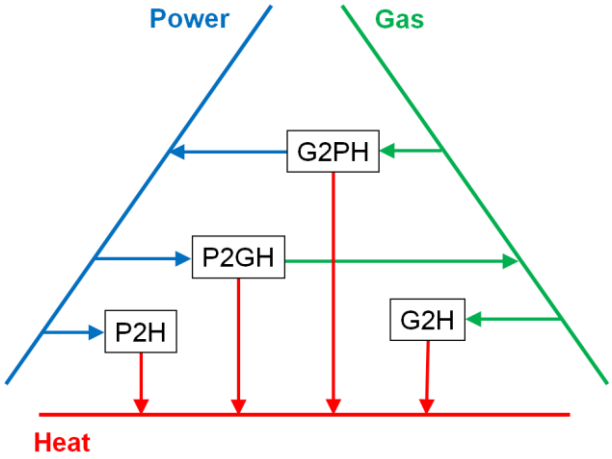

Figure 3-43: Implemented hybrid element pathways in HyFlow.

All four aforementioned hybrid elements and their implementation in hybrid grids must be further characterized. The necessary parameters to define a hybrid element in the *HyFlow* modelling framework are displayed in the following Table 3-10

Table 3-10: Characterization parameters for hybrid elements.

Parameter	**Value [Unit]**	**Description**
Maximum power	positive [W]	Defines the maximum power of a hybrid element. The maximum power is always related to the input factor (e.g. for a P2GH element a maximum power would relate to the input electricity power).
Positive ramp rate	positive [1/h]	The positive ramp rate defines the maximum increase of hybrid element power within a one-hour-period. A value of 1 for a positive ramp rate means that the maximum power of the hybrid element is available within one hour.
Negative ramp rate	positive [1/h]	The negative ramp rate defines the maximum decrease of hybrid element power within a one-hour-period.
Electricity conversion efficiency	$\in \mathbb{R}$ [1]	The electricity conversion efficiency defines the percentage of maximum power to be converted into electricity. The following values for conversion efficiency power are possible: Conversion efficiency = 1: electricity is an input factor Conversion efficiency -1<η<0: electricity is generated Conversion efficiency = 0: no electricity is generated
Heat conversion efficiency	$\in \mathbb{R}$ [1]	The heat conversion efficiency defines the percentage of maximum power to be converted into heat. The range of values for efficiency heat conversion slightly differs from the electricity conversion, because conversion efficiencies exceeding the value of 1 are allowed for heat pumps.
Gas conversion efficiency	$\in \mathbb{R}$ [1]	The gas conversion efficiency defines the percentage of maximum power to be converted into gas. The range of values for efficiency gas conversion is analogous to the efficiency of electricity conversion.
Operation mode	0/1	This parameter defines if the hybrid element operates in response to a specific cell's residual load (parameter = 0) or in response to the electrical residual load of the whole system (parameter = 1). System serving hybrid elements are only activated if the system's residual load exceeds a limit value, in order to avoid activation/deactivation for minor residual loads.

In contrast to energy storage technologies, ramp rates are considered for large hybrid elements. This means that a threshold value for a nominal power of hybrid elements must be defined. All hybrid elements above that value consider the specified ramp rates and the elements not exceeding the limit neglect any ramp rates.

3.5.10 Program Work Flow

The following section describes the workflow of *HyFlow*. It shows first which input parameters need to be specified by the user and second how the calculation process is structured and performed by the program. The third part shows the wide variety of results that can be obtained by *HyFlow*.

There are various input parameters that have to be defined by the user of *HyFlow*. Generally, there are two ways to submit the necessary data: via the input mask in the interface function directly in MATLAB®, or via predefined EXCEL® files. General information, such as the number of cells at each level, the tolerances of abort conditions for iterative calculations and other constant values like the slack voltage, pressure and temperature are defined in MATLAB® directly. Time-dependent values like residual loads of all relevant cells, the corresponding distribution of HE and ESS and their characteristics, as well as all information given in matrices, are to be defined in EXCEL for practical reasons. After the EXCEL® files are read by MATLAB®, a function checks all input data for possible errors automatically. If a deviation is detected, MATLAB® displays an error message and shows the user which data is not supplied in the correct form. Figure 3-44 presents an overview of the necessary input data and the output parameters delivered after the calculation sequence. Table 3-5 (Grids), Table 3-9 (ESS) and Table 3-10 (HE) in section 3.5 give an overview of the necessary characteristics in order to fully describe the necessary elements in *HyFlow*. The mentioned elements need to be assigned to the desired cell, which works through the self-explanatory predefined EXCEL® files.

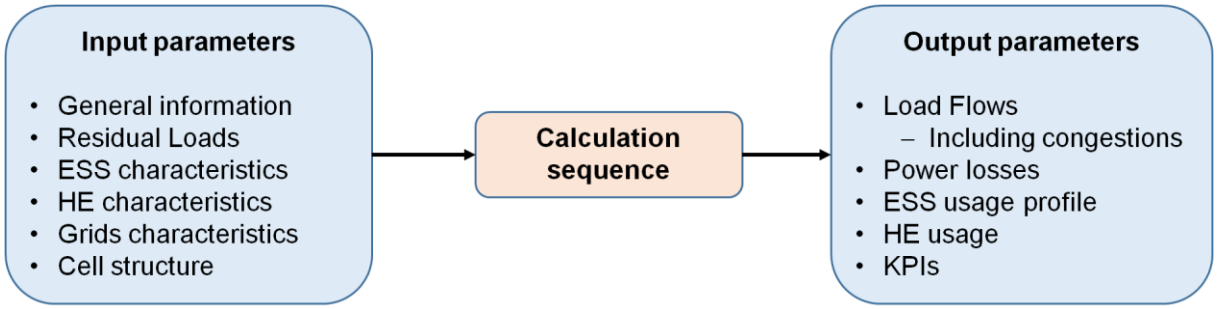

Figure 3-44: Input – and output parameters of HyFlow

The presented program workflow is designed to follow the introduced cellular approach and to balance supply and demand at the lowest possible cell-level. This approach is present at every system level of *HyFlow*, even though the HE and ESS are exclusively implemented in level-1 cells. Only the residual loads, which cannot be balanced on the lowest level are transferred to the superior cell level. If a local energy source of any carrier is available, it will always be prioritized over obtaining energy from the superior grid level. However, an important condition is that all energy demand needs to be met at any time. If this condition is violated for any reason, an error occurs. After the user has specified the system and has provided the necessary residual loads, network connections, ESS – and HE elements, the actual calculation process begins. The labeled steps in the calculation sequence are described step by step and illustrated in Figure 3-45 and Figure 3-46.

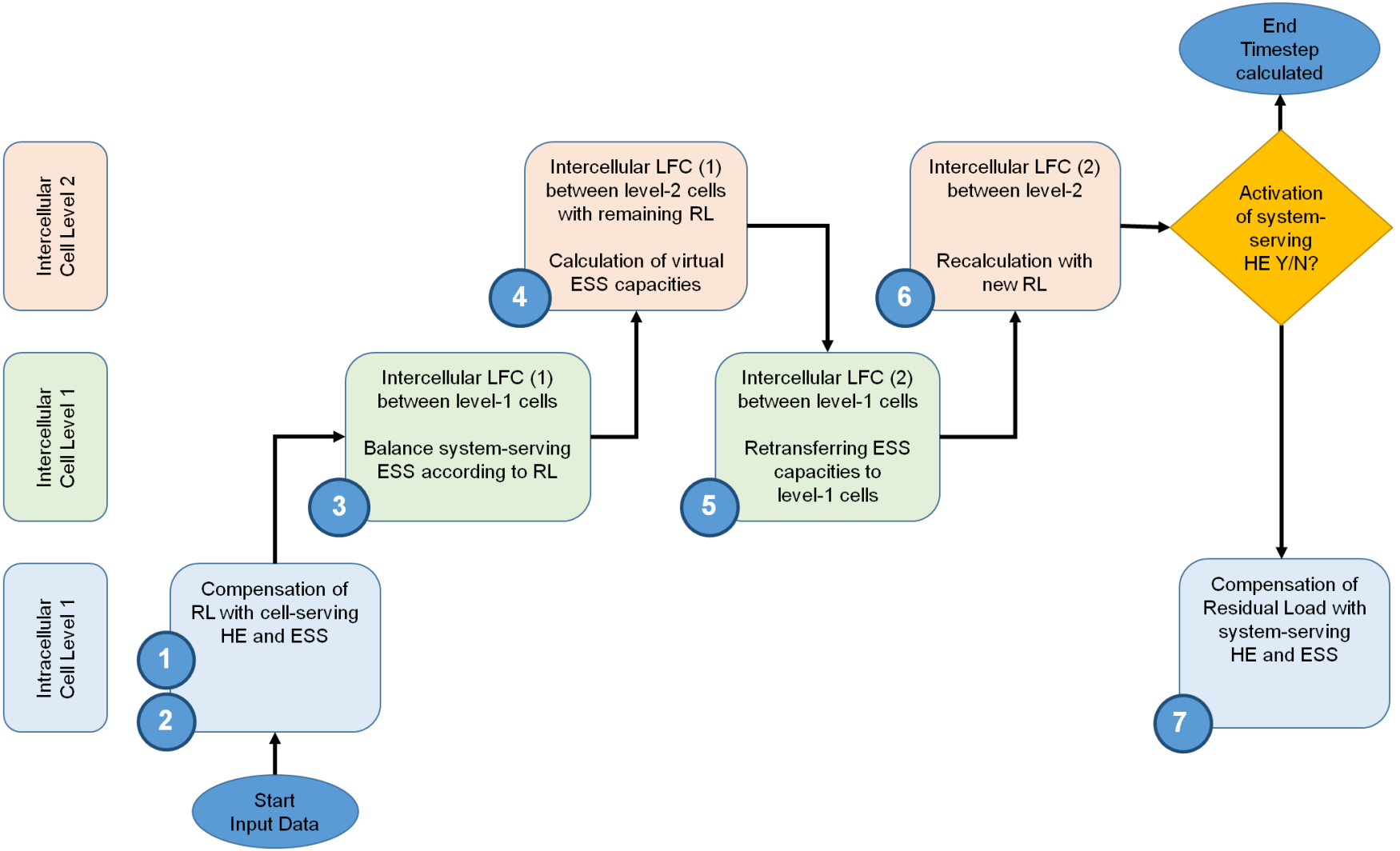

Figure 3-45: Calculation sequence of HyFlow – Illustration 1

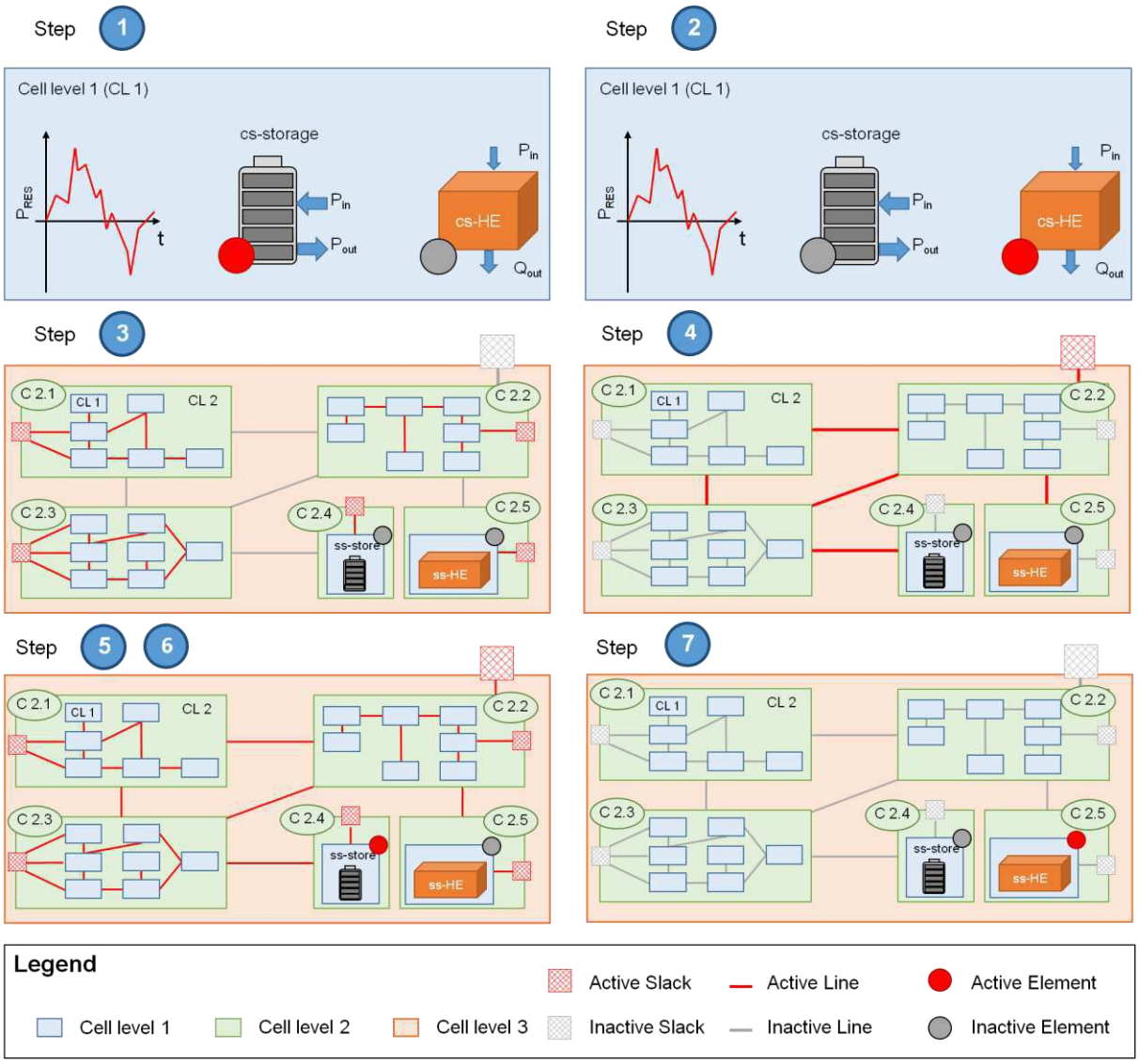

Figure 3-46: Calculation sequence of HyFlow – Illustration 2

Step 1—Compensation with cell-serving storage

In the first step, any available storage in a level-1 cell is used to minimize the residual load of the corresponding level-1 cell. The algorithm that is used, is the “greedy-algorithm”: As soon as the residual load of a cell is negative and storage capacity is available, the excess energy generation is stored. When the residual load turns positive again, energy is immediately prioritized from the storage over the grid. The difference between a cell-serving element and a system-serving element is the associated control strategy. While cell-serving elements minimize solely the residual load of the containing cell (greedy algorithm), the system-serving elements operate based on the residual load of the overall system boundaries (level-3), by using the greedy algorithm as well. A graphic illustration of all process steps is shown in Figure 3-46. All elements marked in red are active in the corresponding process step.

The input parameters are the original residual load and the ESS characteristics according to Table 3-9, the output is the operation scheme of the ESS including the stored energy (SOE) and the charge/discharge power and the modified residual load.

Step 2—Compensation with cell-serving hybrid elements

The usage of cell-serving hybrid elements within a level-1 cell is the next priority. This means that unbalanced residual loads paired with a full/empty storage unit of the same energy carrier lead to the use of cell-serving hybrid elements. For example, a negative residual load in the electricity network combined with full electricity storage can lead to the usage of a heat pump, if there is either a heat demand in the cell or a heat storage system that is not fully charged. In general, three control strategies are implemented in *HyFlow* for cell-serving P2H, G2H and G2PH hybrid elements. The control strategy of P2H as well as G2PH hybrid elements depends on various factors such as the electrical - and heating residual load, and storage level of all energy carriers involved. A G2H element balances heat demand and, if possible, charges the heat storage. It is also possible that a hybrid element is not used as a flexibility option, but as a conventional energy supply source. In the example of a G2H element (e.g., gas boiler) and no connection to the heating grid, the heat demand is supplied over the gas grid.

The mathematical description of an exemplary P2H device is described below: If the electrical residual load $P_{Res[t]}$ is negative after using the cell-serving ESS, while the heat demand $Q_{Res[t]}$ is positive and the absolute value of the residual load $\left|P_{Res[t]}\right|$ multiplied by the conversion efficiency from power to heat η_{PQ} is the same or greater than the actual heat demand $Q_{Res[t]}$, the total heat demand can be met by the residual load of the electricity $P_{Res[t]}$. This means that the new heat demand in this time-step $Q_{Res,new[t]}$ is 0, while the residual load $P_{Res,2[t]}$ becomes less negative by adding the converted power to the previous value of $P_{Res[t]}$. Therefore, the variable is overwritten for reasons of the further calculation process.

$$\left\{P_{Res,2[t]} \wedge Q_{Res,new[t]} \left| \left(P_{Res[t]} < 0 \ \wedge \ Q_{Res[t]} > 0\right) \wedge \left(\left|P_{Res[t]}\right| \cdot \eta_{PQ}\right) \geq Q_{Res[t]}\right)\right\}$$

$$Q_{Res,new[t]} = 0 \tag{3-75}$$

$$P_{Res,2[t]} = P_{Res[t]} + \frac{Q_{Res[t]}}{\eta_{PQ}} \tag{3-76}$$

$$P_{Res,2[t]} = P_{Res[t]} \tag{3-77}$$

The Equations 3-78 to 3-80 work under the same condition than before, with the exception that the absolute value of the residual load $\left|P_{Res[t]}\right|$ multiplied by the conversion efficiency from power to heat η_{PQ} is now smaller than the heat demand $Q_{Res[t]}$. This implies that the

remaining residual load of power $P_{Res,2[t]}$ amounts 0 at the end of the time step and the new remaining heat demand $Q_{Res,new[t]}$ is reduced by the converted power multiplied with conversion efficiency η_{PQ}.

$$\{P_{Res,2[t]} \wedge Q_{Res,new[t]} \mid (P_{Res[t]} < 0 \wedge Q_{Res[t]} > 0) \wedge (|P_{Res[t]}| \cdot \eta_{PQ}) < Q_{Res[t]})\}$$

$$P_{Res,2[t]} = 0 \tag{3-78}$$

$$Q_{Res,new[t]} = Q_{Res[t]} - (|P_{Res[t]}| \cdot \eta_{PQ}) \tag{3-79}$$

$$P_{Res,2[t]} = P_{Res[t]} \tag{3-80}$$

The residual power $P_{Res[t]}$ can also be converted to heat in a cell-serving P2H element, if no heat demand occurs or has been met by the hybrid P2H element before already. This is possible provided that a heat storage unit is defined. If the heat storage unit is not fully charged at the time step of the calculation and surplus power is available, it can be stored as heat. There are two options again: Equations 3-82 and 3-83 describe the situation, where the energy of the residual power $P_{Res[t]}$ times the conversion factor η_{PQ} is greater than the remaining storage capacity.

$$\left\{P_{Res,new[t]} \wedge SOC_{Q,new[t]} \mid \left(P_{Res[t]} < 0 \wedge (Q_{Res[t]} < 0 \vee Q_{Res,new[t]} = 0)\right) \wedge (SOC_{Q[t]} < SOC_{Q,max}) \wedge \left(\frac{|P_{Res[t]}|}{t_{int}} \cdot \eta_{PQ} > (SOC_{Q,max} - SOC_{Q[t]})\right)\right\}$$

$$t_{int} = \frac{timesteps}{hour} \tag{3-81}$$

$$P_{Res,new[t]} = P_{Res[t]} + \frac{(SOC_{Q,max} - SOC_{Q[t]}) \cdot t_{int}}{\eta_{PQ}} \tag{3-82}$$

$$P_{Res,2[t]} = P_{Res[t]} \tag{3-83}$$

$$SOC_{Q,new[t]} = SOC_{Q,max} \tag{3-84}$$

The second option is described by Equations 3-85 and 3-86: the energy of the residual load of electricity $P_{Res[t]}$ is smaller than the available heat storage capacity. This results in a new residual load $P_{Res,new[t]}$ of 0 and a new heat storage content $SOC_{Q,new[t]}$ described by Equation 3-85.

Another option for the P2H elements in *HyFlow* is the usage of stored electricity (in ESS of cell level 1) for the heat demand as well. This option and other hybrid elements such as G2PH or G2H work analogous to the described example below.

$$\left\{P_{Res,new[t]} \wedge SOC_{Q,new[t]} \,\middle|\, \left(P_{Res[t]} < 0 \;\wedge\; \left(Q_{Res[t]} < 0 \;\vee\; Q_{Res,new[t]} = 0\right)\right) \wedge \left(SOC_{Q[t]} < SOC_{Q,max}\right) \wedge \left(\frac{\left|P_{Res[t]}\right|}{t_{int}} \cdot \eta_{PQ} < \left(SOC_{Q,max} - SOC_{Q[t]}\right)\right)\right\}$$

$$SOC_{Q,new[t]} = SOC_{Q[t]} + \left(\left|P_{Res[t]}\right| \cdot t_{int} \cdot \eta_{PQ}\right) \tag{3-85}$$

$$P_{Res,new[t]} = 0 \tag{3-86}$$

The output parameters of step 2 are the modified residual load and the usage profile of any possibly used cell-serving HE.

Step 3—Compensation intercellular level 1

The aim of this step is to balance the residual load of each level-2 cell by shifting energy between level-1 cells in the assigned level-2 cell. All level-1 cells within the level-2 cell are considered and the load flow calculations described in section 3.5 are performed for all energy carriers.

Additionally, system-serving ESS of other level-1 cells in the same level-2 cell can be accessed by other cells, in order to balance the remaining residual load of the containing level-2 cell. Cell-serving storages can only be accessed by the containing cell itself and are not considered in this step. The residual load of the total level-2 cell contains network losses within the grid between level-1 cells. The detailed description of this step and the performed load flow calculations, including the necessary equations, can be found in Section 4.3 load flow calculations.

The output parameters of step 3 are the remaining residual load after the intercellular energy exchange between level-1 cells, the current SOE of all ESS and the remaining charge/discharge power of the ESS.

Step 4—Compensation intercellular level 2

When balancing within level-2 cells is completed, the resulting level-2 residual loads (in consideration of calculated losses of transport lines, losses of storages and hybrid elements) are used to calculate a new load flow calculation between level-2 cells, analogous to the level-1 LFC. Since the placement of ESS and HE is exclusively reserved for level-1 cells, ESS on level 2 are only existing virtually as the sum of all contained level-1 storages of the corresponding level-2 cell. The calculation process and the "greedy-algorithm" is used in the exact same way as described in step 1. The residual load of the level-3 cell also contains network losses within the grid between level-2 cells. If energy storage is used in this step, any changes in storage capacities have to be retransferred to level-1 cells, which requires a recalculation of both load flow calculations. This process is performed in the following step 5 and 6.

The output parameters of step 4 are the preliminary required load flows in and out of the level-2 slack nodes. The virtual storage used, which will be retransferred to the location of the physical ESS.

Step 5 and 6—Transfer of virtual storage and recalculation

Since only "virtual storages" are used in step 4, any usage of the virtual storage units must be retransferred to level-1 cells. Therefore, the charging/discharging has to be carried out in all level-1 cells, where the physical storages are placed. If more than one level-1 cell has free capacities in energy storage, the distribution is divided among them in an iterative process that aims to fill storage units to the same amount. An example of this process is described in Table 3-11. This process step, however, also affects the residual load of selected cells and load flows within the level-2 cell. To cope with these changes, functions similar to step 3 and 4 have to be executed again, to update residual loads, load flows and grid losses. These are also the output parameters of step 5 and 6.

Step 7—Calculate system-serving hybrid element demand

System serving hybrid elements are only activated or deactivated if there is a residual load in the level-3 cell. In case of a power shortage (positive residual load), available G2PH hybrid elements are either ramped up to balance demand or ramped up to maximum power generation if power demand exceeds maximum power. Furthermore, all P2GH hybrid elements are ramped down to the lowest possible power consumption. In case of an excess of power (negative residual load), opposite measures are taken. All G2PH hybrid elements are ramped down to their minimum output, whereas P2GH and P2H hybrid elements are activated. If the electric residual load is close to 0 (within a specified tolerance), all system-serving G2PH and P2GH hybrid elements are ramped down to their lowest possible power.

If system-serving hybrid elements are utilized to balance the overall residual load, steps 1 to 5 must be repeated, because they affect all other load flows significantly.

The usage of a system-serving HE is subject of a control strategy itself. Once the trigger value of the level-3 load flow is exceeded, system-serving HEs are activated. Generally, HE are divided into small decentralized elements (no ramp rates considered) and large, central HE (ramp rates considered). The control strategy is set to use the class of large, central HE, because in reality, it is much easier to use a limited number of large plants like a P2G plant over a large number of small HE (like heat pumps). Only if the capacities of these large, central HE are exhausted, smaller, decentral HE are used for this purpose. This preference can, however, be deactivated as well. Additionally, there has to be a selection process in order to choose which HE is activated/deactivated if the total system capacity of HE exceeds the need to approach a residual load of 0 of the overall system. This measure is in accordance with the principle of the cellular approach to balance the residual load on the lowest possible level in order to minimize the load flows over the slack node. HE in level-2 cells with the highest load flow with the same sign as the level-3 load flow are the first to be used.

In order to make the whole process more understandable, a step-by step procedure is demonstrated with the help of a numeric example. All values of this example are presented in Table 3-11. There are four level-2 cells in the overall system boundary (level-3). All four level-2 cells have a negative residual load $RL_{Rem,2}$, with a total sum of -1,689 MW, which is the total load flow exported of the overall system $LF_{Rem,3}$.

In step 1, the first task is to determine which HE should be used to which extent. In orer to do so, all load flows of level-2 cells in the current time-step are identified. The level-2 cell with the highest contribution to the remaining level-3 load flow is prioritized to supply its system-serving HE capacities. In this case, the residual load of cell 4 contributes most to the remaining load flow, with a negative residual load of -994 MW. This implies a usage of the corresponding HE until its remaining residual load matches with the next cell, which is the case at -397 MW (cell 3). The difference of 597 MW can therefore be used to reduce the level-3 load flow to -1,092 MW.

Step 2 continues to reduce the level-3 load flow by using the HE capacity of level 4 again. Even though two cells (cell 3 and 4) have the same contribution to the level-3 load flow only cell 4 is assigned HE capacities. Since cell 3 doesn’t have any remaining HE capacities, an additional 219 MW in power is used from cell 4, before the residual load of cell 4 equals the residual load of cell 2. Through this measure the level-3 load flow is reduced to -872 MW.

In step 3 the HE capacities of cell 2 and cell 4 are used until the remaining residual load matches with cell 1 with -120 MW. Both residual loads of cell 2 and 4 can be reduced from -178 MW to -120 MW. This measure allows to further reduce the exported level-3 load flow to -757 MW.

Step 4 is further divided in three substeps 4.1, 4.2 and 4.3. In step 4.1 the remaining level-3 load flow of -757 MW is divided by the three remaining cells with HE capacities (cell 1, 2 and 4). This is due to the fact that all three cells with remaining HE capacities have the same remaining residual load of -120 MW. The algorithm aims to use all these HE capacities to the same extent (-757/3) = -252 MW. However, cell 1 and 2 are able to supply the requested power, but cell 4 can only contribute another -126 MW to reduce the level-3 load flow, before its HE capacities are exhausted. This implies, that the difference between the necessary -252 MW and the -126 MW has to be supplied by the other two cells, which is possible for both of them. Therefore, it is possible to completely eliminate the level-3 load flow by the usage of the HE. The results of the individual steps are summed up before the calculated values are implemented in the further calculations of *HyFlow*. The overall results of the example are shown underneath.

- $LF_{Rem,3}$: 1689 MW → 0 MW

By the usage of HE in the following level-2 cells

- Cell 1: 315 MW out of 400 MW (78.8 %)
- Cell 2: 373 MW out of 400 MW (93.3 %)
- Cell 4: 1000 MW out of 1000 MW (100 %)

After all time steps are calculated, a plausibility check is performed by calculating a separate energy balance for each time-step. If a defined tolerance is exceeded, *HyFlow* displays a warning message. Equation 3-87 displays the simplified formula of the energy balance.

$$LF_3 = P_{Res,sum} + \Delta ESS_{sum} + HE_{sum} + P_{Loss,Grid,sum} + P_{Loss,ESS,sum} \quad (3\text{-}87)$$

Table 3-11: Example of the HE capacity usage

	Cell (level-2)	$RL_{rem,2}$	$Cap_{HE,rem}$	$Cap_{HE,max,step}$ (used)	$LF_{rem,3}$
		MW	MW	MW	MW
Step 1	1	-120	400		-1689
	2	-178	400		
	3	-397	0		
	4	-994	1000	597 (597)	
Step 2	1	-120	400		-1092
	2	-178	400		
	3	-397	0	0 (0)	
	4	-397	403	219 (219)	
Step 3	1	-120	400		-872
	2	-178	400	58 (58)	
	3	-397	0	0 (0)	
	4	-178	184	58 (58)	
Step 4.1	1	-120	400	400 (252)	-757
	2	-120	342	342 (252)	
	3	-397	0	0 (0)	
	4	-120	126	126 (126)	
Step 4.2	1	132	148	148 (63)	-126
	2	132	90	90 (63)	
	3	-397	0		
	4	6	0		
Step 4.3	1	195	85		0
	2	195	27		
	3	-397	0		
	4	6	0		

HyFlow gives offers the user a wide range of applications, possible results and corresponding visualizations in case studies in a boad variety of case studies. Depending on the focus of the user, various priorities can be defined. It is possible to model the status quo of a given region (ranging from a small number of consumers, to large regions or states), with all the load flows (for the energy carriers electricity, natural gas and district heating) the user wants to examine.

The focus can be adopted to the task at hand. Whether a task requires information about the voltage level of a critical power line within a distribution network, on the degree of self-sufficiency of a region or on the effects of flexibility options like storage or sector coupling technologies on the energy system. This evaluation of the chosen control strategy (grid-relieving algorithms, self-sufficiency optimized algorithms) which allows us to answer the question of whether a system-serving environment for energy storage units and hybrid elements can have positive effects on the overall system. Additionally, the operation profiles of energy storage systems and hybrid elements can be displayed. This allows the user to design necessary flexibility options. Information regarding the necessary capacities, powers or load hours of HE or total cycles for ESS are also very important for following economic considerations.

All pressure levels, voltages, load flows, power losses, etc. can be displayed, analyzed and evaluated by the user. Another important result is the residual load of the total system (level-3 cell) and the maximum power in the slack-node over the analyzed time frames in order to design infrastructure properties of the network connections of hybrid elements. These results are processed in suitable charts, to provide an overview about stored, consumed and produced power for each energy carrier and comment on how residual loads may be minimized by the use of storages and hybrid elements.

4 APPLICATION RESULTS

In this chapter, the described methodology of section 3 is applied to a variety of selected use cases. The first part consists of the results of the described PV storage system sizing methodology for individual household types (Single-Nodal case studies). In total, 63 predefined household load profiles with individual electricity loads are investigated. The results are technical optima in terms of DSS under the constraint of minimal system size configuration, as explained in section 3.4.6. Additionally, the household load profiles are complemented with load profiles from heat pumps and electric vehicle charging to evaluate the effects of these additional demand types. The outcome is divided into a technical sizing approach and an additional economic assessment as comparison to the introduced technical sizing approach.

Secondly, three case studies with energy systems ranging from a single stub-line to a whole region are investigated within the Multi-Nodal methodology *HyFlow*. The main purpose of the presented use cases is to give an overview of expected results and deepen the understanding of the modelling frameworks functionality.

4.1 Single-Nodal Case studies

The used household load profiles are generated with the help of the *LoadProfileGenerator* developed by Pflugradt [44]. The *LoadProfileGenerator* combines statistical methods with the physical and psychological demand model, developed by Dörner [45,46]. One of the major advantages is the large number of detailed predefined household types. Additionally, there is a wide range of customizing options to modify load profiles in order to fit individual purposes. In this work, the 63 predefined load profiles of households with different occupant compositions are used without changes, for reasons of comparability. They range from single-person households of all ages, from students to seniors, over large families with and without children, employed and unemployed adults to Multi-Generation homes. A complete list of all predefined load profiles and their configuration can be found in [44]. The resulting load profile creates separate load profiles of all appliances used by the specific user group with a temporal resolution of one second. All of these appliances are aggregated to a single overall household load profile. Time frames of 900 seconds are used, in order to create the 15-minute values for the whole year. An exemplary household load profile for a random week is shown in Figure 4-1, in the top row on the left. One can see the relatively low baseload of around 100 Watts and power peaks of around 3.8 kW in this example. The 1st case study consists of the load profiles from the mentioned 63 predefined households, respectively.

The 2nd case study uses the same household profiles and adds a load profile of heat pumps to it: the annual space heating demand is determined based on the number of residents in the corresponding household and data of the average natural gas demand for space heating and hot water purposes, dependent on the household size published by Austria's Statistic Agency in [174]. Depending on the number of residents in a household the average heating demand varies between around 9 MWh for Single Person households and over 15 MWh for households with five persons. Assuming an average coefficient of performance of 3.2, the annual electricity demand of heat pumps amounts to between 2.8 and 4.7 MWh. The actual load profile is calculated with the help of temperature data, according to the methodology published by VDEW Germany, which is described in [175]. It uses the measured outdoor temperature to derive the daily heat demand by determining the daily average mean temperature, which is demonstrated in Equation 4.1. Due to thermal inertia, it does not just take the temperature of the specific day into account, but also considers the temperature on previous days.

$$T_{avg,(d)} = 0.5 \cdot T_{avg,(d)} + 0.3 \cdot T_{avg,(d-1)} + 0.15 \cdot T_{avg,(d-2)} + 0.05 \cdot T_{avg,(d-3)} \qquad (4\text{-}1)$$

After determining the daily mean temperatures, the coefficients of [175] are used to calculate the daily energy demand for space heating and hot water. This value is combined with the load curve of the day, dependent on the season and multiplied with the coefficient of performance of 3.2. The result for an exemplary week is shown in Figure 4-1, in the top row, on the right. The result is also comparable to other publications like [176,177].

In the 3rd case study a charging profile of an electric vehicle is added to the household load profiles of the 63 household load profiles. The development of the time-resolved charging profile for electric vehicles is based on Thormann et al. [178] They use measured charging data of 21 different EV-models, as published in [179], in combination with a probabilistic approach from Rezaee et al. [180]. This probabilistic approach assigns a random number for each vehicle and takes statistical data such as the mileage, route, consumption, EV-type and feasible charging power at the destination into account. For the used load profile, a state of the art charging behavior of EV users, charging with a maximum power of 11 kW at private charging stations, is selected. In both case studies 3 and 4 with an implemented EV load profile, all households are assigned one electric car, with the same charging behavior, independently of the household type. An example of an EV charging profile is depicted in Figure 4-1, in the lower row, on the left. One can see that the maximum power in this example is much higher compared to other household appliances, due to the higher maximum charging power of 11 kW.

In the 4th case study all three separated load profiles are combined in the overall load profile. This means that all 63 households are assumed to use a heat pump and an EV for mobility needs. In the following case studies the three load profiles are abbreviated as follows: LP stands for the synthetic household load profile, HP is the label for the heat pump load profile and EV stands for the charging profile of an electric vehicle. Table 4-1 aims to summarize these case studies and shows the distribution of the annual electricity demand for all load profiles.

Table 4-1: Summary of conducted case studies and corresponding electricity demand distribution

Single-Nodal	Included load profiles	Annual demand in MWh
Case study 1	LP	1.04 – **2.58** – 7.81
Case study 2	LP+HP	3.87 – **6.48** – 12.03
Case study 3	LP+EV	3.45 – **5.06** – 10.30
Case study 4	LP+HP+EV	6.36 – **8.97** – 14.52

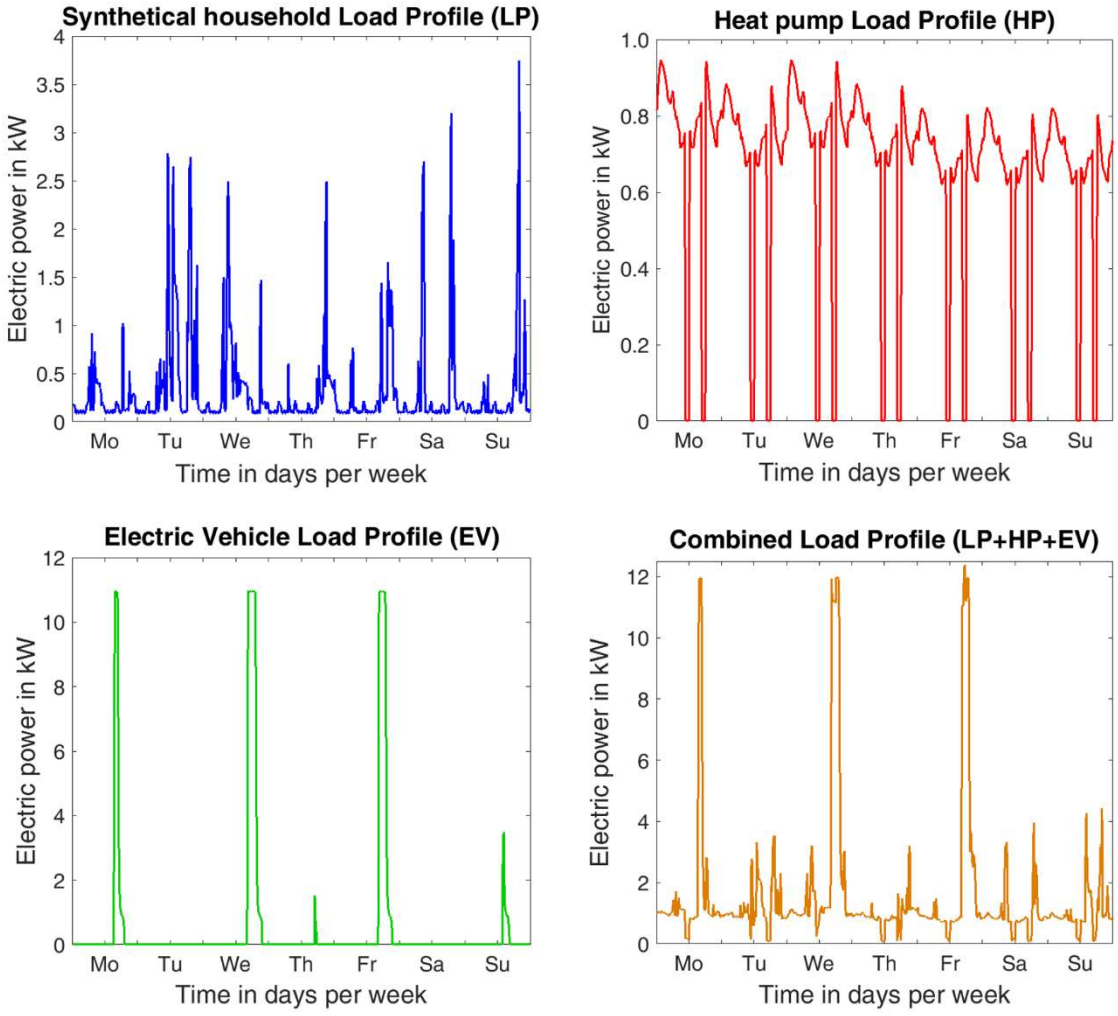

Figure 4-1: The three load profiles (LP, HP, EV) and a combination of them for an exemplary week

4.2 Single-Nodal optimization results

The results for all case studies are divided into the technical sizing approach and the economic assessment, which is solely performed for comparative reasons. Both sizing approaches are performed for all four case studies.

4.2.1 Technical Sizing Results

The technical sizing results are based on the described methodology of section 3.4.6. All parameters are shown for the intersections of the optima function with the DSS indifference curves at levels of 30 %, 50 %, and 70 % to reach comparable results between scenarios and household types. This means that all system configurations shown reflect the minimum PV storage system size to reach the defined DSS levels. Additionally, it has to be noted that all battery system sizes represent the usable battery size. In order to transfer the gained results into total battery sizes, the depth of discharge (DoD) of an individual battery system has to be considered. The relationship between the total battery size, the usable battery size, and the DoD is shown in Equation 4.2. Common DoD levels for stationary PV-battery systems range between 80 - 90 %.

$$Cap_{ESS,total} = \frac{Cap_{ESS,useable}}{DoD} \tag{4-2}$$

The technical results distributions are illustrated in an overview of all system configurations and as box plot diagrams. Box plot diagrams consist of a red line representing the median value of the distributed values, while values inbetween the lower and upper quartile are within the blue boxes. The minimum and maximum value of the data sample is represented by the lower- and upper whisker (black lines). Values outside 1.5 times the IQR (interquartile range) are marked as outliers by a red cross. The IQR is defined as the difference between the higher quartile and the lower quartile and represents the medium 50 % of the data. Additionally, the numeric minimum, maximum and median values for all DSS constraints are shown in tables above the box plots.

4.2.1.1 Case Study 1 - Synthetic Load Profiles (LP)

The general distribution of all technical design optima for the synthetic load profiles is shown in Figure 4-2. All 63 predefined households are depicted in this illustration for the three DSS constraints. Each blue circle represents an ideal system configuration to reach the requested DSS level of 30 %. Especially at such DSS levels, where the distribution is quite narrow, some system configurations are identical to others, which results in fewer markers than the number of analyzed households.

At higher DSS-level constraints, the results are fairly strongly scattered, as seen at the yellow circles in Figure 4-2. Equally noticeable is the much wider variation range of the normalized battery size compared to the relatively narrow variation in the normalized PV system size, especially at lower DSS-levels.

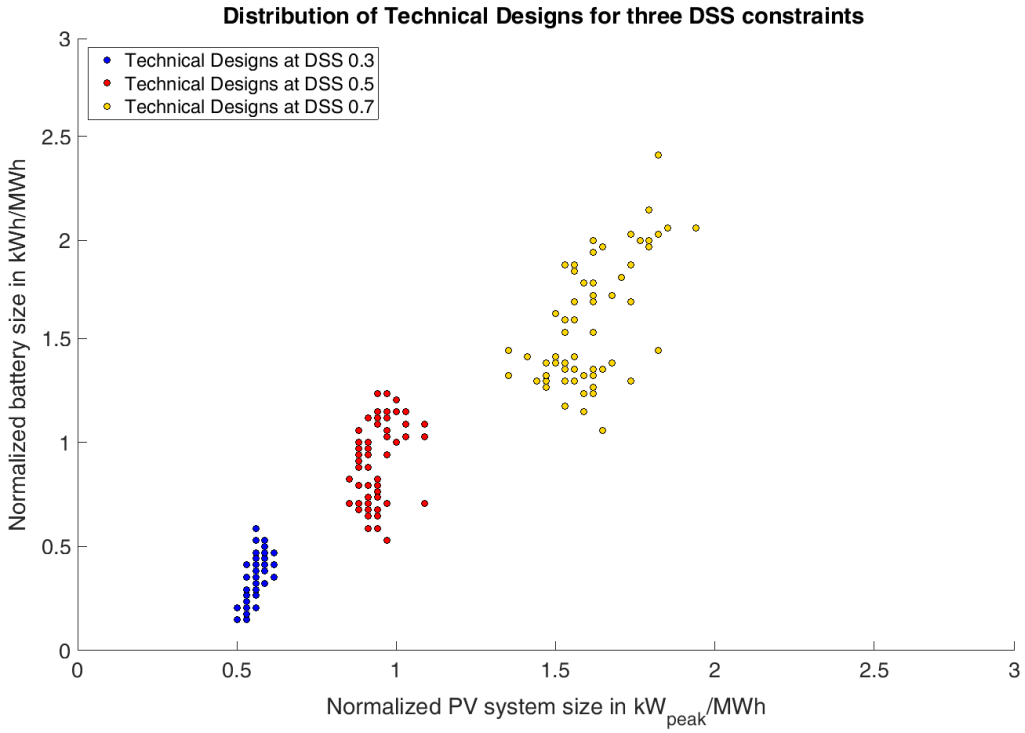

Figure 4-2: Technical design distribution results for all 63 synthetic load profiles and three DSS-level constraints (blue – DSS=0.3, red - DSS=0.5, yellow – DSS=0.7)

Table 4-2 shows the numeric results, complemented by the graphic illustration of Figure 4-3, the corresponding box plot diagram. The whiskers confirm the much higher variety in results for the battery sizes, compared to the narrow distribution in the PV system sizes. The PV/Battery ratio of the ideal technical size steadily declines with growing DSS-level constraints. While the median ratio for DSS 0.3 is 1.89, the value drops to below one for levels of 0.7. Additionally, it has to be noted that the absolute system sizes to reach DSS levels of 70 % are relatively low and range between 1.57 kW_{peak} and 1.57 kWh to 11.6 kW_{peak} and 10.6 kWh, with median values of just over 4 kW_{peak} or 4 kWh

Table 4-2: Numeric sizing results for case study 1 (LP)

	DSS 0.3	DSS 0.5	DSS 0.7
	min-**median**-max	min-**median**-max	min-**median**-max
Normalized PV size in kW_{peak}/MWh	0.48 - **0.52** - 0.61	0.85 - **0.94** - 1.09	1.36 - **1.64** - 1.97
Normalized battery size in kWh/MWh	0.12 - **0.27** - 0.61	0.52 - **0.88** - 1.24	1.06 - **1.61** - 2.42
Absolute PV system size in kW_{peak}	0.53 - **1.45** - 3.79	0.91 - **2.42** - 6.86	1.57 - **4.22** - 11.60
Absolute battery size in kWh	0.27 - **0.75** - 2.22	0.85 - **2.22** - 5.98	1.57 - **4.17** - 10.60
Ratio PV/Battery in kW_{peak}/kWh	0.95 - **1.89** - 4.25	0.76 - **1.03** - 1.88	0.76 - **0.98** - 1.57

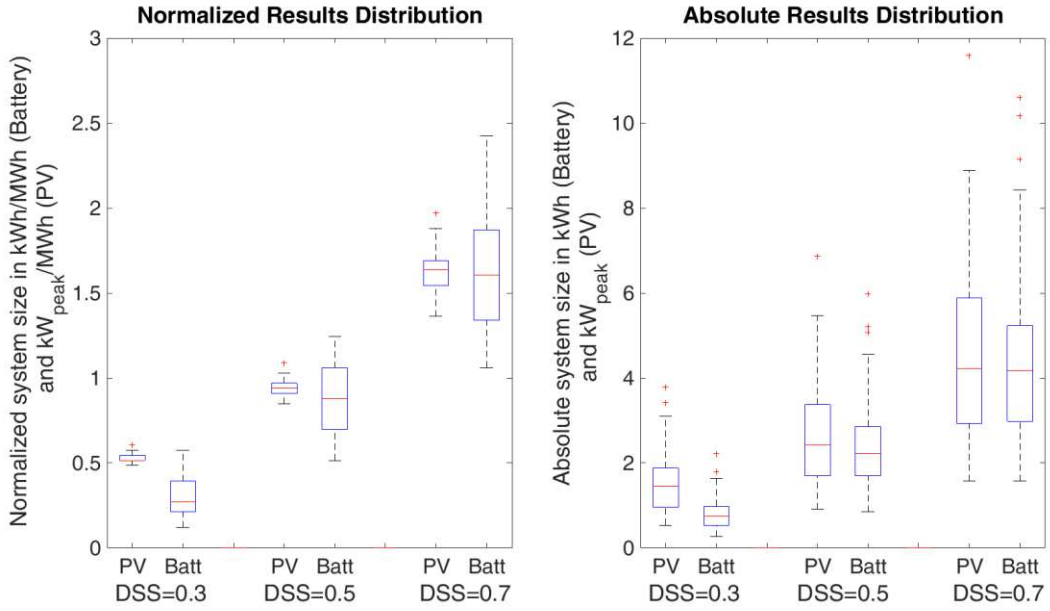

Figure 4-3: Box plot of the PV and battery system size results for LP load profiles

4.2.1.2 Case Study 2 - Synthetic Load Profiles with additional Heat Pumps (LP+HP)

When adding the electric load profiles of heat pumps to the synthetic household load profiles, the distribution of the normalized system design optima changes significantly. While the changes at lower DSS-levels remain moderate, especially the distribution for higher DSS levels (see DSS-level 70 % in Figure 4-4) changes considerably. Compared to the LP results, the necessary normalized PV and battery sizes increase drastically. While most configurations in the LP scenario are below 2 kW_{peak}/MWh in normalized PV system size and below 2 kWh/MWh in normalized battery size, most configurations in the LP+HP scenario are well above these values. This can be explained by the increased electricity demand in the winter months caused by the heat pumps and the lower seasonal PV generation at that time, which makes it generally harder to reach 70 % of self-sufficiency. Only an increase size of PV battery systems can help to achieve these high DSS-levels, due to these unfavorable load profile circumstances.

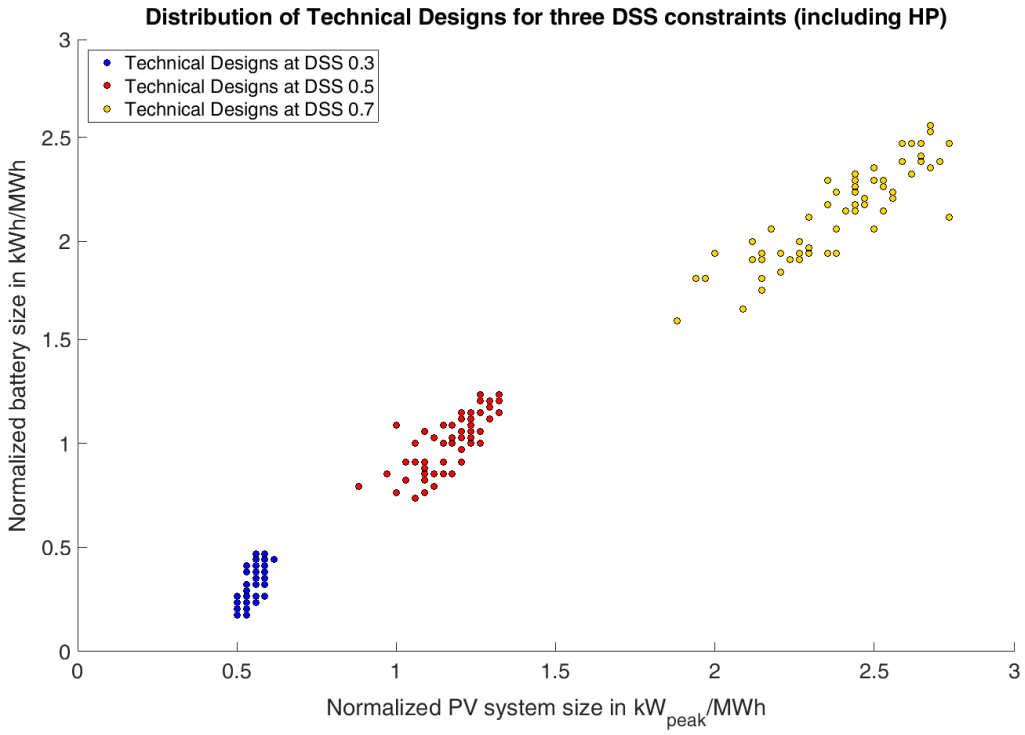

Figure 4-4: Technical design distribution results for all 63 synthetic load profiles with additional heat pumps and three DSS-level constraints (blue – DSS=0.3, red - DSS=0.5, yellow – DSS=0.7)

The increased values for the normalized PV and battery sizes are not the only particularity. It is also noticeable that especially for high DSS-levels all PV/Battery ratios are above 1. This means that the contribution of larger PV systems to the DSS at high levels is still larger than the contribution of an increased battery system size. When analyzing the results of the observed changes between the LP profile and the added heat pumps, one comes to the conclusion that significantly higher normalized PV system and battery sizes are required to reach the same DSS levels. A summary of all values is given in Table 4-3, complemented with a graphic illustration in Figure 4-5.

Table 4-3: Numeric sizing results for case study 2 (LP+HP)

	DSS 0.3 min-**median**-max	DSS 0.5 min-**median**-max	DSS 0.7 min-**median**-max
Normalized PV size in kW_{peak}/MWh	0.48 - **0.55** - 0.61	0.88 - **1.21** - 1.33	1.91 - **2.48** - 2.79
Normalized battery size in kWh/MWh	0.15 - **0.33** - 0.45	0.73 - **1.06** - 1.24	1.61 - **2.18** - 2.58
Absolute PV system size in kW_{peak}	2.23 - **3.56** - 5.83	4.92 - **7.64** - 10.57	10.34 - **16.13** - 22.96
Absolute battery size in kWh	1.20 - **2.04** - 3.44	4.05 - **6.57** - 10.31	8.99 - 1**4.06** - 19.71
Ratio PV/Battery in kW_{peak}/kWh	1.20 - **1.64** - 3.40	0.92 - **1.15** - 1.46	1.04 - **1.13** - 1.31

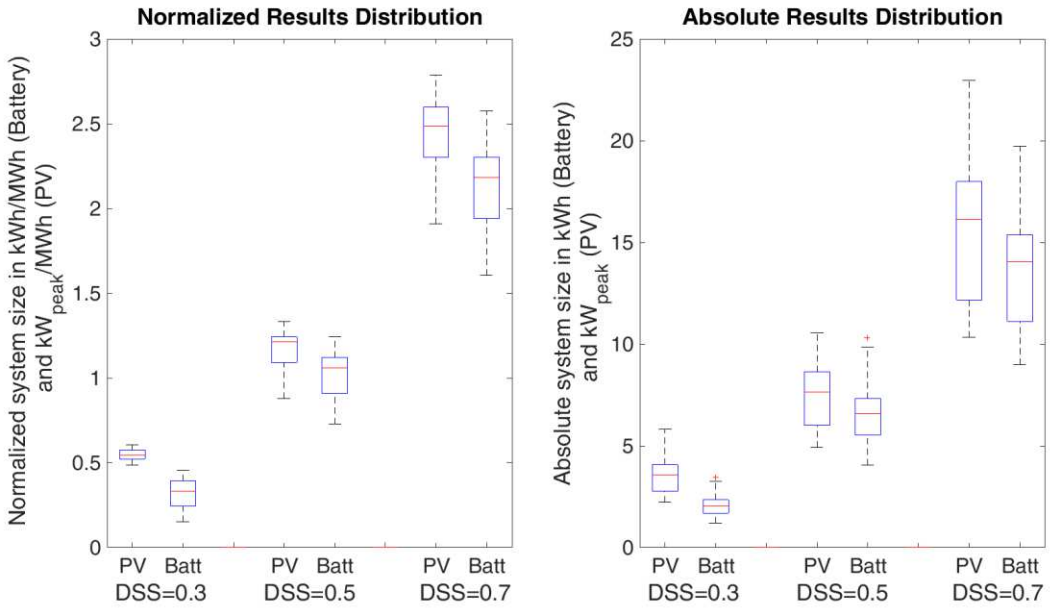

Figure 4-5: Box plot of the PV and battery system size results for LP load profiles with a heat pump

4.2.1.3 Case Study 3 - Synthetic Load Profiles with additional Electric Vehicles (LP+EV)

This section deals with household loads similar to case study 1, with the additional load profile of charging an electric vehicle. As seen in Figure 4-6, the annual energy consumption is in the same range as case study 2 (LP+HP), but the results are very different.

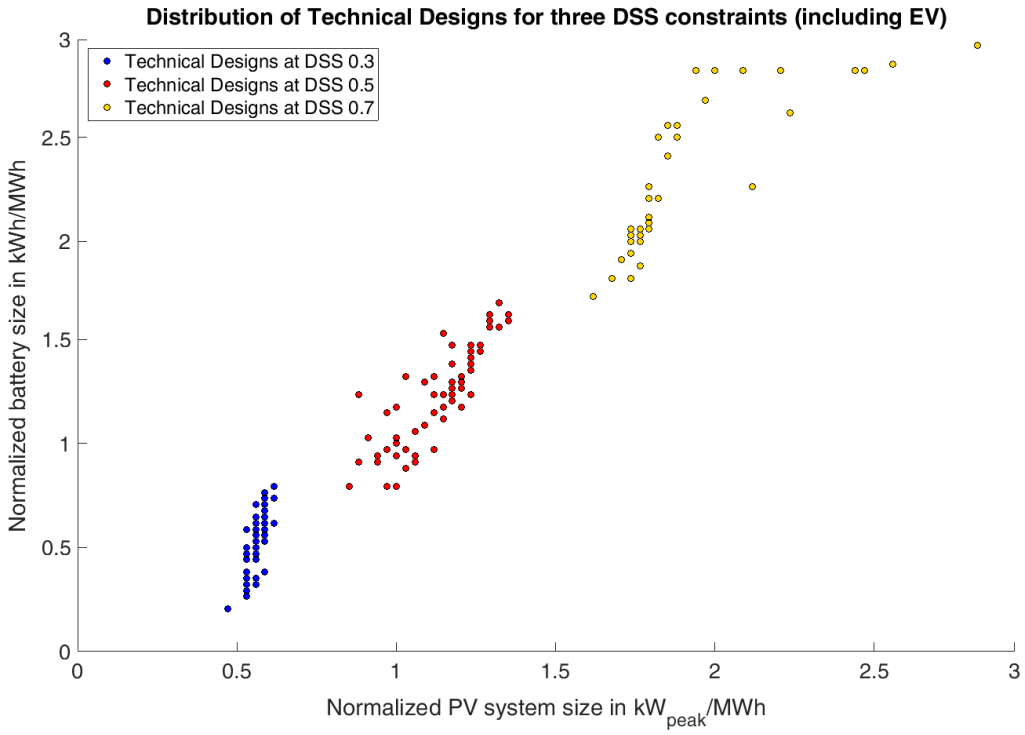

Figure 4-6: Technical design distribution results for all 63 synthetic load profiles with an additional electric vehicle and three DSS-level constraints (blue – DSS=0.3, red - DSS=0.5, yellow – DSS=0.7)

First and foremost, not all households reach the DSS level of 70 % within the normalized size limits of 3 kW_{peak} for PV systems and 3 kWh/MWh for battery systems used in this work. Due to the relatively high power peaks for short periods of time, the PV battery system can sometimes not significantly contribute to meeting this specific demand profile. The overall distribution of all design optima for case study 3 is illustrated in Figure 4-6.

Table 4-4 and the corresponding Figure 4-7 reveal further differences compared to case studies 1 and 2. While the technical optima for higher DSS constraints tend towards a higher PV/Battery ratio for the added heat pump, the opposite development can be observed here. At a DSS level of 30 %, the median PV/Battery ratio is still above 1, but with increased DSS levels, the batteries tend to become larger in size than the PV systems. This case study is the only one, where this effect is observed. At DSS levels of 70 % the median battery size amounts to 2.27 kWh/MWh, while the median PV system size is only 1.85 kW_{peak}/MWh. Hence, it can be concluded that the direct consumption of electricity from PV systems is very limited at higher DSS levels, but larger batteries are able to make an impact even at larger DSS levels.

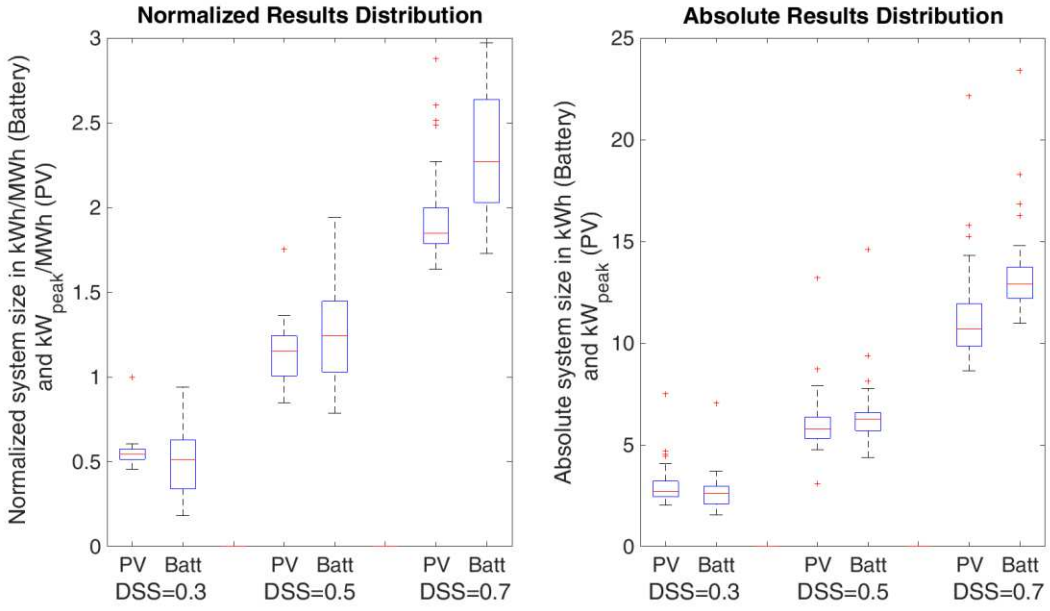

Figure 4-7: Box plot of the PV and battery system size results for LP load profiles with an electric vehicle

Table 4-4: Numeric sizing results for case study 3 (LP+EV)

	DSS 0.3 min-**median**-max	DSS 0.5 min-**median**-max	DSS 0.7 min-**median**-max
Normalized PV size in kW_{peak}/MWh	0.45 - **0.55** - 1.00	0.85 - **1.15** - 1.76	1.64 - **1.85** - 2.88
Normalized battery size in kWh/MWh	0.18 - **0.52** - 0.94	0.79 - **1.24** - 1.94	1.73 - **2.27** - 2.97
Absolute PV system size in kW_{peak}	2.03 - **2.72** - 7.53	3.10 - **5.78** - 13.23	8.63 - **10.69** - 22.17
Absolute battery size in kWh	1.56 - **2.60** - 7.07	4.38 - **6.26** - 14.59	10.97 - **12.90** - 23.41
Ratio PV/Battery in kW_{peak}/kWh	0.76 - **1.06** - 2.50	0.71 - **0.91** - 1.27	0.69 - **0.86** – 0.97

4.2.1.4 Case Study 4 - Synthetic Load Profiles with additional Heat Pumps and Electric Vehicles (LP+HP+EV)

The fourth case study analyzes the same household profiles and implements a heat pump, as well as an electric vehicle to the overall electric load profile. This leads to higher annual electricity consumption with median values of around 9 MWh. Due to this high consumption, the absolute values in size for the PV and battery systems are significantly higher, compared to all previous case studies.

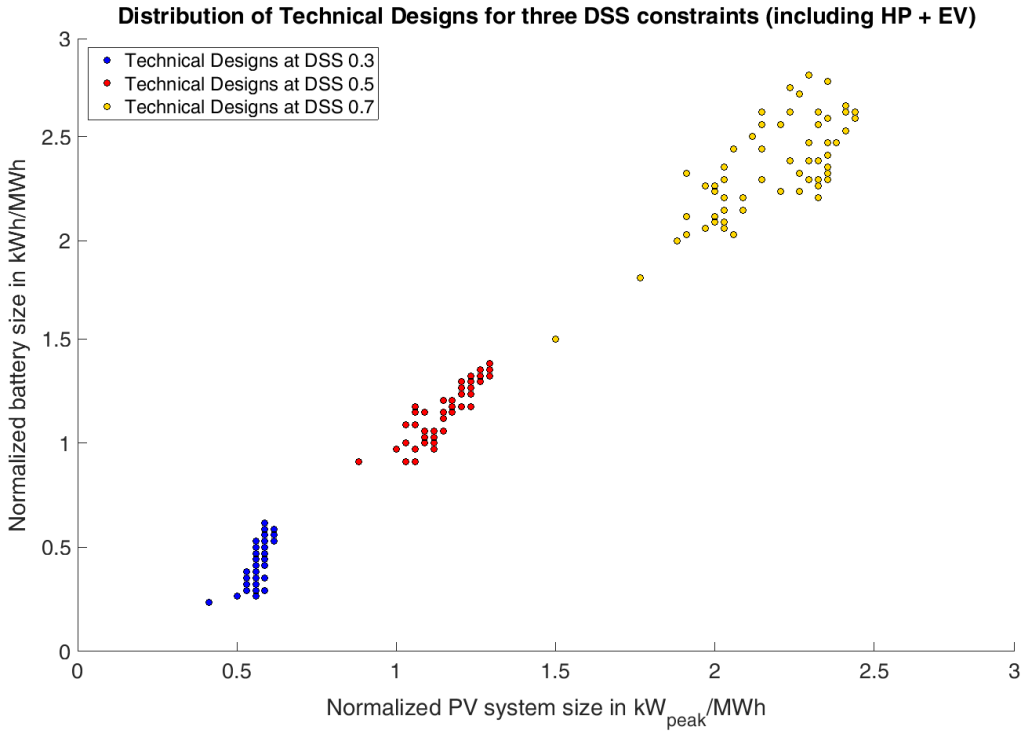

Figure 4-8: Technical design distribution results for all 63 synthetic load profiles with an additional heat pump and an electric vehicle for three DSS-level constraints (blue – DSS=0.3, red - DSS=0.5, yellow – DSS=0.7)

The high share of the HP and the EV of the overall consumption leads to reduced influence of the original household profile. As expected, the result ranges between with neither a strong tendency towards larger PV systems nor towards larger battery systems.

This balanced result is also confirmed by the numeric results shown in Table 4-5and the statistical distribution illustrated in Figure 4-9. The largest difference of the median normalized system sizes between PV and battery system is only 0.13 at the DSS level of 30 %. In this scope, one has to mention that the absolute system sizes to reach DSS levels of 70 % or higher, exceeds currently common PV-battery systems for households with common retail sizes usually not above 12 kW_{peak} and 12 kWh.

Table 4-5: Numeric sizing results for case study 4 (LP+HP+EV)

	DSS 0.3	DSS 0.5	DSS 0.7
	min-**median**-max	min-**median**-max	min-**median**-max
Normalized PV size in kW_{peak}/MWh	0.39 - **0.58** - 0.61	0.88 - **1.18** - 1.30	1.52 - **2.24** - 2.48
Normalized battery size in kWh/MWh	0.21 - **0.45** - 0.61	0.91 - **1.18** - 1.39	1.52 - **2.36** - 2.82
Absolute PV system size in kW_{peak}	2.59 - **4.98** - 7.04	8.21 - **10.51** - 12.76	15.23 - **20.16** - 25.96
Absolute battery size in kWh	1.40 - **3.85** - 5.43	8.29 - **10.39** - 13.47	16.58 - **21.08** - 26.40
Ratio PV/Battery in kW_{peak}/kWh	0.95 - **1.20** - 2.25	0.90 - **1.00** - 1.17	0.82 - **0.95** – 1.07

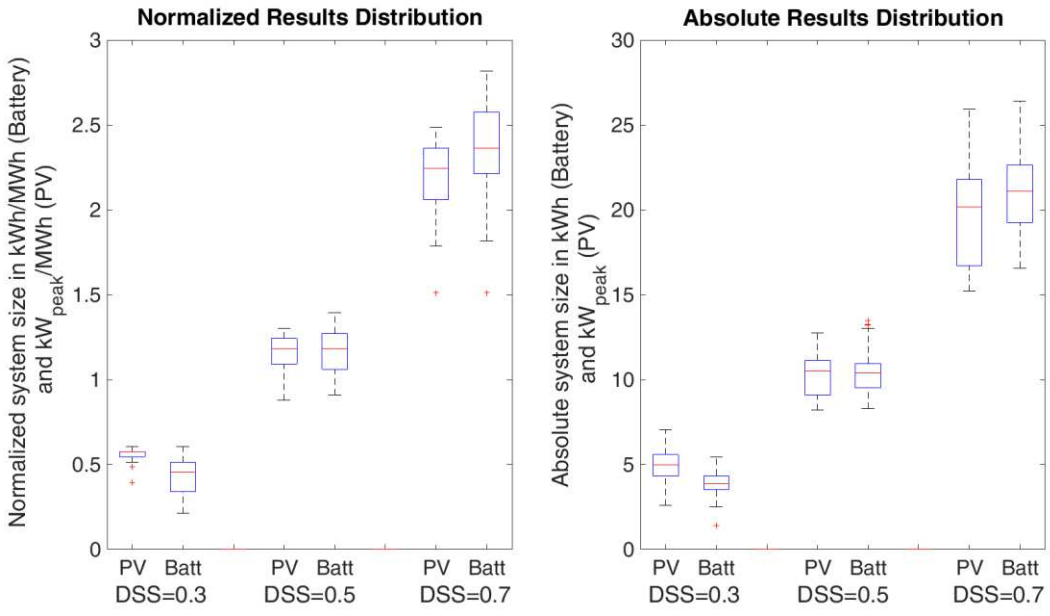

Figure 4-9: Box plot of the PV and battery system size results for LP load profiles with a heat pump and an electric vehicle

4.2.2 Economic Sizing Results

While this thesis primarily focuses on the technical sizing for reasons stated in section 1.1, an economic assessment of the obtained results is also conducted for comparative reasons. It is particularly interesting to find deviations of the technical optima received by the presented design methodology and economic optima.

Most input parameters needed for an economic evaluation are found within the presented data of this technical sizing process. The absolute size of the PV and battery system S_{PV} and S_{Batt} needs to be multiplied with the corresponding specific investment costs Pr_{PV} and Pr_{Batt} of these components to get the total investment costs. The DSS value, the total electricity consumption and the amount of electricity generation from the PV system are necessary to obtain the yearly revenue. Leaving aside details like maintenance, or system degradation, the economic profit/loss can be calculated according to Equation 4-3, which is a function of the DSS. The additional parameters needed are the price for obtained electricity from the grid and feed-in electricity Pr_{Buy} and $Pr_{Feed-in}$ in €/kWh and the expected timeframe a in years. All assumptions for today's and the future's input parameters are listed in Table 4-6.

While the technical parameters are calculated based on calculations of the PV battery model, as described in section 3.4, the economic variables are based on today's values for Austria. Since the cost of PV systems and batteries have dropped significantly and are projected to further decrease in the future, the economic evaluation additionally contains a possible development of future economic optima. The assumed parameters for the future are based on projected values of multiple studies, but are of course exposed to severe uncertainties. However, all conducted sources predict a significant price reduction of both technologies (PV systems and batteries), even though the exact extent of these price reductions varies. It is assumed that the cost of solar PV will drop to below 1,000 €/kW_{peak} by 2025 and battery cost is projected to decrease to approximately 50 % from 2019 until 2030, according to reports and a meta-study by IRENA [181] and the NREL [182]. Since the sole purpose of the economic analysis is the comparison of the technical sizing results with economic optima, no comprehensive sensitivity analysis of the economic input parameters is carried out. In addition to the described projections of investment cost, the prediction of future feed-in tariffs and electricity purchase prices is also a source of uncertainty. In this example, it is assumed that feed-in tariffs for electricity from PV systems will decrease 2 % per year, and purchase prices for households will increase 2 % per year. All assumed values are summarized in Table 4-6.

Table 4-6: Assumed values for the economic assessment for Austria today and in the future [8,111,183]

Variable name	Description of variable and unit	Today	Future
Pr_{Batt}	Price of battery in €/kWh	1300	650
Pr_{PV}	Price of PV system in €/kW_{peak}	1280	950
Pr_{Buy}	Purchase price electricity in €/kWh	0.20	0.27
$Pr_{Feed-in}$	Feed-in tariff in €/kWh	0.0767	0.056
-	Raise of electricity purchase prices in %/year	2	2
-	Decline of feed-in tariffs in %/year	2	2
-	Discount rate in %/year	2	2
a	Lifetime in years	15	15

The formula for the economic assessment is stated in Equation 4-3. It shows the static profit over the system lifetime of 15 years, without the annual price adjustment for purchase prices and feed-in tariffs. Additionally, the discount rate of the performed discounted cash flow analysis is neglected only in the illustration of the equation for better readability.

$$Profit = -(S_{Batt} \cdot Pr_{Batt} + S_{PV} \cdot Pr_{PV}) + a \cdot \Big(\big(DSS * E_{Load} * Pr_{Buy}\big) + (E_{Feed-in} \cdot Pr_{Feed-in})\Big) \quad (4\text{-}3)$$

Investment costs — Reduced electricity fees per year — Electricity feed-in revenues per year

The first indication for comparison can be seen in Figure 4-10. It shows an economic optimum for economic conditions in Austria for today and for a long-term future prediction. A summary of the used parameters can be found in Table 4-6. The published optima for today include (almost) no battery storage, but only a PV system. This shows that the published current economic optima are deviating strongly from the presented technical optima. The future scenario, with lower investment costs, higher electricity consumption prices and lower feed-in tariffs, however, is in the range of the discovered technical design configurations for medium to higher levels of DSS.

The profit according to Equation 4-3 is calculated for all possible system configuratons between 0-3 kW_{peak}/MWh normalized PV size, and 0-3 kWh/MWh normalized battery size. Therefore each system configuration (10,000 possibilities – analogous to the characteristic DSS diagram) is assigned a certain profit or loss.

Figure 4-10 illustrates the distribution of the profitability for all possible PV storage system configurations. The assumed economic values, combined with the results of the technical sizing process, for an exemplary load profile with an annual electricity consumption of 7.88 MWh lead to the economic distribution illustrated in Figure 4-10. It can be seen that the current economic framework in Austria leads to economic optima in the range of rather small PV system sizes with no battery storage. Today's global optimum (marked with a blue dot) in this example is below 500 € with the stated parameters.

With the assumed values for the long-term future (marked with a red dot), a much larger area of profitable system topologies can be observed. All areas marked with green indifference curves are profitable system configurations. The estimated lower investment costs for battery systems, combined with higher electricity prices and lower feed-in tariffs relocate the optimum to areas with larger PV systems and battery systems.

Additionally the global optimum moves towards the technical optima of higher DSS levels, as illustrated in the right illustration of Figure 4-10. In addition to the distribution of the profitability in the two upper visualizations, the obtained DSS level of today's and the future economic optimum is illustrated in the bottom part of Figure 4-10.

The following calculations of all load profiles will confirm that the future economic optimum shifts towards areas with higher DSS levels. Additionally, the PV/Battery ratio of today's economic optimum is infinite, due to the results without any battery. However, at the configuration of the future economic optimum, the PV/Battery ratio approaches the results of the determined technical optimum.

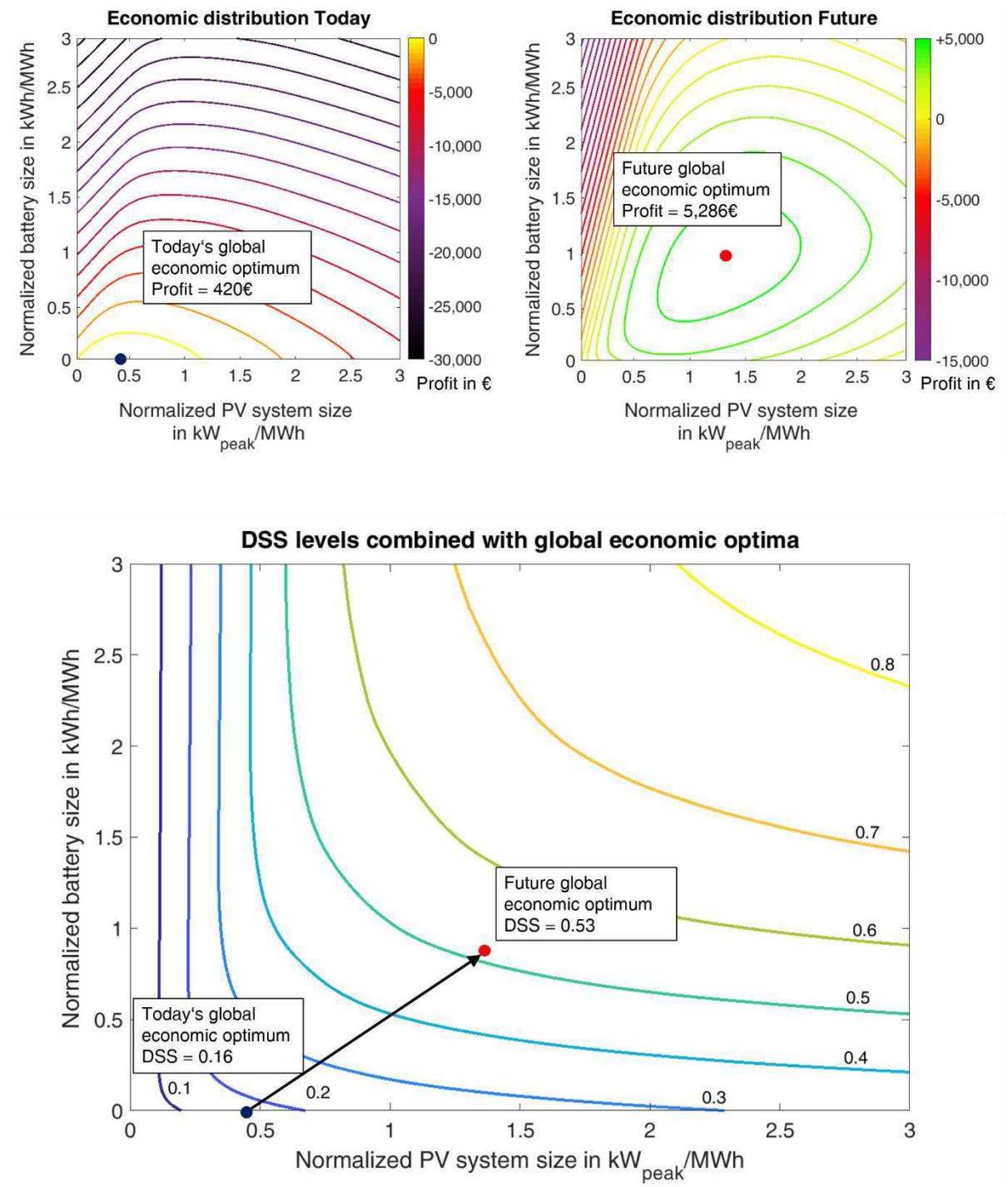

Figure 4-10: Economic evaluation of the profit of PV storage systems today (top left) and the predicted future (top right) for an exemplary household load profile. The global optimum for today (blue dot) and the future (red dot) is additionally shown in the corresponding distribution of DSS levels (lower illustration).

The results for the technical design and the economic optima of three selected load profiles are now outlined in greater detail and presented in Table 4-7. Results of a single adult (employed) with an annual electricity consumption of 1.72 MWh, a single adult (unemployed) with one child and consumption of 3.93 MWh and a multigenerational home with 2 adults (employed) and two seniors in one household and consumption of 7.81 MWh are shown. All technical results are divided into DSS levels of 0.3, 0.5 and 0.7.

Case 1 stands out with its relatively high normalized battery sizes compared to the other cases. Due to a low share of electricity consumption during the day, the DSS can be greatly improved by the installation of a battery, while Case 2 and Case 3 both have unemployed residents, leading to a higher share of electricity consumption during daylight. This is also reflected in the PV/Battery ratio, which is significantly lower for case 1 at all DSS levels compared to the other two Cases.

The results of Case 2 differ significantly from the results obtained in Case 1. A larger PV system is the preferred option of the optimization to reach the required DSS level. Due to the high annual consumption in Case 3, the absolute PV and battery sizes are significantly larger to achieve the defined DSS requirements. A PV installation of 11.6 kW_{peak} combined with a battery unit of 10.18 kWh is the smallest combination leading to 70 % DSS. The small battery sizes of the Cases 2 and 3 at DSS level 0.3 lead to a very large PV/Battery ratio, but even at higher DSS requirements the difference between the cases is significant. At DSS level 0.5 the minima at Case 1 amount to 0.78 kW_{peak}/kWh and 1.88 kW_{peak}/kWh at Case 2. This leads to the conclusion, that a differentiated approach for household profiles is necessary and important.

The second part of Table 4-7 shows today's and the estimated future global profit optima and the according system configuration. As mentioned before, in the current economic surrounding, battery storages are not economically advantageous to the user. Also the profitability (savings) after 15 years is significantly smaller than the future estimation. In addition the PV/Battery ratio is infinite for today's global economic optima, since the global optima are obtained without any battery utilization. This changes for the future estimation, with PV/Battery ratios between 1.3 and 2.25 for the three exemplary cases of Table 4-7.

Table 4-7: Description of the exemplary user groups and the related results

	Case 1	Case 2	Case 3
User group	Single adult (employed)	Single adult – 1 child (unemployed)	2 adults – 2 seniors (2 employed)
(Load Profile Generator Name)	(CHR 35)	(CHR 47)	(CHR 15)
DSS level	0.3-0.5-0.7	0.3-0.5-0.7	0.3-0.5-0.7
Annual electricity consumption in MWh	1.72	3.93	7.81
Normalized PV system size in kW_{peak}/MWh	0.55-**0.97**-1.82	0.52-**0.97**-1.67	0.48-**0.88**-1.48
Normalized battery size in kWh/MWh	0.58-**1.24**-2.15	0.18-**0.52**-1.06	0.12-**0.67**-1.30
Absolute PV system size in kW_{peak}	0.94-**1.67**-3.14	2.03-**3.81**-6.56	3.79-**6.86**-11.60
Absolute (useable) battery size in kWh	0.99-**2.14**-3.71	0.72-**2.03**-4.17	0.95-**5.21**-10.18
(Absolute battery size in kWh – 90 % DoD)	(1.10-**2.38**-4.12)	(0.80-**2.26**-4.63)	(1.06-**5.79**-11.31)
Ratio PV/Battery in kW_{peak}/kWh	0.95-**0.78**-0-85	2.83-**1.88**-1.57	4.00-**1.32**-1.14
Economic Sizing Global Optimum Today	0.3 kW_p – 0 kWh	1.8 kW_p – 0 kWh	4.0 kW_p – 0 kWh
Profit Global Optimum Today in €	198	706	1915
DSS Global Optimum Today	0.12	0.21	0.25
Economic Sizing Global Optimum Future	2.6 kW_p – 2.0 kWh	7.0 kW_p – 3.1 kWh	12.1 kW_p – 7.8 kWh
Profit Global Optimum Future in €	1250	5188	9458
DSS Global Optimum Future	0.67	0.68	0.69

To answer the question of global economic optima in a more generalized fashion, an economic assessment for current and future values is conducted analogously to the previous technical sizing approach. It consists of the same four case studies, as described in section 4.2.1. The economic results generally consist of two different types: the global economic optima and the economic optima with DSS constraints. Economic optima with DSS constraints (0.3, 0.5 and 0.7) means that the global optimum is only considered in areas of the requested DSS level. Additionally, these optima with DSS constraints are compared to the global economic optimum. The results show a more similar distribution compared to the technical optima presented in section 4.2.1. Interestingly, the results of the global optima in the future projection demonstrate that some DSS constraints for lower DSS levels are needless, as all global optima are well above 30 %, sometimes even above 50 %.

4.2.2.1 Case Study 1 - Synthetic Load Profiles (LP)

The distributed results for all households are illustrated in Figure 4-11. It shows the global economic optima (marked with a green circles) and the economic optima with three different DSS constraints. The left illustration summarizes the results for today's economic framework and the right illustration shows the results for the assumed economic framework in the future.

While the economic optima with DSS constraints do not significantly change due to the restrictions in DSS, the global economic optima change a lot. As mentioned before, today's economic framework, and especially today's battery prices, do not allow an economically beneficial utilization of batteries. In contrary to today's global economic optima with small PV system sizes and no batteries, the global economic optima in the future is reached by the implementation of significantly larger PV systems and batteries. In case study 1, the future global optima are in the range of 50-70 % DSS, while current economic optima are in the range of 10-20 % DSS. This means that higher levels of DSS will pay off in the future if the assumed values are proven right.

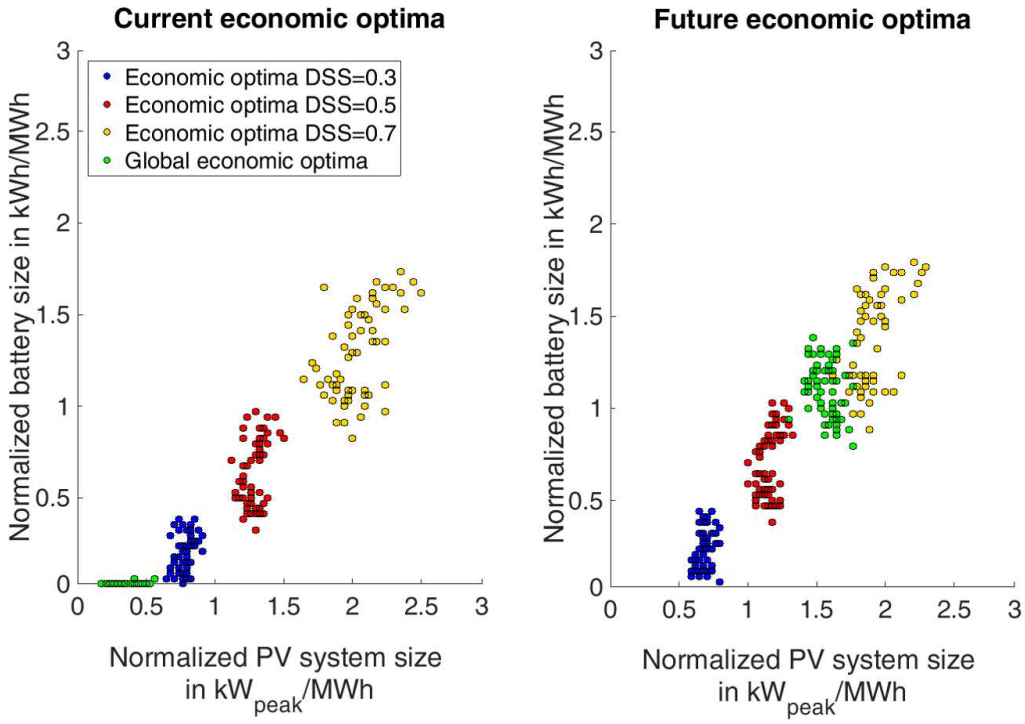

Figure 4-11: Global economic optima and economic optima with DSS constraints - Distribution for case study 1 for the current economic framework and the future projection

The numeric results table is divided into two main parts: the economic design results of today and the future. Both contain results regarding the global optimum and the three constraints. The first three rows show the minimum, median and maximum value of the ideal economic system configurations with the corresponding DSS constraints. The last three rows include information regarding the actual profitability of the global optimum, the optimum with DSS constraints and the reduced profits caused by the DSS constraints.

In accordance with the fact that batteries have a negative impact on the profitability, the PV/Battery ratio remains significantly above 1 in all 63 load profiles and for all DSS levels. The median value range between 4.9 for the DSS level of 30 % and 1.57 for the DSS level of 70 %.

The global economic optimum is positive for all profiles as well, but the absolute profit remains in the range between 123 and 1,916 €. While some load profiles are still slightly profitable with a DSS constraint of 30 %, every single household suffers a loss with a higher DSS constraint implemented. The results differ significantly for the assumed future economic framework. While the PV/Battery ratio remains high, the profitability of the global optima increases to a range of 1,044 to 9,458 €. As seen in Figure 4-11, the global economic optima are achieved by system configurations with DSS levels above 50 %. This made the DSS constraint only applicable to the DSS level of 70 %. The results with that DSS constraint, however, do not significantly reduce the overall profit only marginally.

Table 4-8: Numeric economic results for case study 1

		DSS 0.3	DSS 0.5	DSS 0.7
		min-**median**-max	min-**median**-max	min-**median**-max
Economic Design Today	Absolute PV size in kW_{peak}	0.79 - **2.07** - 4.97	1.32 - **3.34** - 9.70	2.14 - **5.43** - 13.96
	Absolute battery size in kWh	0.00 - **0.31** – 1.37	0.61 - **1.61** – 4.62	1.20 - **3.38** - 8.76
	Ratio PV/Battery in kW_{peak}/kWh	2.00 - **4.90** – NaN	1.32 - **1.89** - 4.30	1.09 – **1.57** - 2.48
	Optimum in € (DSS constraints)	-816 / **+33** / +1847	-278 / **-1092** / -4237	-1258 / **-3451** / -9398
	Global optimum in €		123 / **355** / 1916	
	DSS at global optimum		0.08 / **0.15** / 0.27	
	Reduced profit in €	-1387/ **-305** /-68	-4808/ **-1563** / -546	-9969/ **-3929** /-1431
Economic Design Future	Absolute PV size in kW_{peak}	0.72 – **1.81** - 4.50	1.13 - **3.02** – 8.28	1.89 - **4.93** - 13.96
	Absolute battery size in kWh	0.12 - **0.46** – 1.71	0.68 - **1.79** – 5.13	1.23 - **3.62** - 9.06
	Ratio PV/Battery in kW_{peak}/kWh	1.50 - **3.33** – 26.00	1.15 - **1.50** – 3.25	1.09 – **1.34** - 2.17
	Optimum in € (DSS constraints)	>DSS (0.3)	>DSS (0.5)	+796/ **+2333** / +9350
	Global optimum in €		1044 / **2388** / 9458	
	DSS at global optimum		0.50 / **0.64** / 0.71	
	Reduced profit in €	>DSS (0.3)	>DSS (0.5)	-0/ **-79** /-294

4.2.2.2 Case Study 2 - Synthetic Load Profiles with additional Heat Pumps (LP+HP)

The trend towards large PV systems and high PV/Battery ratios is continued and increased in case study 2. The left illustration of Figure 4-12 shows many configurations with a maxed out PV system size of 3 kW_{peak}/MWh in order to reach the DSS constraint of 70 %, with a minimum in battery size. This is also reflected in the resulting PV/Battery ratio, presented in Table 4-9, where the median value ranges between 1.62 and 5.60 kW_{peak}/kWh, depending on the DSS constraint.

Another difference compared to case study 1 is the changing range of future global optima. While today's values are basically in line with the results from case study 1, the future global optima range between DSS constraint of 30 and 50 %, and are no longer above the DSS levels of 50 %, as previously seen in Figure 4-11.

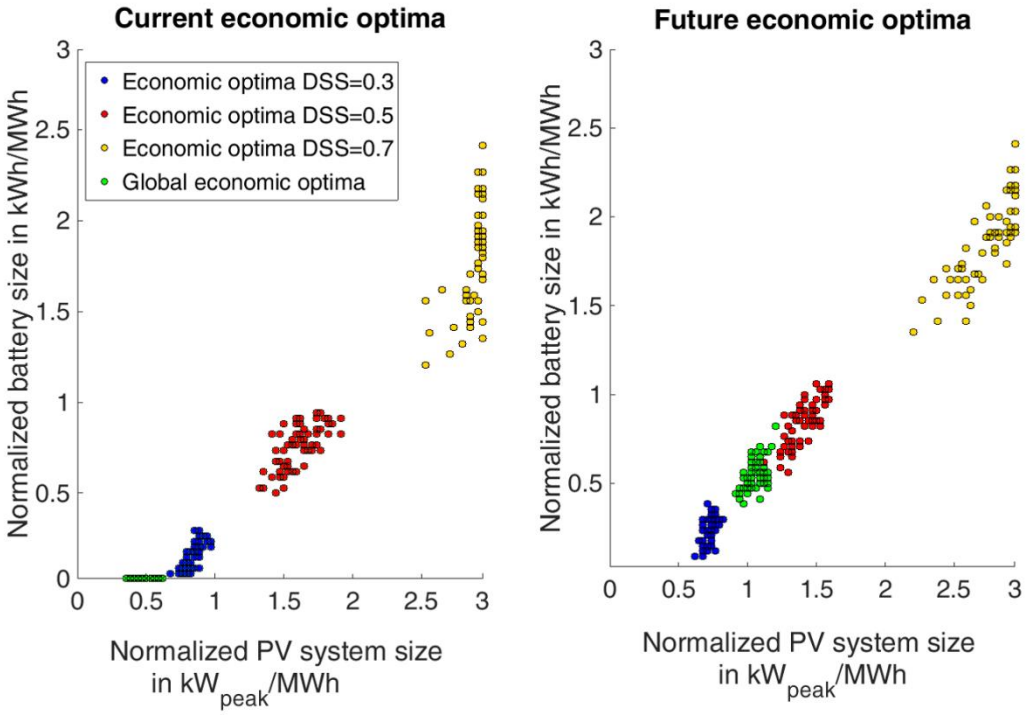

Figure 4-12: Global economic optima and economic optima with DSS constraints – Distribution for case study 2 for the current economic framework and the future projection

The profitability of the global optima can be significantly increased from 722-3,917 € today, to 2,356-11,106 € with future assumptions. Due to the larger necessary size of the PV/Battery system in this case study, the differences in profitability of today's economic optima with DSS constraints and future profitability are very large. The results for the economic optima for a DSS level of 50 % lead to large losses of up to -6,585 €, while future values go as high as +11,078. The complete list of the economic assessment of case study 2 is shown in Table 4-9.

Table 4-9: Numeric economic results for case study 2

		DSS 0.3	DSS 0.5	DSS 0.7
		min-**median**-max	min-**median**-max	min-**median**-max
Economic Design Today	Absolute PV size in kW_{peak}	3.28 - **5.58** - 8.02	6.58 - **10.64** - 16.04	11.60 - **19.24** - 30.98
	Absolute battery size in kWh	0.22 - **0.89** – 1.72	3.00 - **4.71** – 7.74	7.64 – **11.75** - 16.13
	Ratio PV/Battery in kW_{peak}/kWh	3.11 - **5.60** – 27.00	1.72 – **2.12** – 3.00	1.22 – **1.62** - 2.20
	Optimum in € (DSS constraints)	-539/**+344**/+3625	-6585/**-3983**/-1821	-18607/**-14537**/-9237
	Global optimum in €		722 / **1280** / 3917	
	DSS at global optimum		0.15 / **0.19** / 0.27	
	Reduced profit in €	-1661/**-927**/-160	-8011/**-5686**/-3534	-20751/-**15973**/-10425
Economic Design Future	Absolute PV size in kW_{peak}	2.81 - **4.71** - 7.29	5.70 - **9.11** - 13.49	11.60 - **18.31** - 26.97
	Absolute battery size in kWh	0.48 - **1.20** - 2.29	3.36 - **5.48** - 8.31	7.85 - **12.34** - 17.03
	Ratio PV/Battery in kW_{peak}/kWh	1.92 - **3.29** - 11.00	1.42 - **1.64** - 2.39	1.22 - **1.49** - 1.85
	Optimum in € (DSS constraints)	>DSS (0.3)	+1930/**+3810**/+11078	-1442/**+734**/+8530
	Global optimum in €		2356 / **4119** / 11109	
	DSS at global optimum		0.35 / **0.41** / 0.52	
	Reduced profit in €	>DSS (0.3)	-731/**-226**/-10	-4578/**-3256**/-2111

4.2.2.1 Case Study 3 - Synthetic Load Profiles with additional Electric Vehicles (LP+EV)

The distribution of all economic optima for case study 3 is illustrated in Figure 4-13. Today's global optima remain in the range of low PV system sizes and no battery utilization. The global optima in the future shift towards normalized system sizes between DSS levels of 30 and 50 %. Even though the PV system sizes are larger compared to the system sizes of batteries at all DSS constraint levels, the PV/Battery ratio remains lower compared to case study 2.

Analogous to case study 2, today's global optima (only PV systems and no batteries) are throughout positive, but the system design switches towards larger PV battery systems with the assumed values. The maximum profit of today is 3,089 €, while the maximum profit earned with economic assumptions towards the future increases up to 9,779 €. All gathered information on case study 2 is summarized in Table 4-10.

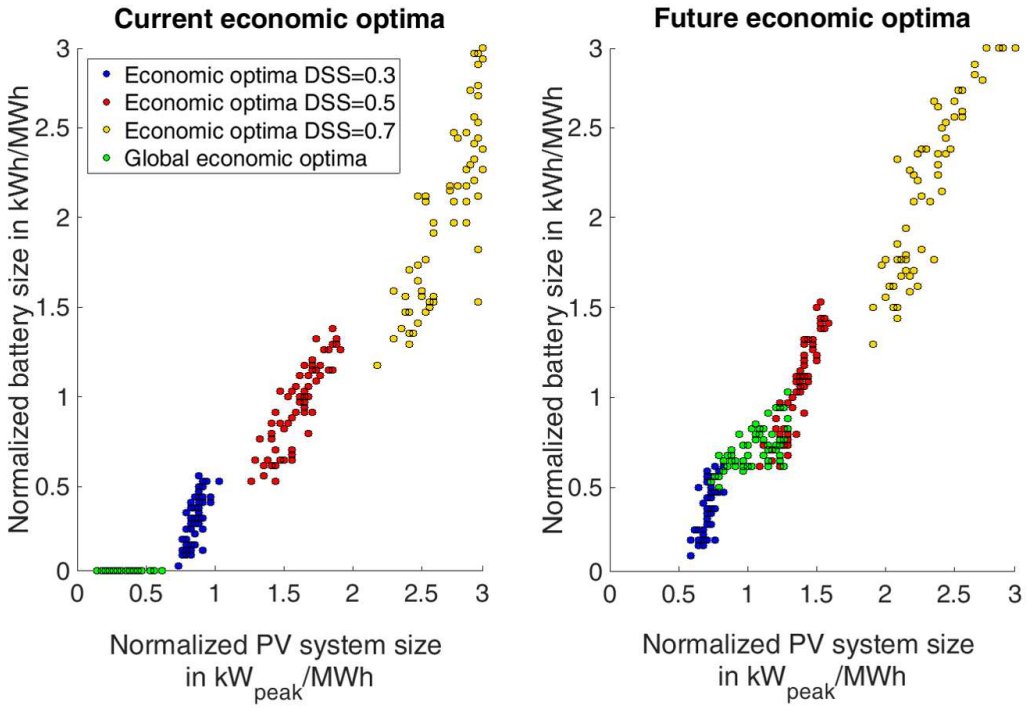

Figure 4-13: Global economic optima and economic optima with DSS constraints – Distribution for case study 3 for the current economic framework and the future projection

Table 4-10: Numeric economic results for case study 3

		DSS 0.3	DSS 0.5	DSS 0.7
		min-**median**-max	min-**median**-max	min-**median**-max
Economic Design Today	Absolute PV size in kW_{peak}	2.61 – **4.33** – 7.49	4.70 – **8.18** - 13.11	8.46 - **13.76** - 22.79
	Absolute battery size in kWh	0.31 – **1.61** – 2.28	1.88 - **4.82** - 6,90	4.49 - **10.53** - 12.82
	Ratio PV/Battery in kW_{peak}/kWh	1.61 - **2.67** – 24.00	1.32 - **1.69** - 2.82	0.99 - **1.32** - 1.92
	Optimum in € (DSS constraints)	-1955/-**877**/+2803	-6174/-**4819**/-1725	-14561/-**12472**/-9162
	Global optimum in €		242 / **607** / 3089	
	DSS at global optimum		0.06 / **0.11** / 0.25	
	Reduced profit in €	-2349/-**1476**/-267	-6727/-**5351**/-3164	-15049/-**13225**/-10600
Economic Design Future	Absolute PV size in kW_{peak}	1.99 - **3.64** - 5.93	4.08 - **7.01** - 11.24	7.32 - **11.66** - 19.98
	Absolute battery size in kWh	0.63 - **1.98** - 2.71	2.19 - **5.38** - 7.64	5.02 - **11.41** - 13.85
	Ratio PV/Battery in kW_{peak}/kWh	1.21 - **1.77** - 6.33	1.00 - **1.31** - 2.05	0.89 - **1.04** - 1.49
	Optimum in € (DSS constraints)	>DSS (0.3)	+557/**2545**/9641	-2405/**+473**/+8814
	Global optimum in €		1293 / **2719** / 9779	
	DSS at global optimum		0.30 / **0.41** / 0.57	
	Reduced profit in €	>DSS (0.3)	-737/-**163**/0	-3800/-**2380**/-964

4.2.2.1 *Case Study 4 - Synthetic Load Profiles with additional Heat Pumps and Electric Vehicles (LP+HP+EV)*

Case study 4 combines all household loads with an electrical heat pump profile and the described charging profile of the assigned electric vehicle. The PV/Battery ratio is in between the range of case studies 2 and 3. In today's economic framework, a battery is not economically feasible, due to the high battery costs. The resulting distribution of all separate DSS constraints seems very isolated and has a narrow distribution without a lot of outliers, as seen in the right representation of Figure 4-14.

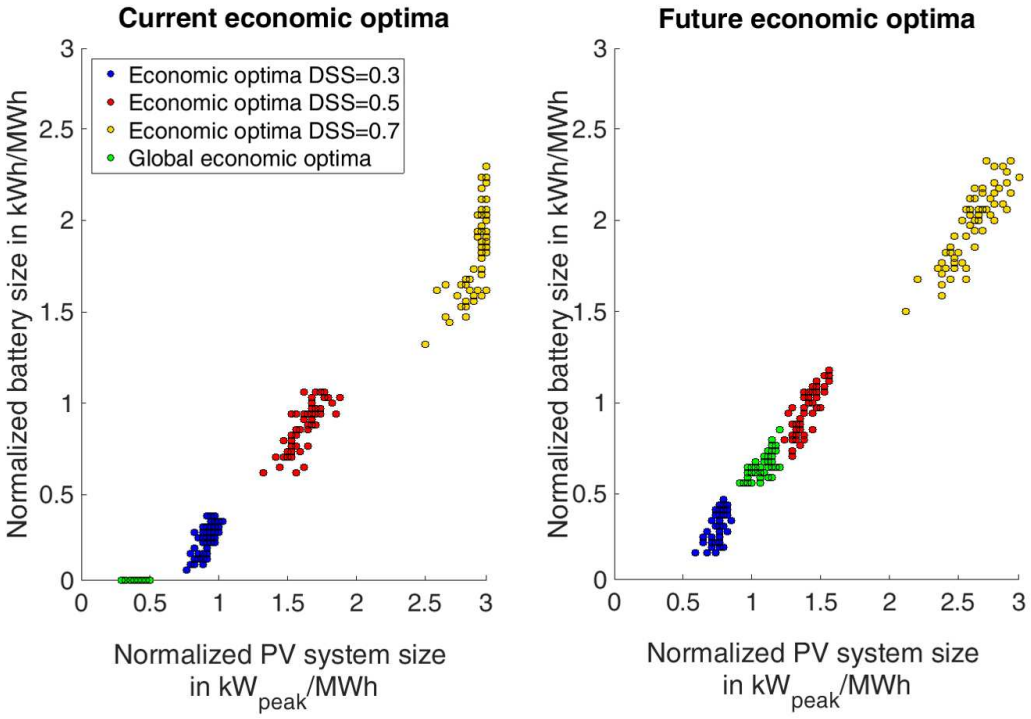

Figure 4-14: Global economic optima and economic optima with DSS constraints – Distribution for case study 4 for the current economic framework and the future projection

In terms of profitability, case study 4 shows the highest possible loss, as well as the highest possible profitability, due to the high consumption caused by combining three load profiles. Today's profitability of the economic optima ranges between 797 € and 4,158 €. This effect is even heightened by the future profitability calculation. While the lowest profitability for future economic global design optima amounts to 2,988 €, the highest profitability reaches up to 12,407 € in the future. The whole list of all data regarding the economic profitability of this case study 4, is presented in Table 4-11.

Table 4-11: Numeric economic results for case study 4

		DSS 0.3	DSS 0.5	DSS 0.7
		min-**median**-max	min-**median**-max	min-**median**-max
Economic Design Today	Absolute PV size in kW_{peak}	5.97 - **8.16** - 11.23	11.32 - **14.74** - 19.36	19.08 - **26.80** - 36.96
	Absolute battery size in kWh	0.88 - **2.15** - 2.90	6.06 - **7.76** - 9.77	13.46 - **16.60** - 20.58
	Ratio PV/Battery in kW_{peak}/kWh	2.50 - **3.67** - 12.50	1.54 - **1.88** - 2.60	1.29 - **1.56** - 1.92
	Optimum in € (DSS constraints)	-1937/**-847**/+3217	-9255/**-7335**/-4623	-23806/**-20553**/-16800
	Global optimum in €		797 / **1403** / 4158	
	DSS at global optimum		0.11 / **0.15** / 0.23	
	Reduced profit in €	-2936/**-2301**/-851	-10599/**-8891**/-7210	-26141/**-22060**/-18094
Economic Design Future	Absolute PV size in kW_{peak}	4.85 - **6.64** - 9.36	9.90 - **12.75** - 16.72	18.19 - **23.51** - 31.24
	Absolute battery size in kWh	1.58 - **2.70** - 3.62	7.04 - **8.68** - 11.22	14.07 - **17.98** - 22.08
	Ratio PV/Battery in kW_{peak}/kWh	1.73 - **2.40** - 4.80	1.31 - **1.44** - 1.87	1.17 - **1.32** - 1.54
	Optimum in € (DSS constraints)	>DSS (0.3)	+2408/**4817**/12406	-1236/**+953**/+9271
	Global optimum in €		2988 / **5071** / 12407	
	DSS at global optimum		0.35 / **0.42** / 0.51	
	Reduced profit in €	>DSS (0.3)	-582/**-276**/-12	-4975/**-4024**/-2973

4.3 Multi-Nodal Case studies

Three case studies with four different scenarios each are presented within this section. The used data comes from various sources. It is a combination of measured data, modelled data and self-made assumptions. All case studies are inspired by real energy systems, but they are complemented with fictive data. The aim of these presented results is not to provide detailed results for a specific energy system of a region with applicable recommendations for action to the responsible institutions, but to provide generic and representative case studies. They should on the one side serve as demonstration examples to understand the working principle of *HyFlow* and present the scope of its functions to possible users. On the other hand they allow to derive generic statements for multiple reference energy systems. Additionally, the applicability for energy systems of all sizes should be demonstrated. Major parts of the input data are derived from a previous research project on the Chair of Energy Network Technology and are therefore identical to the case studies in [167].

4.3.1 Case study overview

First a low voltage stub line (case study 1) is considered in order to show the effects of partially simultaneously appearing charging processes of electric vehicles (EV) and the implementation of PV energy. Case study 2 considers an urban energy system, which is used to show *HyFlow's* ability to calculate load flows of all three energy carriers in meshed networks. Finally case study 3 describes the interaction of the modelled urban energy system from case study 2 with its surrounding districts. This case study is implemented in *HyFlow* in order to point out the ability to simulate scenarios with two different voltage levels (or pressure levels for heat and gas networks) and to show the influence of large P2G plants. All simulations are conducted over a 1-year simulation period, using 15 minutes time-steps.

To show the effect of fluctuating generation, temporarily high consumption due to charging processes for EV, as well as the effect of energy storage systems and sector coupling, three scenario levels are selected for every case study. After solving the reference scenario, which shows the status quo power flow situation without PV- and EV penetration, the mentioned technologies (PV and EV) are implemented into the high-stress scenario with high penetration rates. Finally by taking storage technologies and hybrid elements into account, two improvement scenarios are conducted in order to show the effects of the chosen flexibility options on the power flow situation.

An exemplary illustration of the three scenario levels in each case study is shown in Figure 4-15. The used evaluation indicators for all case studies and scenarios and the corresponding names are listed below: KPIs for electricity are the maximum value of power for imports and exports over the whole year $P_{el,max,year}$, the average of the daily maxima for electricity power $P_{el,\emptyset\,max,day}$ and the overall imported and exported electric energy, natural gas, and district heating E_{el}, E_{gas} and E_{heat}.

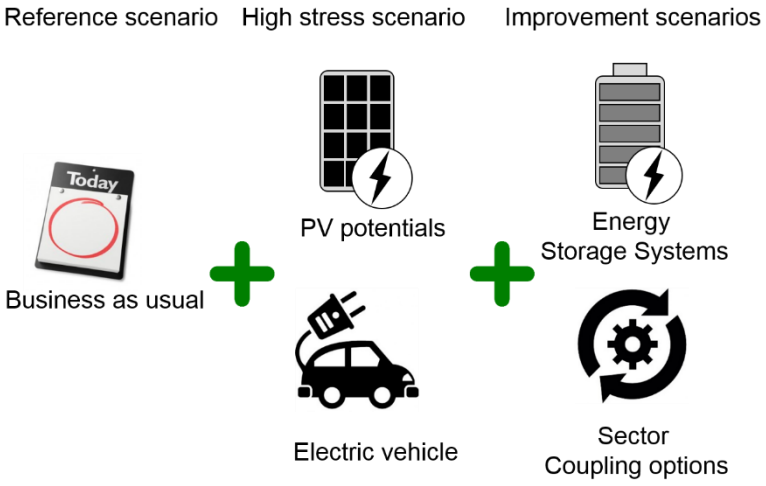

Figure 4-15: Scenario levels for each case study

It has to be stated that the described parameters are only KPIs for the overall system configuration. *HyFlow* additionally supplies the user with time-resolved data of all voltages, pressures, load flows, losses, etc. for every single node or single network connection within the model. Additionally, the usage profile of every single storage unit or hybrid element can be selected and displayed. Since these detailed results would go beyond the scope of this work, only the overall system results are illustrated for all case studies and scenarios. Only excerpts of the more detailed results of individual lines are presented for demonstration reasons in case study 3.

4.3.2 Case study 1

Within this work, case study 1 is the analysis with the smallest energy system investigated. It consists of an analyzed grid stub on the edge of an energy grid, containing 12 Single Family households, representing one cell each. They are connected to a 400 V low-voltage grid and to the local district heating grid.

Case study description

The electricity grid is supplied from a single power transformer 5.25kV/0.4kV, while the district heating branch is supplied by industrial waste heat at a nominal pressure of 17.5 bar. All households were assigned an individual synthetic electricity load profile from the *LoadProfileGenerator*, as described in section 2.2.1. The heating demand is modelled with the help of the described SigLinde approach, as presented in section 2.2.2. A simplified graphic illustration of the topology can be seen in Figure 4-16.

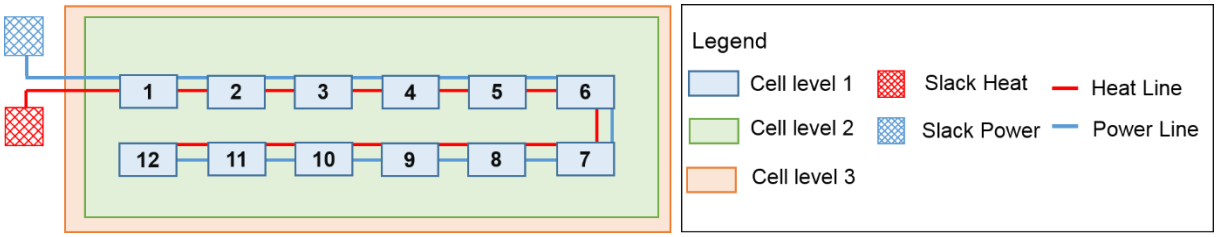

Figure 4-16: Topology of case study 1

The distance of the low voltage power lines or district heating pipes between the cells vary between 40 and 120 meters, the current-carrying capacity I_{therm} is assumed to be 240 A, which allows power flows of approximately 96 kW.

In the reference scenario, the residual loads of both implemented energy carriers are equal to the demand profiles, as there is no generation within the system boundary. This means that the total energy demand is supplied via the slack node from the superior grid levels. The second scenario, labelled as high-stress scenario, simulates the implementation of additional

Photovoltaic energy generation in all cells, with randomly distributed peak powers between 1.4 and 4.6 kW_{peak}. Additionally, one electric vehicle with a maximum charging power of 11 kW is assigned to every household. The modelling of the PV generation and the EV load profiles can be found in section 3.4.2 and 4.1. This implementation leads to higher power peaks on the demand side and also negative residual loads, due to the implemented electricity generation. To analyze the effects of ESS and HE on the energy supply, the volatility of the residual loads and the load flows, improvement scenarios 1 and 2 are introduced. Therefore a Li-ion battery (4.8 kW and 7.2 kWh) is assigned to each cell in improvement scenario 1. Additionally, a heat storage system (9 kW and 80 kWh) and a heat pump (3.3 kW_{el} and 9.9 kW_{th}) is introduced in each cell. The different scenario stages of case study 1 are summarized in Table 4-12.

Table 4-12: Configuration levels for case study 1

Parameter	**Reference scenario**	**High stress scenario**	**Improvement scenario 1**	**Improvement scenario 2**
Demand	Standard	Standard 12 EV	Standard 12 EV	Standard 12 EV
Generation	-	PV potential	PV potential	PV potential
Electric ESS	-	-	57.6 kW - 86.4 kWh	57.6 kW - 86.4 kWh
Thermal ESS	-	-	-	108 kW - 960 kWh
HE	-	-	-	Heat pumps 39.6 kW_{el}

The exemplary results for all four described scenarios of case study 1 are shown in Figure 4-17. It shows the main results of the overall system regarding the occurring power peaks P_i and the total energy amounts per year E_i for all used energy carriers separately for imports and exports. The four shown values are the maximum power of electrical energy over the whole year, the average value of the daily maxima of electrical power imports, the annual electrical energy, and the annual district heating energy.

The average daily maximum is introduced, because the annual maximum power peak is not always an appropriate indicator. A single event in a total year does not influence the average daily power maximum to the same extent, which makes it an informative indicator as well. Two vertical axes are introduced for reasons of better visibility. In the case of Figure 4-17 the first vertical axis represents all values related to electrical power P_{el} and electric energy E_{el} and the second axis represents the energy import of district heating E_{heat} only.

Results description

In the **reference scenario**, no energy is exported out of the considered system. The whole energy supply is based on imports. The annual power maximum of imported electricity is 44.2 kW, while the average daily maximum of imported electricity amounts to 23.8 kW. Over the whole year, the energy imports add up to 41.8 MWh for electricity and to 359 MWh for district heating. After implementing additional PV systems and electric vehicles according to described **high-stress scenario** of Table 4-12, the results change for electricity. The annual power maximum increases to 64.5 kW for electricity imports and to 33.2 kW for electricity exports. Also the average daily maximum of imported electricity rises to 29.5 kW. Annual electricity imports slightly increase to 42.7 MWh, while exported electricity rises to 19.2 MWh.

In **improvement scenario 1** with additional electric ESS, the annual power maximum for electricity imports remains unchanged compared to the high-stress scenario at 64.5 kW, while the average daily maximum of imported electricity decreases to 21.7 kW. The annual power maximum for electricity exports can be reduced to 27.8 kW or 16 % compared to the high-stress scenario. Also the annual electricity imports are reduced to 32.3 MWh, while the exported electricity decreases to 7.2 MWh. This is a decline of 24 % in imports and 63 % in electricity exports compared to the high-stress scenario. The imported energy from the district heating grid does not change compared to the high-stress scenario. **Improvement scenario 2**, with additional heat pumps and thermal ESS, reduces the annual maximal power export to 21.3 kW, while the annual maximal power import remains unchanged at 64.5 kW. The average daily maximum electrical power amounts to 27.1 kW, which corresponds to a reduction of 8 % compared to the high-stress scenario. The overall electricity imports rise 31 % to 55.8 MWh, while the electricity exports decline 90 % to just over 2 MWh. Additionally, the amount of imported energy from the district heating grid reduces to 272.3 MWh, which corresponds to a 14 % reduction compared to the high-stress scenario. All values are summarized in Figure 4-17 and the interpretation of the scenario results is presented in the next paragraph.

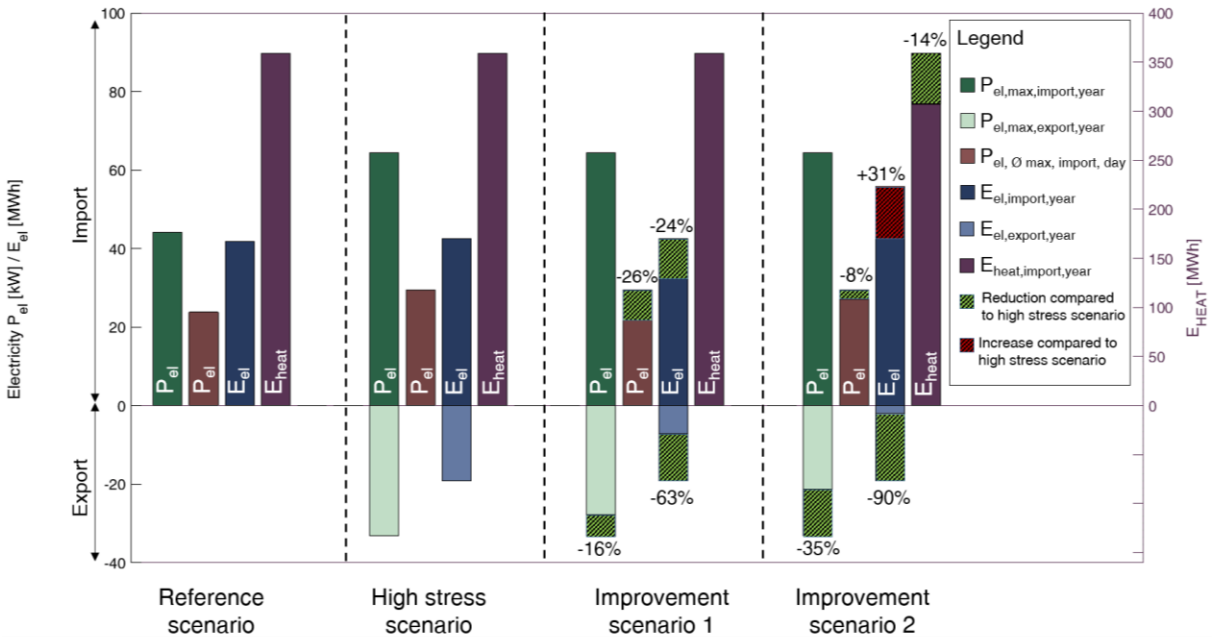

Figure 4-17: Key results of all deployed scenarios of case study 1

Results interpretation

The **reference scenario** shows the status quo of many energy systems today: the total energy supply of all available energy carriers is based on imports. Once PV systems and electric vehicles are added within the framework of the **high-stress scenario**. A clear result of this scenario is the marginal change in terms of energy imports, but large change concerning the obtained power maxima for imported and exported electricity. The additional imports amount to only 0.86 MWh, while the extra exports add up to 19.2 MWh. This means that the total balance of electrical energy is reduced by over 18 MWh, because of the additional PV generation, but the maximum peaks of imports and exports are significantly higher in the high-stress scenario. Additionally, the high-stress scenario with its moderately sized, distributed PV systems shows that the maximum power peak via the local grid transformer is still caused by electricity imports and not by exported PV power. In **improvement scenario 1**, the added Li-ion batteries are capable of improving some parameters, while others are not affected by this measure. Especially the reduced electricity exports of 63 % compared to the high-stress scenario stands out. However, one can see that the reductions in terms of maximal powers via grid transformer, which is especially important for energy infrastructure design, cannot be reduced in the same scope as the amounts of imported and exported energy. The annual maximum power of electricity imports, for example, isn't affected at all. One can conclude that the implemented ESS are capable of reducing energy imports and exports significantly and therefore contribute to the degree of self-sufficiency, but they cannot contribute as much

when it comes to annual power peaks. **Improvement scenario 2** is the only scenario with active sector coupling within case study 1. The effects of the implementation of heat pumps and associated heat storage units are manifold. On the one hand, it allows to actively reduce the obtained energy from the district heating grid and on the other hand it has large effects on the electrical system as well. 90 % of all electrical energy exports can be reduced, with a reduction in the annual power peak of 30 % for electricity. This means that the integration of the heating sector proves to be very effective in terms of export reduction. However, due to the increased electrical consumption of the heat pumps, a significant rise of 31 % in imported electricity compared to the high stress is the result. The annual maximum power import of electricity remains unchanged, despite the increased electrical consumption caused by the implemented heat pumps. Additionally, another side effect is observed: as a result of the usage of surplus electricity for heating purposes, the excess electricity of one household is often no longer transferred to other households with electricity demand at the same time.

4.3.3 Case study 2

Case study 2 represents a medium-sized city in Austria, with around 30,000 inhabitants. The city contains three energy grids (electricity, natural gas, district heating). Some areas are connected to all three grids, while others are only connected to certain energy carriers. Additionally, there is an existing hydroelectric power plant with 10 MW, a biomass power plant with 3.6 MW and other smaller generation facilities, such as PV power plants. The remaining electrical load is supplied by the 110 kV grid connection. The natural gas supply of the town is for the most part fed by the national gas grid, apart from few very small biogas plants. An industrial complex in the western part of the city, with large industrial waste heat potentials, supplies the district heating grid with this energy, as presented in cell 2 of Figure 4-18.

Case study description

The analyzed city is divided into 44 cells, according to the described methodology in section 3.2. Figure 4-18 illustrates the result of this process. The individual cells are colored depending on their access to the three grid-bound energy carriers. The cells in red are connected to the electricity grid only, all blue cells have access to electricity and natural gas and the green cells are supplied with all three grid-bound energy carriers (electricity, natural gas and district heating). Additionally, Figure 4-18 contains existing power plants, with grid connections. They are marked with colored circles within certain cells. The only feed-in into the district heating network is an industrial complex in cell 2, marked with a green circle. Cells with electricity generation are marked with a red dot and cells with both, electricity and

natural gas production are pictured with a blue and red dot. If one wants to model the energy system of the city first and analyze the interaction with the surrounding districts afterward, the cellular approach would allow to further aggregate all 44 cells into a single city cell for further analysis of the whole region, which is done within the next scenario.

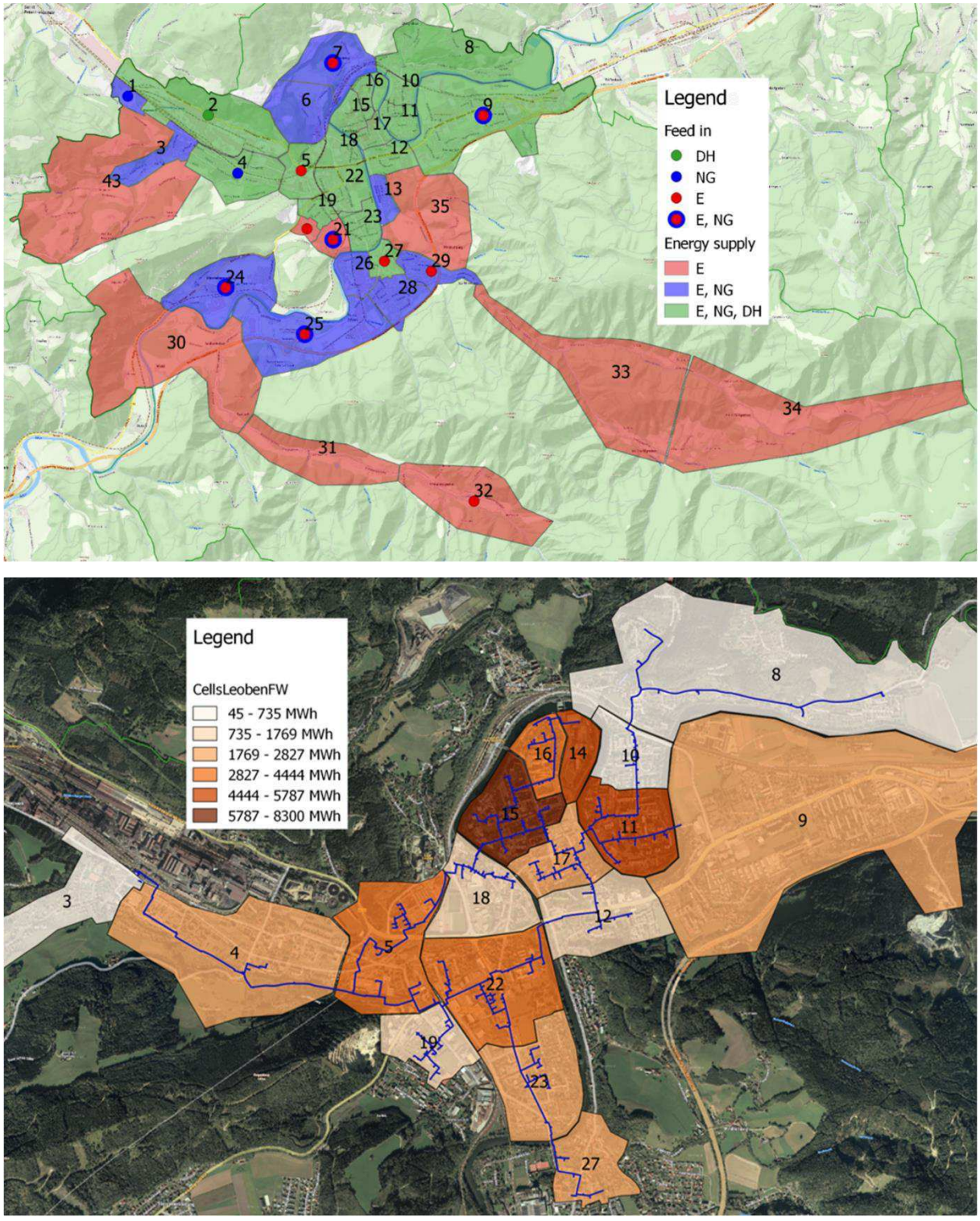

Figure 4-18: Applied cellular approach to the analyzed municipality (top) – District heating network of the analyzed municipality within the cellular approach (bottom)

The lower illustration of Figure 4-18, exclusively shows the cells of the city, where the district heating grid is available. The blue lines represent the piping layout and the individual cells are colored depending on the annual energy consumption of the cell. There are similar illustrations for the power grid and the natural gas grid, which are larger and consist of more meshed branches but they are not shown due to confidentiality reasons. This is why, a simplified grid illustration for all energy carriers, without the spatial localization of the grid infrastructure is presented in Figure 4-19.

One can see that only one level of a load flow calculation is performed, as there is only one level-2 cell. Each level-1 cell represents a specific area in the analyzed city, analogous to Figure 4-18. If there is a grid connection between two cells, it is also represented in the calculation. The electrical grid connecting the cells is a 5.25 kV medium voltage grid, which is connected to the high voltage grid via transformers in the cells 1 and 2. These connections are connected to a fictive slack node in order to perform the load flow calculations with the system boundaries.

It becomes more challenging with the district heating network since the numerical calculation methodology requires a slack node outside the system boundary. However, the necessary heat is not obtained from an external source, such as a superior grid level, but is supplied from a cell (cell 2) within the system boundary. This makes it necessary to introduce a slack node outside the system and connect a lossless line to the actual cell, supplying the industrial waste heat. The actual load flow results of the 17.5 bar district heating grid, which is operated at 90 °C, are not affected by this measure. Finally, the 4 bar gas distribution network has one grid connection to the high-pressure gas grid.

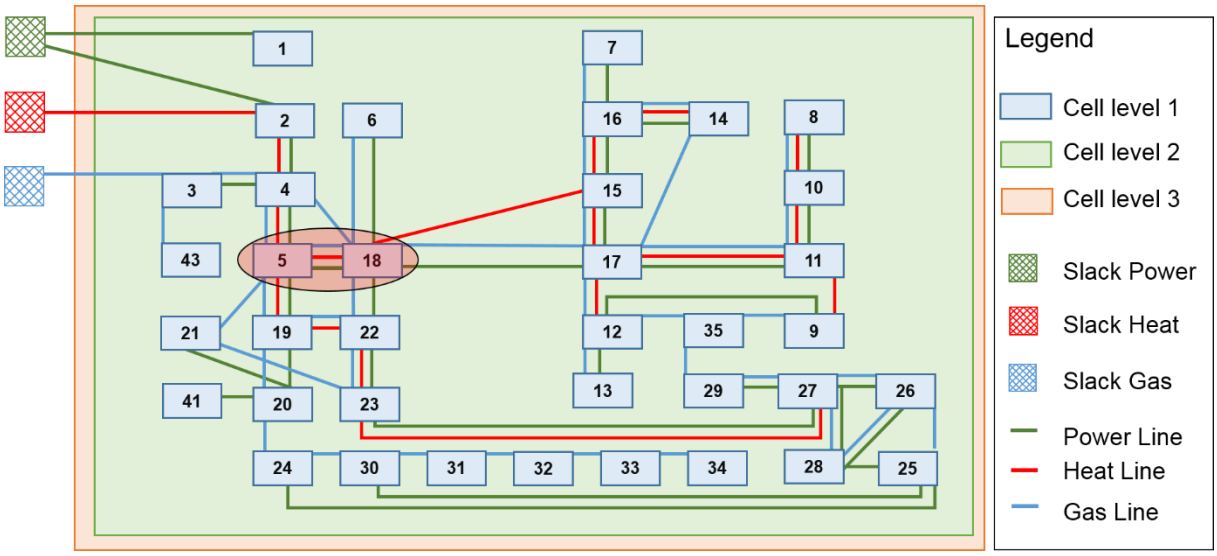

Figure 4-19: Topology of all three energy grids for case study 2

All demand profiles for electricity, natural gas and district heating are illustrated in Figure 4-20. The natural gas demand is further split up in temperature-dependent heating applications and process gas for industrial applications. One can see that the demand for heating applications is dominant at this lower pressure level compared to the industrial application. The standardized load profile for process gas is published in [184].

The electricity demand is modelled by the combination of standard load profiles for the individual building stock in the corresponding cells. The aggregation of many consumers to the presented cells allows the usage of standardized load profiles because there are more than 150 consumers in every cell – see section 2.2.

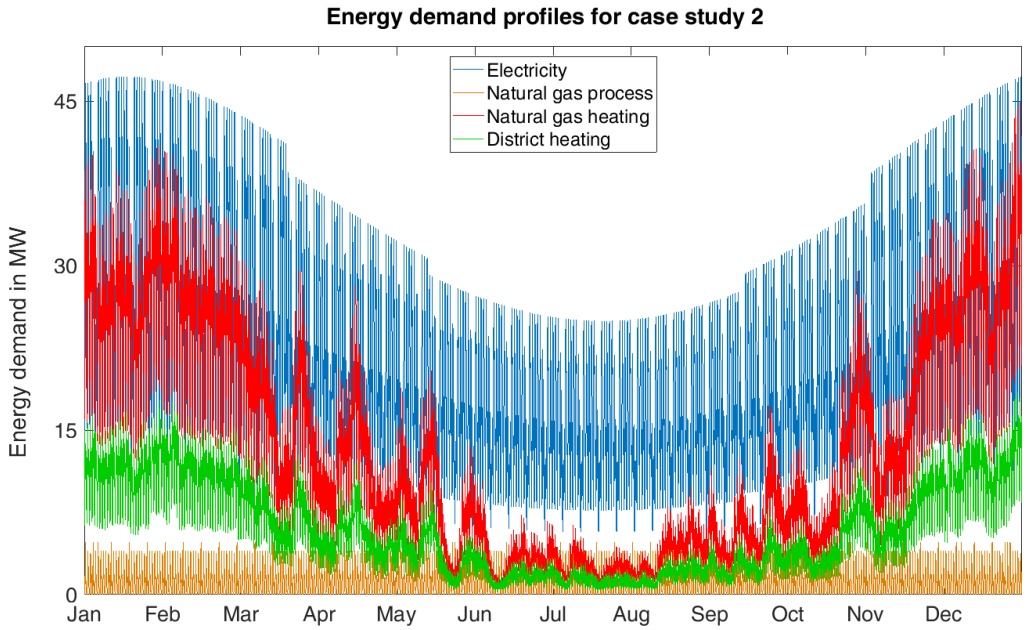

Figure 4-20: Annual energy demand profiles for all energy carriers within case study 2

All level-1 cells have to be parameterized in terms of their residual load and possible energy storage systems or hybrid elements. Analogous to case study 1, this is performed by four scenarios. Table 4-13 summarizes the key attributes of all scenarios within case study 2. The detailed explanations follow in the next paragraph.

Table 4-13: Different scenario configurations within case study 2

Parameter	Reference scenario	High-stress scenario	Improvement scenario 1	Improvement scenario 2
Demand	Standard	Standard 1,600 EV	Standard 1,600 EV	Standard 1,600 EV
Generation	Hydro p.p. Biomass p.p	Hydro p.p. Biomass p.p PV potential (50 %)	Hydro p.p. Biomass p.p PV potential (50 %)	Hydro p.p. Biomass p.p PV potential (50 %)
Electric ESS	-	-	11.5 MWh/7.7 MW	115 MWh/77 MW
Thermal ESS	-	-	-	128 MWh/14.4
HE	-	-	-	Heat pumps

To model the local energy generation, one has to consider two power plants in all four scenarios within the system boundary: generation profiles of the run-of-river power plant with a maximum power of 10.4 MW and a 3.6 MW biomass power plant were confidentially handed over for the year 2014. The generation data is implemented into the cells containing the mentioned power plants and stays constant for all scenarios. [159]

Another constant for all scenarios is the described grid infrastructure for all energy carriers. The maximum current carrying capacity I_{therm} of an electrical power line is dependent on the used cable type. The deciding factors are the nominal voltage and the cross-sectional area of the cable. The maximum power carrying capacity P_{therm} is therefore defined as I_{therm} times the nominal voltage. A specific cable type is assigned to all power lines, via NEPLAN file of the DSO, to the electrical grid. Derived from this data, most power lines are capable of transferring between 1-3.2 MW in power. The maximum transmission power of the district heating grid and the natural gas grid is dependent on the mentioned pressure level, the diameter of the individual pipes and the fluid velocity. While the nominal pressure and the diameter of the pipes are known, the maximal fluid velocity is assumed to be 3.25 m/s for district heating grids and 10 m/s for natural gas grids. These maximum values were gathered from Schmidt [185] and lead to maximum power transports of 20-35 MW for district heating grids and around 3 MW for the low-pressure natural gas grid. With the infrastructure, the energy demand and energy generation defined, the calculation of the reference scenario can be performed.

In order to calculate the high-stress scenario, additional load profiles of electric vehicles have to be calculated and distributed to the cells and additional PV generation capacity is added to all cells, depending on their individual potential. The EV demand is calculated with the approach of Thormann et al. [178], which is already described in section 4.1.

The total number of 1,600 EV is derived from the building count of the city. This follows the assumption that 25 % of all Single Family homes own an EV, and each multi-family home and apartment building is assigned one EV as well, which is consistent with the #mission2030. [3] Due to the stochastic approach and the used probability density function individual load profiles with different charging times are created. These individual profiles can be distributed to the corresponding cells.

The second addition compared to the reference scenario is the added PV potential. An estimation of this future PV potential is based on two datasets: the Styrian Solar-Roof Cadaster [186] and the measured irradiation data provided by ZAMG [159]. The Styrian Solar-Roof Cadaster is publicly available at the website of the regional government of Styria. It classifies all allocable roof areas based on airborne-laser scanning (ALS), into “good” and “very good” applicable roof areas in the whole state, depending on the position and angle of the examined roof. Figure 4-21 shows an exemplary part of the analyzed city and the marked roof areas. All areas with a (partly) south orientation and ideal inclination angles between 0-40 ° are considered as “good” and “very good” applicable rooftop areas. Section 3.4.2 describes the calculation methodology to calculate the time-resolved energy yields from the identified areas.

Figure 4-21: Example of identified rooftop potentials. “Very good” rooftop areas are marked in red – “Good” rooftops areas are marked in yellow

In this high-stress scenario, PV plants with a maximum power of 42.6 MW_{peak} and an annual yield of 43.5 GWh are implemented. This represents 50 % of the identified PV roof-top potentials of each cell of the city, leaving aside certain areas in the historic city center, which is also derived from the goals of the #mission2030 strategy. [3] The distribution of the overall PV rooftop potential per cell is illustrated in Figure 4-22, where the black areas within the cells represent the identified rooftops, analogous to Figure 4-21 above.

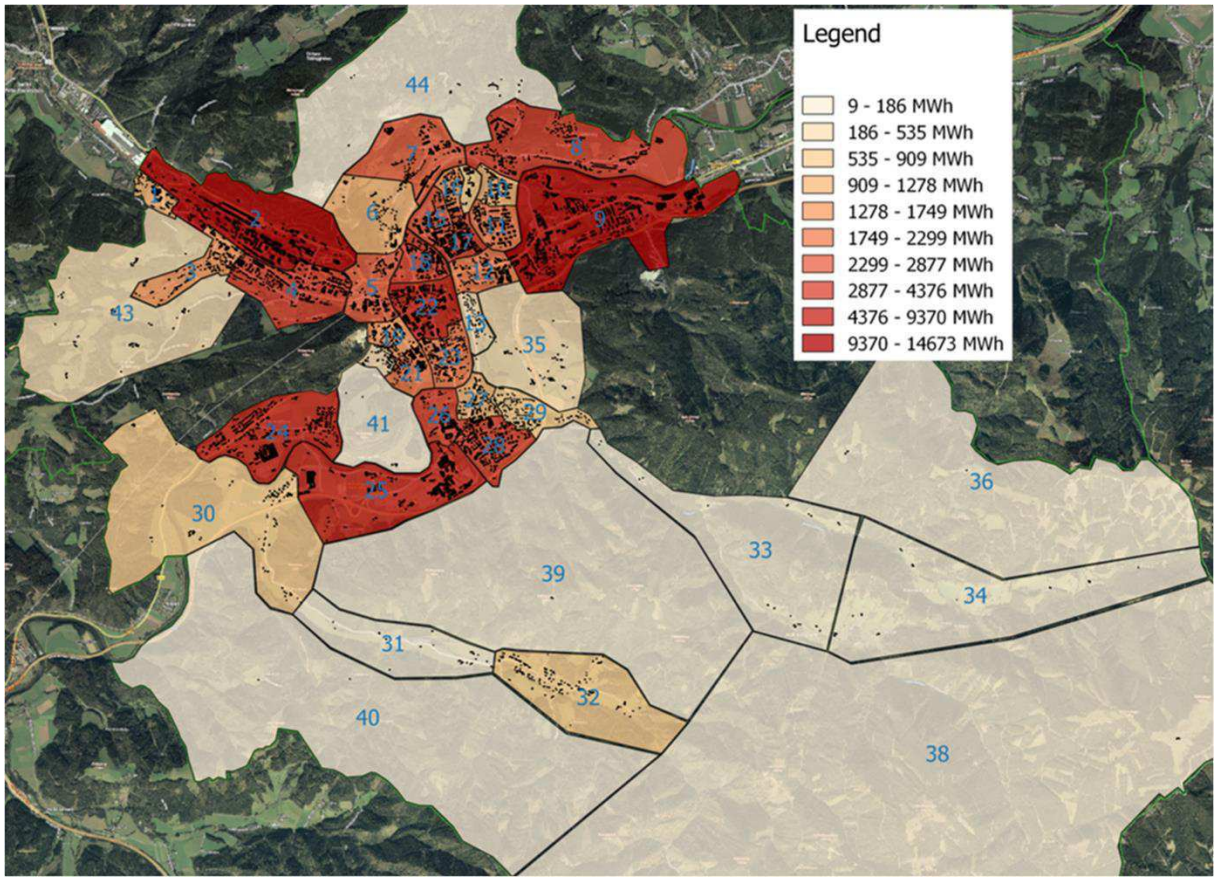

Figure 4-22: Identified PV rooftop potential in the defined cells.

The two improvement scenarios consist of all the identical demand and generation data, as the high-stress scenario, but energy storage and hybrid elements are additionally implemented. In improvement scenario 1, every fourth Single Family home and every Multi-Family home owns a Lithium-Ion battery with 7.2 kWh storage capacity and a charging/discharging power of 4.8 kW. The roundtrip efficiency is assumed to be 95 %.

The same number of homes is assigned a thermal ESS with an energy capacity of 80 kWh and a charging/discharging power of 10 kW. The roundtrip efficiency of the thermal ESS amounts to 99.9 % and the self-discharge due to thermal losses is assumed to be 0.02 %/hour.

Improvement scenario 2 is basically an upscaled version of improvement scenario 1. It consists of ESS with the same specifications, but the numbers of the described ESS are increased tenfold. This corresponds approximately to the number of households, public buildings and commercial building units in the city, meaning that almost every building in the city is equipped with a storage unit. Additionally, the same number of buildings is assigned a heat pump, which substitutes the heat demand by electricity. An overview of all scenarios within this case study is presented in Table 4-13.

Results description

Figure 4-23 summarizes selected KPIs of all energy carriers as exemplary results for the overall urban energy system of case study 2. Due to the significantly higher values compared to the electricity sector, the results of the district heating and the natural gas are depicted on the secondary vertical axis on the right.

In the **reference scenario**, the annual maximum power import amounts to 20.7 MW. 39.5 GWh of electricity need to be imported, while the exported electricity sums up to 5.0 GWh with an annual maximum power export of 8.6 MW. The average daily maximum of power imports is 10.2 MW. The imported heat remains unchanged in the first three scenarios at 58.0 GWh and the gas imports are constant throughout the entire case study 2 at 121.3 GWh. After implementing additional 50 % of the identified PV potentials and electric vehicles according to described **high-stress scenario** of Table 4-13, the electricity-related indicators significantly change. The annual power maximum increases to 26.1 MW for electricity imports and to 46.6 MW for electricity exports. Despite the increase of the annual power maximum, the average daily maximum of imported electricity decreases to 9.3 MW. Annual electricity imports significantly drop to 23.0 GWh, while the exported electricity rises to 42.3 GWh. In **improvement scenario 1** with additional electric ESS, the annual power maximum for electricity imports remains almost unchanged compared to the high-stress scenario with only a minimal decrease of 0.4 MW to 25.7 MW. Also the average daily maximum of imported electricity decreases only slightly to 22.1 MW. The annual power maximum for electricity exports can be reduced to 44.5 MW or 4 % compared to the high-stress scenario. Also the annual electricity imports are reduced to 22.1 GWh, while the exported electricity decreases to 41.6 GWh. This is a decline of 4 % in imports and 2 % in electricity exports compared to the high-stress scenario. The imported energy from the district heating grid and the natural gas grid does not change compared to the high-stress scenario.

Improvement scenario 2, with additional heat pumps and thermal ESS, leads to a reduction in the maximal annual power export to 38.0 MW and a decrease in annual maximal power

import to 24.3 MW. The average daily maximum of electrical power amounts to 6.7 MW, which corresponds to a reduction of 27 % compared to the high-stress scenario. The overall electricity imports drop 18 % to 19.0 GWh, while the electricity exports decline 15 % to 35.9 GWh. Additionally, the amount of imported energy from the district heating grid reduces to 48.4 GWh, which corresponds to a 17 % reduction compared to the high-stress scenario. All values are summarized in Figure 4-23 and the interpretation of the scenario results is presented in the next paragraph.

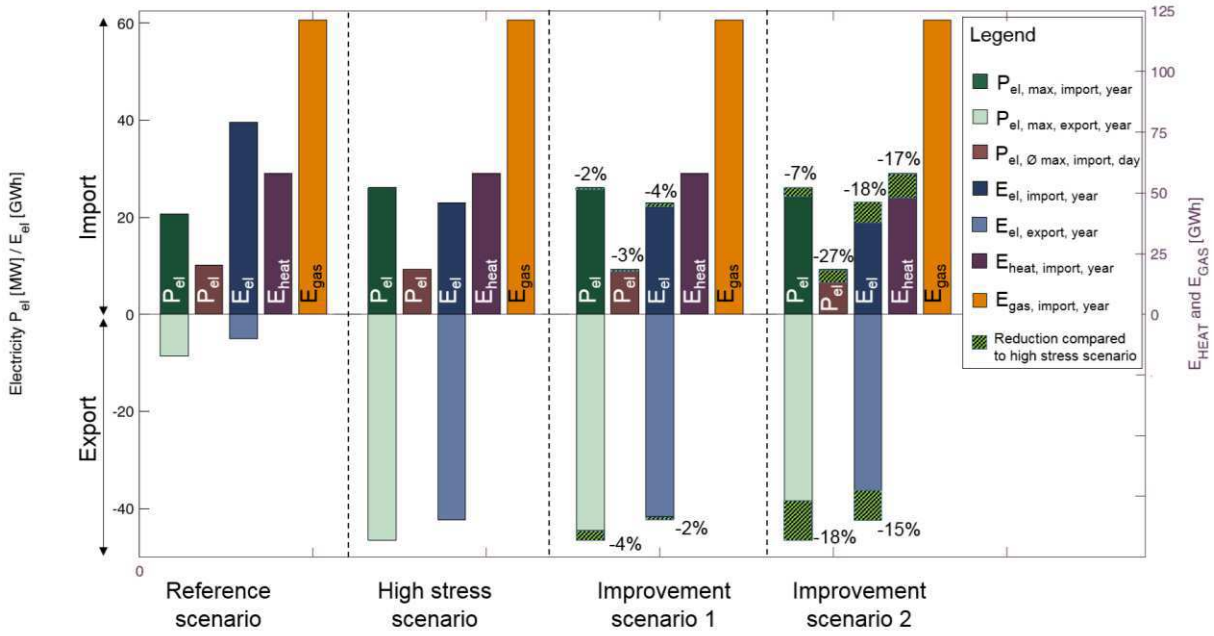

Figure 4-23: Key results of all deployed scenarios of case study 2

Results interpretation

The biggest change in the obtained results can be seen between the **reference scenario** and the **high-stress scenario**. By adding the EVs and the PV potential, especially the positive and negative peaks of electrical power, as well as the energy exports, are increased significantly. In contrary to case study 1, the power peaks of the electricity exports are higher than the power peaks of the electricity import. Another difference between case study 1 and case study 2, is the decrease in the overall electricity imports in the high-stress scenario. This can be explained by the fact that the generated electricity from the implemented PV systems outweighs the additional load caused by electric vehicles. Due to the fact that EVs are only assigned to residential buildings and PV systems are modelled on 50 % of all buildings (including large commercial and industrial rooftops), the PV systems have a larger effect on the overall urban energy system than electric vehicles.

In case study 1, where only a small residential area with households is modelled, exactly the opposite effect is noticeable. The ratio between the implemented PV systems and residential storage causes deviations in the results of **improvement scenario 1** compared to case study 1 as well. While the implementation of electric ESS to the households has a large effect on for instance the exported electricity (-63 %) in case study 1, the impact of battery implementation is only marginal in case study 2. A reduction between 2-4 % in both, electricity exports/imports and power minima for exports and imports shows the minor effect of decentralized energy in this particular urban energy system. The explanation behind that phenomenon is simple: when a whole region including large public buildings, commercial parks and industrial rooftops are used for PV energy generation, household-sized ESS cannot provide enough capacities to deal with an overall PV generation of 43.5 GWh, not even when placed in many households. Utility-sized PV implementation requires utility-sized storages in order to reach the same improvements compared to case study 2. In **improvement scenario 2**, the increased amount of electrical ESS, the additionally implemented heat pumps and thermal ESS show larger effects on all presented KPIs of Figure 4-23, even though the effects cannot keep up with achieved reduction of case study 1.

4.3.4 Case study 3

The third case study aims to analyze the interaction of the urban energy system shown in case study 2 with its surrounding region and the connecting infrastructure. This should demonstrate the modelling framework's ability to perform calculations on two different voltage and pressure levels.

Case study description

To fulfill this task, four level-2 cells are introduced to the case study. The first level-2 cell is the city of case study 2, including all 44 level-1 cells, as previously shown in Figure 4-19. Additionally, an industrial park is placed right next to the city. It was neglected in case study 2, since it is connected to a higher grid level, both in electricity and in natural gas. As there is no data on the actual load profiles of the industrial enterprises and processes within this cell, no further distinction was made and the industrial cell contains only one level-1 cell. Additionally, two surrounding districts are selected as part of the system boundary to investigate the energy exchange of the city and the industrial park with the local surrounding. Both districts are considered without further distinction as one level-1 cell. This means that all consumers, generation and storages in districts 1 and 2 are not provided with the same detailed resolution as in the city cell. This structured view enables to analyze the changed load flows of the city, with the embedding in its surrounding. However, it does not supply any information about the

load flows within the mentioned districts themselves, since these districts were not equipped with the same detailed resolution as the city. This is a big advantage of the applied cellular approach because the level of detail can vary between cells, even within one simulation. Cells of specific interest can be considered in more detail, while the aggregation level of other cells is much higher. Figure 4-24 summarizes the geographical location of the four level-2 cells and shows the grid connection between these cells underneath.

The slack node of the high voltage 110 kV electrical grid is placed next to district 2, which has a connection to district 1. Districts 1 and 2, the industry-cell, as well as the city, are connected to the 110 kV line via substations. The lines, as well as the substations, are modelled with realistic grid data. From district 1, there is an electrical grid connection to the industry cell and the city in district 1. The high-pressure natural gas grid (60 bar), has the same topology as the electrical high voltage grid. The industrial cell is the actual origin of the district heating grid, but as mentioned in case study 2, the numeric calculation procedure demands a slack node outside the system boundary. This problem is solved analogously to case study 2, by introducing a lossless pipe between the industrial cell and the fictional slack node. All grid connections, load profiles and generation facilities of the city in district 1 are identical to the described case study 2. It has to be noted, that due to the lack of complete and consistent data in the industrial cell and both districts, this case study has to be considered as a generic, fictional case study with modeled data. The approaches for modelling demand, generation and renewable potential within these cells are described in the following paragraphs.

Calculating the energy consumption for an entire district is challenging if no measured data is available and requires assumptions, especially regarding the energy consumption of the industrial sector. These assumptions can approach the actual energy consumption, but always leave a margin of error. Due to the fact that this case study does not claim to represent the actual load flow in the analyzed area and timeframe and is rather meant as a generic demonstration example of the presented methodology, this is no cause for any major concern. However, the methodology to model the energy consumption of all energy carriers in the modelled districts is based on Sejkora et al., as published in [12,187]. It combines a top-down approach with a bottom-up approach. Many large industrial companies publish their annual energy consumption voluntarily in sustainability reports. This allows locating approximately 40 % of the industrial energy consumption to districts. The remaining demand is distributed via a top-down approach using publicly available information of industrial energy consumption per industry sector and the employees per sector in all districts, published by Statistics Austria. [188–190]

The residential energy demand is modelled similarly to the two previous case studies. All combined results of the energy demand per energy carrier for the two districts of interest are shown in Table 4-14.

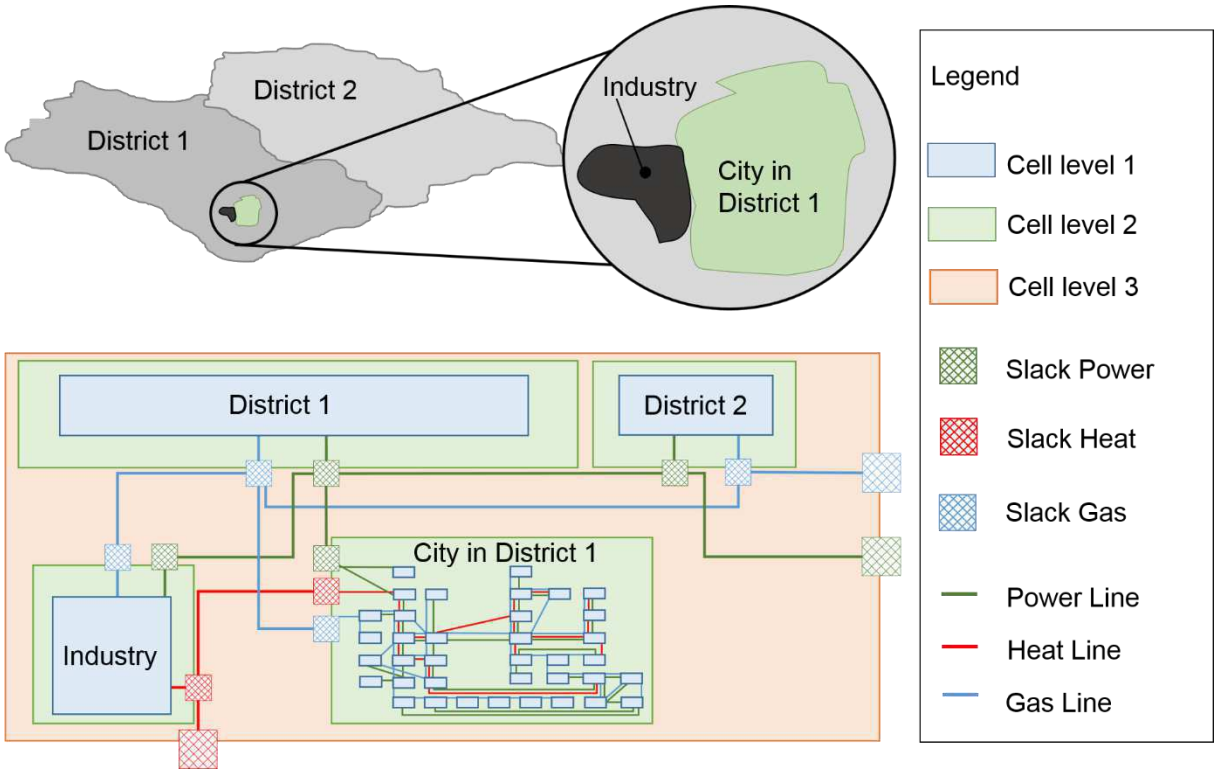

Figure 4-24: Topology of case study 3

Table 4-14: Summary of determined energy consumption for all level-2 cells in case study 3

	Annual Electricity consumption in GWh	**Annual Natural Gas consumption in GWh**	**Annual District Heat consumption in GWh**
District 1	108.8	146.2	-
District 2	855.9	1900.0	-
City in District 1	182.8	120.7	48.6
Industry Cell District 1	212.5	1013.0	-

After dividing the energy demand into residential and industrial energy demand[4], the creation of load profiles is initialized. Standardized load profiles are used for the residential load profiles in electricity and the SigLinde approach is applied to heating applications for natural gas and district heating. The standardized industrial load profile is applied to the industrial electricity demand and the industrial gas demand is considered to be a continuous load. This

[4] The transport sector is neglected, since it is barely covered by grid-bound energy carriers today.

leads to consumption profiles, as shown in Figure 4-25. One can see that the natural gas demand is dominated by the industrial demand, with its approximately 350 MW base-load, while the temperature-dependent share, leading to higher demand in the beginning and at the end of the year is relatively small. When the industrial and the temperature-dependent load profile for natural gas are cumulated, the overall peak-load amounts to approximately 420 MW. The electricity load profile does not show a major seasonal effect in the reference scenario. Once the large PV potential is added to the residual load, very high negative peaks, in the range of approximately 4 times the grid load maximum, can be observed, especially in the summer months. The district heating demand is only located in the city-cell. Therefore it is unchanged compared to case study 2, which is why it is not illustrated again in Figure 4-25.

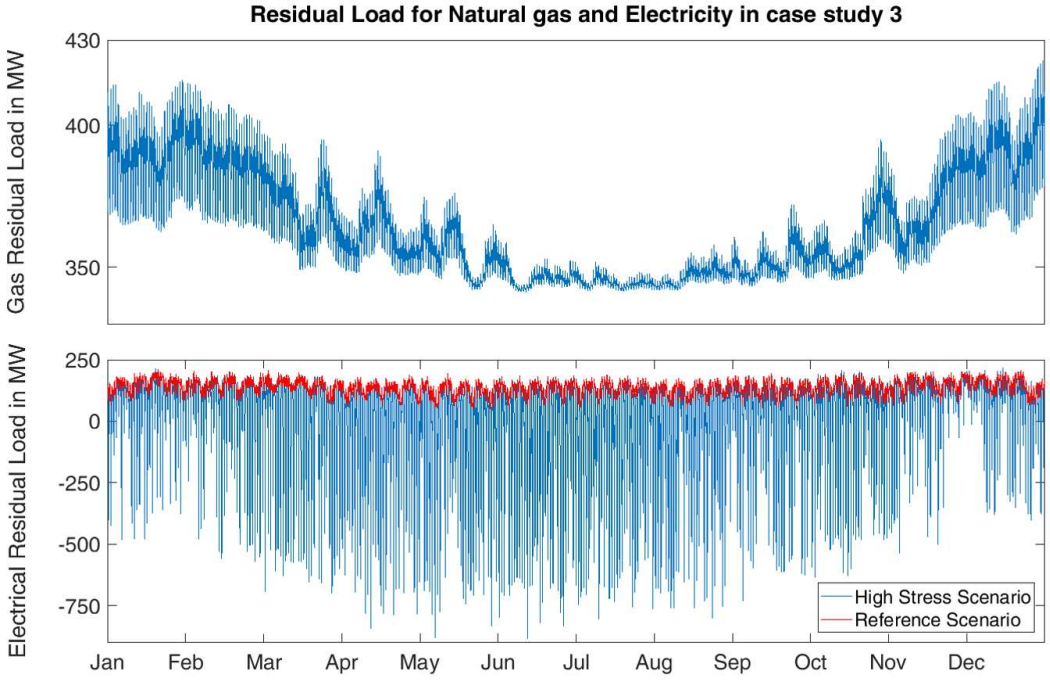

Figure 4-25: Residual load for natural gas and electricity for the reference and high-stress scenario

The scenarios within case study 3 are structured identically to the previous case studies. Modelling of the energy demand in the reference scenario has already been described and the already existing generation units (hydropower plant, biomass power plant) don't change compared to case study 2. For the high-stress scenario, the number of electric vehicles is increased by the number of people in all cells compared to the city's population in case study 2. This leads to a number of 7,900 EVs in all four cells together, which is again consistent with the #mission2030 strategy. [3]

Another change in this case study is the determination of the PV potential. While the rooftop potentials for PV energy is determined according to the previously described Solar Roof cadaster methodology, the potential of solar parks, which are not building-mounted has been evaluated as well. This leads to a total PV potential of 832 GWh per year with an approximate maximum power of 800 MW. [187] In the improvement scenarios electric ESS and thermal ESS are added according to Table 4-15. Additionally, a large Power2Gas plant with a maximum power of 500 MW and an efficiency of 65 % [90,93] is added in improvement scenario 2. All parameters of all scenarios within case study 3 are summarized in Table 4-15.

Table 4-15: Different scenario configurations within case study 3

Parameter	**Reference scenario**	**High-stress scenario**	**Improvement scenario 1**	**Improvement scenario 2**
Demand	Standard	Standard 7,900 EV	Standard 7,900 EV	Standard 7,900 EV
Generation	Hydro p.p. Biomass p.p	Hydro p.p. Biomass p.p PV potential	Hydro p.p. Biomass p.p PV potential	Hydro p.p. Biomass p.p PV potential
Electric ESS	-	-	57 MWh/38 MW	57 MWh/38 MW
Thermal ESS	-	-	-	128 MWh/14.4 MW
HE	-	-	-	Heat pumps 15.8 MW_{th} MW P2G: 500 MW_{el} η=0.65

Results description

Figure 4-26 shows the key results of all conducted scenarios of use case 3. The results of the **reference scenario** show the net energy demand of all energy carriers and power peaks of electricity of the analyzed area. It can be seen that no energy is exported within this scenario. The annual maximum power import for electricity amounts to 242.9 MW with a total import of 1.33 TWh. The average daily maximum of power imports is 188.9 MW. The imported heat and natural gas remain unchanged in the first three scenarios at 58.0 GWh and 3.18 TWh respectively.

After implementing the identified PV potentials and electric vehicles according to described **high-stress scenario** of Table 4-15, the annual power maximum increases to 255.8 MW for electricity imports and to 646.2 MW for electricity exports. Despite the increase of the annual power maximum, the average daily maximum of imported electricity slightly decreases to 181.4 MW. Annual electricity imports significantly drop to 832.9 GWh, while the exported

electricity rises to 474.4 GWh. In **improvement scenario 1** with additional electric ESS, the annual power maximum for electricity imports remains almost unchanged compared to the high-stress scenario with only a small decrease of 8.2 MW to 247.6 MW. Also the average daily maximum of imported electricity decreases only slightly to 177.7 MW. The annual power maximum for electricity exports can be reduced to 615.9 MW or 4.7 % compared to the high-stress scenario. Also the annual electricity imports are reduced to 804.6 GWh, while the exported electricity decreases to 455 GWh. This is a decline of 4 % in imports and 3 % in electricity exports compared to the high-stress scenario.

Improvement scenario 2, with additional heat pumps, thermal ESS and most importantly a large, fictive P2G plant leads to a significant reduction in the maximal annual power export (178.2 MW or minus 72 %), while the annual maximal power import remains unchanged compared to improvement scenario 1. The overall electricity imports decrease slightly to 824.0 GWh, while the electricity exports decline 99 % to 7.0 GWh. Additionally, the amount of imported energy from the district heating grid reduces to 42.4 GWh, which corresponds to a 27 % reduction compared to the high-stress scenario. The relative change in natural gas imports remains limited, with a reduction of 8 %, but in absolute terms this corresponds to a decrease of 244.5 GWh. All values are summarized in Figure 4-26 and the interpretation of the scenario results is presented in the next paragraph.

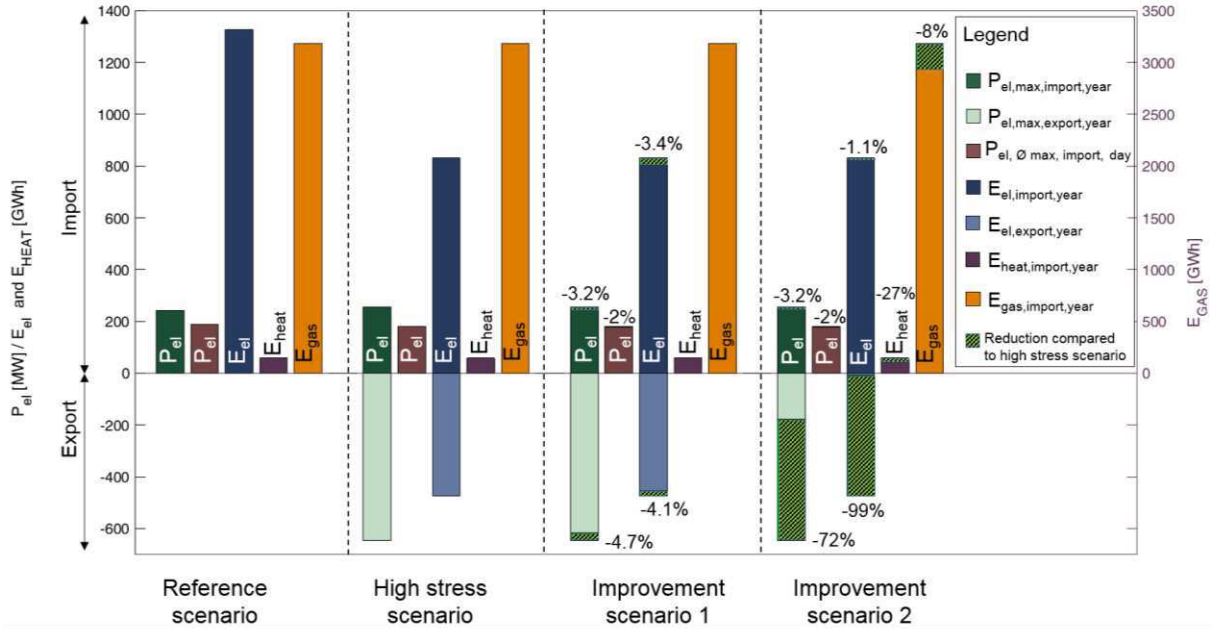

Figure 4-26: Key results of all deployed scenarios of case study 3

Results interpretation

In the **reference scenario**, the large electricity and natural gas imports compared to the other case studies ist noticeable. This is due to the modelled industry, which accounts for most of the electricity and especially natural gas imports. By adding the EVs and the large PV potential of the region in the **high-stress scenario**, especially the negative peaks of electrical power as well as the energy exports are increased significantly, while the necessary electricity imports decline. One can clearly see the mismatch between the annual power peaks of electricity imports and exports and the total electricity imports and exports in terms of energy. While the power peak for export is a huge 646.2 MW, the power peak for electricity import amounts to 255.0 MW, even though the total imported electricity is much higher (832.0 GWh) compared to the electricity exports (474.4 GWh). This is due to the difference in the even electricity load profile of the dominant industrial demand is contrary to the highly intermittent generation of PV electricity.

Improvement scenario 1, with added electrical ESS confirms the results of case study 2. Residential batteries, even when placed in a significant number of households, cannot level out the fluctuating residual loads of large scale PV implementation. A very big change, however, can be observed in **improvement scenario 2**. The large fictional P2G plant is capable of reducing almost the entire exported electric energy, by means of converting it to natural gas. The remaining exported power peaks of 248 MW are still high, but account for only just over 1 % of the exported electricity because these power peaks only occur on rare occasions. Examples for these occasions are higher surplus electricity than the maximum power of the P2G plant or unconvertible power peaks due to the implemented P2G ramp rate restrictions. This means that large central P2G plants have the ability to balance the fluctuations of renewable generation characteristics, however, other challenges may arise. Depending on the location of these large central plants, grid congestions from and to these units are challenging, because all of the excess electricity needs to be transported to one central plant.

Extract of more specific results

Another way to visualize the time-resolved energy imports/exports over the whole year, as well as the calculated power maxima/minima, are load duration curves, shown in Figure 4-27. It shows the sorted power exchange with the superior grid for all three considered energy carriers. One can see, that the electrical power duration curve greatly varies in the four scenarios. Especially the difference between the reference scenario and the high-stress scenario is striking. Around 3,000 hours with negative residual loads and power exports caused by the added fluctuating generation is clearly visible. Improvement scenario 1 with

added storages can add little to reduce exports, but the P2G plant in improvement scenario 2 is able to reduce almost all electrical power exports. This exact phenomenon can also be observed in the visualization of P_{Gas} in Figure 4-27.

At times where electrical exports are reduced by the P2G plant the external demand for gas supply is greatly reduced. The P2G plant is not able to reduce load peaks in neither the electrical nor the gas imports. The visualization of the high stress – and the improvement scenario was waived due to the overlap with the reference scenario in P_{th} and P_{Gas}. In the district heating grid the improvement scenario 2 with added heat pumps and distributed thermal storage units succeeded to reduce the imports throughout the year. The necessary maximum power, however, could not be significantly reduced, because of the small chance of simultaneous appearances of electrical energy surpluses and the maximum heat demand.

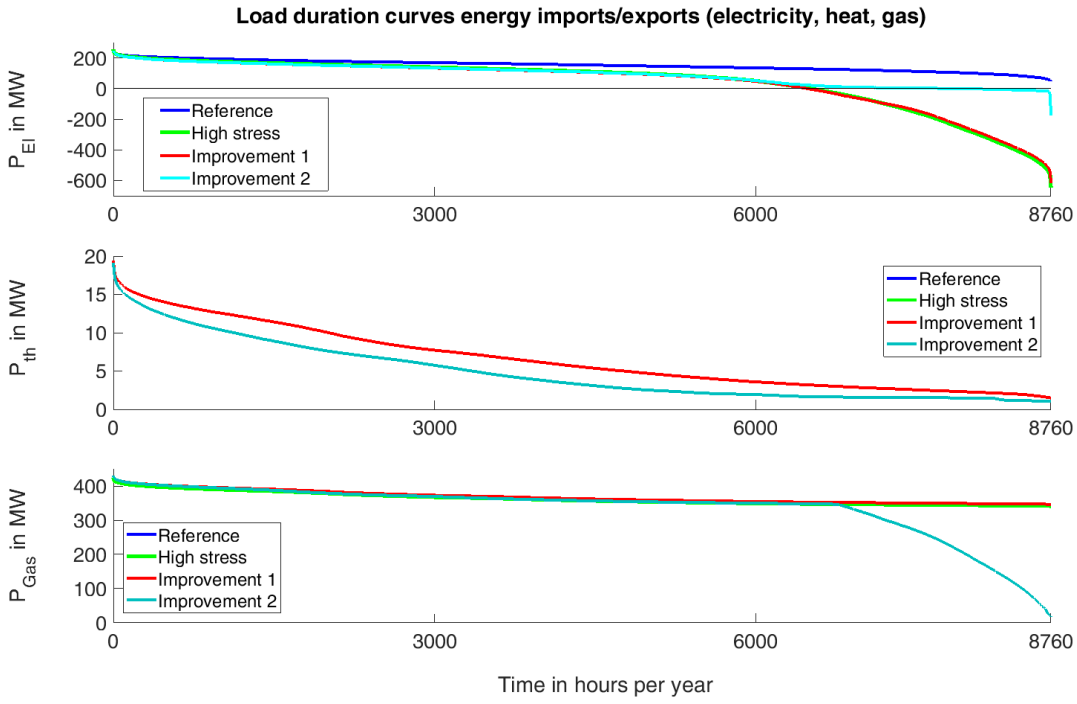

Figure 4-27: Load duration curves of energy imports/exports for all energy carriers and one year

Case study 3 is also used to present some examples of more detailed results, because no results regarding the changed time-resolved residual load, the operation profile of sector coupling elements such as the P2G plant, the SoE of ESS or the load flows on specific lines were presented in the previous case studies.

In Figure 4-28, a selected power line of the city in district 1 between cell 5 and cell 18 (see Figure 4-19) was randomly selected for demonstration purposes only. One can see the time-resolved power flow of all grid-bound energy carriers for a week (left) and as a load duration curve (right). One can see the time-resolved power of all grid-bound energy carriers for a week (left) and as a load duration curve (right) with the data of the high-stress scenario.

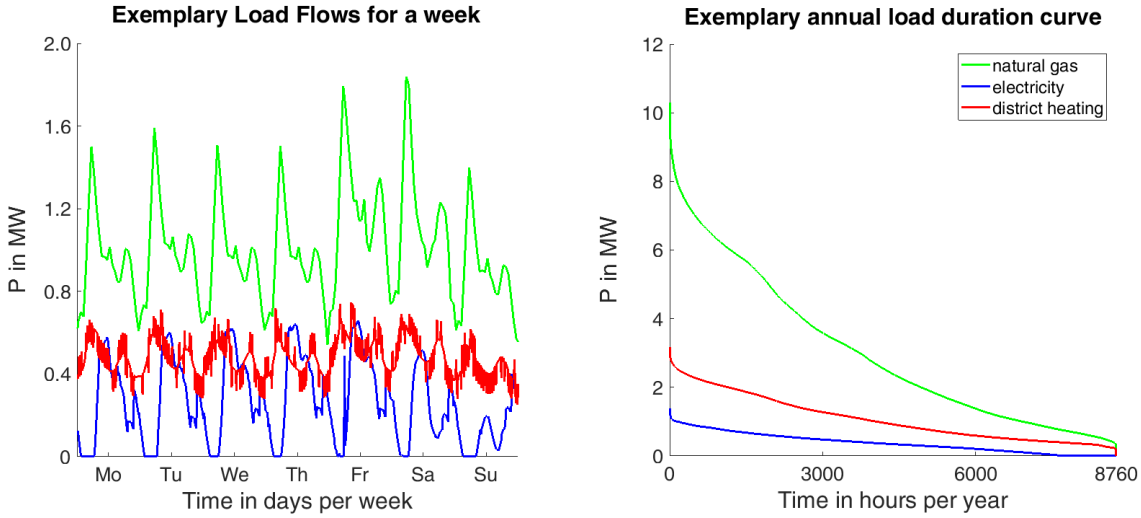

Figure 4-28: Exemplary load flows for a selected week on the power line between cell 5 and cell 18 (electricity, natural gas, heat) and the corresponding annual load duration curve

The maximum current carrying capacity I_{therm} of an electrical power line is dependent on the used cable type. The deciding factors are the nominal voltage and the cross-sectional area of the power line. The maximum power carrying capacity P_{therm} is therefore defined as I_{therm} times the nominal voltage. In the case of a chosen power line of the city center (slack node to cell 1 – see Figure 4-19) P_{therm} amounts to 3.2 MW. One can clearly see the increased negative load flows of the high-stress scenario compared to the reference scenario. At times, where P_{therm} exceeds the allowed value, the graph for the three exemplary days is marked in red. In the case of the three chosen days, only certain peaks of the high-stress scenario induce overloads on the specific power line. The overall load flow duration curve is shown in the right part of Figure 4-29. It shows, that the chosen measures of improvement scenario 2 help to reduce the maximum peak power and to reduce the times, where an overload occurs. In the high-stress scenario, the maximum power of the line is 4.65 MW and the overall duration with a registered overload is 176 hours in the modeled year. The improvement scenario 2 is not able to prevent all occurring overloads, but helps to reduce them to 18 hours per year with an occurring maximum power of 3.2 MW.

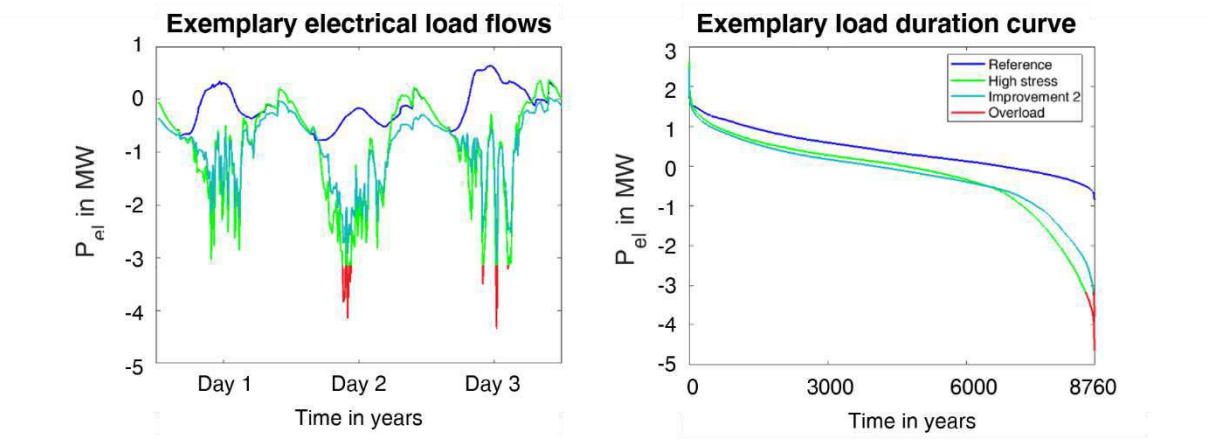

Figure 4-29: Exemplary electrical load flows of the power line Slack-1 in different scenarios.

Figure 4-30 shows the utilization profile of the P2G plant in the improvement scenario 2 for a selected week. The P2G plant operates at times of negative residual loads caused by surpluses of the fluctuating renewable generation. Its set maximum power of 500 MW is rarely used (around 26 hours per year), but the overall hours of operation amount to more than 2,200 hours. This corresponds to approximately 1,130 full load hours, which is an important indicator of the economic viability of P2G plants. Even though P2G plants are not economically feasible today, the number of full load hours is absolutely a key parameter for future economic evaluations. The amount of operation hours is supported by the continuous large demand for natural gas by the industrial cell. If there was a more fluctuating demand profile of natural gas, a gas storage unit would help to ensure a high utilization rate.

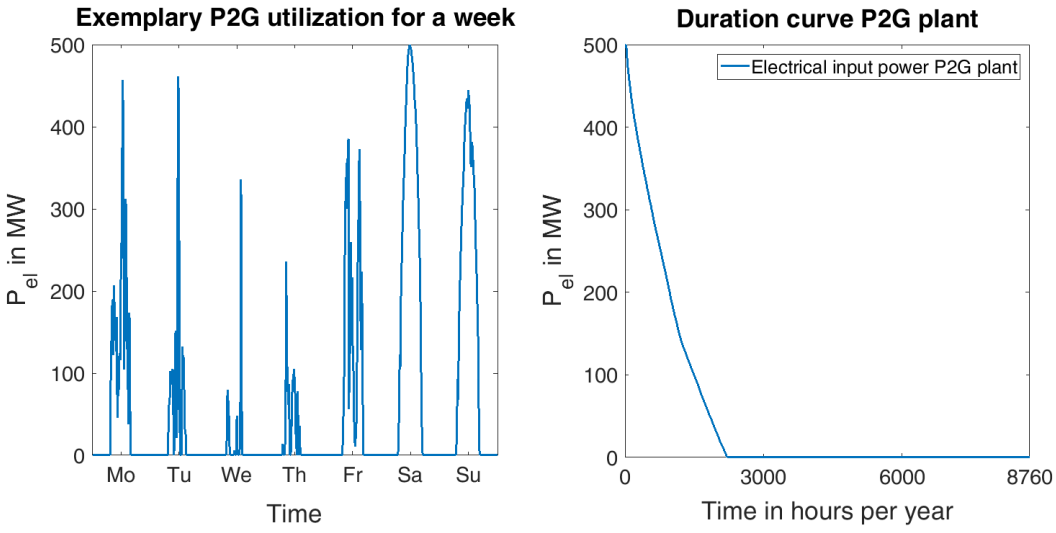

Figure 4-30: Exemplary P2G utilization profile for a chosen week (electrical input power) and the corresponding annual duration curve

In Figure 4-31, one can see a charging/discharging profile of a randomly chosen electric ESS unit and for a randomly chosen week. The visualization shows that the system serving energy storage units are operated in its maximum power very often and show a very evenly distributed charging/discharging cycle. The appearance of both visualizations allows concluding that only a small share of the positive and negative residual loads can be stored within this particular energy storage unit. Predominantly the storage is inactive, because it is either full or empty and cannot react to fluctuations in the corresponding residual load anymore, which can be seen in the duration curve of Figure 4-31.

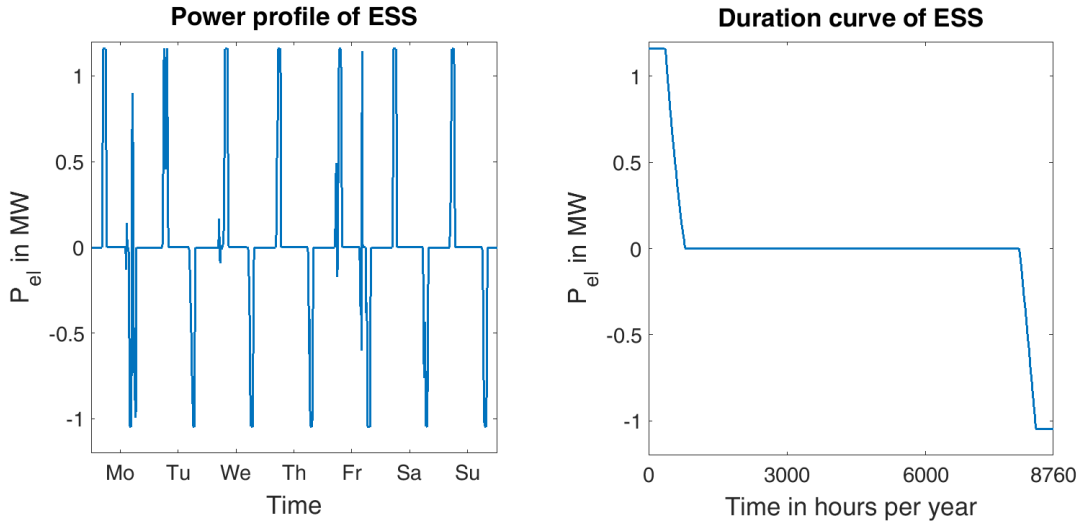

Figure 4-31: Exemplary charging/discharging power of a selected electrical energy storage unit and the corresponding annual duration curve

5 CONCLUSION & OUTLOOK

This section summarizes the achievements of this published thesis with particular regard to the initially defined research questions. Afterward, the key findings are highlighted, before giving an outlook on future research needs and possible improvements.

The published Single-Nodal methodology makes it possible to combine a fluctuating generation model, an individual load profile, an ESS and the corresponding overall system topology in one model. This allows the user to mathematically find a technical optimum of the generation capacity and size of the ESS. It was observed that considering the individual user-group-specific and time-resolved load profile has a major impact on the ideal sizing results. When including new electrical loads, such as electric vehicles or heat pumps the ideal size of the PV battery system changes as well. The results show that electric vehicles especially increase the necessary storage demand, while the implementation of heat pumps leads to an increased PV system size. Additionally, there is a significant difference between the ideal technical design and economic design optima of PV battery systems under today's economic framework. Today, batteries do not contribute to a financial benefit in PV battery systems for households. When the predictions of price reductions for PV - and especially battery systems prove themselves true, the economic design optima move towards the technical optima.

HyFlow, the developed modelling framework, combines numerous calculation possibilities, as required in the set tasks. It allows the user to perform load flow calculations for all grid-bound energy carriers with the possibility of generic ESS implementation and interactions between the different energy grids. All grids, ESS and HE were characterized in a completely generic fashion, enabling technology-independent implementation of all mentioned elements. In addition, the requirement of allowing any kind of spatial scaling was successfully achieved via the presented cellular approach. It is possible to evaluate the effects of implementing more fluctuating energy or new consumer load profiles, such as electric vehicles on load flows and identify possible grid congestions. Additionally, solution strategies like the implementation of ESS or HE can be checked for their effectiveness in providing grid-relieving effects. The results of the case studies show that the usage of a large share of PV potentials, which is necessary for achieving the #mission2030 goals, possibly leads to grid congestions at multiple levels. Smaller decentralized ESS and HE can provide substantial improvements for the grid in residential energy systems, but the fluctuations on a large scale cannot be fully overcome with these technologies. However, larger and more centralized ESS or HE may lead to grid congestions from and to these elements, if high shares of fluctuating energy are implemented. The ideal level of centralization for ESS and HE is the main subsequent research question.

The following paragraph summarizes the most important findings of this thesis:

Key finding 1

The ideal sizing of PV battery systems is highly dependent on the household type and the individual load profile. It should not be designed based on information on the energy consumption only.

Key finding 2

The optima of the technical sizing of PV battery systems deviate greatly from current economic optima. In the future both optima will approach one another. This is mainly due to the increased profitability of batteries.

Key finding 3

The realization of Austria's #mission2030 strategy will lead to negative residual loads in more than 50 % of the year, with negative peaks of above 15 GW. In order to use this excess electricity and prevent grid congestions, energy storage and sector coupling on a large scale is an absolute necessity.

Key finding 4

Numerous decentralized and small-scale energy storage and sector coupling units can significantly smooth most of the municipal residual load. However, the effect on the maximum power peaks is very limited without large scale units.

Key finding 5

When realizing the electricity generation mix according to #mission2030, the only viable option to store the expected large amounts of excess electricity is Power2Gas, despite the lower efficiency compared to Power2Heat.

Key finding 6

The degree of centralization and the placement of sector coupling units is absolutely key to prevent grid congestions on lines from and to these units.

Outlook

The Single-Nodal sizing approach for PV battery systems is already an advanced model without implemented simplifications affecting the accuracy to a significant extent. However, the tool could be applied to different datasets. As this analysis was performed with radiation and temperature values for Austria only, it would also be interesting to evaluate regional differences in sizing results. Contrasting load profiles from other world regions (caused by effects such as different daily routines, more or less electrical heating, temperature difference, etc.), and a different PV power generation profile or other economic frameworks could lead to very different results. This methodology, however, is suitable to point out these differences and give a wider perspective on the regional distribution of ideal PV storage systems. In addition to the implemented PV storage system, which acts as Single-Nodal system, other physical systems, such as wind power generation, or even hybrid generation approaches, can be modelled and combined with the presented sizing approach.

HyFlow is a complex software tool, combining many different calculation procedures with a lot of dependencies, which have to be taken into account. Due to the wide range of applications, certain simplifications were made in order to prevent exorbitant computation times. This leaves several severe improvement possibilities and opportunities to improve the range of functions and calculation accuracy. One of the major simplifications causing deviations in the results is the made assumptions in the load flow calculations. Adopting the electrical load flow methodology from a DC to an AC-LFC, the implementation of real gas instead of ideal gas for natural gas LFC or thermal inertia in the district heating LFC are the key points. Additionally, a probabilistic LFC would help to correctly integrate statistical probabilities in the LFC. Introducing more control strategies of the energy storage elements and the sector coupling units would also help to answer a wider range of research questions. Possible control strategies could minimize congestions and operate on behalf of the grid. Also, economic approaches, such as nodal pricing, dependent on the actual grid status could further improve *HyFlow*. A graphical user interface could help to reach a wider range of users without programming skills. Another major focus should be on the appliance of the software. A correct representation of the Austrian grid of all energy carriers could help to successfully realize the energy transition in this country. Particular attention should be paid to the placement of flexibility options within an integrated approach.

6 DISCUSSION

This section is dedicated to uncertainties of the published methodology and of the results, due to simplifications in the used models and the assumptions made. Albert Einstein allegedly said that everything must be made as simple as possible, but not simpler. A similar thought is also formulated by George E.P. Box in his book about empirical model-building in 1987. [191]

"Remember that all models are wrong. The practical question is how wrong do they have to be, to not be useful."

The following section describes the main simplifications, assumptions and if possible gives an estimation of potentially implied errors. This should enable the reader to evaluate if the published methodologies are useful for their individual tasks. Since all introduced models are technical models based on physical laws, most errors relate to the simplifications of fundamental thermodynamic and electrodynamic processes. The second major assumption, affecting all model parts is the static approach, neglecting all dynamic events. Additionally, major parts of introduced models are based on weather conditions, which are subject to statistical fluctuations we cannot control and predict. The following list aims to describe the limitations, assumptions and simplifications in a more detailed fashion.

- Weather data uncertainty

  The weather is subject to natural variability. Weather data is used for three major purposes in this thesis: PV generation modelling, energy demand modelling for heating and natural gas, and to calculate the necessary generation capacities to reach the #mission2030 goals. PV modelling requires temperature and irradiation data. In this case measured data from ZAMG for the weather year 2014 was selected, as it was a representative year, according to ZAMG. An alternative is the usage of TRY weather data, but even with these representative years, variations to future years are unavoidable. These uncertainties are also affecting the modeled heating demand. Additionally, to the temperature and irradiation data, fluctuations in wind speeds and precipitation cause uncertainties in the national energy mix through wind power and hydropower.

- Demand modelling

  The energy demand for electricity, natural gas and district heating are modelled with the help of synthetic load profiles and standardized load profiles. The advantages, disadvantages and the right usage of both tools are described in section 2.2. Also, the

expected error, by using standardized load profiles is discussed and illustrated depending on the number of aggregated users. It has to be noted that in the Single-Nodal results, the household energy consumption is considered to be constant for the following years. Depending on possible energy efficiency measures, or electrification effects, the future electricity demand may increase or decrease, which is a potential error source for the Single-Nodal results.

- Single-Nodal model

  The single diode PV generation model including a series and parallel resistance within the Single-Nodal model is already detailed and sophisticated, covering the most important losses of the PV panels. Other system components like the inverter and the battery are also simulated with state of the art models. Load-dependent efficiencies are included, as well as the depth of discharge and losses in the power electronics. However, a few effects are not taken into consideration. Thermal inertia of the PV panels, as well as control and standby losses of the PV-battery system, are neglected. Additionally, the control strategy does not include any forecasts on weather conditions or the expected electricity demand.

- Electrical LFC

  The electrical LFC and the used simplifications are already thoroughly discussed in section 2.3.1. Additionally, all simplifications leading from the most sophisticated AC-LFC model to the DC-LFC model are explained in the same section. However, depending on the X/R ratio of the electric lines, deviations in the load flows of up to 5 % in high voltage grids and potentially more in medium or low-voltage grids are possible.

- Natural gas LFC

  The natural gas load flow calculation is based on ideal gases, without the consideration of molecular interactions. Rüdiger [63] analyzed the differences in results depending on the pressure levels. His conclusion was that in low-pressure grids (30 mbar) the deviations in terms of the flow rate are between 0.0 and 2.9 %, and in high-pressure grids (120 bar), the amount of the deviation varies between 0.01 and 2.63 %. As mentioned in the outlook, it is planned to adopt the *HyFlow* software to real gases in the near future. Additionally, the grids do not have any additional installations, such as bends and consist solely of straight pipes, which reduces the accuracy of the pressure losses within the system. Furthermore, possible mixtures of hydrogen and natural gas in the pipeline infrastructure is not implemented in *HyFlow*.

- District heating LFC

  The district heating LFC has numerous simplifications. One of the major assumptions is the return flow temperature at the start of each consumer is constant. This means that the flow rate is perfectly controlled, in order to reach this constant backflow starting temperature. Another major simplification is the neglect of thermal inertia and dynamic effects. Additionally, the ambient temperature around the underground pipes is considered to be constant over the whole year. The heat exchangers at the consumers are assumed to operate without losses. In the calculation of the case studies, differences in altitude have been neglected as well.

- Efficiencies ESS and HE

  While part-load efficiencies of ESS are considered in the Single-Nodal model, all efficiencies of ESS are considered constant in the Multi-Nodal model, due to the effects on the computation time. This is also applicable to HE.

- System boundaries HE

  Some sector coupling technologies are only considered within certain system boundaries. This limitation is especially important for the heat pump - and P2G technology. Heat pumps within *HyFlow* do not take the (low-temperature) heat source into account and assume that it is available at a constant temperature and without limits. In terms of the P2G technology, it has to be noted that the availability of H_2O for the electrolysis or CO_2 for a possibly following methanization is not considered within the *HyFlow* modelling framework.

- Control strategies ESS and HE

  The operational profile of ESS and HE are largely based on two control strategies. While the user-oriented control strategy, labeled as “cell-serving” aims to maximize the internal energy usage and therefore its own DSS, the “system-serving” algorithm is based on optimizing the DSS of the overall system. Other relevant control strategies, especially economic or technical optimizations, with included forecasts are not implemented in the *HyFlow* software. Other control strategies might lead to deviations compared to the published results of this work.

7 REFERENCES

[1] *A new world*: *The geopolitics of the energy transformation*, Global Commission on the Geopolitics of Energy Transformation, Abu Dhabi, United Arab Emirates, 2019.

[2] V. Masson-Delmotte, H.-O. P. Zhai, D. Pörtner et al., *Global warming of 1.5°C*, IPCC, [Geneva, Switzerland], 2018.

[3] "mission2030: Austrian Climate and Energy Strategy," September 2018, https://mission2030.info/wp-content/uploads/2018/10/Klima-Energiestrategie_en.pdf.

[4] European Commission, "Energy 2020: A strategy for competitive, sustainable and secure energy," https://ec.europa.eu/energy/en/topics/energy-strategy/2020-energy-strategy [cited 28.10.15].

[5] European Commission, "Energy 2030 - Communication from the Commission to the European Parliament, the Council, the European Economic and Social Committee and the Committee of the Regions: A policy framework for climate and energy in the period from 2020 to 2030," January 2014, https://eur-lex.europa.eu/legal-content/EN/TXT/PDF/?uri=CELEX:52014DC0015&from=EN.

[6] "Report of the Conference of the Parties on its twenty-fourthsession, held in Katowicefrom 2to 15December 2018," Conference of the Parties, March 2019, https://unfccc.int/sites/default/files/resource/10a1.pdf?download.

[7] United Nations Framework Convention of Climate Change, ed., *United Nations Framework Convention on Climate Change*: *Adoption of the Paris agreement*, United Nations, Paris, 2015.

[8] "Trilemma Index," 4/8/2019, https://www.worldenergy.org/wp-content/uploads/2018/10/World-Energy-Trilemma-Index-2018.pdf.

[9] Oesterrreichs Energie, "Vorschlag von Oesterreichs Energie zur Umsetzung des Erneubaren-Ausbauziels gemäß #mission2030 durch das Erneuerbaren Ausbau Gesetz: Stand Jänner 2019," 01/2019, https://oesterreichsenergie.at/positionen-standpunkte/fahrplan-2030-umsetzung-mission2030.html.

[10] "Actual Load 2016: Total final electricity consumption in the control area APG, including grid losses - 15min values," https://www.apg.at/en/markt/Markttransparenz/load/Ist-Last.

[11] "Generation per type - 2016: Net power plant feed-in in 15min values," https://www.apg.at/de/markt/Markttransparenz/erzeugung/Erzeugung%20pro%20Typ.

[12] C. Sejkora and T. Kienberger, “Dekarbonisierung der Industrie mithilfe elektrischer Energie?,” in *15. Symposium Energieinnovation,* Technische Universität Graz, Ed., 2018.

[13] J. M. Alemany, B. Arendarski, P. Lombardi et al., “Accentuating the renewable energy exploitation: Evaluation of flexibility options,” *International Journal of Electrical Power & Energy Systems*, vol. 102, pp. 131–151 ,doi: 10.1016/j.ijepes.2018.04.023, 2018.

[14] C. Mazur, S. Hall, J. Hardy et al., “Technology is not a Barrier: A Survey of Energy System Technologies Required for Innovative Electricity Business Models Driving the Low Carbon Energy Revolution,” *Energies*, vol. 12, no. 3, p. 428 ,doi: 10.3390/en12030428, 2019.

[15] “Global Solar Atlas: Global horizontal irradiation,” https://globalsolaratlas.info/.

[16] S. A. Kalogirou, *Solar energy engineering*: *Processes and systems*, AP Academic Press/Elsevier, Amsterdam, 2014.

[17] B. Zhao, C. Wang, and X. Zhang, *Grid-integrated and standalone photovoltaic distributed generation systems*: *Analysis, design and control*, Wiley; China Electric Power Press, Hoboken, NJ, USA, 2018.

[18] J. L. Gray, “The Physics of the Solar Cell,” in *Handbook of Photovoltaic Science and Engineering,* A. Luque and S. Hegedus, Eds., vol. 19, pp. 82–129, John Wiley & Sons, Ltd, Chichester, UK, 2010.

[19] C. Synwoldt, *Dezentrale Energieversorgung mit regenerativen Energien*, Springer Fachmedien Wiesbaden, Wiesbaden, 2016.

[20] S. Philipps, “Photovoltaics Report,” February 2018, https://www.ise.fraunhofer.de/content/dam/ise/de/documents/publications/studies/Photovoltaics-Report.pdf.

[21] V. J. Chin, Z. Salam, and K. Ishaque, “Cell modelling and model parameters estimation techniques for photovoltaic simulator application: A review,” *Applied Energy*, vol. 154, pp. 500–519 ,doi: 10.1016/j.apenergy.2015.05.035, 2015.

[22] N. M. A. Alrahim Shannan, N. Z. Yahaya, and B. Singh, “Single-diode model and two-diode model of PV modules: A comparison,” in *2013 IEEE International Conference on Control System, Computing and Engineering*, pp. 210–214, IEEE, 29.11.2013 - 01.12.2013.

[23] V. Tamrakar, G. S.C, and Y. Sawle, “Single-Diode Pv Cell Modeling And Study Of Characteristics Of Single And Two-Diode Equivalent Circuit,” *Electrical and Electronics*

Engineering: An International Journal, vol. 4, no. 3, pp. 13–24 ,doi: 10.14810/elelij.2015.4302, 2015.

[24] "Erzeugung nach Typ," 1/18/2018, https://www.apg.at/de/markt/Markttransparenz/erzeugung/Erzeugung%20pro%20Typ.

[25] "2018 - Hydropower Status Report: Sector trends and insights," https://www.hydropower.org/sites/default/files/publications-docs/iha_2018_hydropower_status_report_4.pdf.

[26] D. Aigner, C. Sorooshian, and P. Kerwin, "Conditional Demand Analysis for Estimating Residential End-Use Load Profiles," *The Energy Journal,* Vol. 5, No. 3, pp. 81–98, 1984.

[27] R. Bartels, D. G. Fiebig, M. Garben et al., "An end-use electricity load simulation model," *Utilities Policy*, vol. 2, no. 1, pp. 71–82 ,doi: 10.1016/0957-1787(92)90055-N, 1992.

[28] M. Parti and C. Parti, "The Total and Appliance-Specific Conditional Demand for Electricity in the Household Sector," *The Bell Journal of Economics*, vol. 11, no. 1, p. 309 ,doi: 10.2307/3003415, 1980.

[29] A. Grandjean, J. Adnot, and G. Binet, "A review and an analysis of the residential electric load curve models," *Renewable and Sustainable Energy Reviews*, vol. 16, no. 9, pp. 6539–6565 ,doi: 10.1016/j.rser.2012.08.013, 2012.

[30] VDEW, *Zuordnung der VDEW-Lastprofile zum Kundengruppenschlüssel*.

[31] E-Control, *Sonstige Marktregeln Strom Kapitel 6 - Zählwerte, Datenformate und standardisierte Lastprofile*.

[32] B. Gao, X. Liu, and Z. Zhu, "A Bottom-Up Model for Household Load Profile Based on the Consumption Behavior of Residents," *Energies*, vol. 11, no. 8, p. 2112 ,doi: 10.3390/en11082112, 2018.

[33] N. Pflugradt and U. Muntwyler, "Synthesizing residential load profiles using behavior simulation," *Energy Procedia*, vol. 122, pp. 655–660 ,doi: 10.1016/j.egypro.2017.07.365, 2017.

[34] I. Richardson, M. Thomson, D. Infield et al., "Domestic electricity use: A high-resolution energy demand model," *Energy and Buildings*, vol. 42, no. 10, pp. 1878–1887 ,doi: 10.1016/j.enbuild.2010.05.023, 2010.

[35] M. Stokes, *Removing barriers to embedded generation : a fine-grained load model to support low voltage network performance analysis,* PhD Thesis, De Montfort University, 2005.

[36] C. F. Walker and J. L. Pokoski, “Residential Load Shape Modelling Based on Customer Behavior,” *IEEE Transactions on Power Apparatus and Systems*, PAS-104, no. 7, pp. 1703–1711 ,doi: 10.1109/TPAS.1985.319202, 1985.

[37] J. Widén, M. Lundh, I. Vassileva et al., “Constructing load profiles for household electricity and hot water from time-use data—Modelling approach and validation,” *Energy and Buildings*, vol. 41, no. 7, pp. 753–768 ,doi: 10.1016/j.enbuild.2009.02.013, 2009.

[38] R. Yao and K. Steemers, “A method of formulating energy load profile for domestic buildings in the UK,” *Energy and Buildings*, vol. 37, no. 6, pp. 663–671 ,doi: 10.1016/j.enbuild.2004.09.007, 2005.

[39] I. Knight, *European and Canadian non-HVAC electric and DHW load profiles for use in simulating the performance of residential cogeneration systems*: *A report of Subtask A of FC+COGEN-SIM, the Stimulation of Building-Integrated Fuel Cell and Other Cogeneration Systems, Annex 42 of the International Conservation in Buildings and Community Systems Programme*, [Natural Resources Canada], [Ottawa], 2007.

[40] A. Capasso, W. Grattieri, R. Lamedica et al., “A bottom-up approach to residential load modeling,” *IEEE Transactions on Power Systems*, vol. 9, no. 2, pp. 957–964 ,doi: 10.1109/59.317650, 1994.

[41] J. Widén and E. Wäckelgård, “A high-resolution stochastic model of domestic activity patterns and electricity demand,” *Applied Energy*, vol. 87, no. 6, pp. 1880–1892 ,doi: 10.1016/j.apenergy.2009.11.006, 2010.

[42] M. Metz, *Flexible Energieversorgung*: *Modellierung der Last- und Erzeugungssituation dezentraler Versorgungsgebiete zur Bestimmung der Systemflexibilität,* Dissertation, Technische Universität Dortmund, 2013.

[43] D. Fischer, A. Härtl, and B. Wille-Haussmann, “Model for electric load profiles with high time resolution for German households,” *Energy and Buildings*, vol. 92, pp. 170–179 ,doi: 10.1016/j.enbuild.2015.01.058, 2015.

[44] N. Pflugradt, *Modellierung von Wasser- und Energieverbräuchen in Haushalten,* Dissertation, Technische Universität Chemnitz, 04/2016.

[45] D. Dörner, *Bauplan für eine Seele*, Rowohlt Verl., Reinbek bei Hamburg, 1999.

[46] D. Dörner and C. Storck, *Die Mechanik des Seelenwagens*: *Eine neuronale Theorie der Handlungsregulation*, Huber, Bern, 2002.

[47] T. Gobmaier, *Entwicklung und Anwendung einer Methodik zur Synthese zukünftiger Verbraucherlastgänge,* PhD, Technische Universität München, 2013.

[48] T. Hofmann, *Modellierung zur Ermittlung von elektrischen Industrielastgängen,* Bachelorarbeit, Montanuniversitaet Leoben, 06/2018.

[49] Y. Karadede, G. Ozdemir, and E. Aydemir, "Breeder hybrid algorithm approach for natural gas demand forecasting model," *Energy*, vol. 141, pp. 1269–1284 ,doi: 10.1016/j.energy.2017.09.130, 2017.

[50] D. Sen, M. E. Günay, and K. M. Tunç, "Forecasting annual natural gas consumption using socio-economic indicators for making future policies," *Energy*, vol. 173, pp. 1106–1118 ,doi: 10.1016/j.energy.2019.02.130, 2019.

[51] W. Zhang and J. Yang, "Forecasting natural gas consumption in China by Bayesian Model Averaging," *Energy Reports*, vol. 1, pp. 216–220 ,doi: 10.1016/j.egyr.2015.11.001, 2015.

[52] "Weiterentwicklung des Standardlastprofilverfahrens Gas," 2015.

[53] R. Mirkov, H. Friedl, H. Leövey et al., "Sigmoid Models Utilized in Optimization of Gas Transportation Networks," *Proceeding IWSM*, vol. 2010.

[54] W. Medjroubi, U. P. Müller, M. Scharf et al., "Open Data in Power Grid Modelling: New Approaches Towards Transparent Grid Models," *Energy Reports*, vol. 3, pp. 14–21 ,doi: 10.1016/j.egyr.2016.12.001, 2017.

[55] C.-L. Chen, C.-T. Lai, and J.-Y. Lee, "Transshipment model-based MILP (mixed-integer linear programming) formulation for targeting and design of hybrid power systems," *Energy*, vol. 65, pp. 550–559 ,doi: 10.1016/j.energy.2013.11.021, 2014.

[56] DIgSILENT GmbH, *DIgSILENT PowerFactory*, DIgSILENT GmbH, Gomaringen, 2018.

[57] NEPLAN AG, *NEPLAN*, NEPLAN AG, Küsnacht, 2018.

[58] Siemens AG, *PSS SINCAL*, Siemens AG.

[59] Göran Andersson, "Power System Analysis: Power Flow Analysis Fault Analysis Power System Dynamics and Stability," September 2012, http://research.iaun.ac.ir/pd/bahador.fani/pdfs/UploadFile_6990.pdf.

[60] J. J. Grainger and W. D. Stevenson, *Power system analysis*, McGraw Hill, New York, NY, 1994.

[61] K. Purchala, L. Meeus, D. van Dommelen et al., "Usefulness of DC power flow for active power flow analysis," in *IEEE Power Engineering Society General Meeting, 2005*, pp. 2457–2462, IEEE, June 12-16, 2005.

[62] D. Brkić, “Iterative Methods for Looped Network Pipeline Calculation,” *Water Resources Management*, vol. 25, no. 12, pp. 2951–2987 ,doi: 10.1007/s11269-011-9784-3, 2011.

[63] J. Rüdiger, *Gasnetzsimulation durch Potentialanalyse,* Dissertation, Helmut-Schmidt-Universität; Universität der Bundeswehr Hamburg, 2009.

[64] D. Brkić and P. Praks, “Short Overview of Early Developments of the Hardy Cross Type Methods for Computation of Flow Distribution in Pipe Networks,” *Applied Sciences*, vol. 9, no. 10, p. 2019 ,doi: 10.3390/app9102019, 2019.

[65] H. Cross, “Analysis of flow in networks of conduits or conductors,” https://www.ideals.illinois.edu/bitstream/2142/4433/1/engineeringexperv00000i00286_tei.xml.

[66] Harald Raupenstrauch and Andrea Werner, *Vorlesungsunterlagen Wärmeübertragung*, Montanuniversitaet Leoben, 2013.

[67] D. Olsthoorn, F. Haghighat, and P. A. Mirzaei, “Integration of storage and renewable energy into district heating systems: A review of modelling and optimization,” *Solar Energy*, vol. 136, pp. 49–64 ,doi: 10.1016/j.solener.2016.06.054, 2016.

[68] B. Talebi, P. A. Mirzaei, A. Bastani et al., “A Review of District Heating Systems: Modeling and Optimization,” *Frontiers in Built Environment*, vol. 2, no. 16, p. 7839 ,doi: 10.3389/fbuil.2016.00022, 2016.

[69] C. Weber, F. Maréchal, and D. Favrat, “Design and optimization of district energy systems,” in *17th European Symposium on Computer Aided Process Engineering*, vol. 24, pp. 1127–1132, Elsevier, 2007.

[70] L. Brand, A. Calvén, J. Englund et al., “Smart district heating networks – A simulation study of prosumers’ impact on technical parameters in distribution networks,” *Applied Energy*, vol. 129, pp. 39–48 ,doi: 10.1016/j.apenergy.2014.04.079, 2014.

[71] T. Laajalehto, M. Kuosa, T. Mäkilä et al., “Energy efficiency improvements utilising mass flow control and a ring topology in a district heating network,” *Applied Thermal Engineering*, vol. 69, 1-2, pp. 86–95 ,doi: 10.1016/j.applthermaleng.2014.04.041, 2014.

[72] H. Lund, S. Werner, R. Wiltshire et al., “4th Generation District Heating (4GDH),” *Energy*, vol. 68, pp. 1–11 ,doi: 10.1016/j.energy.2014.02.089, 2014.

[73] R. Lund and S. Mohammadi, “Choice of insulation standard for pipe networks in 4 th generation district heating systems,” *Applied Thermal Engineering*, vol. 98, pp. 256–264 ,doi: 10.1016/j.applthermaleng.2015.12.015, 2016.

[74] H. Madsen, K. Sejling, H. T. Søgaard et al., “On flow and supply temperature control in district heating systems,” *Heat Recovery Systems and CHP*, vol. 14, no. 6, pp. 613–620 ,doi: 10.1016/0890-4332(94)90031-0, 1994.

[75] A. Vandermeulen, B. van der Heijde, and L. Helsen, “Controlling district heating and cooling networks to unlock flexibility: A review,” *Energy*, vol. 151, pp. 103–115 ,doi: 10.1016/j.energy.2018.03.034, 2018.

[76] G. Schweiger, R. Heimrath, B. Falay et al., “District energy systems: Modelling paradigms and general-purpose tools,” *Energy*, vol. 164, pp. 1326–1340 ,doi: 10.1016/j.energy.2018.08.193, 2018.

[77] H.-A. Loeliger, *Zeitdiskrete und statistische Signalverarbeitung,* Vorlesungsskriptum, ETH Zürich, 2016.

[78] M. Sterner and I. Stadler, *Energiespeicher - Bedarf, Technologien, Integration*, Springer Vieweg, Berlin, 2014.

[79] “Speicherunternehmen und Speicherkapazitäten in Österreich: Stand 2. September 2019,” https://www.e-control.at/marktteilnehmer/gas/gasmarkt/speicher.

[80] “Anzahl der Privathaushalte in Österreich von 2008 bis 2018,” 4/4/2019, https://de.statista.com/statistik/daten/studie/75454/umfrage/oesterreich-anzahl-der-haushalte/.

[81] Dirk Uwe Sauer, Peter Elsner, Isolde Arzberger et al., “Energiespeicher - Technologiesteckbrief zur Analyse „Flexibilitätskonzepte für die Stromversorgung 2050“,”.

[82] G. Fuchs, B. Lunz, M. Leuthold et al., “Technologischer Überblick zur Speicherung von Elektrizität: Überblick zum Potenzial und zu Perspektiven des Einsatzes elektrischer Speichertechnologien,” RWTH Aachen, 09/2012, https://www.researchgate.net/profile/Dirk_Sauer/publication/322478141_Technologischer_Uberblick_zur_Speicherung_von_Elektrizitat/links/5b6ef78692851ca65055dbaa/Technologischer-Ueberblick-zur-Speicherung-von-Elektrizitaet.pdf.

[83] C. Hewicker, J. Raadschelders, O. Werner et al., “Energiespeicher in der Schweiz: Bedarf, Wirtschaftlichkeit und Rahmenbedingungen im Kontext der Energiestrategie 2050,” 12/2013, https://www.energie-aktuell.ch/uploads/news/Studie_Energiespeicher_20131212.pdf.

[84] X. Luo, J. Wang, M. Dooner et al., “Overview of current development in electrical energy storage technologies and the application potential in power system operation,” *Applied Energy*, vol. 137, pp. 511–536 ,doi: 10.1016/j.apenergy.2014.09.081, 2015.

[85] A. Streitmayer, *Modell zur Evaluierung von Energiespeichertechnologien unter Berücksichtigung auftretender Verluste,* Bachelorarbeit, Montanuniversität Leoben, 11/2017.

[86] E. Guelpa, A. Bischi, V. Verda et al., “Towards future infrastructures for sustainable multi-energy systems: A review,” *Energy*, vol. 184, pp. 2–21 ,doi: 10.1016/j.energy.2019.05.057, 2019.

[87] H. Lund, P. A. Østergaard, D. Connolly et al., “Smart energy and smart energy systems,” *Energy*, vol. 137, pp. 556–565 ,doi: 10.1016/j.energy.2017.05.123, 2017.

[88] P. Mancarella, “MES (multi-energy systems): An overview of concepts and evaluation models,” *Energy*, vol. 65, pp. 1–17 ,doi: 10.1016/j.energy.2013.10.041, 2014.

[89] A. Bloess, W.-P. Schill, and A. Zerrahn, “Power-to-heat for renewable energy integration: A review of technologies, modeling approaches, and flexibility potentials,” *Applied Energy*, vol. 212, pp. 1611–1626 ,doi: 10.1016/j.apenergy.2017.12.073, 2018.

[90] M. Bailera, P. Lisbona, L. M. Romeo et al., “Power to Gas projects review: Lab, pilot and demo plants for storing renewable energy and CO 2,” *Renewable and Sustainable Energy Reviews*, vol. 69, pp. 292–312 ,doi: 10.1016/j.rser.2016.11.130, 2017.

[91] J. D. Holladay, J. Hu, D. L. King et al., “An overview of hydrogen production technologies,” *Catalysis Today*, vol. 139, no. 4, pp. 244–260 ,doi: 10.1016/j.cattod.2008.08.039, 2009.

[92] M. Ni, Leung, Michael K. H., and Leung, Dennis Y. C., “Technological development of hydrogen production by solid oxide electrolyzer cell (SOEC),” *International Journal of Hydrogen Energy*, vol. 33, no. 9, pp. 2337–2354 ,doi: 10.1016/j.ijhydene.2008.02.048, 2008.

[93] T. Smolinka, M. Günther, and J. Garche, “NOW-Studie: Stand und Entwicklungspotenzial der Wasserelektrolyse zur Herstellung von Wasserstoff aus regenerativen Energien,” Fraunhofer ISE, 2011, http://www.now-gmbh.de/fileadmin/user_upload/RE_Publikationen_NEU_2013/Publikationen_NIP/NOW-Studie-Wasserelektrolyse-2011.pdf.

[94] P. Balcombe, D. Rigby, and A. Azapagic, “Environmental impacts of microgeneration: Integrating solar PV, Stirling engine CHP and battery storage,” *Applied Energy*, vol. 139, pp. 245–259 ,doi: 10.1016/j.apenergy.2014.11.034, 2015.

[95] H. Yu, T. Gundersen, and X. Feng, “Process integration of organic Rankine cycle (ORC) and heat pump for low temperature waste heat recovery,” *Energy*, vol. 160, pp. 330–340 ,doi: 10.1016/j.energy.2018.07.028, 2018.

[96] P. Biermayr, “Erneuerbare Energie in Zahlen 2018: Entwicklung in Österreich - Datenbasis 2017,” 12/2018, https://www.bmnt.gv.at/dam/jcr:939cb822-6f5f-41e3-bad4-6546feaf88e5/eEiZ2018-Brosch%C3%BCre.pdf.

[97] A. Bejan, “Fundamentals of exergy analysis, entropy generation minimization, and the generation of flow architecture,” *International Journal of Energy Research*, vol. 26, no. 7, pp. 0–43 ,doi: 10.1002/er.804, 2002.

[98] F. Khalid, I. Dincer, and M. A. Rosen, “Energy and exergy analyses of a solar-biomass integrated cycle for multigeneration,” *Solar Energy*, vol. 112, pp. 290–299 ,doi: 10.1016/j.solener.2014.11.027, 2015.

[99] J. Rosen, *The future role of renewable energy sources in European electricity supply*: *A model-based analysis for the EU-15*, Univ.-Verl. Karlsruhe, Karlsruhe, 2008.

[100] G. F. Frate, M. Antonelli, and U. Desideri, “A novel Pumped Thermal Electricity Storage (PTES) system with thermal integration,” *Applied Thermal Engineering*, vol. 121, pp. 1051–1058 ,doi: 10.1016/j.applthermaleng.2017.04.127, 2017.

[101] L. Kriechbaum, B. Böckl, J. Vopava et al., “SmartExergy – Primary Energy Efficient and Hybrid Grid Solutions for Municipal Energy Supply Systems,” in *NEIS Conference 2016,* D. Schulz, Ed., pp. 133–139, Springer Fachmedien Wiesbaden, Wiesbaden, 2017.

[102] P. Bertoldi, *Talk at the International Workshop on Demand Response in Europe: Status, Barriers, Opportunities and Outlooks*, Ispra/Italy, 03.-04. March 2010.

[103] “A National Assessment of Demand Response Potential,” 2009, https://www.ferc.gov/industries/electric/indus-act/demand-response/dem-res-adv-metering.asp.

[104] J. Strueker and C. Dinther, “Demand Response in Smart Grids: Research Opportunities for the IS Discipline,” *AMCIS 2012 Proceedings 7*.

[105] N. G. Paterakis, O. Erdinç, and J. P.S. Catalão, “An overview of Demand Response: Key-elements and international experience,” *Renewable and Sustainable Energy Reviews*, vol. 69, pp. 871–891 ,doi: 10.1016/j.rser.2016.11.167, 2017.

[106] “380-kV Salzburgleitung: Projektinformation - Zahlen & Fakten,” https://www.apg.at/de/Projekte/380-kV-Salzburgleitung.

[107] “Bedarfsermittlung 2017-2030: Zusammenfassung der Konsultationsergebnisse,” Dezember 2017, https://www.netzausbau.de/SharedDocs/Downloads/DE/Publikationen/ZFBedarfsermittlung2030.pdf;jsessionid=1D1E1A540D3C6115BDD9428225CC74B3?__blob=publicationFile.

[108] “Fünf Schritte des Netzausbaus,” https://www.netzausbau.de/SharedDocs/Downloads/DE/Publikationen/Poster_Beteiligung.pdf;jsessionid=1D1E1A540D3C6115BDD9428225CC74B3?__blob=publicationFile.

[109] G. Calabrese, “Generating Reserve Capacity Determined by the Probability Method,” *Transactions of the American Institute of Electrical Engineers*, vol. 66, no. 1, pp. 1439–1450 ,doi: 10.1109/T-AIEE.1947.5059596, 1947.

[110] V. Pillai N, “Loss of Load Probability of a Power System,” *Journal of Fundamentals of Renewable Energy and Applications*, vol. 05, no. 01 ,doi: 10.4172/2090-4541.1000149, 2014.

[111] J. Figgener, D. Haberschusz, K.-P. Kairies et al., “Wissenschaftliches Mess- und Evaluierungsprogramm Solarstromspeicher 2.0: Jahresbericht 2018,” RWTH Aachen, 07/2018, https://www.bves.de/wp-content/uploads/2018/07/Speichermonitoring_Jahresbericht_2018_ISEA_RWTH_Aachen.pdf.

[112] P. Pearce and R. Slade, “Feed-in tariffs for solar microgeneration: Policy evaluation and capacity projections using a realistic agent-based model,” *Energy Policy*, vol. 116, pp. 95–111 ,doi: 10.1016/j.enpol.2018.01.060, 2018.

[113] “Installierte Leistung (kumuliert) der Photovoltaikanlagen in Deutschland in den Jahren 2000 bis 2017 (in Megawattpeak): Statista 2018,” 02/2018, https://de.statista.com/statistik/daten/studie/13547/umfrage/leistung-durch-solarstrom-in-deutschland-seit-1990/.

[114] D. Topic, G. Knezevic, D. Kosic et al., “Simplified Model for Optimal Sizing of the Off-Grid PV System Regarding Value of Loss of Load Probability,” *Tehnicki vjesnik - Technical Gazette*, vol. 25, Supplement 2 ,doi: 10.17559/TV-20171203150754, 2018.

[115] A. Fragaki and T. Markvart, “Stand-alone PV system design: Results using a new sizing approach,” *Renewable Energy*, vol. 33, no. 1, pp. 162–167 ,doi: 10.1016/j.renene.2007.01.016, 2008.

[116] P. Arun, R. Banerjee, and S. Bandyopadhyay, “Optimum sizing of photovoltaic battery systems incorporating uncertainty through design space approach,” *Solar Energy*, vol. 83, no. 7, pp. 1013–1025 ,doi: 10.1016/j.solener.2009.01.003, 2009.

[117] C. V. T. Cabral, D. O. Filho, A. S. A. C. Diniz et al., “A stochastic method for stand-alone photovoltaic system sizing,” *Solar Energy*, vol. 84, no. 9, pp. 1628–1636 ,doi: 10.1016/j.solener.2010.06.006, 2010.

[118] S. Semaoui, A. H. Arab, S. Bacha et al., “Optimal Sizing of a Stand-alone Photovoltaic System with Energy Management in Isolated Areas,” *Energy Procedia*, vol. 36, pp. 358–368 ,doi: 10.1016/j.egypro.2013.07.041, 2013.

[119] J. Hoppmann, J. Volland, T. S. Schmidt et al., “The economic viability of battery storage for residential solar photovoltaic systems – A review and a simulation model,” *Renewable and Sustainable Energy Reviews*, vol. 39, pp. 1101–1118 ,doi: 10.1016/j.rser.2014.07.068, 2014.

[120] J. Weniger, T. Tjaden, and V. Quaschning, “Sizing of Residential PV Battery Systems,” *Energy Procedia*, vol. 46, pp. 78–87 ,doi: 10.1016/j.egypro.2014.01.160, 2014.

[121] K. R. Khalilpour and A. Vassallo, “Technoeconomic parametric analysis of PV-battery systems,” *Renewable Energy*, vol. 97, pp. 757–768 ,doi: 10.1016/j.renene.2016.06.010, 2016.

[122] R. Khalilpour and A. Vassallo, “Planning and operation scheduling of PV-battery systems: A novel methodology,” *Renewable and Sustainable Energy Reviews*, vol. 53, pp. 194–208 ,doi: 10.1016/j.rser.2015.08.015, 2016.

[123] D. Magnor and D. U. Sauer, “Optimization of PV Battery Systems Using Genetic Algorithms,” *Energy Procedia*, vol. 99, pp. 332–340 ,doi: 10.1016/j.egypro.2016.10.123, 2016.

[124] M. Bost, B. Hirschl, and A. Aretz, “Effekte von Eigenverbrauch und Netzparität bei der Photovoltaik: Beginn der dezentralen Energierevolution oder Nischeneffekt?,” 2011,

https://www.ioew.de/uploads/tx_ukioewdb/Effekte_der_Netzparit%C3%A4t_-_Langfassung.pdf.

[125] J. Moshövel, G. Angenendt, D. Magnor, et al., eds., *Tool to determine economic capacity dimensioning in PV battery systems considering various design parameters*, Regional Center for Renewable Enegy and Energy Efficiency, 14.09-18.09.2015.

[126] D. Connolly, H. Lund, B. V. Mathiesen et al., "A review of computer tools for analysing the integration of renewable energy into various energy systems," *Applied Energy*, vol. 87, no. 4, pp. 1059–1082 ,doi: 10.1016/j.apenergy.2009.09.026, 2010.

[127] I. van Beuzekom, M. Gibescu, P. Pinson et al., "Optimal planning of integrated multi-energy systems," in *2017 IEEE Manchester PowerTech*, pp. 1–6, 2017.

[128] P. Mancarella, G. Andersson, J. A. Pecas-Lopes et al., "Modelling of integrated multi-energy systems: Drivers, requirements, and opportunities," in *2016 Power Systems Computation Conference (PSCC)*, pp. 1–22, IEEE, 2016.

[129] S. Collins, J. P. Deane, K. Poncelet et al., "Integrating short term variations of the power system into integrated energy system models: A methodological review," *Renewable and Sustainable Energy Reviews*, vol. 76, pp. 839–856 ,doi: 10.1016/j.rser.2017.03.090, 2017.

[130] A. D. Hawkes and M. A. Leach, "Impacts of temporal precision in optimisation modelling of micro-Combined Heat and Power," *Energy*, vol. 30, no. 10, pp. 1759–1779 ,doi: 10.1016/j.energy.2004.11.012, 2005.

[131] M. Welsch, D. Mentis, and M. Howells, "Long-Term Energy Systems Planning," in *Renewable Energy Integration,* L. E. Jones, Ed., pp. 215–225, Elsevier, 2014.

[132] I. van Beuzekom, M. Gibescu, and J. G. Slootweg, "A review of multi-energy system planning and optimization tools for sustainable urban development," in *2015 IEEE Eindhoven PowerTech*, pp. 1–7, 2015.

[133] N. Good, L. Zhang, A. Navarro-Espinosa et al., "High resolution modelling of multi-energy domestic demand profiles," *Applied Energy*, vol. 137, pp. 193–210 ,doi: 10.1016/j.apenergy.2014.10.028, 2015.

[134] V. Corrado, E. Fabrizio, and M. Filippi, "Modelling and optimization of multi-energy source building systems in the design concept phase," in *Proceedings of Clima 2007*: *WellBeeing indoors*, 2007.

[135] H. Lund and B. V. Mathiesen, “Energy system analysis of 100% renewable energy systems—The case of Denmark in years 2030 and 2050,” *Energy*, vol. 34, no. 5, pp. 524–531 ,doi: 10.1016/j.energy.2008.04.003, 2009.

[136] J. R. Pillai, K. Heussen, and P. A. Østergaard, “Comparative analysis of hourly and dynamic power balancing models for validating future energy scenarios,” *Energy*, vol. 36, no. 5, pp. 3233–3243 ,doi: 10.1016/j.energy.2011.03.014, 2011.

[137] M. Heimberger, T. Kaufmann, C. Maier et al., “Energieträgerübergreifende Planung und Analyse von Energiesystemen,” *e & i Elektrotechnik und Informationstechnik*, vol. 134, no. 3, pp. 229–237 ,doi: 10.1007/s00502-017-0504-4, 2017.

[138] F. Li, *Spatially explicit techno-economic optimisation modelling of UK heating futures,* PhD, University College London, 2013.

[139] S. Thiem, *Multi-modal on-site energy systems*: *Development and application of a superstructure-based optimization method for energy system design under consideration of part-load efficiencies,* PhD, Technische Universität München, 2017.

[140] M. Geidl, G. Koeppel, P. F. Perrod et al., “Energy hubs for the future,” *IEEE Power and Energy Magazine*, vol. 5, no. 1, pp. 24–30 ,doi: 10.1109/MPAE.2007.264850, 2007.

[141] M. Geidl and G. Andersson, “Optimal Power Flow of Multiple Energy Carriers,” *IEEE Transactions on Power Systems*, vol. 22, no. 1, pp. 145–155 ,doi: 10.1109/TPWRS.2006.888988, 2007.

[142] M. Geidl and G. Andersson, “Optimal power dispatch and conversion in systems with multiple energy carriers,” in *Proceedings of the 15th power system computation conference (PSSC)*, 2005.

[143] T. Krause, F. Kienzle, S. Art et al., “Maximizing exergy efficiency in multi-carrier energy systems,” in *Energy Society General Meeting*, pp. 1–8, 2010.

[144] G. Koeppel, *Reliability Considerations of Future Energy Systems:*: *Multi-Carrier Systemsand the Effect of Energy Storage,* Dissertation, ETH Zürich, 2007.

[145] P. E. Dodds, I. Staffell, A. D. Hawkes et al., “Hydrogen and fuel cell technologies for heating: A review,” *International Journal of Hydrogen Energy*, vol. 40, no. 5, pp. 2065–2083 ,doi: 10.1016/j.ijhydene.2014.11.059, 2015.

[146] I. Staffell, D. Scamman, A. Velazquez Abad et al., “The role of hydrogen and fuel cells in the global energy system,” *Energy & Environmental Science*, vol. 12, no. 2, pp. 463–491 ,doi: 10.1039/c8ee01157e, 2019.

[147] H. R. Ellamla, I. Staffell, P. Bujlo et al., “Current status of fuel cell based combined heat and power systems for residential sector,” *Journal of Power Sources*, vol. 293, pp. 312–328 ,doi: 10.1016/j.jpowsour.2015.05.050, 2015.

[148] B. Böckl, L. Kriechbaum, and T. Kienberger, “Analysemethode für kommunale Energiesysteme unter Anwendung des zellularen Ansatzes,” in *14. Symposium Energieinnovation*: *Energie für unser Europa,* Institut für Elektrizitätswirtschaft und Energieinnovation, Ed., TU Graz, Graz, 2016.

[149] Thomas Kienberger, Benjamin Böckl, and Lukas Kriechbaum, eds., *Hybrid approaches for municipal future enegy-grids*.

[150] P. Esslinger and R. Witzmann, eds., *Entwicklung und Verifikation eines stochastischen Verbraucherlastmodells für Haushalte*, 2012.

[151] J. Duffie and W. A. Beckman, *Solar Engineering of Thermal Processes*, Wiley, Hoboken, 2006.

[152] Patrick Pretschuh, *Solares Energiepotential kleiner und mittlerer Städte*, Montanuniversität Leoben, April 2016.

[153] Annette Hammer, *Anwendungsspezifische Solarstrahlungsinformationen aus Meteosat-Daten,* Disseration, Universität Oldenburg, 2001.

[154] John A. Duffie, William A. Beckman, *Solar Engineering of Thermal Processes, 4th Edition*, 2013.

[155] B. Y.H. Liu and R. C. Jordan, “The long-term average performance of flat-plate solar-energy collectors,” *Solar Energy*, vol. 7, no. 2, pp. 53–74 ,doi: 10.1016/0038-092X(63)90006-9, 1963.

[156] A. Skartveit and J. Asle Olseth, “Modelling slope irradiance at high latitudes,” *Solar Energy*, vol. 36, no. 4, pp. 333–344 ,doi: 10.1016/0038-092X(86)90151-9, 1986.

[157] T. M. Klucher, “Evaluation of models to predict insolation on tilted surfaces,” *Solar Energy*, vol. 23, no. 2, pp. 111–114 ,doi: 10.1016/0038-092X(79)90110-5, 1979.

[158] M. Mesri, A. Choucha, and L. Chaib, “Evaluation of Global Solar Radiation Models for Inclined Surfaces,” in *Proceedings of the 2015 International Conference on Electrical, Automation and Mechanical Engineering*, Atlantis Press, Paris, France, 26.07.2015 - 27.07.2015.

[159] ZAMG, “Einstrahlungsmessdaten und Temperaturmesswerte des Jahres 2014 für Leoben und Kapfenberg,”.

[160] H. Bellia, R. Youcef, and M. Fatima, “A detailed modeling of photovoltaic module using MATLAB,” *NRIAG Journal of Astronomy and Geophysics*, vol. 3, no. 1, pp. 53–61 ,doi: 10.1016/j.nrjag.2014.04.001, 2014.

[161] A. Kollros, *Simulation and operational modes of a plug and play storage for photovoltaic power,* Master Thesis, Montanuniversitaet Leoben, 09/2018.

[162] J. Weniger, S. Maier, L. Kranz et al., “Stromspeicher-Inspektion 2018,” November 2018, www.stromspeicher-inspektion.de.

[163] A. Mohapatra, B. Nayak, P. Das et al., “A review on MPPT techniques of PV system under partial shading condition,” *Renewable and Sustainable Energy Reviews*, vol. 80, pp. 854–867 ,doi: 10.1016/j.rser.2017.05.083, 2017.

[164] G. Sandou, S. Font, S. Tebbani et al., “Predictive Control of a Complex District Heating Network: Conference on Decision and Control, and the European Control Conference 2005, Seville, Spain,” in *Proceedings of the 44th IEEE*.

[165] B. Boeckl and T. Kienberger, ““Sizing of PV storage systems for different household types”,” *Journal of Energy Storage*, vol. 24, p. 100763 ,doi: 10.1016/j.est.2019.100763, 2019.

[166] Matthias Greiml, *Modellierung eines hybriden Netzes zur Ermittlung potentieller Speicherdienstleistungen,* Master Thesis, Montanuniversitaet Leoben, 09/2018.

[167] Lukas Leitner, *Methodik zur Speicherbedarfsermittlung und Lastflussminimierung im zellularen Ansatz,* Master Thesis, Montanuniversitaet Leoben, 09/2018.

[168] K. Manjunatha Prasad and R. B. Bapat, “The generalized Moore-Penrose inverse,” *Linear Algebra and its Applications*, vol. 165, pp. 59–69 ,doi: 10.1016/0024-3795(92)90229-4, 1992.

[169] D. Gladwin, R. Todd, A. J. Forsyth et al., “Battery energy storage systems for the electricity grid: UK research facilities,” in *8th IET International Conference on Power Electronics, Machines and Drives (PEMD 2016)*, p. 6, Institution of Engineering and Technology, 19-21 April 2016.

[170] Rainer Vor Dem Esche, “Benefits of Flywheels for Short Term Grid Stabilisation,”.

[171] M. Bianchi, L. Branchini, A. de Pascale et al., “Pump Hydro Storage and Gas Turbines Technologies Combined to Handle Wind Variability: Optimal Hydro Solution for an Italian Case Study,” *Energy Procedia*, vol. 82, pp. 570–576 ,doi: 10.1016/j.egypro.2015.11.872, 2015.

[172] S. Manchester and L. Swan, “Compressed Air Storage and Wind Energy for Time-of-day Electricity Markets,” *Procedia Computer Science*, vol. 19, pp. 720–727 ,doi: 10.1016/j.procs.2013.06.095, 2013.

[173] A. R. Mazhar, S. Liu, and A. Shukla, “A state of art review on the district heating systems,” *Renewable and Sustainable Energy Reviews*, vol. 96, pp. 420–439 ,doi: 10.1016/j.rser.2018.08.005, 2018.

[174] Statistik Austria, *Energiearmut in Österreich 2016*: *Haushaltsenergie und Einkommen*, 2019.

[175] C. Fünfgeld and C. Fiebig, “Bestimmung von Lastprofilen für unterbrechbare Verbrauchseinrichtungen: Abschlussbericht,” 2002, https://www.bdew.de/media/documents/Abschlussbericht-Bestimmung-Lastprofilen-unterbrechbare-Verbrauchseinrichtungen.pdf.

[176] J. Conrad and S. Greif, “Modelling Load Profiles of Heat Pumps,” *Energies*, vol. 12, no. 4, p. 766 ,doi: 10.3390/en12040766, 2019.

[177] J. Love, A. Z.P. Smith, S. Watson et al., “The addition of heat pump electricity load profiles to GB electricity demand: Evidence from a heat pump field trial,” *Applied Energy*, vol. 204, pp. 332–342 ,doi: 10.1016/j.apenergy.2017.07.026, 2017.

[178] *Evaluation of grid relieving measures for integrating electric vehicles in a suburban low-voltage grid*, 03-06.06.2019.

[179] A. Sulzenbacher, *Niederfrequente Netzrückwirkungen von Elektrofahrzeugen*, TU Graz, 2016.

[180] S. Rezaee, E. Farjah, and B. Khorramdel, “Probabilistic Analysis of Plug-In Electric Vehicles Impact on Electrical Grid Through Homes and Parking Lots,” *IEEE Transactions on Sustainable Energy*, vol. 4, no. 4, pp. 1024–1033 ,doi: 10.1109/TSTE.2013.2264498, 2013.

[181] “The power to change: Solar and wind cost reduction potential to 2025,” 06/2016, https://www.irena.org/-/media/Files/IRENA/Agency/Publication/2016/IRENA_Power_to_Change_2016.pdf.

[182] W. Cole and A. W. Frazier, “Cost Projections for Utility-Scale Battery Storage,”.

[183] Bundesministerium für Wissenschaft, Forschung und Wirtschaft, *408. Verordnung Ökostrom-Einspeisetarifverordnung*: *ÖSET-VO 2018*, 2018.

[184] Austria Gas Clearing & Settlement, “Lastprofile Prozessgas ab 01.04.2019,” https://www.agcs.at/de/clearing/technisches/lastprofile/lastprofile_ab_01.04.2009.

[185] D. Schmidt, *Steinmüller-Taschenbuch Rohrleitungstechnik*, Vulkan-Verl., Essen, 1995.

[186] Amt der Steiermärkischen Landesregierung, “Solardachkataster Steiermark,” 05/2013, http://www.gis.steiermark.at/cms/beitrag/11864478/73081691/.

[187] S. Moser, S. Goers, K. de Bruyn et al., “Renewables4Industry: Abstimmung des Energiebedarfs von industriellen Anlagen und der Energieversorgung aus fluktuierenden Erneuerbaren,” 2018.

[188] “Energy balances,” May 25th, 2018, https://www.statistik.at/web_en/statistics/EnergyEnvironmentInnovationMobility/energy_environment/energy/energy_balances/index.html.

[189] “Register-based Census 2011 - Persons employed on the Local Unit,” https://www.statistik.at/web_en/statistics/Economy/enterprises/local_units_of_employment_from_census_2011/index.html.

[190] “Useful energy analysis,” December 19th, 2019, https://www.statistik.at/web_en/statistics/EnergyEnvironmentInnovationMobility/energy_environment/energy/useful_energy_analysis/index.html.

[191] G. E. P. Box and N. R. Draper, *Empirical model-building and response surfaces*, John Wiley & Sons, Oxford, England, 1987.